HIGH ENERGY PHYSICS

VECTOR MESON PRODUCTION IN MESON-NUCLEUS AND PROTON-NUCLEUS COLLISIONS AT 530 GEV/c

Subramanian Kartik

Submitted to the faculty of the Graduate School in partial fulfillment of the requirements of the degree

Doctor of Philosophy

in the Department of Physics Indiana University

June 1991

INDIANA UNIVERSITY

Physics Department, Bloomington, IN 47405

Accepted by the Graduate Faculty, Indiana University, in partial fufillment of the requirements of the degree of Doctor of Philosophy.

Prof. Alex Dzierba, Ph.D

Doctoral Committee

Prof. Andrzej Zieminski, Ph.D

Prof. Jack Martin, Ph.D

July 1, 1991

Prof. Don Lichtenberg, Ph.D

VECTOR MESON PRODUCTION IN MESON-NUCLEUS AND PROTON-NUCLEUS COLLISIONS AT 530 GEV/C

Subramanian Kartik

ABSTRACT

Data were collected with proton and π^- beams of momentum 530 GeV/c incident on nuclear targets. The E672 dimuon spectrometer, located in the Meson West beamline at Fermi National Accelerator Laboratory, was used for this purpose. The vector mesons ρ, ω ϕ and J/ψ are studied in this dissertation.

The vector mesons were observed in their decay into a $\mu^+\mu^-$ pair. One part of the data collected was using thick nuclear targets of Carbon, Aluminum, Copper and Lead with an incident π^- beam. The J/ψ was clearly visible in the dimuon mass spectrum with its nominal mass. Using the parametrization of A^α for the A-dependence of J/ψ production, α was determined to be 0.85 ± 0.06. No significant dependence of α on the Feynman-x (x_F) or the transverse momentum (p_t) of the dimuon was observed.

The other part of the data taking was with beams of 530 GeV/c protons and π^- incident on thin targets of Beryllium and Copper. The low-mass vector mesons, the ρ, ω and ϕ were clearly visible in the dimuon mass spectrum in addition to the J/ψ. The inclusive forward cross sections for the vector mesons wre measured for this energy with both beam types. The differential distributions in x_F and p_t were also obtained and compared to other experiments.

Recent results from nucleus-nucleus collisions indicate that the production of ϕ mesons is enhanced as a function of the transverse energy of the event, a possible signature of the onset of Quark-Gluon Plasma. The relative rate of ϕ to $\rho + \omega$ production was investigated as a function of the scalar p_t-sum of the charged tracks in the associated event (a measure of the inelasticity of the event) for this experiment. This rate was seen to increase as a function of the event inelasticity, with the increase being more pronounced with higher dimuon

transverse momentum. This experiment's prelimnary results indicate that this is due to the suppression of the $\rho + \omega$, and not the enhancement of the ϕ.

Prof. Alex Dzierba

Prof. Jack Martin

Prof. Andrzej Zieminski

Prof. Don Lichtenberg

TABLE of CONTENTS

page

1. INTRODUCTION . . . 1

1.1.1 Quark model of hadrons . . . 1

1.1.2 Quarks and partons . . . 3

1.1.3 Classification of hadrons in the quark model . . . 4

1.1.4 The charm quark . . . 4

1.1.5 Vector Mesonsand E672 . . . 5

1.2.1 Kinematics of vector meson production . . . 5

1.2.2 $x_{1,2}$ dependence on x_F and $\sqrt{s}$ . . . 7

1.2.3 Structure functions and the Parton Fusion Model . . . 8

1.3.1 Overview of the physics explored in this thesis . . . 11

1.3.2 Low-mass vector meson production mechanisms . . . 11

1.3.3 J/ψ production mechanisms . . . 12

1.4.1 A-dependence of J/ψ production . . . 14

1.4.2 Mechanisms for A-dependence . . . 15

1.5.1 ϕ enhancement as a signal for QGP . . . 16

1.5.2 Experimental status of ϕ enhancement . . . 17

1.6.1 The Experiment E672 . . . 17

References . . . 19

2. OVERVIEW OF THE APPARATUS . . . 31

2.1.1 The E672/E706 apparatus: Layout . . . 31

2.1.2 The E672 spectrometer: Overview . . . 32

2.1.3 The E706 spectrometer: Overview . . . 32

2.2.1 The beamline . . . 33

2.2.2 Secondary beam production . . . 34

2.2.3 Beam Ĉerenkov counter . . . 34

2.2.4 Spill structure . . . 35

2.3.1 Halo Veto Wall . . . 36

CONTENTS (*continued*)

2.3.2 Targets used in the '87 run 36

2.3.3 Targets used in the '88 run 37

2.3.4 Beam and interaction definition counters 38

2.4.1 The Silicon Strip Detector system 39

2.4.2 The E706 PWC system 39

2.4.3 Analysis Dipole Magnet 40

2.4.4 The Liquid Argon Calorimeter 41

2.4.5 The Forward Calorimeter 42

References 43

3. THE DIMUON SPECTROMETER 56

3.1.1 Construction details for the Muon Chambers 56

3.1.2 Operation of the muon chambers 58

3.2.1 Construction details for the pretrigger hodoscopes . . 59

3.2.2 Light collection from the hodoscopes 60

3.2.3 Performance of the hodoscopes 61

3.3.1 Construction details of the toroid 61

3.3.2 Toroid operation 62

3.4.1 The D-station PWC: Geometry 63

3.4.2 D-station operation 63

3.5.1 Beam Dump 64

3.5.2 Sheilding 64

References 65

4. TRIGGERING AND DATA ACQUISITION 74

4.1.1 Readout for the pretrigger hodoscopes 74

4.1.2 Readout for the muon and D-station chambers 75

4.1.3 Veto Wall readout 76

4.1.4 The Dimuon Trigger Processor 77

4.2.1 Interaction definition for the '87 run 79

4.2.2 Pretrigger definition for the '87 run 80

CONTENTS (*continued*)

4.2.3 TRIGGER FOR THE '87 RUN 80
4.2.4 THE BUSY AND RESET FOR THE EXPERIMENT 81
4.2.5 DATA ACQUISITION FOR THE '87 RUN 82
4.3.1 INTERACTION DEFINITION FOR THE '88 RUN 84
4.3.2 PRETRIGGER FOR THE '88 RUN 84
4.3.3 THE TRIGGER FOR THE E672/E706 '88 RUN 85
4.3.4 DATA ACQUISITION FOR THE E672/E706 '88 RUN 86
REFERENCES 87

5. DATA REDUCTION FOR THE A-DEPENDENCE ANALYSIS 98
5.1.1 DESCRIPTION OF THE DATA 98
5.1.2 AVW AND TVW SAMPLES 99
5.2.1 EVENT SELECTION AND DATA REDUCTION 100
5.2.2 CUTS USED IN DATA REDUCTION 100
5.3.1 ESTIMATION OF BACKGROUND 102
5.3.2 BACKGROUND SUBTRACTION 102
5.3.3 NUMBER OF J/ψ FROM EACH TARGET 104
REFERENCES 105

6. J/ψ CROSS SECTIONS AND A-DEPENDENCE 113
6.1.1 CORRECTIONS TO THE DATA 113
6.2.1 GEOMETRICAL AND KINEMATIC ACCEPTANCE 114
6.2.2 APPARATUS DETECTION EFFICIENCY 115
6.2.3 SOFTWARE RECONSTRUCTION LOSSES 115
6.2.4 J/ψ TAIL LOSSES 115
6.3.1 CORRECTION FOR TARGET BACKSCATTER 116
6.3.2 NON-TARGET INTERACTIONS 118
6.3.3 TARGET THICKNESS AND RESCATTERING EFFECTS 120
6.4.1 INTERACTION CROSS SECTIONS 122
6.4.2 J/ψ PRODUCTION CROSS SECTIONS 123
6.5.1 FEYNMAN-X (x_F DISTRIBUTIONS FOR THE J/ψ 125

CONTENTS (*continued*)

6.5.2 TRANSVERSE MOMENTUM (p_t) DISTRIBUTIONS FOR THE J/ψ . . 125
6.5.3 x_F DEPENDENCE FOR α 126
6.5.4 p_t DEPENDENCE FOR α 126
6.5.5 RATIO OF MASS SPECTRA FOR C AND PB 126
6.5.6 COMPARISON OF J/ψ CROSS SECTION WITH OTHERS 126
REFERENCES 127

7. DATA REDUCTION FOR VECTOR MESON ANALYSIS . 142
7.1.1 DESCRIPTION OF THE DATA 142
7.1.2 DATA REDUCTION AND PRESELECTION 143
7.1.3 DETERMINATION OF THE MUON TRAJECTORY 144
7.2.1 LINKING MUON AND PWC TRACKS 146
7.2.2 SSD-PWC-MUON LINKING 148
7.2.3 DETERMINATION OF THE VERTEX 149
7.3.1 GENERAL FEATURES OF THE RECONSTRUCTED DATA 150
7.3.2 VERTEX RECONSTRUCTION 150
7.3.3 CHARECTERISTICS OF SSD-PWC-MUON LINKED TRACKS . . 151
REFERENCES 152

8. VECTOR MESON CROSS SECTION CALCULATION . . . 165
8.1.1 PROPERTIES OF VECTOR MESONS AND THE DATA SAMPLE . . . 165
8.2.1 GENERAL FEATURES OF THE DIMUON SAMPLE 166
8.2.2 DATA CUTS FOR CROSS SECTION CALCULATION 166
8.2.3 BACKGROUND ESTIMATION AND SUBTRACTION 168
8.3.1 MONTE CARLO SIMULATION 169
8.3.3 ACCEPTANCES FROM MONTE CARLO 170
8.3.4 ACCEPTANCE CORRECTIONS TO THE NUMBER OF EVENTS . . . 171
8.4.1 CORRECTIONS FOR TAIL LOSSES 171
8.4.2 RESONANCE TAIL CONTAMINATION LOSSES 172
8.4.3 DECONVOLUTION OF THE ρ AND ω RESONANCES 172
8.4.4 PRESELECTION LOSSES 173

CONTENTS (*continued*)

8.4.5 Trigger processor losses 174

8.4.6 Total software corrections 174

8.5.1 Luminosity calculations 175

8.5.2 Corrections to the Luminosity 176

8.5.3 Hardwaree corrections 177

8.6.1 Cross section calculation 178

8.6.2 Cross sections 178

8.6.3 Estimation of systematic errors 179

8.6.4 J/ψ cross sections 180

8.6.5 Summary of results 182

8.7.1 A-dependence of massive dimuon production 183

8.8.1 Extrapolation of cross sections to $x_F \geq 0$ 184

8.8.2 A-dependence correction to the cross section 185

8.8.3 Vector meson forward cross sections 185

8.8.4 Ratio of ϕ to ω cross sections 186

References 187

9. PROPERTIES OF VECTOR MESON PRODUCTION . . . 197

9.1.1 Vector meson x_F distributions 197

9.1.2 $\rho + \omega$ x_F distributions 198

9.1.3 ϕ x_F distributions 198

9.1.4 Ratios of x_F distributions 198

9.2.1 Vector meson p_t^2 distributions 199

9.2.2 $\rho + \omega$ p_t^2 distributions 199

9.2.3 ϕ p_t^2 distributions 200

9.2.4 Summary of p_t^2 results 200

9.3.1 Average charged multiplicity vs. dimuon mass 201

9.4.1 Enhancement of $\sigma(\phi)/\sigma(\omega)$ with event inelasticity . . . 202

9.4.2 Results from this experiment 202

9.4.3 Interpretation of the results 203

CONTENTS (*continued*)

References 204

10. CONCLUSIONS 222

10.1.1 A-dependence of J/ψ production 222

10.1.2 A model to understand the A-dependence 223

10.1.3 Comparison of results with theoretical calculations . 223

10.2.1 Vector meson inclusive cross sections 224

10.2.2 Vector meson kinematic distributions 225

10.2.3 A-dependence of low mass vector mesons 227

10.3.1 The ratio of $\sigma(\phi)/\sigma(\rho)$ 227

10.3.2 $\phi/\rho+\omega$ as a function of event inelasticity 227

10.4.1 Conclusions 228

References 228

ACKNOWLEDGMENTS

The number of people, without whose help this dissertation would have been impossible, is staggering. I can only attempt to do justice to them in this acknowledgement. Firstly, I would like to acknowledge the support I received from my parents and grandparents all through my life. I thank them for their love, patience, tolerance, advice and most importantly for their faith in me in the darkest periods of my life, where even I had lost faith in myself. Their support carried me when I could not walk by myself. I would especially like to thank my father; whose gentle guidance and encouragement in my formative years stimulated my interest in physics and mathematics; who taught me to be curious and open-minded about life; and who impressed upon me the importance of experimenting and reaching my own conclusions about the nature of my reality. And my mother; through her love, affection and deep concern for my welfare taught me valuable lessons in the strength of the family and the nature of caring and sharing in good and bad times. I also thank my uncles and aunts around the country for their support and help through my graduate years.

In my stay at Indiana University, I have been fortunate to meet two people who have had a profound influence on my life; and to whom I owe an immeasurable debt of gratitude. I would like to express my deepest gratitude to my thesis advisor, Prof. Alex Dzierba. Alex and I have known each other for four years, a period in which he molded me into a Ph.D starting from a green inexperienced graduate student. In his own incisive way, he patiently taught me the fruitfullness of approaching physics in a simple, direct fashion. He coached me in the use of crisp presentations to elicit constructive feedback from the group and to get my own ideas across without distortion. While he guided me carefully towards my research goals, he also gave me the intellectual freedom to approach a problem with my own creativity and imagination, allowing me to breathe the exhilarating air of personal discovery, the stuff that makes physics fun. But most importantly, I am extremely grateful for his concern for my personal welfare and safety. In the years that I have known him, in spite of the hard situations and tough decisions I somehow managed to face him with, he never gave up on me and stood in my corner through the roughest of times. His compassion and timely intervention in the personal crises which seemed to dominate my life probably saved it. I thank him for being my friend, in addition to being my mentor.

The other person who has helped me immensely through my graduate years is Prof. Andrzej Zieminski. I will always be in awe of his command and depth of knowledge of physics, which he was always willing to share with me without reservation. His objectivity, sincerity and hard work will be an inspiration to me for many years to come. He taught me how to be meticulous and thorough in experimental physics, and guided me with penetrating insight through pieces of analysis which were confusing to me, to say the least. His advice and support through the course of my graduate studies were invaluable to me. On a personal level too, he did not lose faith in me through the hardest times of my life, and helped me regain lost ground in spite of my past problems. The warmth of his personality often kept me going when all other motivation seemed to be absent. I am eternally grateful for the opportunity to have had such close contact with these two people for whom I have the utmost respect and admiration, and who have done so much for me. This dissertation would not have been possible but for the help and support I received from Alex and Andrzej.

I would like to thank Prof. Ray Crittenden from whom I learnt most of my hardware skills, and also to never pretend to understand something that I didn't. Prof. Jack Martin helped me a lot in the software connected with the experiment, and my frequent discussions with him were extremely helpful in understanding the underlying physics. Special thanks to Thom Sulanke, who helped me way beyond the call of duty with the computers at IU, and made life a whole lot more pleasant as well. Other people connected with the experiment I'd like to thank;

Paul Smith, Tom Marshall; the Serpukhov contingent of Volodia Sirotenko, Volodia Glebov, Yuri Antipov, Yuri Gorin, Victor Abramov, Victor Koreshev, Boris Baldin and Sergeii Denisov; the Chicago Circle people Julius Solomon, Howard Goldberg and Sy Marguiles; Chris Davis and Loretta Dauwe; Keith Welch and Wendy Corning, and of course, Donna Martin. I would like to thank Prof. Don Lichtenberg for agreeing to be on my dissertation committee.

I would also like to thank June Dizer, Beverly Carson and Pat Washel for their assistance and moral support through the past years. Susan Salmon and Leslie Cadavid helped me on more than one occasion to sort out my affairs with the INS, and I am very grateful for the help I got from them. Some of my fellow graduate students whom I'd like to thank; Nana Fadnis, Rami Mehrem and Prasad Akavoor for being the best friends I could ask for; Chris Murphy, Rob Lindenbusch, Todd Foxford, John Schuler, Rui Li and Martin Knudsen for putting up with me at work. I would also like to thank Prof. P.P. Singh with whose help I came to Indiana University, and Prof J.N.S. Murthy, who showed me for the first time that Hilbert spaces could be fun.

Some very important friends outside of physics; Richard Mass who took me in when I was homeless and helped me in the non-material aspects of my life; Hovhannes Koujanian, who taught me all the acting I know and how to be a true friend; his wife Amy Ploeger whose sculpture still sends tingles up my spine; Cindy Jewell, for teaching me about relationships; and Cheryl Greenwood, for showing me the need to be honest with my feelings.

Last but not the least, I would like to thank, from the bottom of my heart, a very special set of friends I have had the privilege to get to know in the past year. Foremost, I thank Bill Guinee for guiding me through a very difficult period of growth, and for being such an inspiration to me. Other special friends include David Moore, Sue Morrison, Danny Sissoon, Star Brady, Sue Pate, Steve Franz, Gerry McTernan, Freddie, 'One-day-at-a-time' Fred, and every one at Back-to-Basics and the 12-24 Club. I would not be where I am today without them, and I thank them for their lives and mine.

I dedicate this dissertation to my parents and grandparents

PREFACE

The E672 experiment was performed by a collaboration of physicists from Caltech, Fermilab, University of Illinois (Chicago), Indiana University, University of Louisville, University of Michigan (Flint) and Serpukhov (USSR). The experiment was proposed in 1981 and the first data taking run was in 1984. The author joined the High Energy Physics Group at Indiana University in August 1986 and worked on the E672 experiment since then. A list of Collaborators in this experiment is give in Appendix A of this dissertation. The analysis for this dissertation, using the reconstructed information from the E672/E706 detector from the 1987-1988 data run , was carried out in Indiana University by the author.

During the course of the 1987-1988 run, the author was posted at Fermilab, and worked on rebuilding and commissioning of the pretrigger hodoscopes, the commissioning of the multiwire proportional chambers, and on maintaining the fast electronics and the data acquisition system. The author was also involved in the data selection and reduction process.

Unless otherwise stated, the analysis in the dissertation was performed by the author after the reconstruction of the information from various pieces of the experiment. The reconstruction of the data, described in Chapter 7, was done by J. Martin.

CHAPTER 1
INTRODUCTION

This thesis presents results from experiment E672 done at the Fermi National Accelerator Laboratory (Fermilab) on proton-nucleus and pion-nucleus collisions. The production of some of a class of particles, the vector mesons ρ, ω, ϕ and the J/ψ are studied and results on their properties are presented. The center-of-mass energy of this experiment is equal to 31.5 GeV, which corresponds to an incident beam momentum of 530 GeV/c.

In this chapter, a brief introduction to the quark-parton model is given, describing the niche occupied by the vector mesons in this picture. Next, the production mechanisms for these vector mesons are reviewed and the distributions for various kinematical variables are discussed. The A-dependence of J/ψ production and models proposed to explain it are presented. The proposed signature for Quark Gluon Plasma, ϕ enhancement is discussed and current results are presented.

Section 1.1

1.1.1 Quark model of hadrons

Around the early 1960's, the number of mesons and baryons, collectively known as hadrons, had become uncomfortably large. About a hundred or so were known and there seemed to be no end in sight. The first hints of an underlying structure for hadrons came from hadron spectroscopy. In 1962, Gell-Mann[1] and Ne'eman[2] proposed a scheme of classifying the known hadrons into representations of the special unitary Lie group SU(3) based on their spin J and parity P.

In 1964, Gell-Mann[3] and independently Zweig[4] speculated that hadrons were made up of sub-constituents, which Gell-Mann called quarks. If the vector representation of SU(3) was considered to represent three spin-1/2 fermions, namely quarks, the hadrons could be understood as composites of quarks; the mesons were interpreted as quark-antiquark bound states an the baryons were understood as three quark states. The three quarks postulated were labelled the up, down and strange (u, d and s) quarks.

Strong isospin invariance was known to hold in nuclear interactions and the Gell-Mann-Nishijima [5–6] relation

$$Q = I_3 + \frac{Y}{2} \tag{1.1}$$

where Q is the electric charge in multiples of the proton charge, I_3 is the third (diagonal) component of the isospin and Y is the hypercharge [Y=Baryon number(B) + Strangeness(S)], was known to hold for hadrons. Assigning the up and down quarks to an isospin doublet with strangeness zero gave the charges of the s and d quarks to be $-1/3$ and that for the u to be $+2/3$ using the Gell-Mann-Nishijima relation.

In SU(3) flavor, mesons were formed by the direct product of the quark and anti-quark representations, i.e. the **3** and the $\bar{\mathbf{3}}$ representations to give

$$\mathbf{3} \otimes \overline{\mathbf{3}} = \mathbf{8} \oplus \mathbf{1} \tag{1.2}$$

an octet and a singlet. The baryons were formed from three quarks as

$$\mathbf{3} \otimes \mathbf{3} \otimes \mathbf{3} = \mathbf{1} \oplus \mathbf{8} \oplus \mathbf{8} \oplus \mathbf{10} \tag{1.3}$$

and could be classified into octets and decuplets.

It was soon realised that some of the baryons apparently violated the Pauli Exclusion Principle, i.e. they had quark wave functions that were symmetric in spin, space and flavor, in spite of having spin-1/2. This problem was overcome by postulating a new degree of freedom for the quarks, color. Quarks were assigned one of three colors, say red, blue and green, and the antiquarks had corresponding anti-colors. Interactions between the constituents of hadrons were presumed to be invariant under SU(3) transformations of the color fields. All the observable hadrons were required to be "colorless", or belonging to the color singlet representation of $SU_{Color}(3)$. A non-Abelian gauge theory, Quantum Chromo Dynamics (QCD) was developed with $SU_{Color}(3)$ invariance built into it to try to understand the interactions between quarks. The gauge bosons of this theory, called gluons, belong to the adjoint representation of SU(3), and are 8 in number. QCD is considered to be the best candidate for the theory of strong interactions.

1.1.2 Quarks and Partons

In the late 60's Feynman[7] , Bjorken [8–9] and others explored the consequences of substructure in hadrons, particularly in processes like deep-inelastic lepton-hadron and hadron-hadron collisions. Results from the deep-inelastic scattering experiments done at SLAC[10] were interpreted by Bjorken and Feynman as evidence for point-like constituents in nucleons, which were called "partons" by Feynman. The quarks and gluons were subsequently identified as the partons, and the quark-parton model of hadronic interactions was developed. Experimentally, the gluons were seen to carry about 50 % of the momentum in the nucleon. The combining of QCD with the parton picture was very successful in describing many of the features of strong interactions.

1.1.3 Classification of hadrons in the quark model

The baryons were classified into octets and decuplets on basis of their spin and parity (J^P). It was noticed that for a given J^P, there was a striking regularity in the number of baryons in terms of their strangeness and isospin. The most famous example of this is the J=3/2 P=+1 baryon decuplet, shown in Figure 1.1. At the time of the advent of the quark model, the Ω^- had not yet been discovered, and its prediction and subsequent observation was a triumph for the model.

The mesons are interpreted as quark-antiquark bound states, and as the antifermion is involved, the classification is done taking into consideration the charge congugation quantum number (C) as well. The vector meson nonet is shown in Figure 1.1. This is the $J^P = 1^-$ nonet and has 8 symmetric states and 1 antisymmetric state under flavor SU(3), whose neutral members have $C = -1$ (eigenstates of C).

The ρ has isospin I=1 and comes in three charge states. The mass eigenstates for the I=0 members are the ω and ϕ. The octet I=0 state and the singlet I=0 state mix[11] as they have the same isospin quantum numbers and $SU_{flavor}(3)$ is broken. Experimentally, the mixing "ideal", in the sense that the ϕ is almost pure s$\bar{\text{s}}$ and the ω is made up of only u and d quarks.

1.1.4 The charm quark

At the time of the quark model, an emperical rule was known about decays of strange hadrons, namely; almost all the decays obeyed the simple rule

$$\Delta Q = \Delta S \tag{1.4}$$

i.e. strangeness always changes with a charged current. In the model of hadrons in terms of the u,d and s quarks, strangeness changing *neutral* currents were expected, but highly suppressed experimentally. Glashow, Iliapolous and Maiani[12] proposed the addition of a new quark flavor, with the same charge as the up quark, to explain the suppression. The presence of this quark, labelled charm, allowed for a cancellation of the diagrams which contributed to the strangeness changing neutral current decays.

In 1974, a narrow resonance was observed in simultaneous experiments at SLAC[13] and Brookhaven[14] at a mass of 3.1 GeV/c^2. This resonance was named the J/ψ and was interpreted as a bound state of the charm and anticharm quarks. The J/ψ is also a vector meson with $J^{PC} = 1^{--}$. The J/ψ can only decay weakly as there are no charmed hadrons which are light enough for it to decay into.

1.1.5 Vector mesons and E672

The vector mesons ρ^0, ω, ϕ and the J/ψ have decay modes into a pair of muons. The E672 spectrometer is designed to detect massive dimuon pairs, and is sensitive to these decay modes of vector mesons. This thesis is concerned with the production of the said vector mesons and their subsequent decay into a $\mu^+\mu^-$ pair.

Section 1.2

1.2.1 Kinematics of vector meson production

In this thesis, the vector mesons production kinematics are defined in terms of their dimuon final state. Figure 1.2 shows the variables used to describe the production of vector mesons, (V^0). The process depicted is the interaction of two partons, one from the target and one from the incident beam, with and intermediate state where the vector meson is formed, and subsequently decays into a $\mu^+\mu^-$ pair.

If, in the center-of mass system, the beam parton carries a fraction x_1 of the beam momentum, and x_2 is the momentum fraction of the target parton, the variable Feynman-x (x_F) is defined as

$$x_F = \frac{2p_z^{CM}}{\sqrt{s}} = x_1 - x_2 \tag{1.5}$$

where p_z^{CM} is the longitudinal momentum component of the vector meson, and s is the Mandelstam invariant, the square of the center-of-mass energy of the system. The Lorentz-invariant mass of the vector meson V^0 can be expressed in terms of the four-momenta of the muons it decays into. If p_1^μ and p_2^μ are the four-momenta, and θ is the opening angle between the muons in the lab frame (with three momentum magnitudes p_1 and p_2), then the invariant mass $M_{V^0}^2$ is

$$M_{V^0}^2 = (p_1 + p_2)^\mu (p_1 + p_2)_\mu \tag{1.6}$$

and ignoring the masses of the muons

$$M_{V^0}^2 \approx 2p_1 p_2 (1 - \cos\theta) \tag{1.7}$$

If the opening angle is small, this expression can be further simplified to

$$M_{V^0}^2 \approx p_1 p_2 \theta^2 \tag{1.8}$$

. We can also define a variable $\tau = x_1 x_2$ which is connected to the mass of the V^0 by

$$M_{V^0}^2 = x_1 x_2 s = \tau s \tag{1.9}$$

(if the mass of the quarks are ignored).

The transverse momentum of the vector meson can be defined as

$$p_t = \sqrt{(p_x^2 + p_y^2)} = (p^2 - p_z^2)^{1/2} \tag{1.10}$$

The quantities M_{V^0}, x_F and p_t are Lorentz-invariant for an incident beam along the z-axis. The invariant cross sections is written as

$$E\frac{d^3\sigma}{dp^3} = E\frac{d^3\sigma}{dp^3}(x_F, p_t, \sqrt{s}) \tag{1.11}$$

and can be transformed using the azimuthal symmetry of the initial state to

$$E\frac{d^3\sigma}{dp^3} = \frac{E_{CM}}{\sqrt{s}}\frac{d^2\sigma}{dx_F dp_t^2} \tag{1.12}$$

Experimentally, the measured distributions are usually parametrized as

$$\frac{d\sigma}{dx_F} \sim (1 - |x_F - x_0|)^c \tag{1.13}$$

where x_0 is an offset which is zero for proton beams and small, positive for meson beams (~ 0.2 for the J/ψ; for example) and

$$\frac{d\sigma}{dp_t^2} \sim \exp(-\alpha p_t^2) \tag{1.14}$$

1.2.2 $x_{1,2}$ dependence on x_F and $\sqrt{s}$

Knowing x_F and $M^2_{V^0}$ one can reconstruct the momentum fractions x_1 and x_2 as

$$x_{1,2} = \frac{1}{2}\left[\sqrt{x_F^2 + 4\tau} \pm x_F\right] \tag{1.15}$$

The dependence of x_1 and x_2 on the x_F of the vector meson for the ϕ and the J/ψ is shown in Figure 1.3 for the center-of-mass energy of this experiment $\sqrt{s} = 31.5$ GeV. The range of x_2 probed is shown as a function of the center-of-mass energy in Figure 1.4.

For the energy at which this experiment is performed, the x_2 region probed for the J/ψ is $0.013 \le x_2 \le 0.124$, and for the ϕ the range is $0.0017 \le x_2 \le 0.0094$.

1.2.3 Structure functions and the Parton Fusion Model

If hadrons are assumed to be made up of point-like partons, their structure can be investigated by scattering from hadrons at sufficiently high energies. With a charged leptonic probe (electrons, muons), the nature of the charged partons in a hadron is revealed in deep-inelastic scattering (DIS) experiments. The cross sections can be written generally[11] as

$$\frac{d^2\sigma}{dq^2 d\nu} = \frac{4\pi\alpha^2 E'}{q^4 EM}\left[2F_1(q^2,\nu)\sin^2\frac{\theta}{2} + F_2(q^2,\nu)\cos^2\frac{\theta}{2}\right] \tag{1.16}$$

where q^2 is the square of the four-momentum transfer of the exchanged virtual photon, and $\nu = E - E'$ is the energy lost by the incoming lepton of energy E. The functions F_1 and F_2 are called hadron structure functions corresponding to the two possible polarization states of the mediating photon.

In 1969, Bjorken[8] argued that in the limit of $q^2 \rightarrow \infty$ and $\nu \rightarrow \infty$ such that the dimensionless ratio

$$x = \frac{q^2}{2M\nu} \tag{1.17}$$

was finite, the structure functions should be non-zero and finite functions of x alone. That is

$$MF_1(q^2, \nu) \longrightarrow F_1(x) \tag{1.18}$$

and

$$\nu F_2(q^2, \nu) \longrightarrow F_2(x) \tag{1.19}$$

The quantity x was interpreted as the fraction of momentum carried by the point-like parton in the nucleon by Feynman[7] . This dependence of the structure functions on x alone is referred to as Bjorken scaling.

If the identification of the charged partons in the nucleon was made with spin-1/2 quarks, then it was shown by Callan and Gross[15] that

$$F_2(x) = 2xF_1(x) \tag{1.20}$$

a result which has been verified experimentally.

The structure functions in turn could be interpreted in terms of the quark momentum distribution functions, i.e. the probability that a given quark in a hadron has a momentum fraction x. For example,

$$F_2(x) = x \sum_i e_i^2 [Q_i^{val}(x) + Q_i^{sea}(x)] \tag{1.21}$$

In this expression, e_i is the quark charge ($= +2/3$ for the u and $= -1/3$ for the d and s quarks). The functions Q_i^{val} are the quark momentum fraction distribution functions for the so-called valence quarks which make up the hadron, and Q_i^{sea} are the "sea" quark distributions, which arise from vacuum fluctuations giving rise to quark-antiquark pairs. The sum is over all quark flavors and anti-flavors important at a given energy.

The charged partons in a hadron, the quarks, carry half the momentum of the hadron, while the rest is carried by the gluons. The gluons are described by a gluon distribution function G(x). Figure 1.5 shows the valence and sea quark distributions for a nucleon, obtained from deep-inelastic neutrino and anti-neutrino experiments. The sea antiquarks($\bar{Q}$) are concentrated at small values of x while the distribution for the valence quarks peaks at about $x = 0.2$. The gluon distribution function is also peaked at low x and has a slightly harder distribution than for the sea quarks.

The production of vector mesons has been described in terms of the interactions between these partons (quarks and gluons), in a model known as the parton fusion model. A review of such models[16] is described elsewhere. Briefly, the production of the vector mesons is thought to proceed by the fusion of partons, one from the incoming projectile and the other from the target. The model makes quantitative predictions with leading order perturbative QCD calculations, valid at high enough momentum transfers. Some authors[17] have argued that the model is valid for Q^2 of the order of 1 $(\mathrm{GeV/c})^2$, for $x_F \leq 0.5$ or so.

The QCD calculations within the framework of the parton fusion model are dependent on the knowledge of the structure functions for valence and sea quarks, as well as the gluon structure functions over the range of target and projectile momentum fractions probed. In this experiment, the structure functions at very low x are needed to make model predictions.

Section 1.3

1.3.1 Overview of the physics explored in this thesis

The physics topics investigated using the data collected by the E672 spectrometer in this thesis are the following:

— The production mechanisms for the vector mesons ρ, ω, ϕ and the J/ψ.

— Propagation of colored objects through nuclear matter; specifically, the effect of nuclear matter on the production properties of vector mesons

— Flavor production dependence on the inelasticity of the collision.

These topics are discussed in the following subsections.

1.3.2 Low mass vector meson production mechanisms

The term "low-mass" refers to the vector mesons ρ, ω and the ϕ mesons. Due to the low-Q^2 associated with the production of these mesons, perturbative QCD calculations are harder to do. Low-mass vector meson production has been studied in a number of experiments in hadron-hadron collisions. These include the inclusive production of the ρ alone [18–20], the ϕ alone [21–26], the ρ and ω [27–29] and the ρ, ω and ϕ [30].

The production of vector mesons can be visualized in terms of the parton fusion model. For the ρ and the ω, the production can proceed through light quark (u, d) fusion or gluon fusion. The target and projectile contain the light quarks that make up the ρ and ω, and the mechanism would be OZI-allowed [31–33] fusion (the OZI rule states that a process that proceeds through a disconnected quark-line diagram is suppressed as compared to connected diagrams) of initial state quarks, would be expected to dominate. Gluon fusion could contribute to the low x_F production region.

The ϕ quark is unique in the sense that it is the lowest mass vector meson with a quark-antiquark pair not present in the initial set of valence quarks. In the framework of the parton fusion model, three mechanisms are thought to contribute to ϕ production, i.e. to the production of an $s\bar{s}$ pair in the final state:

— OZI-allowed strange quark fusion: Here the production proceeds through connected quark-line diagrams with two $s\bar{s}$ pairs being created from the vacuum. Such production is therefore expected to be accompanied by strange hadrons like the K's or the Λ's. This has in fact been seen experimentally[23,24].

— OZI-suppressed light quark fusion: This proceeds via a disconnected quark line diagram, and is expected to be suppressed. No strange particles are expected to accompany a ϕ produced in this manner.

— Gluon fusion: Here, like for the J/ψ, a final state gluon must be present to conserve C-parity and to ensure that the $s\bar{s}$ is colorless.

These three mechanisms are depicted in Figure 1.6. The relative weight of the three processes depends on the choice of structure functions used for the calculations.[24]

1.3.3 J/ψ production mechanisms

The production of the J/ψ can also be thought of in terms of the parton fusion model. The charm quark is only present in the sea for the target and the projectile. Due to the large mass of the J/ψ, perturbative QCD calculations can be done with some confidence for J/ψ production within the parton fusion model.

At the energies of this experiment ($\sqrt{s}$ = 31.5 GeV), there are three dominant mechanisms thought to contribute to J/ψ hadroproduction.

— Strong quark-antiquark annihilation: Here the quark and antiquark (either valence or from the sea) annihilate with the exchange of gluons between the quark current and the charm current.

— Gluon fusion: Gluons from the target and the beam interact to produce a $c\bar{c}$ pair, which radiates soft gluons to compensate for color and to conserve C-parity , and emerges as the J/ψ.

— χ production: Here too, gluon fusion takes place, but the $c\bar{c}$ pair forms an intermediate χ state which decays into a J/ψ radiatively.

These mechanisms are shown in Figure 1.7. The hadroproduction of heavy quarks can be looked upon as arising from the production of a $c\bar{c}$ pair from $q\bar{q}$ annihilation and gg fusion. The cross sections for these processes have been calculated [34–35] in leading order perturbative QCD. It must be noted that these processed do not predict the p_t dependence of the production, which depends on the intrinsic p_t dependence of the partons and higher order processes like $q\bar{q} \rightarrow J/\psi g$, $gg \rightarrow J/\psi g$ etc. The dependence at high p_t has been investigated elsewhere [36–37] . These cross sections are then convoluted with the appropriate structure functions for the quarks and gluons to understand the observed data. The structure functions have been analyzed[38] in next-to-leading order in QCD using all the available data recently.

Strong $q\bar{q}$ annihilation depends on whether the incident beam hadron is a meson or a baryon. Meson beams have a valence antiquark, while baryon beams have only sea antiquarks. This process would be expected to dominate for meson beams. Such a process with a meson beam would also be expected to dominate at high x_F over a baryon beam as there are only two initial state beam valence quarks, resulting in an x_1 which is higher.

Gluon fusion[35] could be expected to contribute to processes which impart a high p_t to the resulting J/ψ. As the J/ψ has $C = -1$, a gluon must be radiated in the final state. The resulting cross sections are also expected to be the same for all incident beam types. The gluon momentum distributions are softer than those for the quarks, and one would expect this process to be significant for lower x_F, i.e. more central production of J/ψ. Three gluon fusion has also been suggested[39] as a possible mechanism for J/ψ production.

There are indications [40–42] that a large fraction of J/ψ come from radiative χ decay. As χ production can proceed by the fusion of 2 gluons, the process is simpler than that for J/ψ production. The radiated photon is soft (300-400 MeV) and is therefore not expected to contribute much to the p_t of the J/ψ. Several authors [43–44] have argued that this process is at least as important as gluon fusion.

The dependence of the cross section on energy has been parametrized[45] as

$$\sigma(pN \longrightarrow J/\psi) = 1700 \exp(-17\sqrt{\tau}) \text{ nb} \tag{1.22}$$

for all x_F and

$$\sigma(\pi^- N \longrightarrow J/\psi) = 500 \exp(-10\sqrt{\tau}) \text{ nb} \tag{1.23}$$

for $x_F \geq 0$.

Section 1.4

1.4.1 A-dependence of J/ψ production

The cross section for a hadron, h, scattering off of a nuclear target of atomic weight A is usually parametrized by the expression $\sigma(\mathrm{h}+\mathrm{A} \rightarrow J/\psi + \mathrm{X}) = \sigma_0 \cdot \mathrm{A}^{\alpha}$, with $\alpha < 1$ implying a decreasing effectiveness of J/ψ production with increasing A. This A - dependence has been studied previously in several experiments up to a center-of-mass energy, $\sqrt{s}$, of 38 GeV. This experiment was performed at $\sqrt{s} = 31.5$ GeV. For J/ψs produced at large Feynman-x (x_F) and with small values of transverse momentum (p_t), the values of α were found to be less than one.[46–52]

1.4.2 Mechanisms for A-dependence

A number of mechanisms have been proposed for the A-dependence of J/ψ production and nuclear suppression at large x_F . At large $\sqrt{s}$, x_F of the J/ψ is well approximated by $x_F = x_1 - x_2$, where x_1 and x_2 are fractions of the beam and target momenta, respectively, carried by the interacting partons. The x_2 region probed by this experiment for the J/ψ is $0.013 \leq x_2 \leq 0.124$. Therefore, any mechanism which hardens the momentum distribution (suppression of the low-x component) of the target parton will decrease the probability of producing a J/ψ at large x_F.

As gluon fusion is expected to contribute significantly[39] to J/ψ production, processes which affect the momentum distribution of target gluons will also influence J/ψ production from nuclei. In particular, the nucleons surrounding the target nucleon of a heavy nucleus could produce a "shadowing" effect where the soft gluon component of the target is absorbed by the other nucleons, leaving the harder component intact .[53]

Another class of models explains the observed A-dependence of J/ψ production as due to the scattering of the beam particle before the J/ψ is produced [54–56] ,or the scattering of the J/ψ itself before it escapes the nuclear target.[52] These effects decrease the number of J/ψs at large x_F and increase their average p_t . However, it was pointed out recently by Brodsky and Mueller[57] that the most likely explanation for the observed J/ψ suppression are final state interactions of the J/ψ with co-moving spectator partons. Recently, it has been noted[58] that the intrinsic charm content (from the sea) in the target and the projectile may be important to explain the x_F dependence of the data for heavy and light nuclei at high x_F.

The A-dependence of J/ψ production is also relevant for studies of quark–gluon plasma (QGP). The suppression of J/ψ production has been suggested as the signature of the onset of QGP in nucleus–nucleus collisions [59–60] . In order to understand suppression effects, recently observed in nucleus–nucleus collisions,[61] it is important to first see if there is any suppression in π^-–nucleus or p–nucleus collisions, as this may provide a way to discriminate between various models .

Section 1.5

1.5.1 ϕ/ω enhancement as a signal for QGP

It has been suggested[62] that at sufficiently large energy densities, nuclear matter would dissolve into quarks and gluons no longer confined to their individual hadrons, a phase known as quark-gluon plasma (QGP). Recently, it has been noted[63] that in a QGP phase, the OZI-suppression for ϕ production would be absent and that there would be a large abundance of strange quarks in the plasma. Also, the ϕ would not re-scatter significantly and would retain information about the conditions in the hot plasma.

The collision of nuclei appears[64] to be the best way of creating such a phase of nuclear matter. It has been shown[65–66] that such a plasma would result in enhanced ϕ production, perhaps as high as 10-50 times that observed in ordinary nucleon-nucleus collisions.

In particular, it has been pointed out[63] that the ratio of ϕ to ω production should be a sensitive probe of QGP, as both resonances are close in mass and have the same quantum numbers, differing mainly in the fact that the ϕ is almost pure $s\bar{s}$ and the ω is made up of u and d quarks. The suppression of J/ψ with respect to the continuum has been linked[67] to the enhancement of the ϕ/ω ratio as a signature of QGP.

1.5.2 Experimental status of ϕ enhancement

Recent experimental results[68] from nucleus-nucleus collisions indicate than in addition to J/ψ suppression [69–70] there is an enhancement of the $\phi/(\rho+\omega)$ ratio by a factor of 2-3 (over the nucleon-nucleus results) for events with high inelasticity. The enhancement was seen to be more pronounced for high transverse momentum of the ϕ.

It is interesting to see whether these effects can be seen and understood at the energies of E672, where we do not expect to have sufficiently high energy densities for QGP formation. Models have also been proposed [71–72] to explain the ϕ enhancement in terms of production and absorbtion of secondary vector mesons due to the rescattering of hadrons, and are able to describe the experimental results.

Section 1.6

1.6.1 The Experiment E672.

Experiment E672 is designed to study the dimuon spectrum over the forward region $x_F \geq 0$ in an open geometry environment. Information from the associated event was also available due to the sharing of data acquisition systems of Experiment E706 which ran in the same beamline. Proton and pion beams of momentum 530 GeV/c were used on nuclear targets.

The goals of this thesis include:

— The measurement of the A-dependence of J/ψ production in the kinematically forward region ($0.1 \leq x_F \leq 0.8$).

— The measurement of the inclusive forward cross sections for the vector mesons ρ, ω, ϕ and the J/ψ for different beams.

— The measurement of the kinematic distributions in Feynman-x (x_F and p_t) for the vector mesons

— The study of $\phi/(\rho + \omega)$ dependence on event inelasticity.

The thesis is organized as follows. Chapters 2 and 3 give a description of the experimental apparatus for the E672/E706 spectrometers. Chapter 4 is devoted to the readout of the apparatus, the triggering scheme and the data acquisition system. Chapters 5 and 6 give the details of the analysis leading to the measurement of the A-dependence of J/ψ production for 530 GeV/c π^- beams. Chapters 7 concerns the reconstruction of the data, collected with the E706 spectrometer information available, for the low-mass vector meson analysis. Chapter 8 describes the vector meson cross section calculation. Chapter 9 gives the measured properties of vector meson production. The conclusions are presented in Chapter 10.

REFERENCES

1) M. Gell-Mann., *Phys. Rev.* **125**, 1067 (1962) .

2) Y. Ne'eman., *Nucl. Phys.* **26**, 222 (1961)

3) M. Gell-Mann., *Phys. Lett.* **8**, 214 (1964) .

4) G. Zweig., CERN Preprint, CERN-TH-401, unpublished.

5) M. Gell-Mann., *Phys. Rev.* **92**, 833 (1953) .

6) K. Nishijima., *Prog. Theor. Phys* **13**, 285 (1955) .

7) R. P. Feynman., *Phys. Rev. Lett.* **23**, 1415 (1969) ; also in "Photon Hadron Interactions", Benjamin, 1972

8) J. Bjorken et al., *Phys. Rev.* **185**, 1975 (1969) .

9) S. Berman et al., *Phys. Rev.* **D4**, 3388 (1971) .

10) H. Kendall et al., *Ann. Rev. Nucl. and Part. Sci.* **2**, 203 (1972) .

11) D. Perkins, "Introduction to High Energy Physics", Addison-Wesley Publishing Co.

12) S. Glashow et al., *Phys. Rev.* **D2**, 1285 (1970) .

13) J. Augustin et al., *Phys. Rev. Lett* **33**, 1406 (1974) .

14) J. Aubert et al., *Phys. Rev. Lett* **33**, 1404 (1974) .

15) C. Callan, R. Dashen and D. Gross., *Phys. Rev.* **D19**, 1826 (19 79) .

16) K. Fialkowski and W. Kittel., *Rep. Prog. Ther. Phys.* **46**, 1283 (1983) .

17) H. Dijkstra et al., *Z. fur Phys.* **C31**, 391 (1986) .

18) M. Albrow et al., *Nucl. Phys.* **B155**, 39 (1979) .

19) D. Drijard et al., *Z. fur Phys.* **C9**, 293 (1981) .

20) J. Bailey et al., *Z. fur Phys.* **C36**, 545 (1987) .

21) B. Ghidini et al., *Phys. Lett.* **68B**, 186 (1977) .

22) C. Akerlof et al., *Phys. Rev. Lett.* **39**, 861 (1977) .

23) C. Daum et al., *Phys. Lett.* **98B**, 313 (1981) .

24) C. Daum et al., *Nucl. Phys.* **B186**, 205 (1981) .

25) C. Daum et al., *Z. fur Phys.* **C18**, 1 (1983) .

26) H. Dijsktra et al., *Z. fur Phys.* **C31**, 375 (1986) ,, *Z. fur Phys.* **C31**, 391 (1986) .

27) V. Blobel et al., *Nucl. Phys.* **B69**, 237 (1974) .

28) V. Blobel et al., *Phys. Lett* **48B**, 73 (1974) .

29) G. Jansco et al., *Nucl. Phys.* **B203**, 27 (1982) .

30) M. Aguilar-Benitez et al., *Z.fur Phys.* **C44**, 531 (1989) .

31) G. Zweig., CERN preprint CERN TH 412 (1964).

32) S. Okubo., *Phys. Lett.* **5**, 165 (1963) .

33) J. Iizuka., *Supp. Prog. Theor. Phys.* **37-38**, 21 (1966) .

34) V. Barger, W. Keung and R. Phillips., *Phys. Lett.* **91B**, 253 (1980) .

35) V. Barger, W. Keung and R. Phillips., *Z. fur Phys.* **C6**, 169 (1980)

.

36) S. Gavin and M. Gyulassy., *Phys. Lett.* **214B**, 241 (1988) .

37) J. Hufner, Y. Kurihara and H. Priner., *Phys. Lett.* **215B**, 218 (1988) .

38) P. Harriman et al., *Phys. Rev.* **D42**, 798 (1990) .

39) L. Clavelli et al., *Phys. Rev.* **D32**, 619 (1985) .

40) T. Kirk et al., *Phys. Rev. Lett.* **42**, 619 (1979) .

41) J. Cobb et al., *Phys. Lett.* **72B**, 619 (1978) .

42) Y. Lemoigne et al., *Phys. Lett.* **113B**, 509 (1982) .

43) R. Baier et al., *Z. fur Phys.* **C19**, 251 (191981) .

44) C. Carlson et al., *Phys. Rev.* **D18**, 760 (1978) .

45) L. Lyons., *Prog. in Part. and Nucl. Phys.* **7**, 169 (1981) .

46) Yu. Antipov et al., *Phys. Lett.* **72B**, 278 (1977) , *Phys. Lett.* **76B**, 225 (1978) .

47) K. J. Anderson et al., *Phys. Rev. Lett.* **42**, 944 (1979) .

48) M. Corden et al., *Phys. Lett.* **110B**, 415 (1982) .

49) J. Badier et al., *Z.Phys.* **C20**, 101 (1983) .

50) S. Katsanevas et al., *Phys.Rev.Lett.* **60**, 2121 (1988) .

51) K. McDonald, Proceedings of the QCD Workshop, St. Croix, V.I., Oct. 1987; to be published.

52) C. Brown, Invited talk at the APS Baltimore Meeting, May 1989 (unpublished).

53) J. Qui., *Nucl.Phys.* **B291**, 746 (1987) .

54) B. Kopeliovich & F. Niedermayer, Dubna preprint, JINR-E2-84-834 (1984) (unpublished).

55) B. Kopeliovich & F. Niedermayer., *Sov. J. Nucl. Phys.* **42**, 504 (1985) .

56) T. Hoang., *Phys. Rev.* **D39**, 2050 (1989) .

57) S. Brodsky and A. Mueller, SLAC preprint, NSF-ITP-88-22, 1988 (unpublished).

58) R. Vogt, S. Brodsky and P. Hoyer, SLAC preprint SLAC-PUB-5421 (T/E) 1991.

59) T. Matsui and H. Satz., *Phys. Lett.* **178B**, 416 (1978) .

60) J. Milana., *Phys. Rev. Lett.* **62**, 2921 (1989) .

61) C. Baglin et al., *Phys. Lett.* **220B**, 471 (1989) .

62) H. Satz., *Nucl. Phys.* **A400**, 451 (1981) .

63) A. Shor., *Phys. Rev. Lett.* **54**, 1122 (1985) .

64) M. Jacob., *Nucl. Phys.* **A418**, 7c (1984) .

65) J. Rafelski and B. Muller., *Phys. Rev. Lett* **48**, 1066 (1982) .

66) J. Rafelski., *Nucl. Phys.* **A418**, 215c (1984) .

67) P. Koch et al., *Z. fur Phys.* **C47**, 477 (1990) .

68) NA38 Collaboration, A. Baldisseri et al. Annecy preprint LAPP-EXP-89-15, to appear in the Proceedings of the International Conference on HEP, Madrid Sept. 1989.

69) A. Bossiere et al., *Z. fur Phys.* **C38**, 117 (1988) .

70) L. Klugberg et al., *Nucl. Phys.* **A488**, 613c (1988) .

71) U. Heinz, Regensburg Preprint TPR-89-48 (1989).

72) P. Koch et al, University of Regensburg preprints TPR-90-7 and TPR-90-8 (1990).

Baryon and Meson multiplets

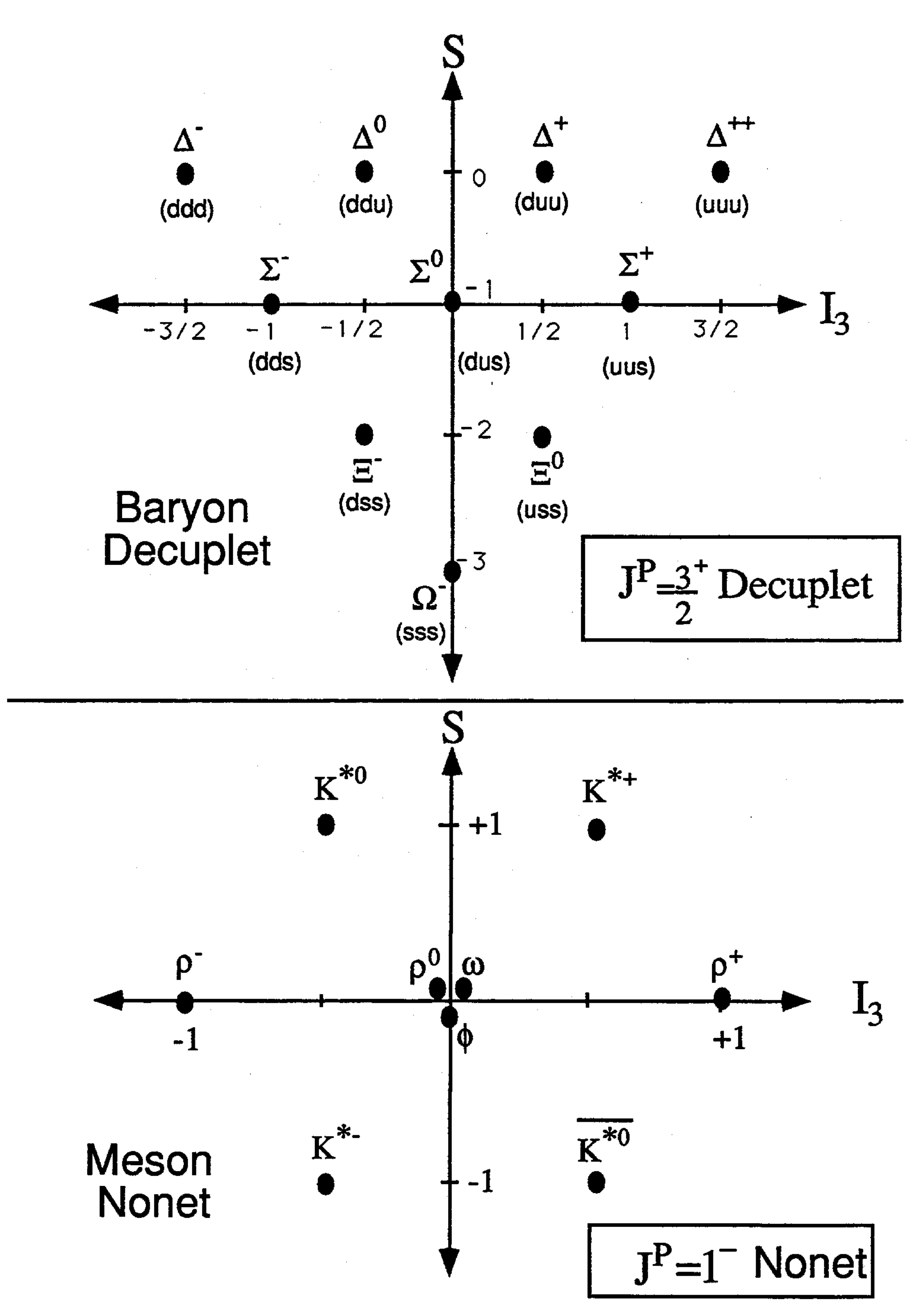

FIGURE 1.1

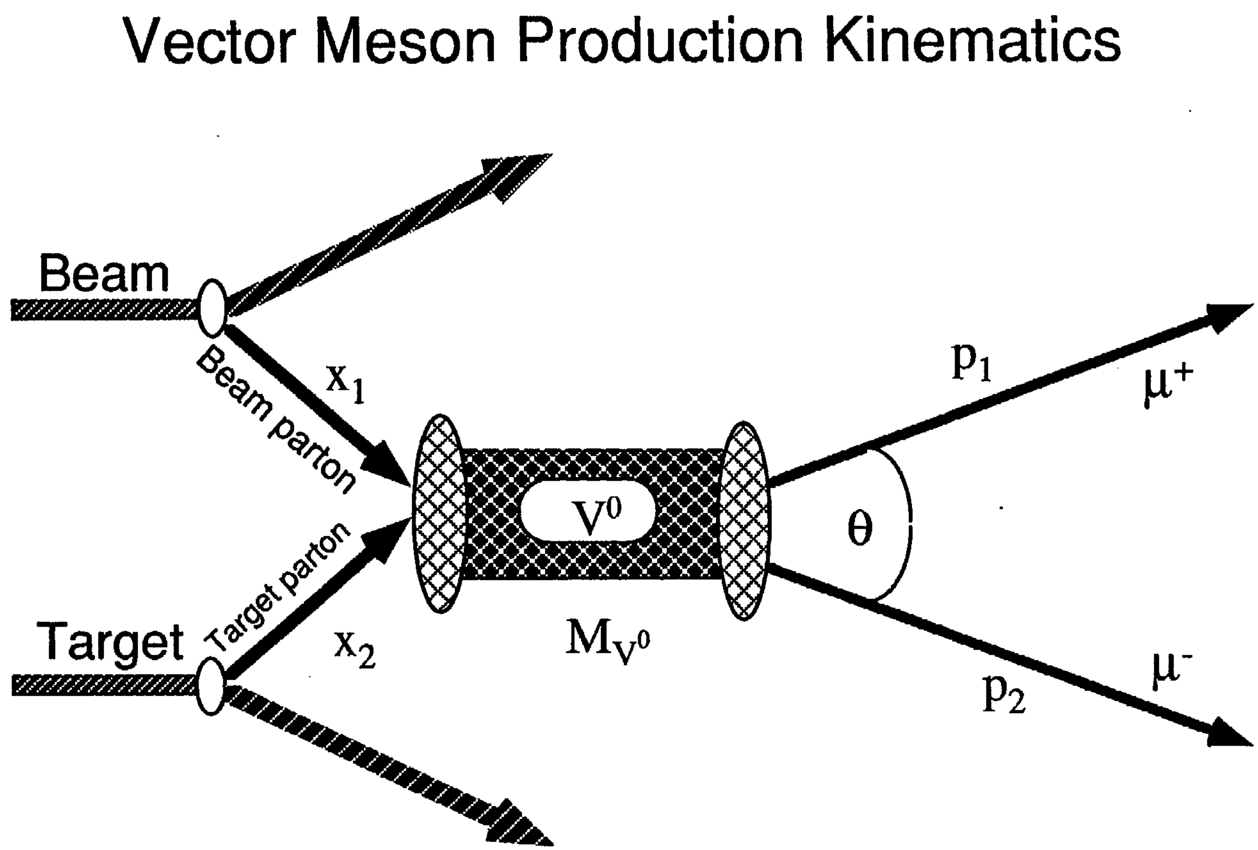
Vector Meson Production Kinematics
Beam
Target
Beam parton
Target parton
x1
x2
V0
MV0
θ
p1
p2
μ+
μ-

FIGURE 1.2

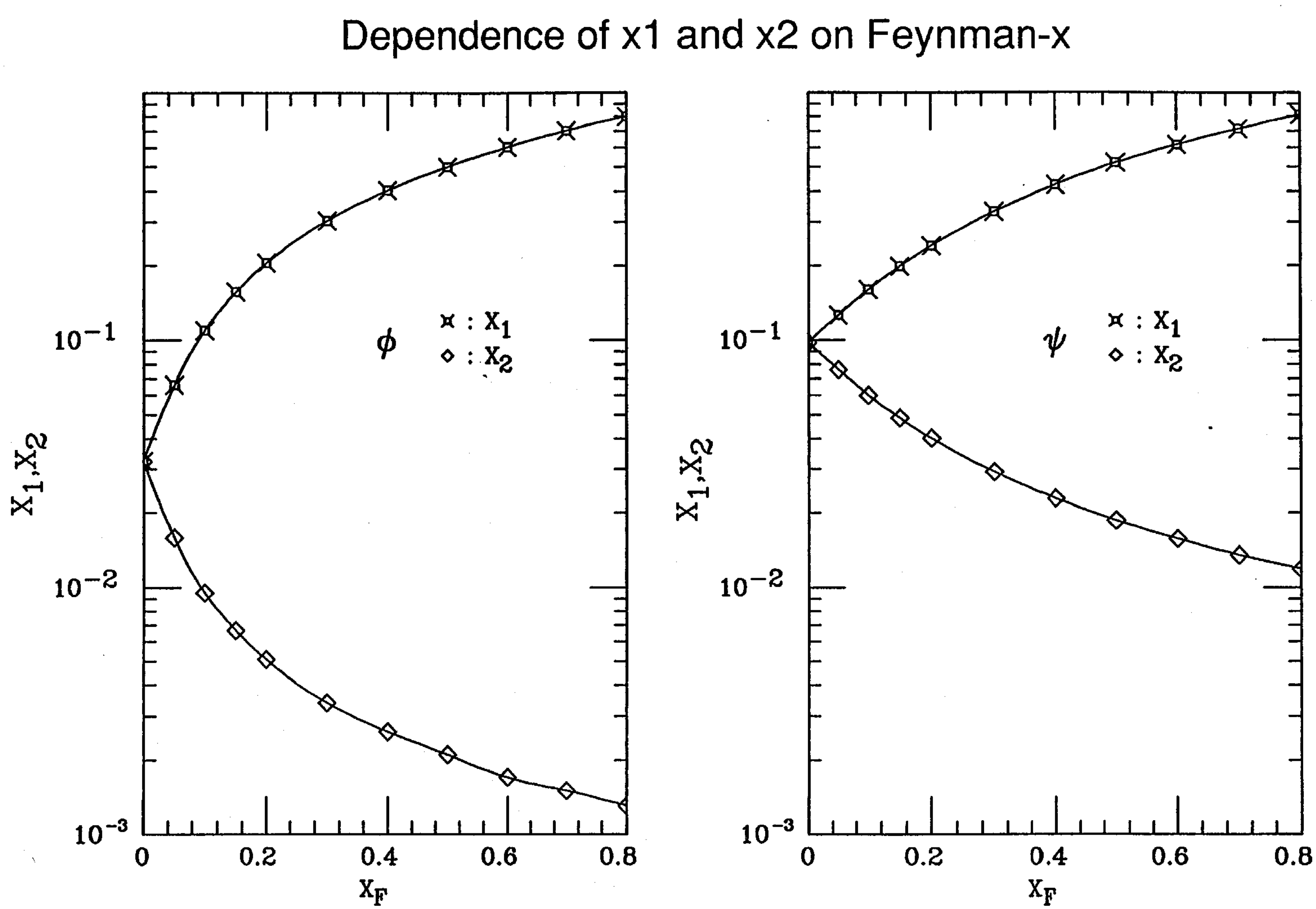
Dependence of x1 and x2 on Feynman-x
x_1, x_2
10^{-1}
10^{-2}
10^{-3}
0
0.2
0.4
0.6
0.8
x_F
ϕ
: x_1
: x_2
ψ

FIGURE 1.3

Dependence of x2 on center-of-mass energy

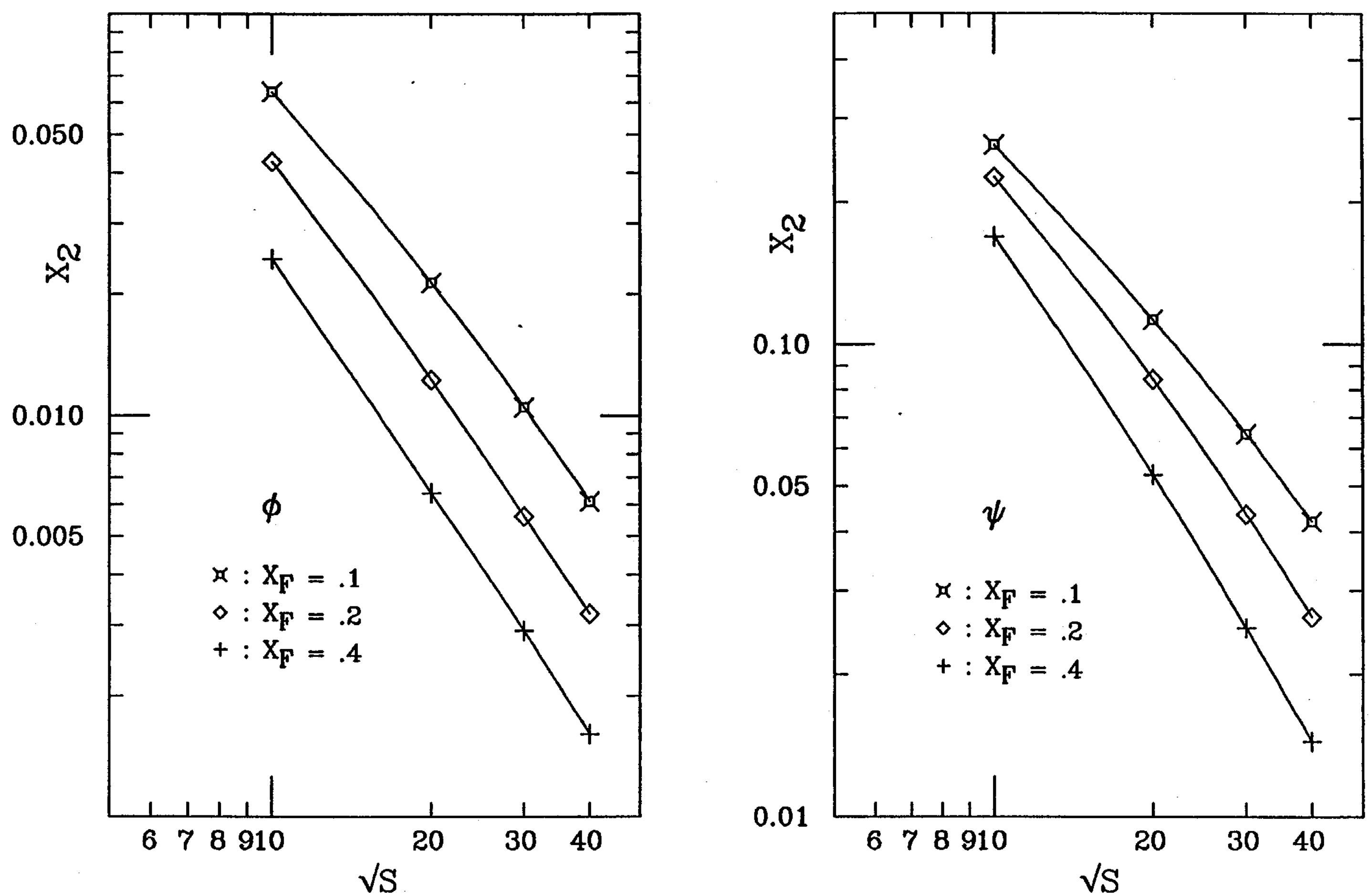

FIGURE 1.4

Valence and sea quark momentum
distribution functions

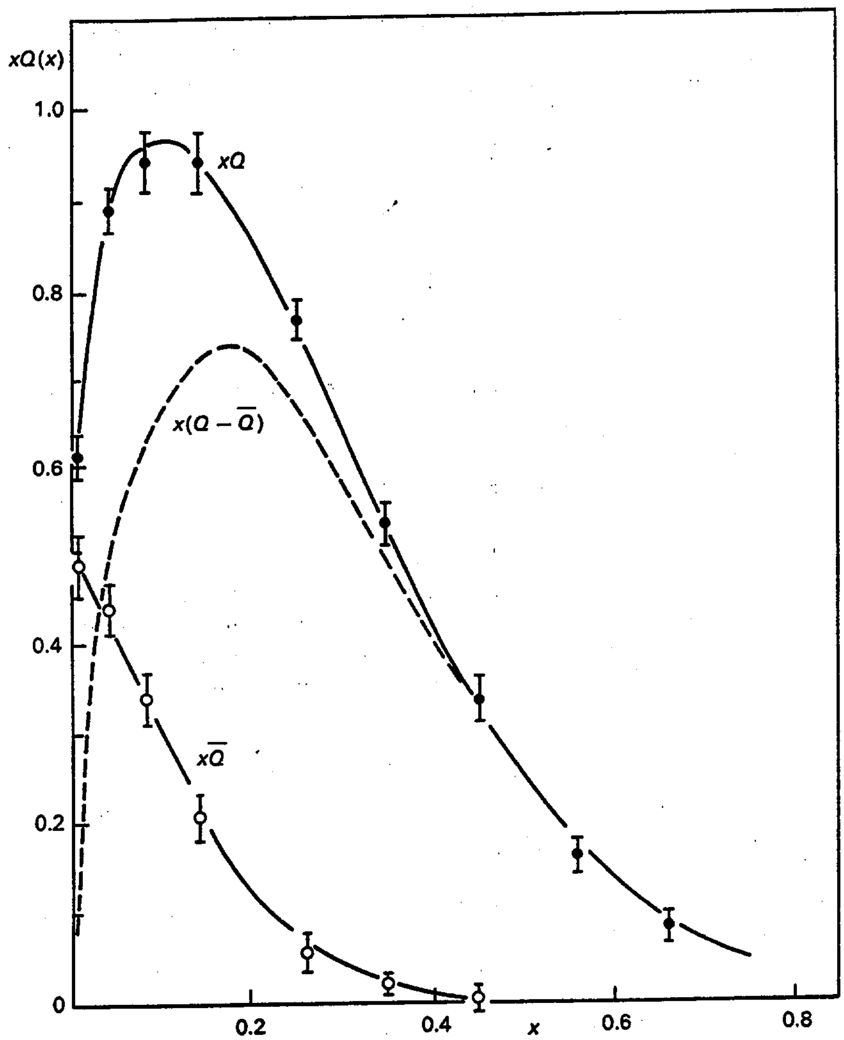

FIGURE 1.5

ϕ- production mechanisms

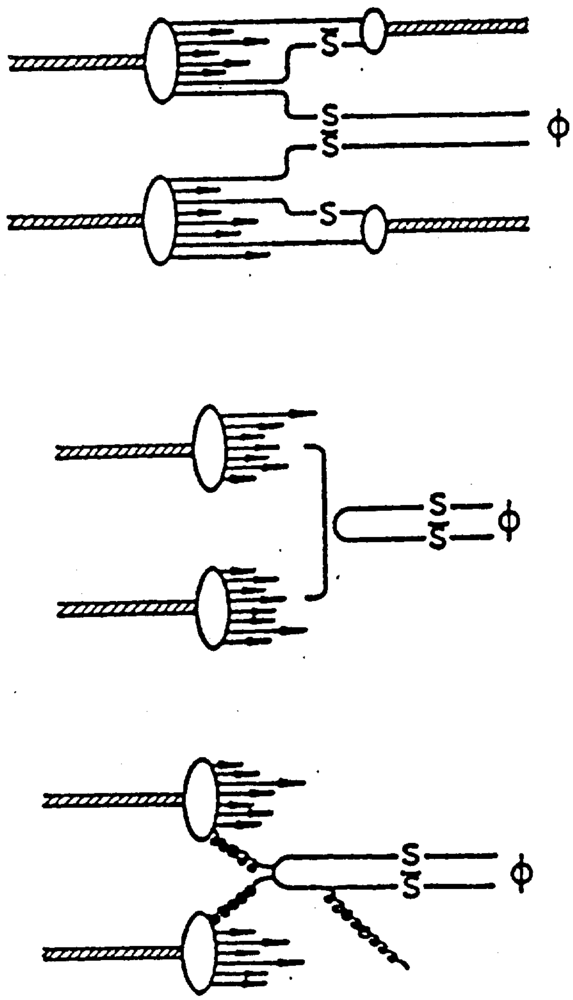

a) **OZI-allowed**

b) **OZI-suppressed**

c) **Gluon Fusion**

FIGURE 1.6

29

J/psi production mechanisms

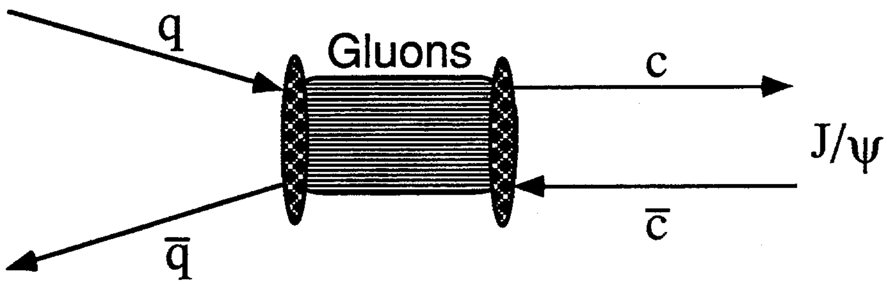

Strong quark-antiquark annihilation

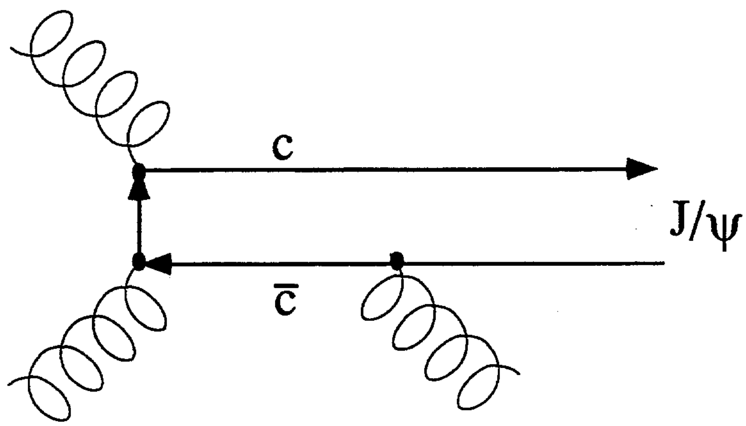

Two-gluon fusion

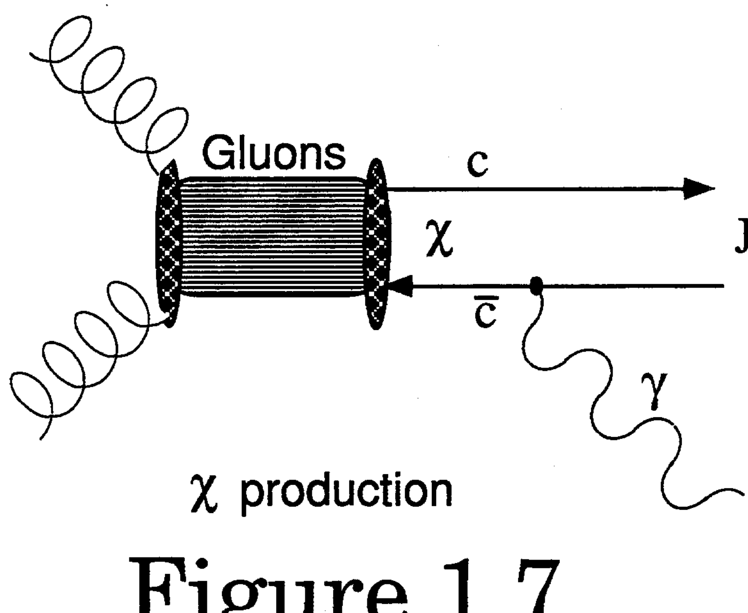

χ production

Figure 1.7

CHAPTER 2
OVERVIEW OF THE APPARATUS

The experiments E672 and E706 both share the Meson West beam line at Fermilab, and collect data simultaneously. Being a dimuon detector, the E672 spectrometer is located downstream of the E706 apparatus. The experimental apparatus for experiments E672/E706 for the 1987/88 run is described in this chapter. The common part of the experiments like the beam line, targets and some parts of the E706 spectrometer are described briefly. The E672 apparatus is described in Chapter 3.

Data for this analysis were collected in two running periods. In the first period, September '87, only information from the E672 spectrometer was available, and data were collected for π^- beams incident on 'thick' nuclear targets. For the second part of data collection, Jan-Feb '88, both the E706 and E672 spectrometers were read out by a shared data acquisition system, and the information was available to both experiments. Both proton and π^- beams were used in the second period of running.

Section 2.1

2.1.1 The E672/E706 apparatus: Layout

The E672/E706 spectrometers are located in the MW9 experimental hall at the end of the Meson West (MW) beamline at FNAL. The layout of the two experiments is shown in Figure 2.1. The positive z-axis is chosen to be along the beam axis in the same direction as the incoming beam. This direction will be referred to as 'downstream' and the opposite direction 'upstream'. The positive y-axis is chosen to be the vertical direction upwards, and the positive x-axis is chosen so as to form a right-handed orthogonal coordinate system with the y and z axis. The positive x-axis is to the right while looking downstream. The origin of the coordinate system is 9 m upstream of the Liquid Argon Calorimeter.

2.1.2 The E672 spectrometer: Overview

Th E672 spectrometer is a dimuon detector which is located 20 m downstream of the target. The main components of the spectrometer are:

— A set of four 3-plane Multiwire Proportional Chambers (MWPC's).

— A Dimuon Trigger Processor (DTP) used to calculate the dimuon invariant mass online for use in the trigger definition.

— Two 16-segment scintillator hodoscopes used in the pretrigger definition, and a CAMAC[1] multiplicity module[2] to set the coincidence level.

— An iron toroid with an average p_t-kick of 1.3 GeV/c for momentum determination.

— A 3-plane MWPC located upstream of the toroid.

— Two muon halo veto scintillator walls upstream of the target.

The E672 spectrometer is described in detail in Chapter 3.

2.1.3 The E706 spectrometer: Overview

The E706 experiment measures the production of direct photons, and is located upstream of the E672 spectrometer. Both experiments shared the beamline and in addition, various fast logic signals. Data from both experiments were read out simultaneously by an integrated data acquisition system, with information from both spectrometers available when either had a valid trigger.

The main components of the E706 spectrometer are:

— A 14-plane Silicon Strip Detector (SSD) system surrounding the target region.

— A set of four 4-plane Proportional Wire Chambers (PWC's).

— A dipole magnet with an average p_t-kick of 450 MeV/c.

— A Liquid Argon Calorimeter (LAC) with an electromagnetic and hadronic section.

— A Forward Calorimeter (FCAL).

These components are briefly described in Section 2.4.

Section 2.2

2.2.1 The beam line

The experiment is located in the Meson West (MW) beamline at Fermilab. The beam line is designed to transport positive and negative beams with momenta ranging from 25 GeV/c to 1000 GeV/c. The MW beam line is a secondary beamline and is used to transport particles produced by colliding a fixed energy proton beam onto a production target.

The horizontal position of the components of the MW beam line are shown as a function of displacement along the beam line in [3] Figure 2.2 (a). Figure 2.2 (b) gives the legend for the symbols used for the beamline devices. The naming convention for the beam devices is described in detail else where[3] . The polarity and the momentum of the beam were selected by adjusting the current in a string of dipole magnets, labelled MW6W in Figure 2.2 (a), and transported through the beamline.

The intensity impinging on the target is controlled by a set of collimators (MW8CV and MW8CH). The settings for the secondary beam tune are controlled by experimenters by means of the Experimental Physics Interactive Control System[4] (EPICS), whereby non-critical beamline devices could be manupilated as needed.

2.2.2 Secondary beam production

Production targets of Beryllium, Aluminum or Tungsten are used for the 800 GeV/c primary proton beam to generate a 530 GeV/c secondary beam. The production angle[3] is 1.4 mrad . The spread in the secondary beam momentum is about 1 %. The yield of π^- for a 0.75 interaction length Aluminum production target is 4.1×10^7 for an incident primary flux of 10^{12} protons, and is 5×10^8 secondary protons for the same incident flux.

2.2.3 Beam Čerenkov counter

The MW beamline has a gas-filled differential Čerenkov counter for particle identification of the incident beam. This detector has a total length of 130 ft. and the nominal Čerenkov angle is 4.998 mrad. Helium gas under pressure is used as a radiator, with the index of refraction changing with the pressure of the gas. Two 4 in $\times$ 4 in scintillation counters, one upstream and one downstream of the Čerenkov counter are used in coincidence to define a beam particle. Two different sized rings of six phototubes each were used to collect the Čerenkov light and these phototubes were read out by the data acquisition system.

The counter is used to distinguish between pions and protons in the incident beam, and is also able to differentiate kaons and antiprotons. Figure 2.3 shows the pressure curve[3] for the Čerenkov gas for negative beams of 530 GeV/c, and Figure 2.4 shows the pressure curve for positive beams.

For a 530 GeV/c negative beam produced from the Aluminum production target , the observed fractions of π^- is 96.9 %, of K^-s is 2.9 % and for $\bar{\text{p}}$ is 0.2 %, with about 1 % electrons and muon contamination. For positive beams, The beam is about 91.4 % protons, 7.1 % π^+ and 1.5 % K^+. The yields from the other production targets are almost identical to that from Aluminum.

2.2.4 Spill structure

Beam is sent to the experimental areas from the Tevatron on a cyclic basis, called the 'spill cycle'. The protons accelerated in the Tevatron are extracted in the Switchyard and distributed to the experimental areas.

The spill cycle is 57.2 seconds long, with the actual spill of beam to the experimental areas being 23 seconds. Most beam line magnets were ramped in order to conserve energy and to reduce chances of overheating. The spill cycle is depicted in Figure 2.5, with the beam being delivered to the experiment in the interval between T5 and T6 as shown.

The protons in the primary beam occur in very narrow time intervals, known as 'buckets', which are about 1 ns wide. The beam buckets were spaced 19.7 ns apart, and on the average, the probability of bucket occupancy is 10 %. The chance of double occupancy is 2 %.

Section 2.3

2.3.1 Halo Veto Wall

The secondary beam is accompanied by muons and hadrons travelling parallel to it. Most of these were swept away by 'spoiler' magnets in the beam line upstream of the target. The hadrons that accompanied the beam were attenuated by an iron hadron shield. The muons which were not swept away by the spoilers were detected by two walls of scintillator detectors, called the Veto Walls (VW) located downstream of the hadron shield.

Each Veto wall consists of 32 50 cm $\times$ 50 cm scintillators counters supported by a frame. The wall is divided into 4 quadrants. The two walls have an offset of 10 cm between them in the x-y plane to cover the gaps in the other wall. A coincidence between the walls is used in the interaction definition to veto events accompanied by a halo muon for some part of the run. Figure 2.6 shows the layout of the counters in the veto walls.

2.3.2 Targets used in the 1987 run

The data collected in the 1987/88 run is divided into two running periods. in the first running period, in September 1987, data was collected using only the information from the E672 detector, as the E706 apparatus was not fully operational at that time. Thick nuclear targets were used for the run, and the data is referred to as "Thick Target" data for the rest of this thesis. The targets used are listed in Table 2.3.1.

Table 2.3.1

Targets used for Thick Target running

Target	Thickness cm	Thickness gm/cm^2	% Interaction length (π^- beam)
Carbon	4.0	7.1	6.1
	10.2	18.2	15.5
	20.3	36.4	31.1
Aluminum	3.8	10.3	7.4
	12.7	34.3	24.8
	16.5	44.6	33.0
Copper	5.1	45.5	26.6
	10.2	91.0	53.1
Lead	0.95	10.8	4.5
	5.1	57.6	24.2
	7.6	86.5	33.7

2.3.3 Targets used in the '88 run

For the second part of running, information from both the E672 and E706 experiments was available. E706 is a direct photon experiment, and the targets were chosen so as to minimize the radiation lengths of the targets while ensuring a reasonable interaction rate.

Beryllium, Carbon and Copper targets were used for this period of running. For most of the data collected, the target consisted of twenty 2 mm Beryllium slices separated by 1.55 mm gaps. For the latter part of the run, two 0.8 mm slices of Copper were added 3.2 mm upstream of the Beryllium target, also separated by 1.55 mm. Figure 2.7 shows the target configuration. Table 2.3.2 gives details on the targets used[5]

Table 2.3.2

Targets used for second period of running

Parameters	Be	Cu	C
Length (cm)	4.0	0.16	4.0
Density (g/cm^2)	1.85	8.96	1.79
Radiation length (%)	11.33	11.19	21.28
π interaction length (%)	6.90	0.83	7.78
p interaction length (%)	9.24	1.03	10.24

2.3.3 Beam and interaction definition counters

For the 'thick target' running, the beam is defined by three scintillation counters located upstream of the target. These were 4 in $\times$ 4 in counters, one of them with a hole in it. A valid beam particle required a coincidence between two of the counters and no signal from the third hole counter. The interaction is defined by a set three 4 in $\times$ 4 in square interaction counters located in front of the LAC, and an interaction is defined as a signal from any of these counters in coincidence with a valid beam signal.

For the part of running where both E672 and E706 were operational, the beam signal is defined by three scintillation counters located immediately downstream of the veto wall, about 1.5 m in front of the target. Two of them, BA and BB, were 1 in $\times$ 1 in counters and the third, BH, is a 5 in $\times$ 5 in counter with a 3/8 in diameter hole in the center. The scintillator counters SE1 and SW1, were located out of the beam axis around 35 cm downstream of the target, and SE2 and SW2 were located 370 cm from the target. These four counters were used to define an interaction, and were matched in size to cover the full acceptance of the spectrometer, with holes around the beam axis.

Section 2.4

2.4.1 The Silicon Strip Detector system

The Silicon Strip Detector (SSD) system[6] contains seven modules of silicon strip wafers, each containing one vertical (X) and one horizontal (Y) plane. The system has 7,120 active channels. All wafers have a pitch of 50 μm and a thickness of 250 to 300 μm. A schematic of the SSD system and the target region is shown in Figure 2.7

Three of these modules are made of 3 × 3 cm wafers and are located upstream of the target to obtain the trajectory of the beam particle. The remaining four are located downstream of the target, with one of them being 3 × 3 cm and the rest 5 × 5 cm. The signals from the SSD strips are sent to charge-sensitive preamplifiers and eventually are digitized and stored for possible readout.

2.4.2 The E706 PWC system

There are four Proportional Wire Chambers (PWC's) in the E706 apparatus[7] , each of which contain a set of four anode wire planes (X, Y, U and V). The U plane is tilted at an angle of 37° to the vertical and the V-plane is tilted at an angle of 53° to the vertical. The X and Y-planes are horizontal and vertical respectively.

The total number of channels for the PWC system is 13,440. The anode planes are made up of 0.02 mm diameter gold-plated tungsten wires with a wire spacing of 2.54 mm between them. Each anode plane has a graphite coated mylar cathode plane on each side. The separation between the anode and cathode planes in 0.57 cm. Figure 2.8 shows a schematic of the planes in one chamber.

The four PWCs are dimensioned so as to maintain approximately constant angular acceptance. The first chamber is 1.63 m $\times$ 1.22 m, the second and the third are 2.03 m $\times$ 2.03 m and the last chamber is 2.44 m $\times$ 2.44 m.

The gas mixture used for the operation of the system is 79.7 % argon, 18 % isobutane, 2.2 % isopropyl alcohol and 0.1 % freon. Typically, the PWCs were operated at a high voltage of 2.8 kVolts. The signals from the wires were amplified by preamplifier cards and then digitized for readout.

2.4.3 Analysis Dipole Magnet

The analysis magnet (MW9AN) is a dipole magnet which provided a p_t-kick to charged tracks in the x-direction for momentum determination. The dipole is located between the SSD system and the PWC system, and knowing the trajectory of the track before and after the dipole gave the momentum of the track.

The magnet has a length of 328 cm along the beamline. There were two mirror plates installed on the upstream and downstream ends of the dipole to reduce the effect of the fringe fields. The acceptance of the magnet is determined by the holes in the mirror plates, which were 17.8 cm $\times$ 12.7 cm for the upstream end, and 68.6 cm $\times$ 62.4 cm for the downstream end.

The magnetic field in the dipole was mapped by using the ZIPTRAK[8] system developed at Fermilab. Details of the field parametrization are given elsewhere[7]. The operating current for the dipole is chosen to be 1050 Amps, which corresponds to a p_t-kick of 450 MeV/c for each charged track.

2.4.4 The Liquid Argon Calorimeter (LAC)

The Liquid Argon Calorimeter (LAC)[9] is the central part of the E706 detector. The data from the LAC is not used for the analysis presented in this thesis, so only a brief description of the system is presented. The LAC is divided into two sections, an electromagnetic section (EMLAC) and a hadronic section (HALAC). The EMLAC [10–11] and the HALAC[12] are mechanically independent of each other, and share a common cryostat. When assembled, there is a hole of 42.2 cm diameter in the center of the LAC for the beam.

The EMLAC is used to measure positions and energies of particles showering electromagnetically, like (γ, e^+, e^-). The EMLAC has transverse dimensions of 3.1 m and is divided into 8 octants. Each octant consists 66 layers of 2-mm thick lead plates interlaced with alternate layers of 1.6-mm thick G-10 (G-10 is a glass epoxy, but does not contain any fire retardant additives which can contaminate the liquid argon) readout boards. The readout boards are in two views, the radial view (r-view) and the azimuthal view (ϕ-view). The argon gaps are 2.5 mm thick. Each r-view board consists of 254 concentric strips, each one being around 5.5 mm wide. The exact width of each strip varies according to the radius of its location so as to subtend the same solid angle as seen from the target.

The ϕ-view is divided into two regions, the outer and the inner regions. Each inner strip subtends an azimuthal angle of 16.4 mrad and the outer strips an angle of 8.2 mrad. The longitudinal readout of the EMLAC is divided into two, with the front section having 22 layers (10 radiation lengths) and the back layer with 44 layers (20 radiation lengths). The energy resolution for the LAC is given by

$$\frac{\sigma(E)}{E} = \frac{14.0\%}{\sqrt{E}(GeV)} \tag{2.1}$$

for energies above 10 GeV. The EMLAC is about 2 interaction lengths of material.

The HALAC consists of 52 stainless steel plates, each of 2 cm thickness. In between the plates are detector planes with charge collecting pads for readout. The pads are arranged so as to provide a 'tower' structure when viewed from the target. The HALAC has two sections longitudinally, the front section with 2.6 interaction lengths and the back section with 7.2 interaction lengths. The collection pads are triangular in shape and vary in size depending on their location from 10.8 cm/side to 13.7 cm/side. The energy resolution of the HALAC can be described by

$$\frac{\sigma(E)}{E} = \frac{69\%}{\sqrt{E}(GeV)} \tag{2.2}$$

for E in GeV. The LAC is shown in Figure 2.9 suspended within the cryostat.

2.4.6 Forward Calorimeter

The Forward Calorimeter (FCAL)[13] is designed to measure the energy of the particles which go through the hole in the LAC. The FCAL is located about 17 m downstream of the target behind the LAC. It is divided into three modules, the first two with 28 steel plates, 1.9 cm thick with a diameter of 114 cm. The third module has 32 plates.

The plates were separated by 0.46 cm sheets of acrylic scintillator. The plastic and steel plates have a hole of 3.2 cm diameter to allow the passage of non-interacting beam. The scintillator and plates have holes in them for BBQ doped wave shifter rods for readout by a phototube on the end. The bases for the phototubes were designed to perform at rates of up to 10 MHz. The signals are sent via coaxial cable to be digitized by a flash-ADC system, which strobed the system every 10 ns. The FCAL is depicted in Figure 2.10.

Data from the FCAL are not used in the analysis presented in this thesis. The next chapter describes the E672 spectrometer.

REFERENCES

1) CAMAC Instrumentation and Interface Standards, IEEE 1982, ISBN 0-471-89737-X.

2) R. Crittenden et al., *Nucl. Instr. and Meth.* **A270**, 99 (1988) .

3) I. Kourbanis, Ph.D thesis, Northeastern University, Boston, (1989.

4) V. Frohne, "A short guide to The EPICS Beamline Control System", Fermilab Publication, 1985.

5) C. Yosef , Ph.D Thesis, Northeastern University, August 1990.

6) E. Engels Jr. et al., *Nucl. Inst. and Meth.* **A279**, 272 (1989) .

7) S. Easo, Ph.D. Thesis, Pennsylvania State University, 1989.

8) ZIPTRAK Manual, FNAL Computing Department, publication PN267.0.

9) W. Desoi, Ph.D. thesis, University of Rochester 1990.

10) F. Lobkowicz et al., *Nucl. Inst. and Meth.* **A235**, 332 (1985)

11) J. Huston et al. Paper submitted to XXIV Int. Conf. on HEP, Munich, 1988.

12) C. Lirakis, Ph.D. thesis , Northeastern University, 1989.

13) R. Benson, Ph.D. thesis, University of Minnesota, 1990.

The E672/E706 Apparatus

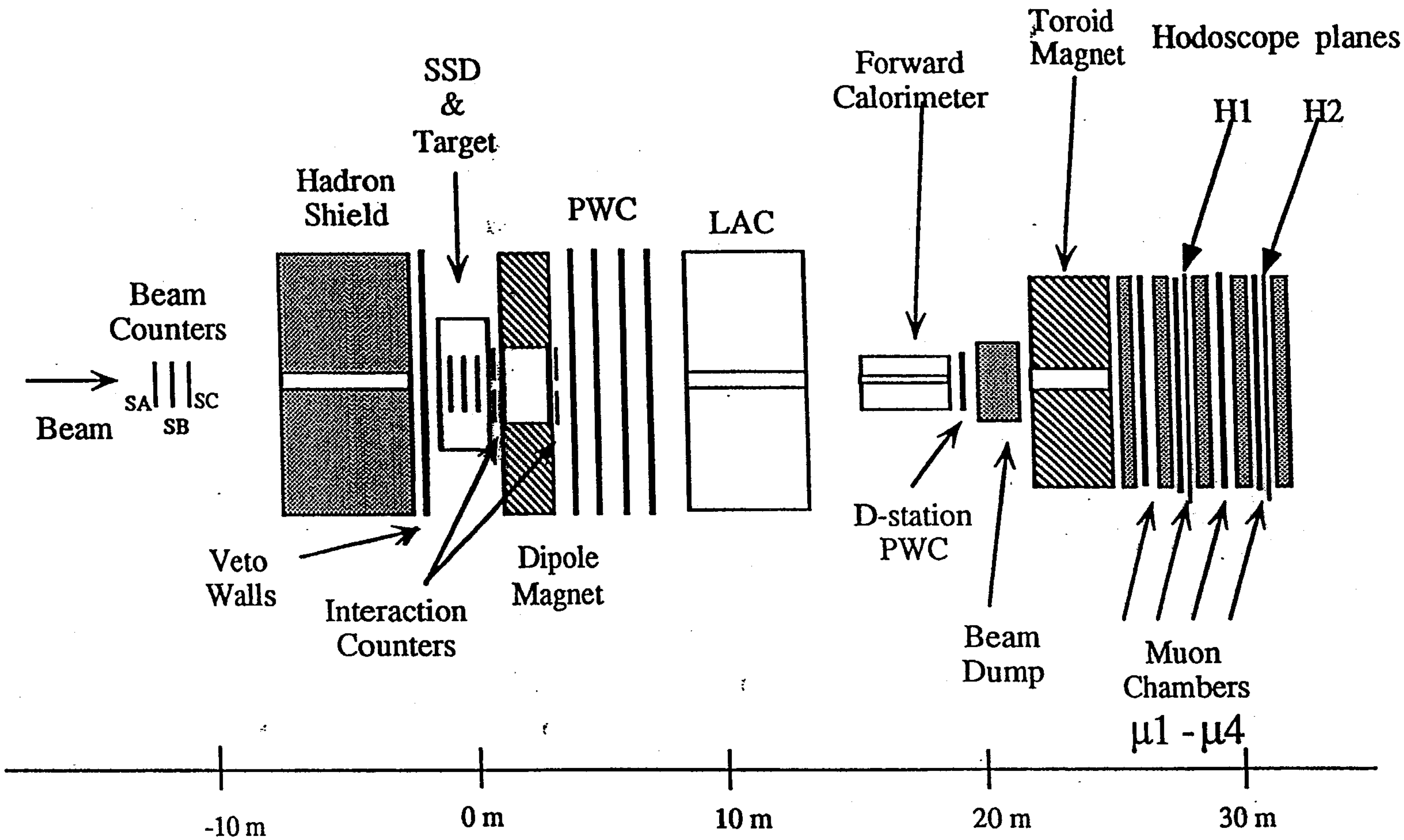

FIGURE 2.1

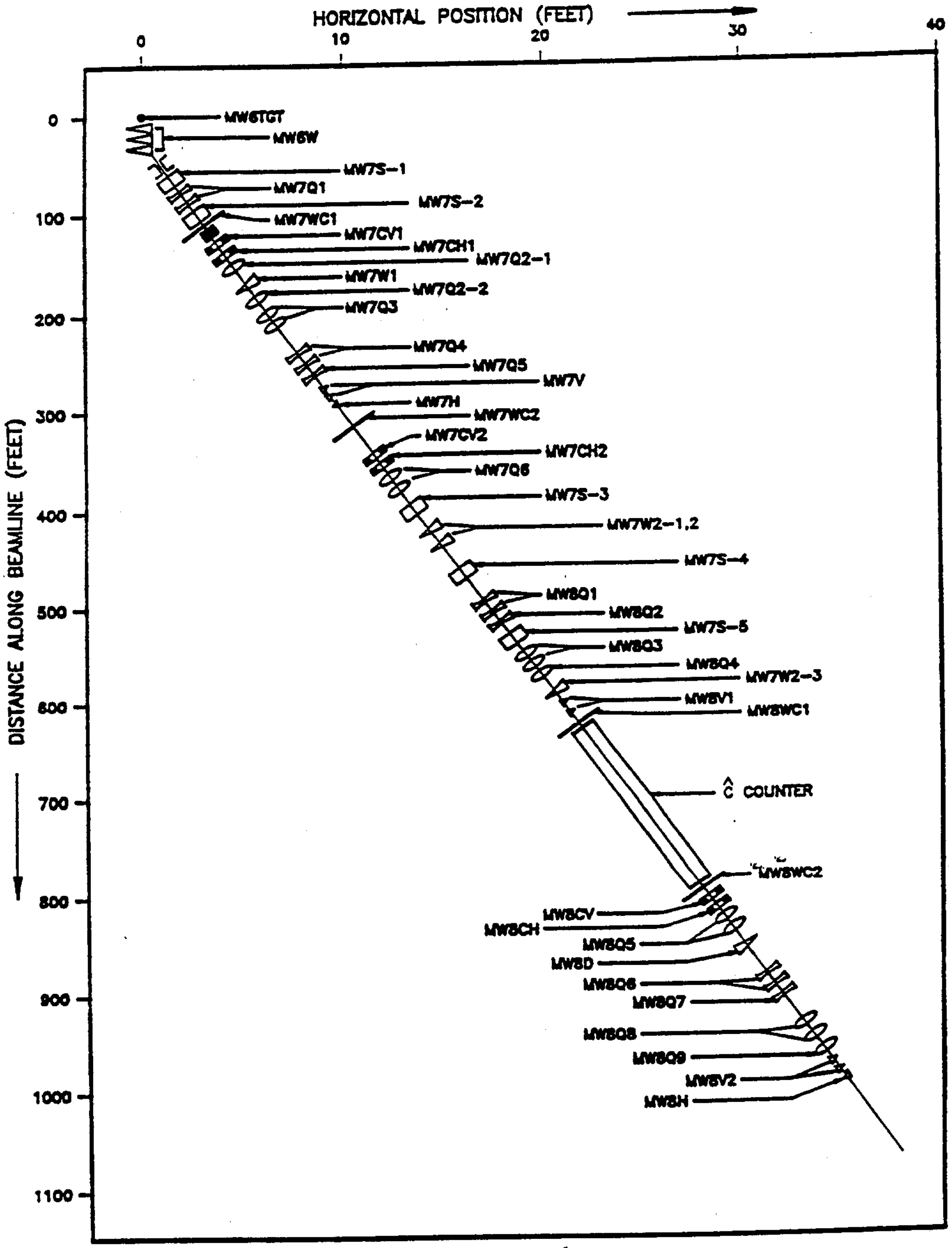
HORIZONTAL POSITION (FEET)
0
10
20
30
40
DISTANCE ALONG BEAMLINE (FEET)
0
100
200
300
400
500
600
700
800
900
1000
1100
MW6TGT
MW6W
MW7S-1
MW7Q1
MW7S-2
MW7WC1
MW7CV1
MW7CH1
MW7Q2-1
MW7W1
MW7Q2-2
MW7Q3
MW7Q4
MW7Q5
MW7V
MW7H
MW7WC2
MW7CV2
MW7CH2
MW7Q6
MW7S-3
MW7W2-1,2
MW7S-4
MW8Q1
MW8Q2
MW7S-5
MW8Q3
MW8Q4
MW7W2-3
MW8V1
MW8WC1
Ĉ COUNTER
MW8WC2
MW8CV
MW8CH
MW8Q5
MW8D
MW8Q6
MW8Q7
MW8Q8
MW8Q9
MW8V2
MW8H

FIGURE 2.2 (a)

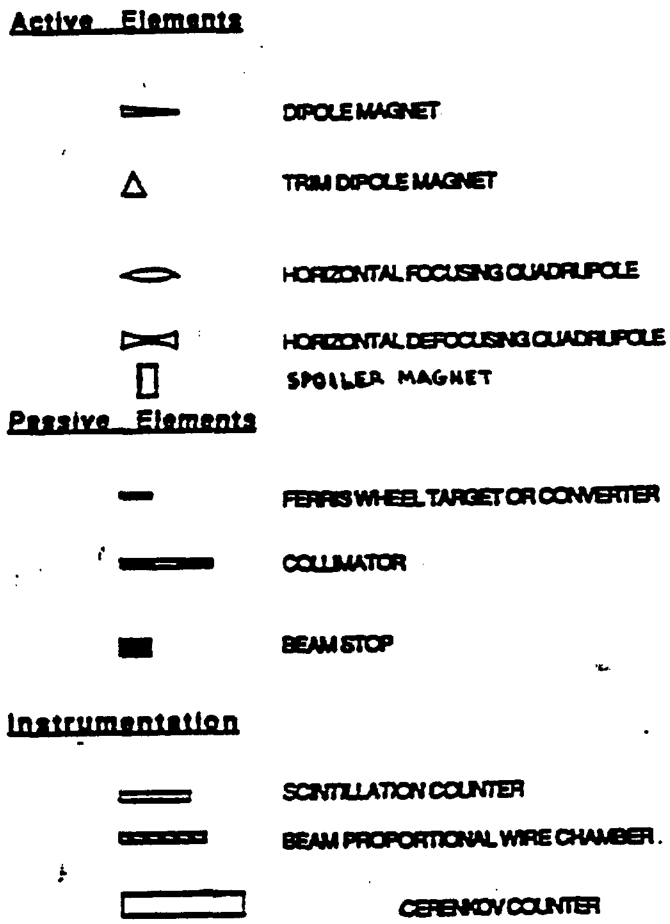
Active Elements
DIPOLE MAGNET
TRIM DIPOLE MAGNET
HORIZONTAL FOCUSING QUADRUPOLE
HORIZONTAL DEFOCUSING QUADRUPOLE
SPOILER MAGNET
Passive Elements
FERRIS WHEEL TARGET OR CONVERTER
COLLIMATOR
BEAM STOP
Instrumentation
SCINTILLATION COUNTER
BEAM PROPORTIONAL WIRE CHAMBER.
CERENKOV COUNTER

FIGURE 2.2 (b)

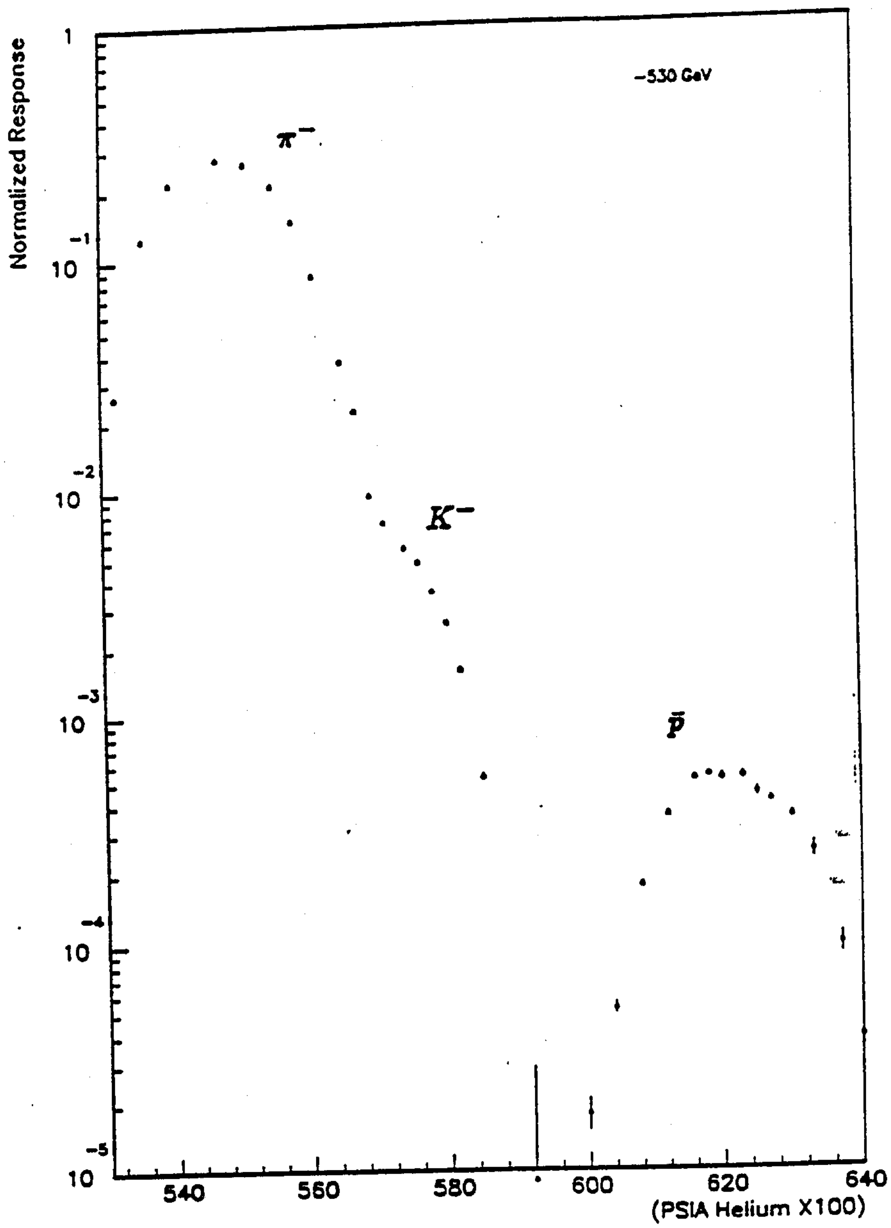

Normalized Response
1
10⁻¹
10⁻²
10⁻³
10⁻⁴
10⁻⁵
−530 GeV
π⁻
K⁻
p̄
540
560
580
600
620
640
(PSIA Helium X100)

FIGURE 2.3

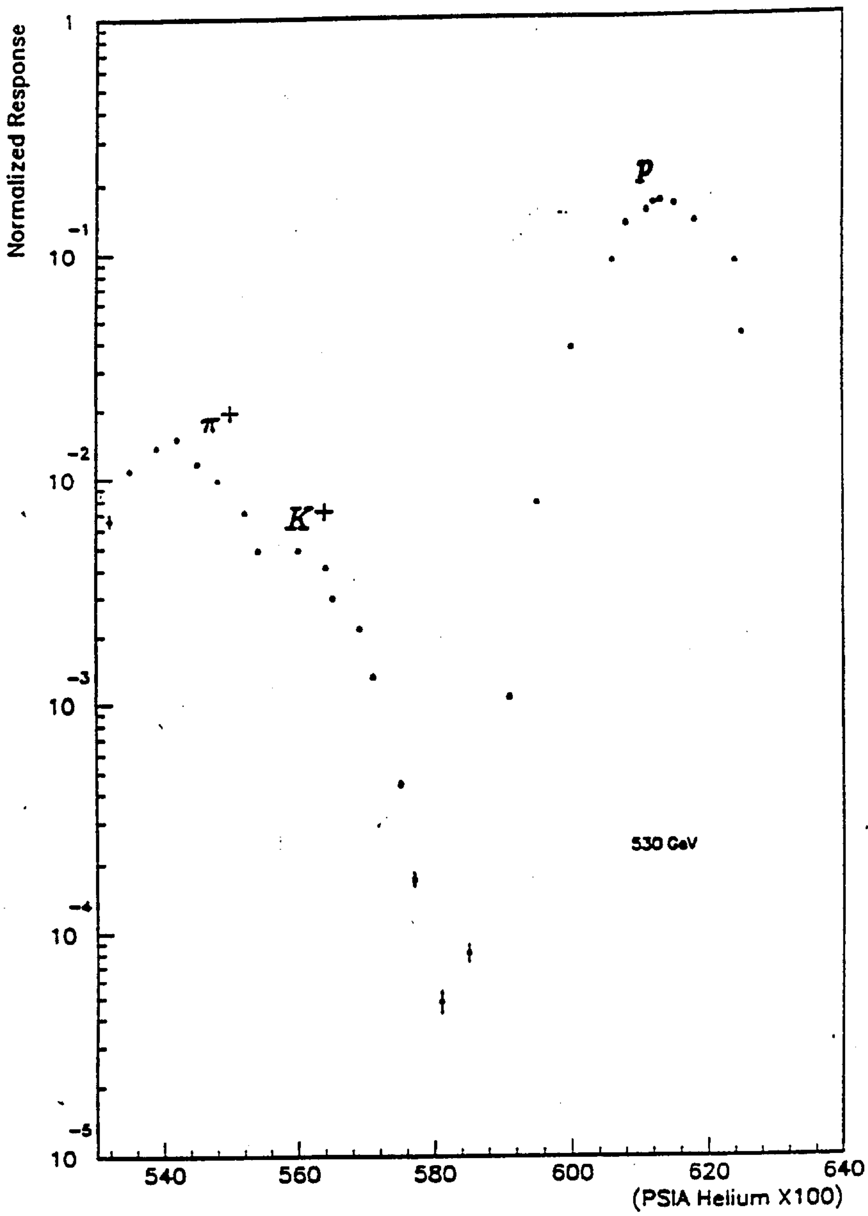
Normalized Response
1
10^-1
10^-2
10^-3
10^-4
10^-5
p
π+
K+
530 GeV
540
560
580
600
620
640
(PSIA Helium X100)

FIGURE 2.4

Accelerator Spill Cycle

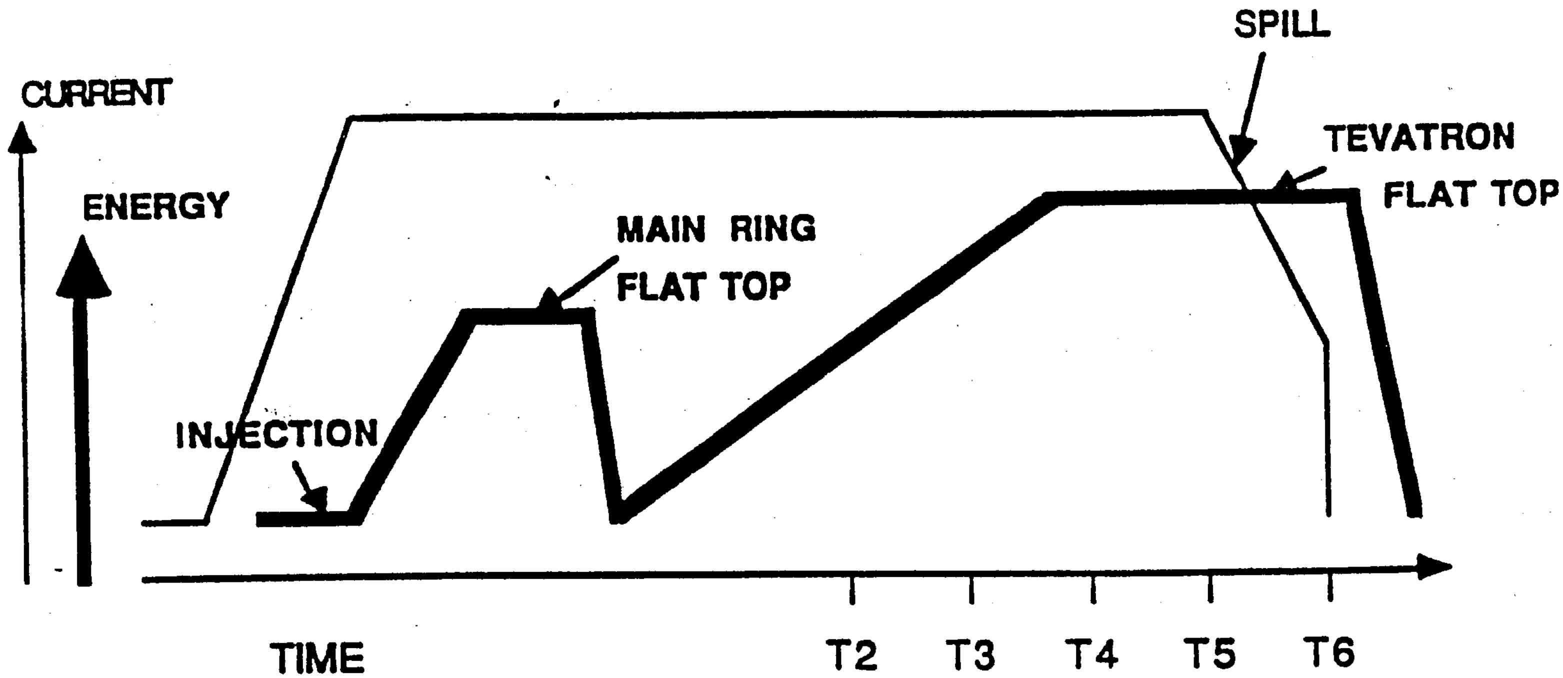

FIGURE 2.5

VETO WALL: SCHEMATIC

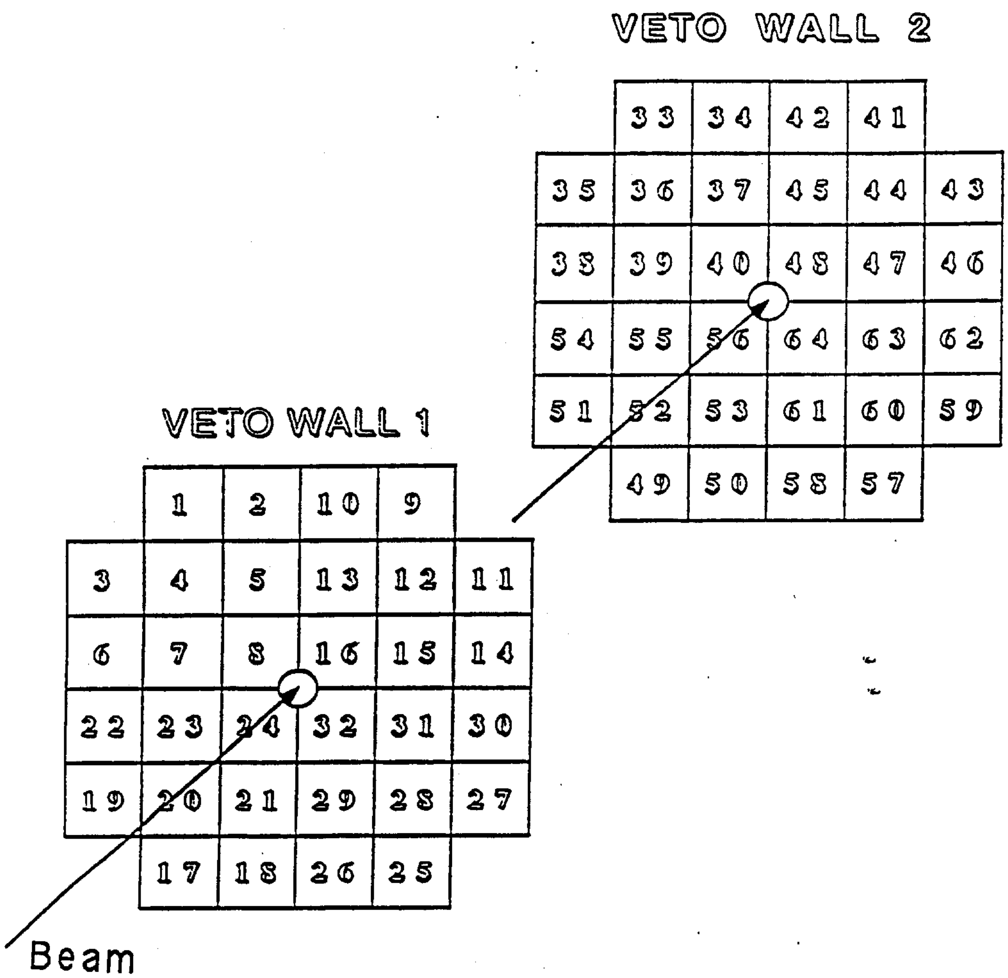

FIGURE 2.6

SSD and Target configuration

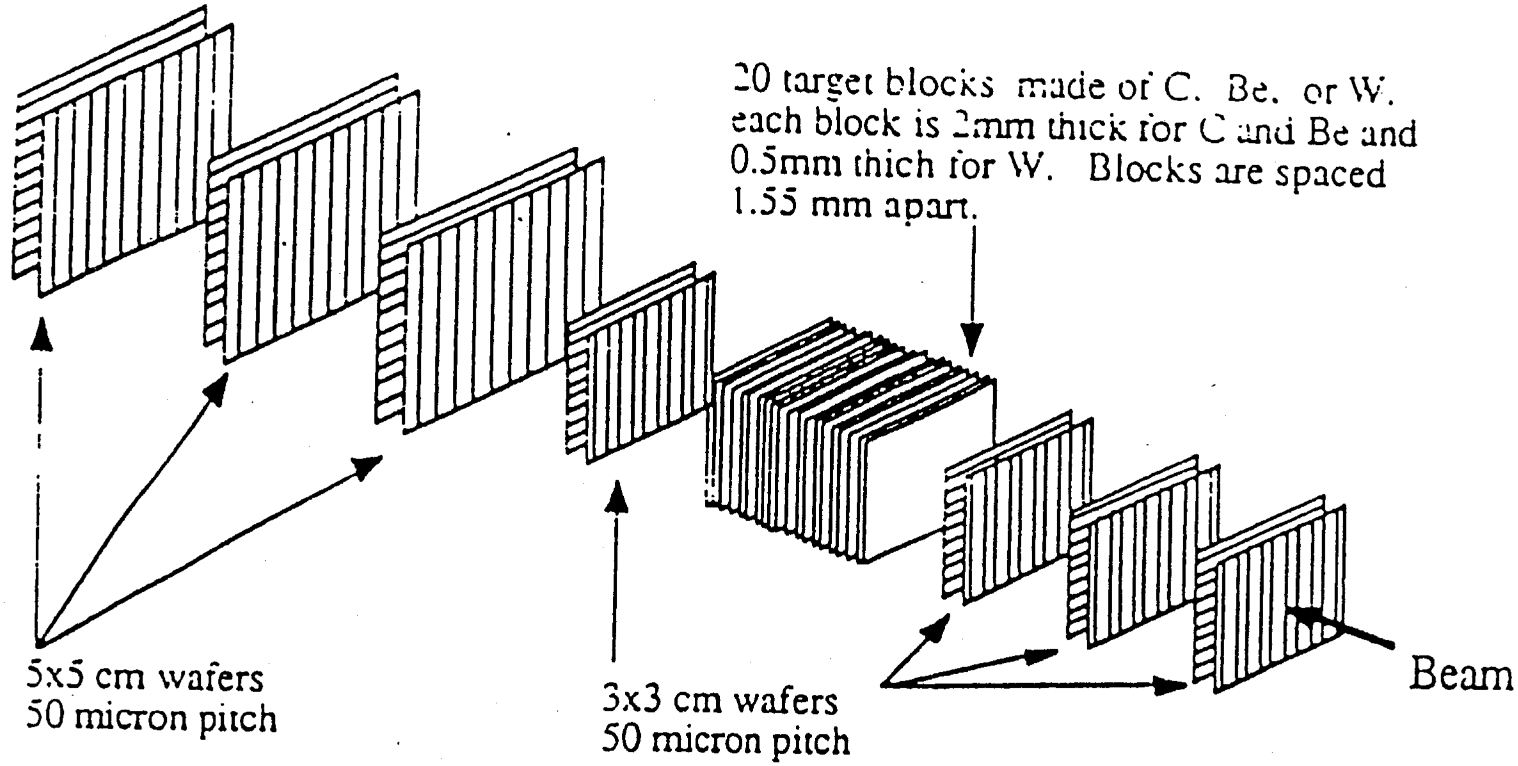

FIGURE 2.7

E706 PWC planes: Schematic

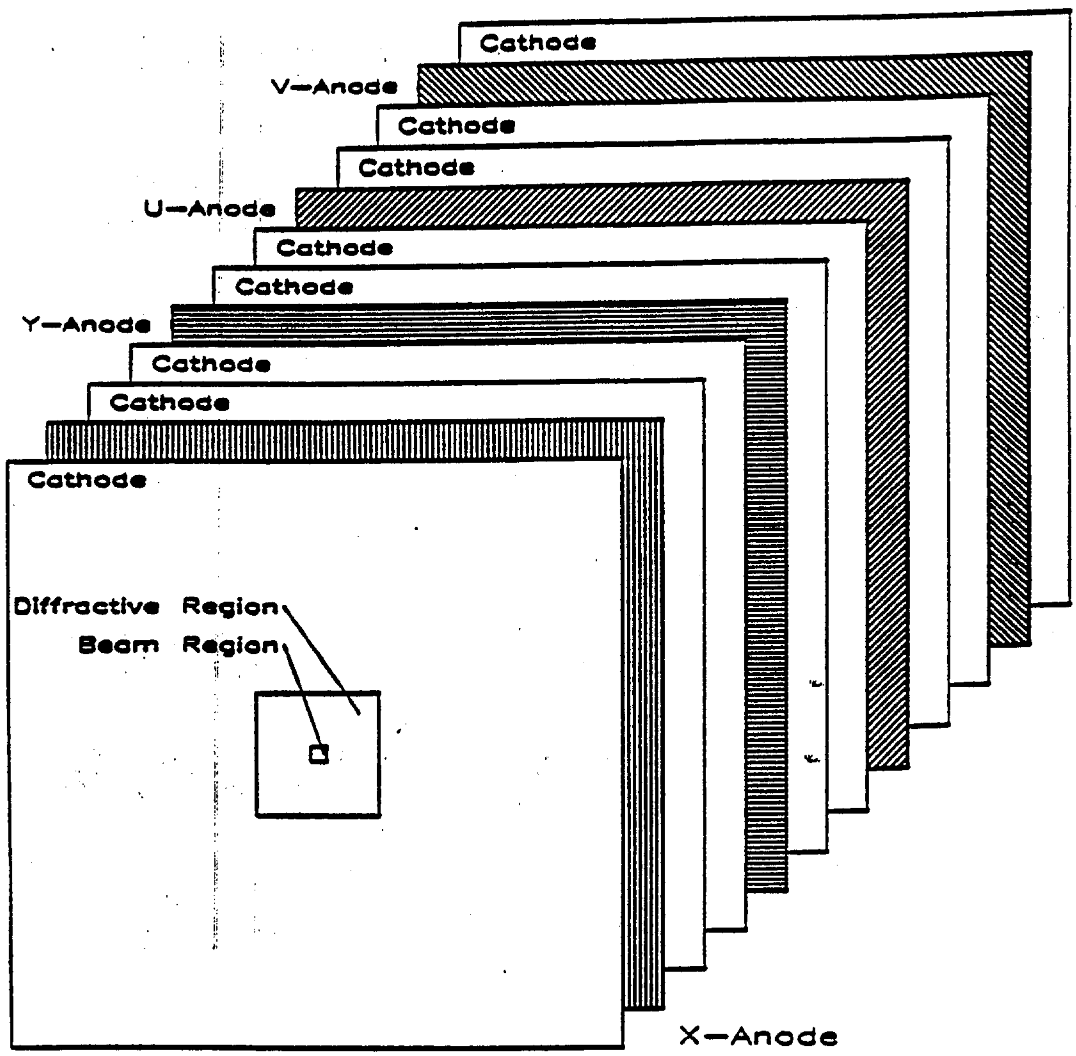

FIGURE 2.8

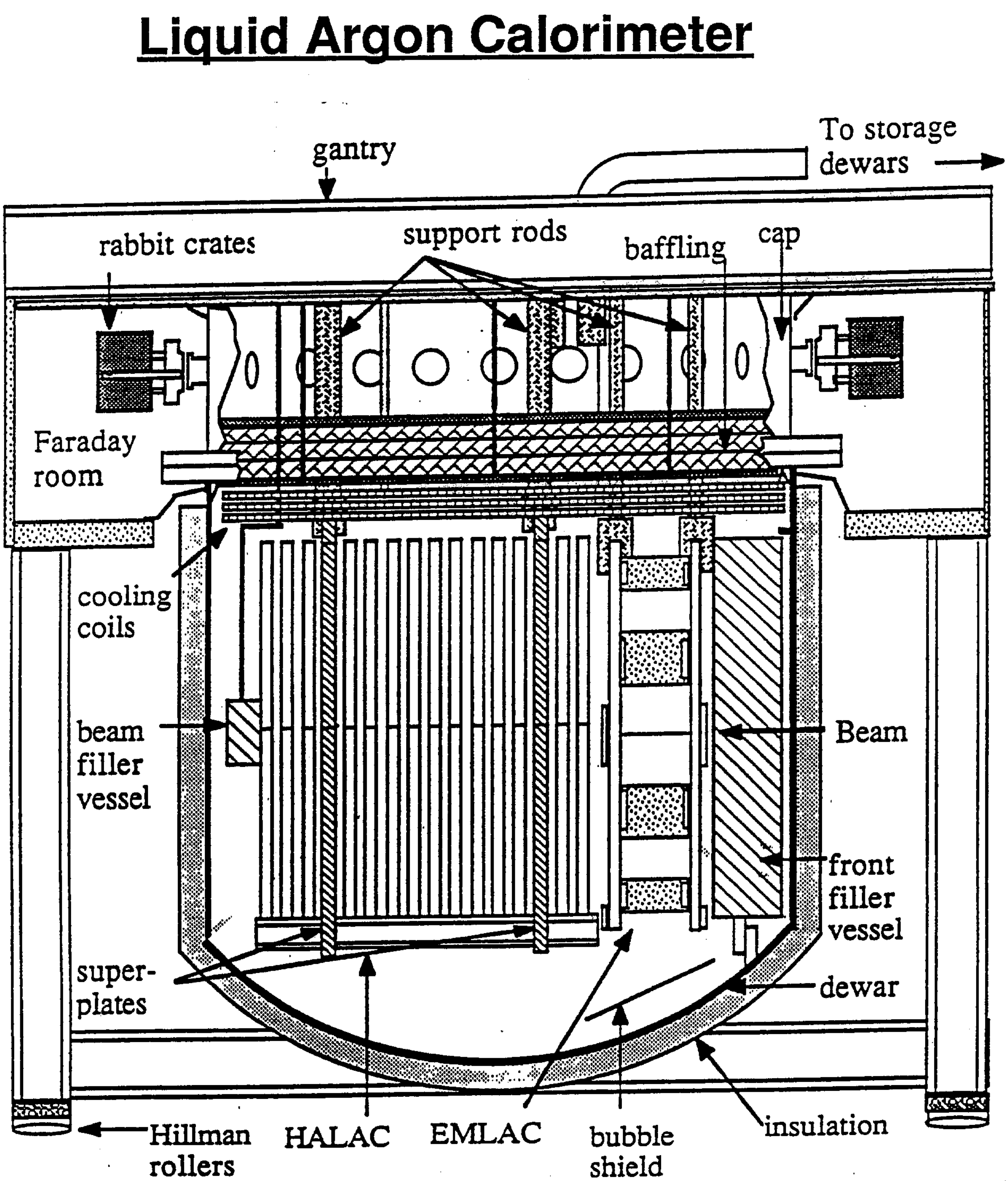
Liquid Argon Calorimeter
gantry
To storage dewars
rabbit crates
support rods
baffling
cap
Faraday room
cooling coils
beam filler vessel
Beam
front filler vessel
super-plates
dewar
Hillman rollers
HALAC
EMLAC
bubble shield
insulation

FIGURE 2.9

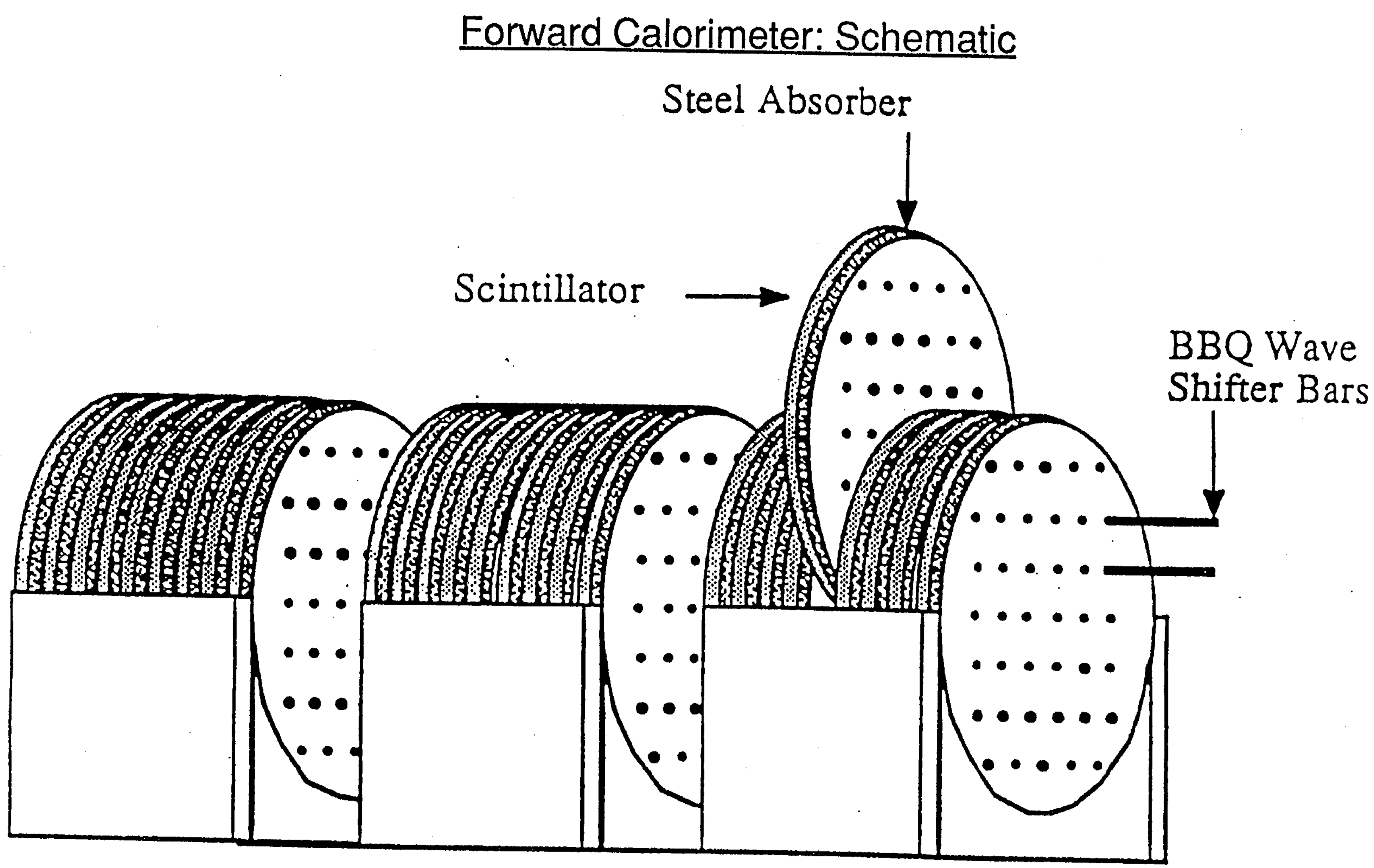
Forward Calorimeter: Schematic
Steel Absorber
Scintillator
BBQ Wave
Shifter Bars

FIGURE 2.10

CHAPTER 3
THE DIMUON SPECTROMETER

The components of the E672 detector are listed in Section 2.1.2 of chapter 2 of this thesis. A schematic of the E672 detector is shown in Figure 3.1. The detector is located 20 m downstream of the target.

The central part of the apparatus is a set four of Multiwire Proportional Chambers (MWPC) used for tracking muons. The four MWPCs are described in Section 3.1. The two pretrigger hodoscopes and their performance is discussed in Section 3.2 The E672 toroid magnet and its performance is presented in Section 3.3. Section 3.4 gives a description of the 3-chamber "D-station" PWCs. The last section gives details of the beam dump and the shielding around the E672 apparatus.

Section 3.1

3.1.1 Construction details for the Muon Chambers

The particles traversing the material in the Liquid Argon Calorimeter (LAC), the Forward Calorimeter (FCAL), the toroid and the concrete shielding are detected using a set of four 3-plane Multiwire Proportional Chambers (MWPC's). These chambers will be referred to as the "muon chambers", μ_1, μ_2, μ_3 and μ_4. Each chamber has a multiwire anode plane between two grounded cathode planes. These provide three coordinate measurements for the passage of a charged particle. All the charged particles which survive the material between the target and the muon chambers are assumed to be muons.

The details of the chamber construction are described elsewhere[1] ; only a brief description will be given here. The four chambers are constructed in a similar manner. The active area of the chambers is an annulus of outer radius 1.35 m and an inside radius between 0.15 m and 0.2 m, depending on the z-position of the chamber.

The anode planes for three of the chambers (μ_1, μ_3 and μ_4) consist of 2 $\times$ 223 gold-plated tungsten wire of 25 micron diameter wound at a tension of 80 gm. The spacing between the wires is 0.6 cm, and two wires are connected to one preamplifier channel to give an effective pitch of 1.2 cm. The wires are vertical in the final orientation of the chambers; the coordinate associated with the anode plane is labelled "w". The MWPC μ_2 has 3 $\times$ 223 wires with a wire spacing of 0.4 cm, and three wires connected to one preamplifier channel to give the same effective pitch as the other chambers.

The two cathode planes are labelled "u" and "v"; each plane consists of 255 copper strips with a pitch of 1.05 cm. These strips are oriented at an angle of $\pm 45°$ to the vertical. The spacing between the cathode and anode planes is 9.5 mm. Some of the chamber parameters[1] are summarized in Table 3.1.1.

Table 3.1.1

Parameters for the muon chambers

Parameter	Chamber	Value
Inner radius	μ_1	0.15 m
	μ_2	0.15 m
	μ_3	0.18 m
	μ_4	0.20 m
Outer radius	All	1.34 m
Channels	u, v planes	255
	w plane	223
Effective pitch	u, v planes	1.05 cm
	w plane	1.20 cm
Anode-cathode gap	All	0.95 cm

Figure 3.2(a) shows a schematic of the construction details of the muon chambers, with a cutaway view showing the anode and the two cathode planes. Figure 3.2 (b) shows the cross section of the chamber.

3.1.2 Operation of the muon chambers

The gas system for the operation of the chambers is described elsewhere[2] The gas mixture for the muon chambers is chosen to be 76.0 % Argon, 15.0 % isobutane, 8.9 % methylal and 0.1 % freon. This gas mixture is chosen based on the performance of a 1 mm chamber used in an experiment at Brookhaven and CERN[3] . The total gas flow rate is 0.4 liters/minute under normal operating conditions.

The high voltage system is also described in Reference [3].[3] . The chambers μ_1, μ_3 and μ_4 were operated at 3400 V and chamber μ_4 is operated at

4200 Volts. There is also provision to deaden the inner area of the chambers around the beam axis by applying a voltage of about 1 kVolts to a copper-clad ring of G-10 epoxy around the inner hole. The deadener is not used in the this run of the experiment.

The anode threshold setting is typically +8 Volts and the cathode threshold is -1.5 volts. The typical singles rates for the chambers are around 2-4 kHz for the nominal operating voltage[4] . The gate width for the chamber signals is 150 ns (the pulses from the chamber are 120 ns wide, typically, with a jitter of about 30 ns). The anode cluster widths are 1.2 wire widths, and the cathode cluster widths are 2 strip spacings.

The signals from the chamber are first amplified and discriminated by preamplifier cards attached to the chambers. The details and circuit diagrams for the preamplifier cards[1] are described elsewhere[3] Each card has 16 channels and has an input impedance of 510 Ω. The outputs of the preamplifier cards are ECL signals which are sent from the chambers to the readout system (described in the next chapter) by flat Spectra Strip cables.

Section 3.2

3.2.1 Construction details of the pretrigger hodoscopes

Two circular 16-segment scintillator hodoscopes are used as a pretrigger for the duration of the run. The first hodoscope (H1) is located behind the muon chamber μ_2 and the second (H2) behind μ_4. Two or more hits in both H1 and H2 in coincidence with a valid interaction constituted the pretrigger for most part of the data taking.

Each hodoscope consists of four quadrants of PS-10 plastic scintillator, manufactured by the Polycast. Each quadrant has four segments, roughly triangular in shape, encased in aluminum sheet material. The light output from each segment is collected by means of a BBQ doped waveshifter, and transmitted to an RCA 8575 photomultiplier tube.

The hodoscopes are both 5 ft. in radius; H1 has an inner radius of 12 inches and H2 has an inner radius of 16 inches. The plastic scintillator for both the hodoscopes is 1.5 inches thick. The active area of the dimuon chambers is matched by the active area of the hodoscopes. The edges of the assembly are taped with black tape to minimize light leaks. Adjacent quadrants of the hodoscope are not in the same plane, but staggered by the thickness of the quadrant. The whole assembly is held in place on a Uni-strut frame. The schematic diagram of the hodoscope is shown in Figure 3.3.

The phototubes are mounted on metal plates screwed on to the edge of the perimeter of the hodoscope with the help of clamps. The phototubes showed persistent light leaks in three places; the base, the region where the base is connected to the tube and the region near the photocathode. The light leaks were fixed by the use of heat shrink tubing (commercially manufactured by ALPAN corporation) around all mechanical junctions. The tube is encased in a μ-metal shield. The wave shifter end is centered on the photocathode by means of a slotted aluminum disk with an O-ring around it, and then coupled with optical grease to the end of the photocathode. Figure 3.4 shows the assembly of the photomultiplier tubes to the end of the wave shifter.

3.2.2 Light collection from the hodoscopes

The scintillator plastic light emission spectrum has a maximum at 410 nanometers wavelength. The wave shifter is suitably doped to absorb the emitted light, and then transmit it to the phototube at a wavelength of 510 nanometers. Although the RCA 8575 has a quantum efficiency which peaks at 410 nm while the wave shifter emission spectrum peaks at 510 nm, the overall efficiency of the counters was acceptable.

The 32 photomultipliers are selected from a set of about 60 by using an α source to investigate the pulse-height vs. high voltage response of the tubes.

3.2.3 Performance of the hodoscopes

The photomultipliers are operated at a high voltage of around 2100 Volts. The noise rate at this high voltage is about 300 Hz/PMT, and about 5 kHz for each hodoscope.

The signals from the phototubes are sent to a CAMAC multiplicity module[5] which is used to set the multiplicity level for the pretrigger. The input impedance of the module is large, and so the signals are 'bounced' off it to ADC's for pulse height analysis. The implementation of the fast logic signals for the pretrigger formation is described in the next chapter.

Section 3.3

3.3.1 Construction details of the Toroid

The construction of the iron toroid[1] and its operation [6–7] is described in detail elsewhere. The momentum analysis for the E672 Dimuon Trigger processor (DTP) is done using a polarized toroid, with an axial field whose average value is 18.4 kGauss for a nominal current of 1700 Amps. The toroid provides an average p_t-kick of 1.35 GeV/c in the radial direction to charged particles in the active area of the toroid.

The toroid is 2.44 m long and weighs about 125 tons. The outer radius of the toroid is 1.35 m and the inner radius at the upstream end in 0.168 m. There is a hole in the center of the toroid with a taper of about 11 mrad, which corresponds to the inner radius at the down stream end of 0.197 m. The total power consumption for the toroid is 61 kW and the coils are cooled by water. The beams-eye view of the toroid is shown in Figure 3.5 (a) and Figure 3.5 (b) shows the side view.

3.3.2 Toroid operation

The nominal operating current for the toroid is 1700 A. The operation of the toroid is controlled by the EPICS system[8] and is assigned the label MW9T in the system. In the NORMAL polarity of the toroid, the magnetic field is such that a positive charged particle would get bent radially *inwards.* The relative polarities of the dipole and the toroid are read by a NIM module which monitored the field directions. This information is input to the trigger processor for the online dimuon mass calculation. The field in the toroid is also monitored by a Hall probe connected to a gaussmeter. The Hall probe is movable along the radius of the toroid, and is inserted in a slot at the center of the toroid perpendicular to the beam axis.

The field at nominal operating conditions is calculated to be 2.24 T at the inside radius and 1.74 T at the outside radius, which corresponded to a p_t-kick between 1.27 and 1.64 GeV/c. There is no measurable dependence of the field on the azimuthal angle.

Section 3.4

3.4.1 The D-Station PWC: Geometry

The D-station is a set of three proportional wire chamber (PWCs) which are located upstream of the toroid and the beam dump. The three chambers are labelled DX, DY and DU for each view. The physical dimensions of the three chambers and their final assembly are shown in Figure 3.6.

The chambers DX and DY are identical in construction, and each has 1024 wires with a two cathode wire planes and one anode wire plane. The spacing for the anode wires is 1.95 mm and the wires are made of 0.0008 inch diameter gold-plated tungsten. The cathode wires are spaced at 0.98 mm and are made of 0.004 inch diameter silver-coated beryllium-copper wire. Only the central 576 wires in each anode plane are instrumented. The distance between the anode and cathode plane is about 0.25 inches. The DU chamber has 845 wires of which the central 736 are instrumented.

The DU chamber is mounted such that the anode wires make an angle of 30° with the horizontal. The DX chamber has its wires vertical and the DY has its wires horizontal when mounted in their final configuration.

Each chamber is enclosed in two mylar windows of 0.002 inch thickness. Two sheets of aluminum coated mylar laminate provide shielding from external noise. The centers of the chambers are deadened around the beam region.

3.4.2 D-station operation

The D-station chambers are read out using Nanometrics N-227-C 16-channel preamplifier-discriminator cards located on the chamber. The output signals are transmitted to the readout system via flat Spectra Strip cables.

The chambers are operated with the same gas mixture as for the muon chambers, namely Argon-isobutane-methylal-freon in 76%-15%-8.9%-0.1% proportion. The high voltage is nominally around 3500 Volts, and the singles rates are around 10 kHz per chamber. The intersection of the active area of the chambers is a square of side 1.1 meters centered on the beam axis.

Section 3.5

3.5.1 Beam Dump

In order to stop the beam particles which have not interacted in the target, a beam dump is constructed between the D-station and the toroid. It consisted of 94 cm of 10 in $\times$ 10 in. steel and 18 inches of 8 in $\times$ 8 in tungsten. The whole assembly is surrounded by concrete. The steel and tungsten are about 10 interaction lengths thick together.

3.5.2 Shielding

Shielding is used to cut down the background in the muon chambers from hadrons which survive the calorimeters and the beam dump. Immediately after the toroid and between the muon chambers there are walls of about 1 meter thick concrete for shielding and support for the muon chambers and the hodoscopes. The center of the concrete, around the beam axis, is a 1 ft $\times$ 1 ft slab of iron, with a core of lead which acted as a beam stop for any forward going particles which did not stop in the beam dump. The area above the forward calorimeter and the D-station is covered by concrete blocks for radiation safety reasons.

REFERENCES

1) P. Draper, Ph.D. thesis, Indiana University 1987

2) K. Welch, "Gas system for Dimuon Chambers",E672 Internal Memo No.149, 1987.

3) R. Crittenden et al., *Nucl. Instr. and Meth.* **185**, 75 (1981)

4) S. Kartik et al.,"Noise and efficiencies for the Dimuon chambers", E672 Internal note No. 139 1987.

5) R. Crittenden et al., *Nucl. Instr. and Meth.* **A270**, 99 (1988)

6) P. Draper, "BURT Manual", E672 Internal Note No. 116 (1986).

7) P. Smith, "The E672 Analysis magnets", E672 Internal Note No. 176, (1987).

8) V. Frohne, "A short guide to the EPICS Beamline Control System", Fermilab publication, 1985.

9) S. Marguiles, "D-Station parameters", E672 Internal Note No. 155, 1986.

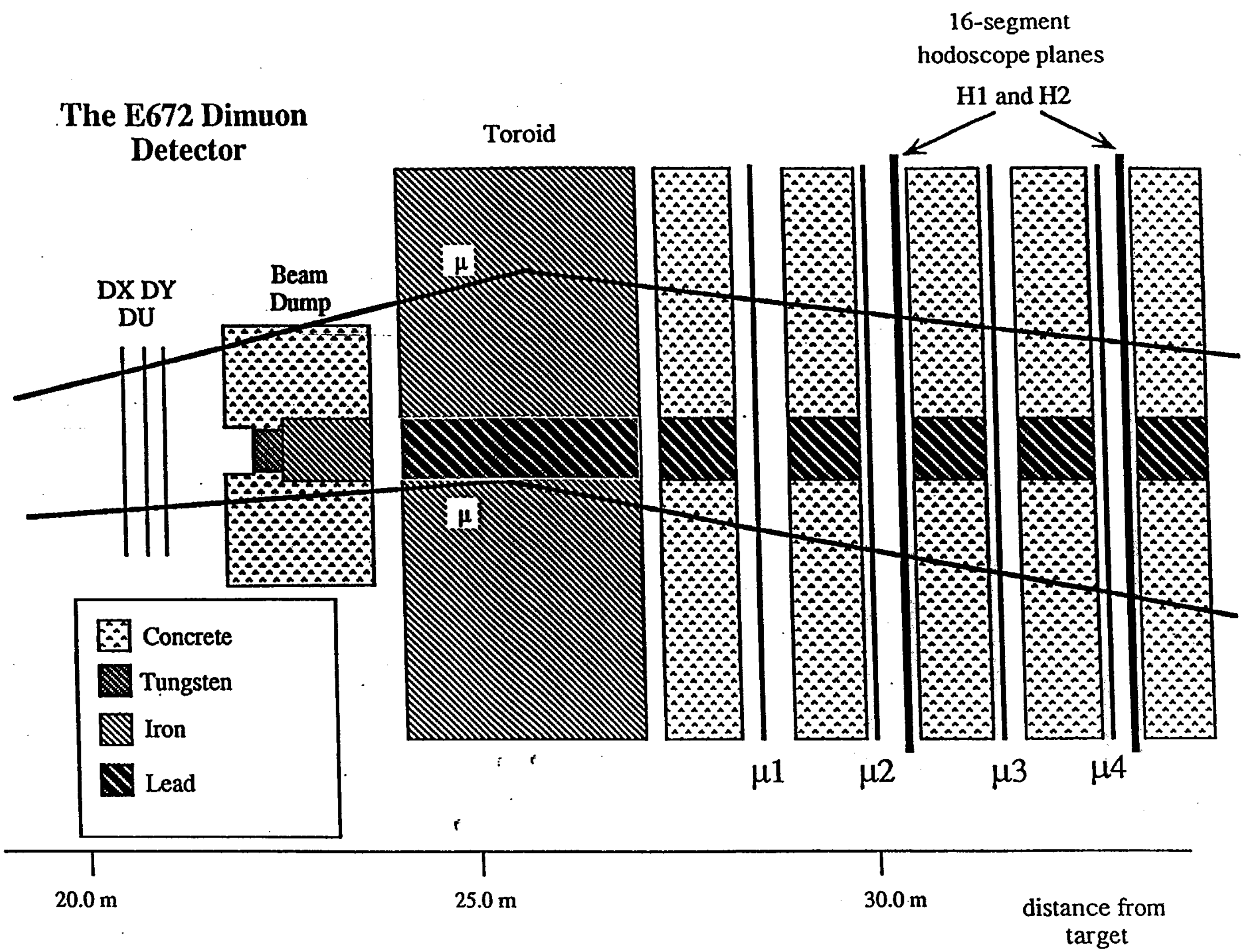
The E672 Dimuon Detector
16-segment hodoscope planes
H1 and H2
Toroid
Beam Dump
DX DY
DU
μ
μ
Concrete
Tungsten
Iron
Lead
μ1
μ2
μ3
μ4
20.0 m
25.0 m
30.0 m
distance from target

FIGURE 3.1

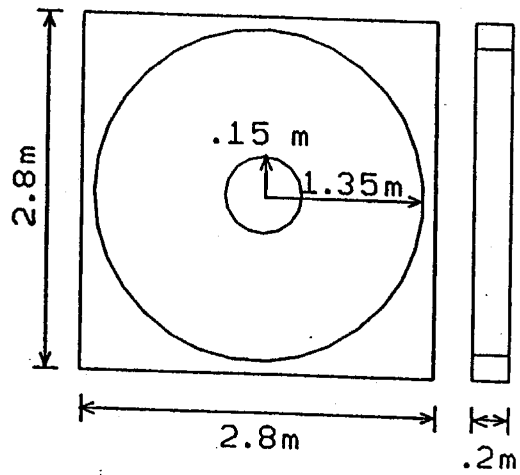

Figure 2-11
Dimuon Detector
Proportional Chamber

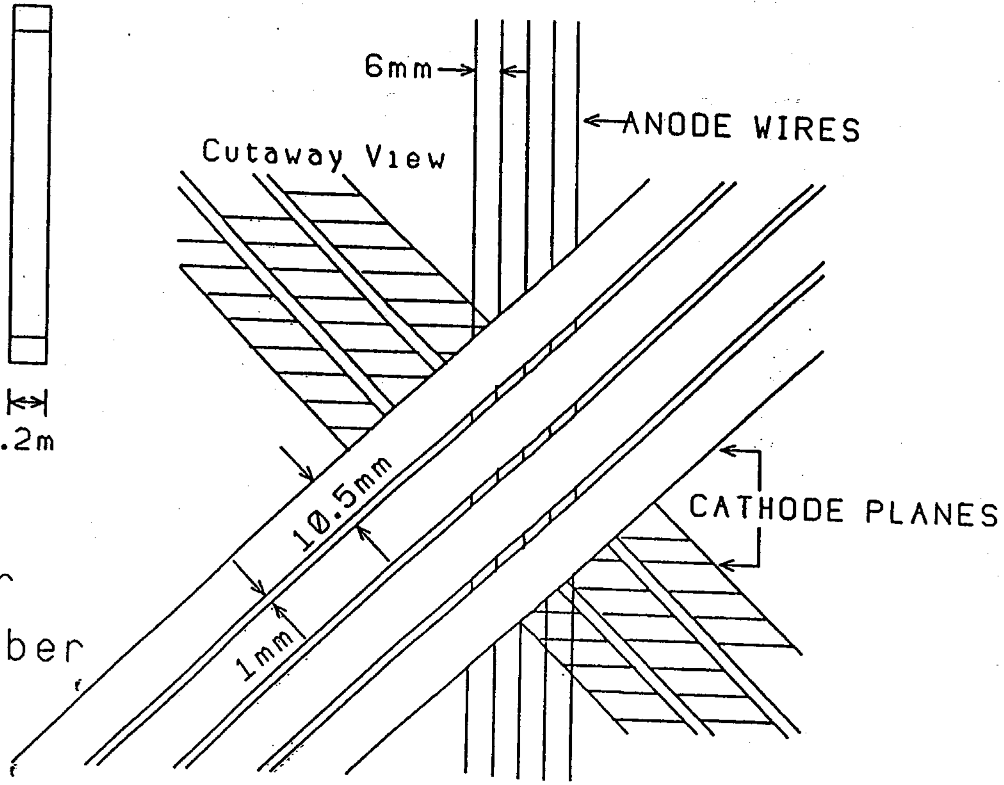

FIGURE 3.2 (a)

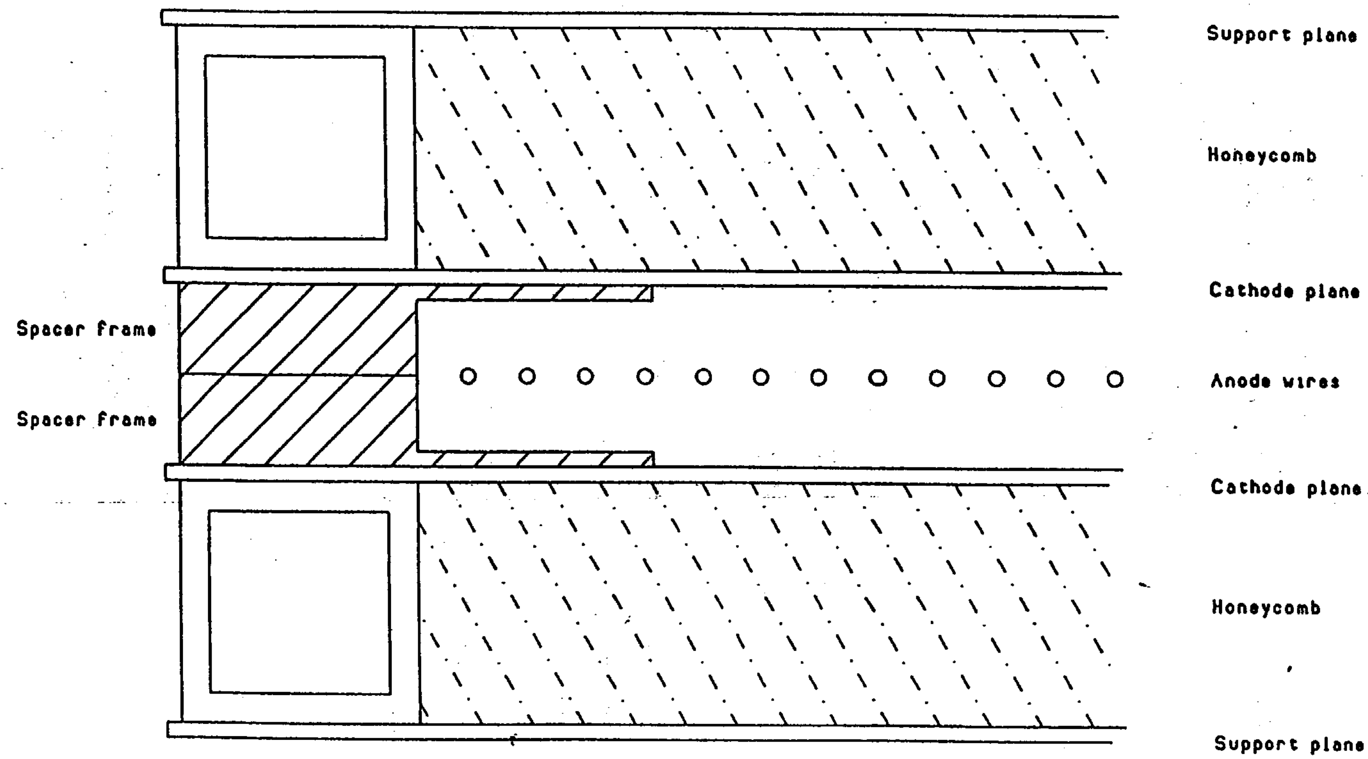
Support plane
Honeycomb
Cathode plane
Anode wires
Cathode plane
Honeycomb
Support plane
Spacer frame
Spacer frame

FIGURE 3.2 (b)

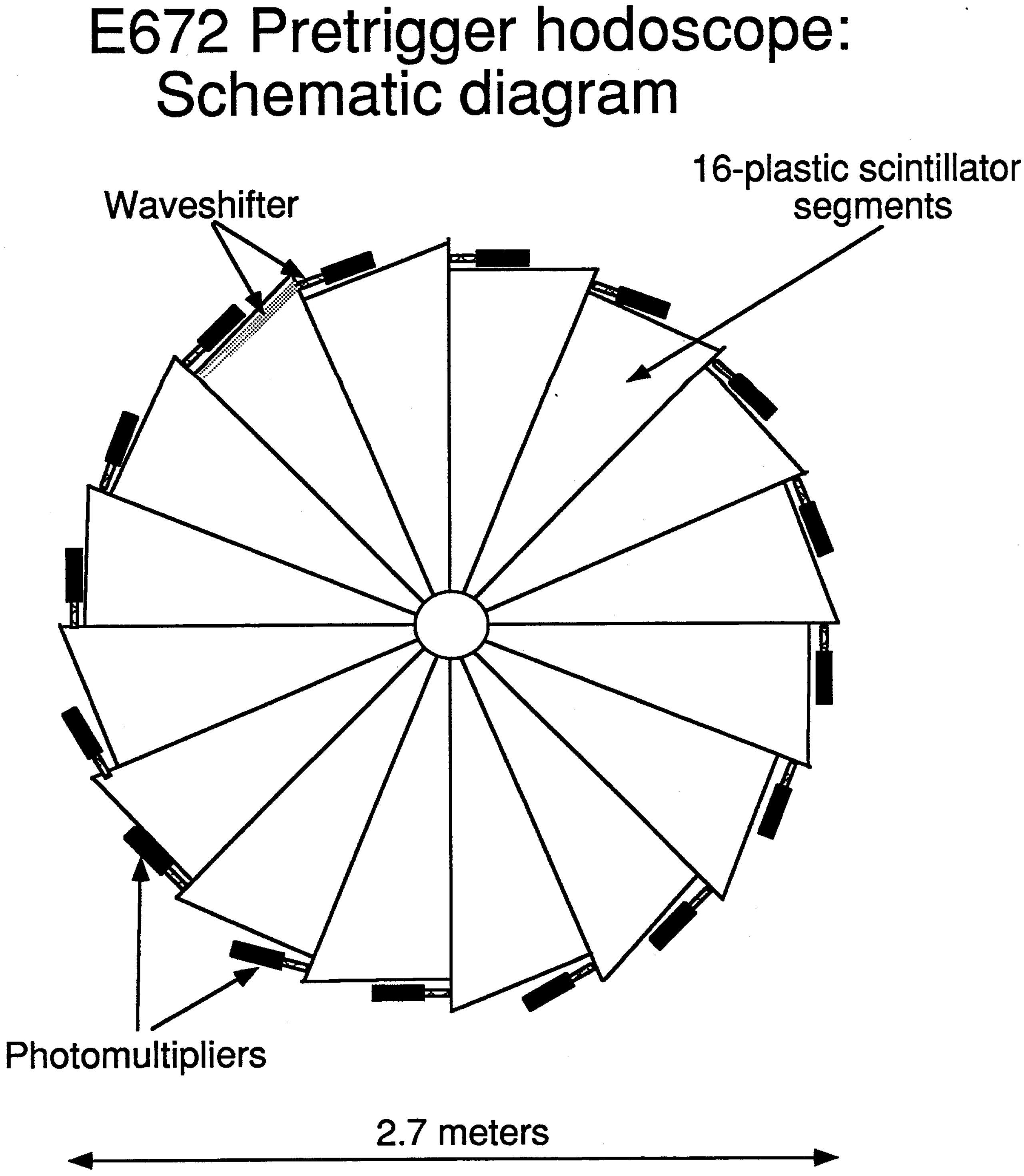
E672 Pretrigger hodoscope:
Schematic diagram
Waveshifter
16-plastic scintillator
segments
Photomultipliers
2.7 meters

FIGURE 3.3

Photo Multiplier Assembly: Exploded view

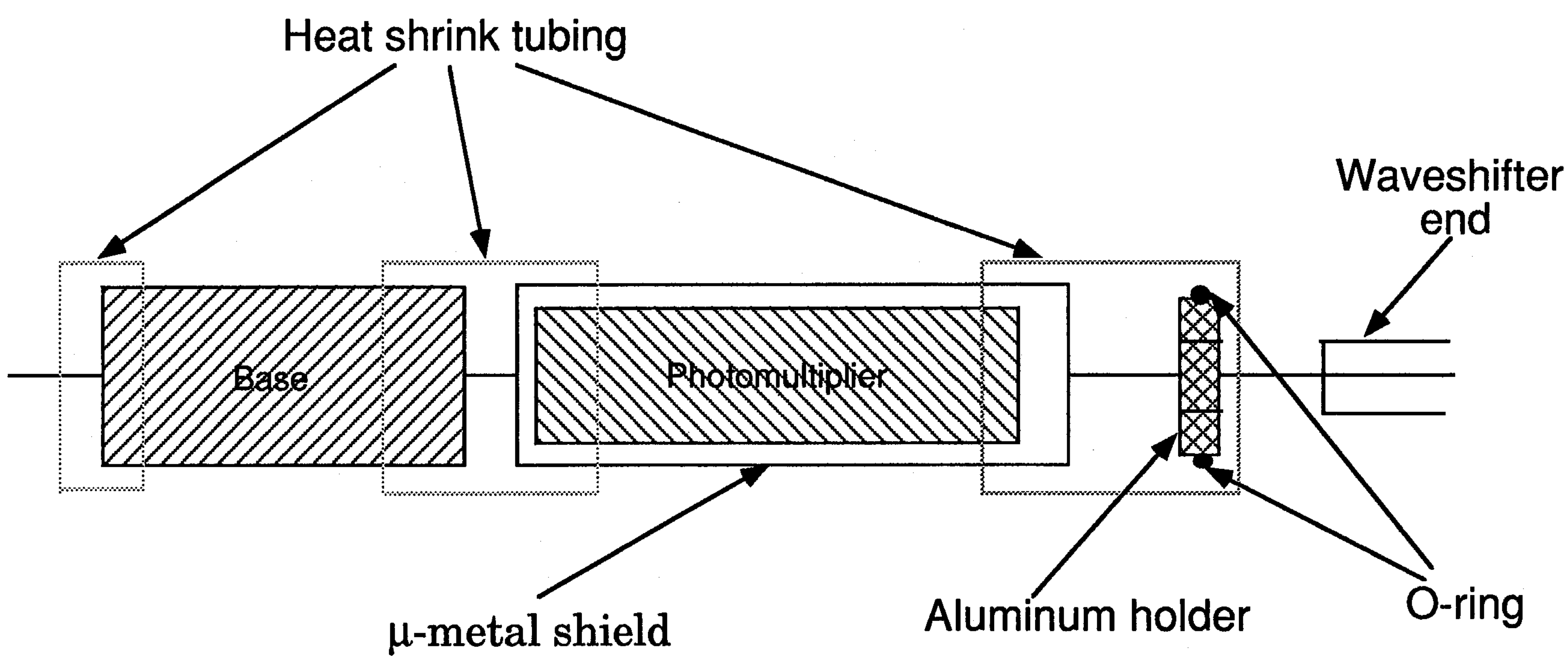

FIGURE 3.4

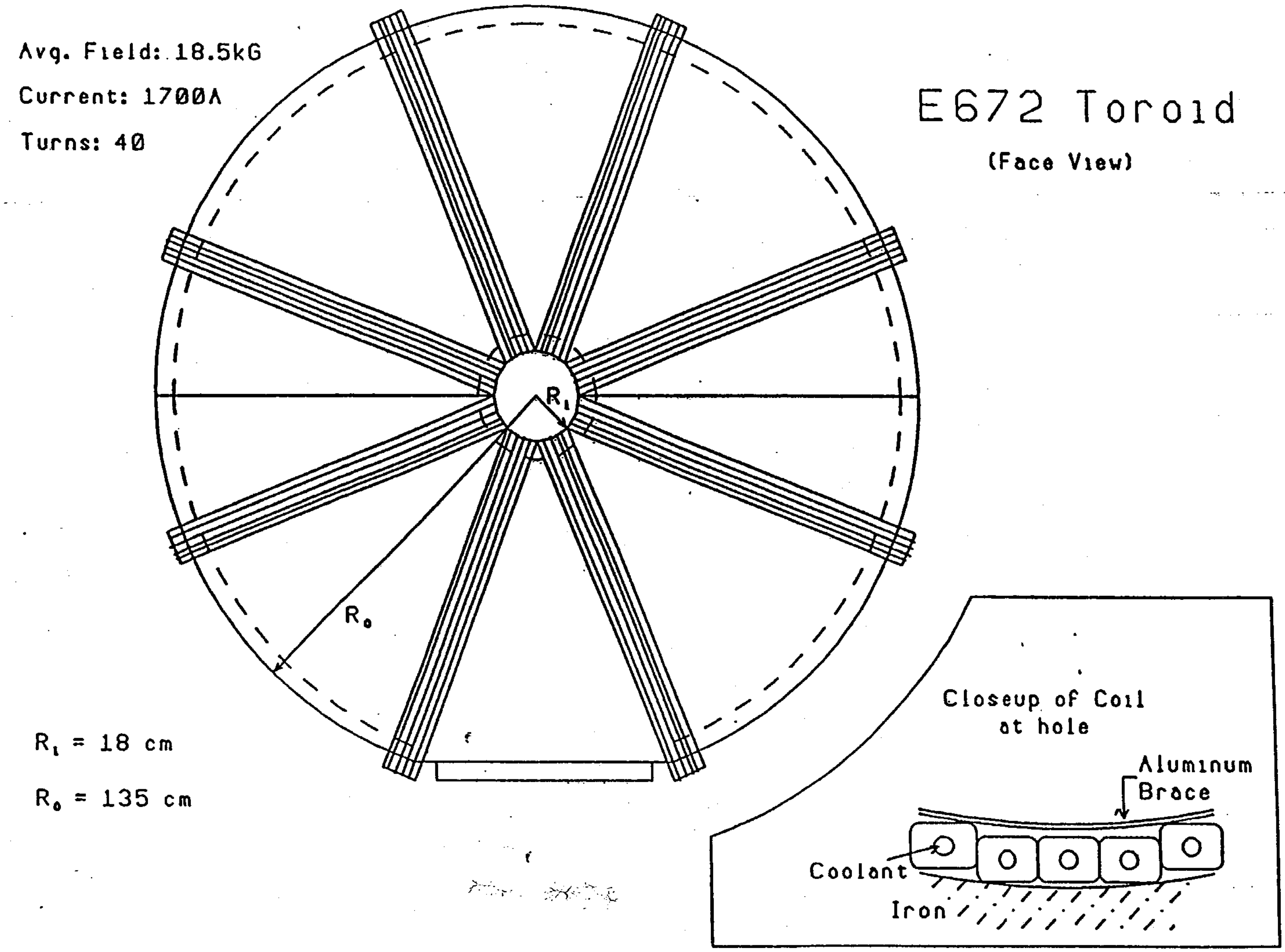
Avg. Field: 18.5kG
Current: 1700A
Turns: 40
E672 Toroid
(Face View)
R_i
R_o
R_i = 18 cm
R_o = 135 cm
Closeup of Coil at hole
Aluminum Brace
Coolant
Iron

FIGURE 3.5 (a)

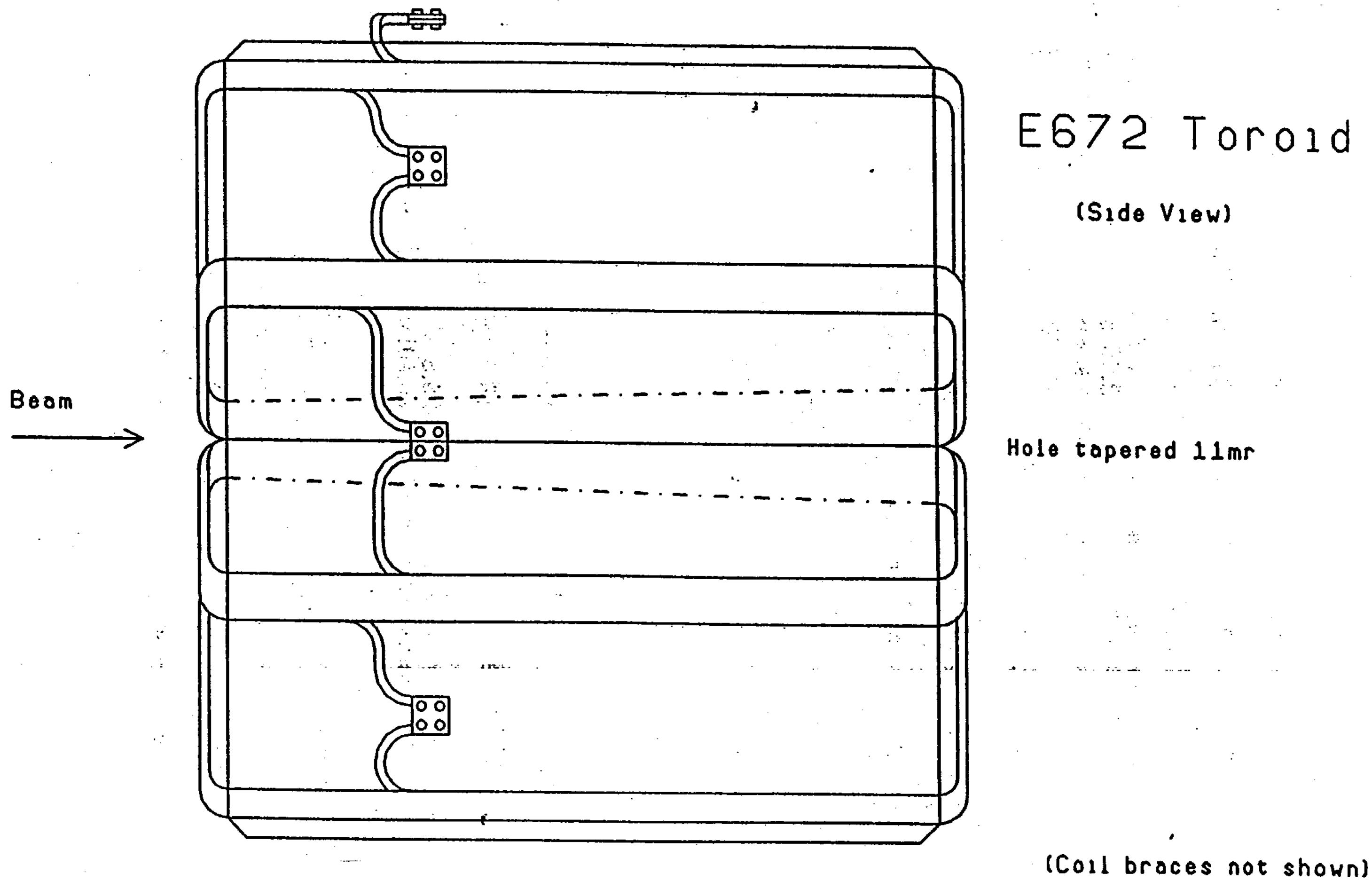
E672 Toroid
(Side View)
Beam
Hole tapered 11mr
(Coil braces not shown)

FIGURE 3.5 (b)

D-station chambers looking downstream

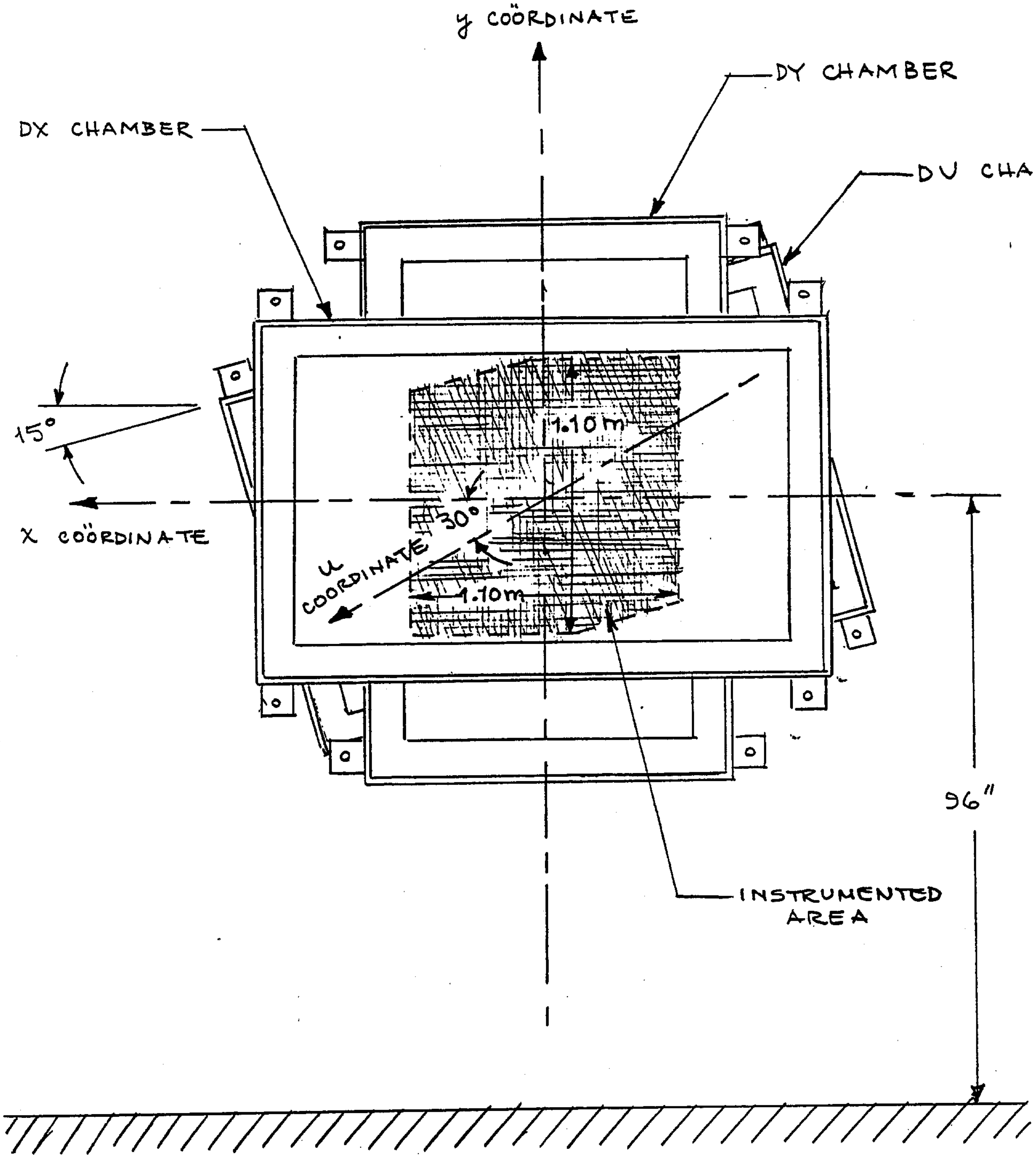

FIGURE 3.6

CHAPTER 4
TRIGGERING AND DATA ACQUISITION

The readout and data acquisition system for the E672 spectrometer is discussed in this chapter. The Dimuon Trigger Processor (DTP) is discussed and its implementation in the trigger is described. The fast electronics and triggering for the two parts of the run (E672 alone and E672/E706 running) is presented.

Section 4.1

4.1.1 Readout for the pretrigger hodoscopes

The signals from the 32 phototubes (16 for each hodoscope) are transmitted by RG58-C coaxial cable to two 16-channel CAMAC Multiplicity Logic Units [1–3] . The module discriminates the signals from the phototubes and sets a latch for any channel that exceeds a voltage threshold during an external gate. The module then calculates the multiplicity of the latch bits. The module has a presettable multiplicity threshold, and if the calculated multiplicity is greater than of equal to the set threshold, a NIM level is output. This level is stable after about 40 ns after the end of the gate.

The module is a double width CAMAC[4] module. The latched data, multiplicity threshold, calculated multiplicity and final output can be read out using CAMAC[4] . The multiplicity calculation and comparison is done using ECL digital logic. All the channels have the same voltage threshold which can be set manually. The input impedance of the module is modified to be very high, and the phototube signal is then transmitted to CAMAC[4] –readable LeCroy 2249A Analog -to-Digital Converters (ADCs) to record the pulse height.

The module also needs an external RESET in addition to the NIM gate. The latched data, the latched OR and the OR of the discriminated outputs are also available as NIM or ECL outputs. The voltage threshold for every channel is set to 50 mV. During normal data taking, the multiplicity threshold is set to 2 for both modules.

4.1.2 Readout for the muon and D-station chambers

The signals from the 16-channel preamplifier cards for the muon chambers and the D-station chambers were transmitted by flat Spectra Strip cables to the LeCroy PCOS III encoding system. This system is the dedicated Proportional Chamber Operating System . The basic unit of the system is a 32-input (ECL) Delay and Latch module (LeCroy 2731). Each crate could hold up to 23 modules and in addition a PCOS III crate controller[5] (LeCroy 2738) double width module which is connected to the data highway. Each module also has a software settable delay for each input ECL line up to 750 ns.

The muon chambers $\mu_1 - \mu_4$ each require 23 LRS 2731 modules for their encoding. The D-station DX and DY chambers require 18 modules and the chamber DU requires 23 modules. Each chamber thus has a dedicated CAMAC[4] crate associated with it. The channels with signals arriving within an external gate (150 ns) are latched by the system and held until readout or reset. The PCOS also provides a fast OR signal for the 'PROMPT' signals and the 'LATCHED' signals. The PCOS is used in 'non-clusterized' mode, so each active channel produces a 16-bit data word with 3 plane identifier bits and 8 wire address bits. The crate controller queries each LeCroy 2731 module in the crate and stores the addresses of active channels in an internal buffer for transfer to the data acquisition.

The prompt-OR's and the latched-OR's from each LeCroy 2731 are sent to a fast-OR module which provides OR's of the prompt and latched inputs for each chamber. This is used to implement coincidences between the chambers for some diagnostic runs.

Communication with the data acquisition system is achieved by the use of a LeCroy Model 4299 DataBus Interface through which the LRS 2738 crate controller transfers the data.

The data from the muon chambers $\mu_1 - \mu_4$ is also available to the trigger processor through the controller. The 2738 has an ECLport which is capable of transferring data at 10 times the rate of CAMAC[4] . The trigger processor reads and uses the information from the ECLport for its online calculations.

4.1.3 Veto wall readout

For the first part of the data taking (E672 alone) the signals from the veto wall were discriminated and amplified using the same preamplifier cards as for the muon chambers. The 32 outputs from each veto wall were then input into repeater modules and the OR of the outputs from each phototube is formed. The OR's from each wall were ANDed and the signal is used for as an online veto for the interaction for the first part of the run. The signals from each veto wall were also input into a LeCroy 2228 Time-to-Digital Converter (TDC) to get timing information of the signal; the signals were also input into a LeCroy 2341S register to 'tag' a hit in the veto wall. The TDCs and the registers were read out with the rest of the data.

For the second part of the data taking (E672/E706 operational), the readout for the 64 veto wall counters is done using the so-called "Minnesota latches" [6], which read out the status of each counter every beam bucket, and stored the history of the veto wall hits for 15 beam buckets centered around the interaction bucket. The signals from each quadrant of the veto wall were also discriminated and OR'ed by the fast electronics and were used as an online veto of the pretrigger for the duration of the run.

4.1.4 The Dimuon Trigger Processor

The Dimuon Trigger Processor [7–8] (DTP [9]) is used to do an online calculation of the invariant mass of a muon pair, seen by the muon chambers. The DTP has a presettable invariant mass threshold, and produced a trigger if at least one of the masses were above the threshold. The DTP could be set to trigger on any dimuon or only unlike sign dimuons, though throughout the run, any dimuon sign is accepted to reduce the bias due to the pattern recognition in the DTP algorithm.

The encoded data from the PCOS III system for the muon chambers are transferred by the 2738 PCOS III controller through the fast-transfer ECLport to the trigger processor. The average encoding time for the PCOS is about 5.7 μs. The schematic for the trigger processor is shown in figure 4.1. The data from μ_1 and μ_4 are accepted by the two POINT modules of the DTP and a list of space points is calculated in parallel by both the modules. The algorithm is described in detail elsewhere [9]. Briefly, the u,v and w data are clusterized (with a programmable cluster width set to 3) and sets of (u,v) compared to the set of w's to look for matches. The resulting list of points are checked to ensure that they are in the fiducial volume of the chamber. Random access Memories (RAM) are used to store the list and look-up tables in Programmable Read Only Memories (PROMs) are used to decide if a point is valid. The PROMs for the point modules are described elsewhere[10] .

The list of valid points for μ_1 and μ_4 are input into X and Y TRACK modules, which calculate possible tracks for the space points. In addition to the u and v information from the PCOS for μ_2 and μ_3 is transferred to both the track modules. The TRACK module algorithm[9] and the TRACK module PROMs[11] are described elsewhere. The X and Y TRACK modules calculate valid tracks in the X and Y views (these views are in internal coordinates along the u and v coordinates) in parallel and output the track list to the MOMENTUM module.

The MOMENTUM module calculates the momentum for each X and Y view track pair, and outputs a bit tagging a valid track (consistent with bending in the toroid) with a momentum for that track to the MASS module. The momentum calculation is pipelined in the MOMENTUM module. The PROMs for the MOMENTUM module are described elsewhere[12] .

The MASS module calculates the invariant mass of each muon pair using

$$M_{\mu\mu}^2 \approx p_1 p_2 \theta^2 \tag{4.1}$$

where p_1 and p_2 are the momenta for the two muons respectively and θ is the opening angle between them. The MASS module PROMS are described in detail elsewhere[13] . The mass is calculated for only valid tracks and the mass list is scanned to see if there is at least one above the preset mass threshold. If so, the DTP outputs a SUCCESS signal which is used as the trigger.

The DTP is started by a signal generated from the experiment pretrigger, and generates a BUSY signal while it is calculating. In case of a failure to find a dimuon satisfying the trigger requirements, or due to too little data or too much data, the trigger processor sends out a FAILURE signal. In the case of a SUCCESS or a FAILURE, the DTP outputs a DONE signal to signify the end of the decision making process.

Figure 4.2 (a) shows the time taken for a decision from the DTP. The time excludes the PCOS encoding time of 5.7 μs. Figure 4.2 (b) shows the time taken for a SUCCESS. On the average, the DTP makes a decision in about 6 μs after the pretrigger.

The online mass distribution from the DTP is shown in Figure 4.3 for SUCCESSes. The mass threshold used for the run was usually 0.2 to 0.5 GeV, depending on the trigger rate requirements. Figure 4.4 shows the variation of the trigger rate as a function of the invariant mass of the dimuon. Typically, at a threshold of 0.5 GeV, the rate is a factor of 5 less than the pretrigger rate.

Section 4.2

4.2.1 Interaction definition for 1987 run

Three scintillation counters SA, SB and SC (with a hole of diameter 1.5 in.) defined the beam upstream of the hadron shield for the data taking with only the E672 spectrometer. A valid BEAM signal is formed as $SA \cdot SB \cdot \bar{SC}$; i.e a coincidence in SA and SB with no signal in SC.

The interaction is defined using two interaction counters (described in Chapter 2) IC_EAST and IC_WEST just upstream of the LAC and off the beam axis. A signal in either of these in coincidence with a BEAM signal is used to generate an INTBEAM signal denoting an interaction. A valid interaction, when the experiment is 'live' is defined as the AND of INTBEAM and BUSYN, where BUSYN is the NOT of the grand BUSY signal for the experiment. The BUSY is discussed in subsequent sections. The live interaction is labelled LIVE_INT and is fanned out for various purposes. The interaction logic is shown in Figure 4.5 along with the logic for the veto walls. Other coincidences are formed and scaled visually as well as with CAMAC[4] –readable scalers.

4.2.2 Pretrigger definition for 1987 run

One of the fanned LIVE_INT signals is used to generate a 250 ns pulse PTM_BUSY to disable any inputs to the logic while the pretrigger decision is being made. The 30 ns gate for the pretrigger multiplicity module (PTM) is generated using the LIVE_INT signal, and if any of the inputs to the PTM are active within this gate, they are latched and processed. As described in Section 4.1.1, the PTM has stable NIM outputs if the multiplicity threshold (set to 2 for both modules) is satisfied after about 40 ns of the PTM gate. The coincidence of the NIM outputs from the PTM is strobed by a 20 ns PTM_STROBE signal generated using the LIVE_INT signal which gas been suitably delayed. The resulting signal is the experiment PRETRIGGER. The fast logic diagrams are shown in Figure 4.6

4.2.3 The trigger for the 1987 run

For some part of the run, the veto wall signal is used to veto the PRETRIGGER; this data sample is referred to as the Anti-Veto Wall (AVW) sample. The trigger for the AVW sample is therefore PRETRIGGER·VWN where VWN is the NOT of the veto wall signal, and is set to be 200 ns wide. Once it was realized that the backscatter from the target was causing spurious veto wall signals and otherwise good events were being lost, the veto wall requirement was removed from the trigger requirement, and only read out as part of the data. This part of the data sample is referred to as the Tagged Veto Wall (TVW) sample.

The trigger processor (DTP) is started by the PRETRIGGER for each PRETRIGGER, but the SUCCESS is not used as a trigger for the run. Provision was made to be able to run with either the trigger processor SUCCESS or the PRETRIGGER signals. The trigger is then used to send an interrupt PDP_INT to the data acquisition PDP-11/34 computer, as well as to generate various BUSY signals to disable the experiment while it is being read out. The trigger logic is shown in Figure 4.7.

4.2.4 The BUSY and RESET for the experiment

The signals which defined when the experiment was unable to accept an event are shown in Figures 4.6 and 4.7. The BUSY[14] for the experiment is formed as an OR of a number of different BUSY signals for different parts of the fast logic and readout. The experiment is considered busy if any of the following signals is active;

— BEAM_GATEN: This is the NOT of the BEAM_GATE, which denotes the active period of the beam spill.

— PTM_BUSY: This is a 250 ns pulse generated by the LIVE_INT signal to allow time for the PTM to make its multiplicity decision.

— START_DTP_BUSY: This is a 1 μs pulse to disable inputs other than the PCOS to the DTP until the DTP outputs its BUSY signal

— DTP_BUSY: This signal is output by the DTP while the online calculations are performed.

— RESET_BUSY: This is a 2 μs pulse to keep the experiment busy while various devices are being reset.

— PDP_INT_BUSY: This is a 1 μs signal to keep the experiment busy while the PDP is being interrupted to initiate the readout.

— PDP_BUSY: This signal is generated by the PDP during readout.

The timing diagram for the BUSY is shown in Figure 4.8. The readout for the PDP takes about 8 ms. Typically, around 1200 16-bit words are read per event. The RESET for most components of the experiment is generated by the FAILURE signal from the DTP. The muon and D-station chamber PCOS, the DataBus interfaces, the ADCs, the TDCs and the registers are reset by the RESET pulse. The RESET is inhibited if the experiment is being read out at that time. The PTM reset is done with the edge of the ending of the BUSY signal, which is used to generate an 20 ns wide END_BUSY signal.

4.2.5 Data Acquisition for the '87 run

The E672 apparatus is read out using a PDP-11/34 minicomputer. The data acquisition software is the RSX-DA running under the RSX operating system for the PDP-11. A schematic of the data acquisition system is shown in Figure 4.9.

The PDP-11/34 is connected to an interrupt handling device called the BISON BOX[15] developed by Fermilab. The BISON BOX[15] accepts begin and end spill interrupts, as well as event interrupts (triggers). It has an input register (BISON Input Register, BIR[15]) where the devices to be read can be specified by setting the appropriate bits on the front panel. On receiving an interrupt, the BISON BOX[15] interrupts the PDP-11/34 which reads the preset BIR contents and starts to execute the appropriate data acquisition commands. The read commands are specified in a CAMAC definition file[16] resident on the PDP.

The PDP-11/34 communicates with a CAMAC[4] interface, the Jorway-411, which in turn interrogates the CAMAC crates on a serial CAMAC[4] highway. Four CAMAC crates are read out for each event. The first in the chain contains the LeCroy PCOS III DataBus Interfaces (LeCroy 4299) for the muon and D-station chambers which read the PCOS data for the chambers. In addition, the ADCs, TDCs and the Pretrigger Multiplicity modules are also located in this crate. The next crate has a CAMAC clock, a set of 24-bit scalers (Jorway 85 and 85A), a pulser and a LeCroy dual gate generator. The next two crates contain the Dimuon Trigger Processor modules which also have direct access to the muon chamber PCOS data through the fast ECLport. Details of what the ADCs, TDCs, registers and scalers read are given elsewhere[16] .

The overall control of the run, tape logging, monitoring etc. is done by the VAXONLINE[17–18] data acquisition package developed by Fermilab. The PDP-11/34 transfers data to the so-called "event pool" on a dedicated Digital Equipment Corporation MicroVAX II on which VAXONLINE[17] is run. Several processes run under the VAXONLINE umbrella, allowing simultaneous data logging on disk or 6250 bpi magnetic tape and online monitoring. The online monitoring is done using a package GHIS[19] developed at Indiana University by J. Martin.

Section 4.3

4.3.1 Interaction definition for 1988 run

The incident beam particle is defined by using two scintillation counters BA and BB located upstream of the target. A coincidence between these constituted a beam signal. The logical OR of for interaction scintillation counters, SE1, SE2, SW1 and SW2, as described in Chapter 2, in coincidence with the beam is defined as the interaction signal. In addition a pile-up filter[20] was constructed in the fast logic to ensure that there is no other interaction within ± 60 ns of the current interaction. A scintillator counter BH, with a hole, was used in anti-coincidence with the interaction to reduce the muon halo. The signal is then gated with the signal COMP_RDY (computers un-BUSY) to form a signal LINT1. This interaction signal is sent to the E672 fast logic for use in the pretrigger formation instead of the LIVE_INT signal described in section 4.2. 1, and is called GINT1.

4.3.2 Pretrigger for the E672/E706 1988 run

The pretrigger for the E672 spectrometer, formed by strobing the outputs of the Pretrigger Multiplicity Modules (PTM) with the interaction signal, is then sent to the Faraday cage above the Liquid Argon Calorimeter. The pretriggers for the LAC (LACPRET) and the E672 pretrigger (PRETRIGGER) were logically OR'ed in the Faraday cage to form a signal for a common pre-trigger. In addition, about 1 % of the pretriggers were from prescaled beam or prescaled interactions for data to study trigger biases.

The LAC pretrigger, described elsewhere[20] , is vetoed under two conditions; if there is a veto wall signal within ±75 ns of the interaction or if there is noise from the 400 Hz power supplies in the Faraday cage which faked a LAC pretrigger. The LAC pretrigger in coincidence with noise was vetoed by a 30 μs signal called SCRKILL. For E672, the pretrigger is killed with SCRKILL and if there is a signal in the Veto wall within ±35 ns of the interaction. If there is no veto, a signal 672PRET is created.

If either there is a LACPRET, a 672PRET or a prescaled beam/ interaction signal (PRPRET) , a LOAD signal is sent to all parts of the E672/E706 apparatus to latch the information from the detectors. To summarize

$$672PRET = LINT1 \cdot PRETRIGGER \cdot \overline{SCRKILL} \cdot \overline{VW} \qquad (4.2)$$

and

$$LOAD = LACPRET + 672PRET + PRPRET \qquad (4.3)$$

4.3.3 The trigger for the E672/E706 1988 run

The trigger for the experiments is the OR of the triggers for E672 and E706. The E706 trigger is described elsewhere[20] . The E672 trigger is formed with the Dimuon Trigger Processor, described in section 4.1. 4. The DTP is started with the LOAD signal from the LAC Faraday cage, and a valid trigger for E672 is the SUCCESS signal from the DTP. The readout computers are interrupted when either experiment has a trigger. All the gates for the E672 system are generated by the LOAD instead of the PRETRIGGER as in section 4.2. The mass thresholds for the DTP were set to 0.2 or 0.3 GeV for the early part of the run, and to 0.5 GeV for the latter part. At a threshold of 0.5 GeV, about 30 % of the triggers were E672 triggers.

4.3.4 Data Acquisition for the E672/E706 1988 run

In the common running mode, the two experiments are subdivided into four separate sections. Each section is assigned to a PDP-11 minicomputer. The E672 apparatus is read by a PDP-11/34 (as in section 4.2.5) labelled MU. The LAC was read out by a PDP-11/45 labelled MX; the SSDs, E706 PWCs and the discrete logic, (like scalers, Čerenkov etc.) were read out by a PDP-11/34 labelled NEU. The Forward Calorimeter is read out by a PDP-11/34 labelled ROCH. Some of the online analysis and software development is done on a DEC VAX 11/780. The configuration of computers used in the data acquisition is shown in Figure 4.10.

The readout for the PDP-11/34s is done using standard CAMAC[4] devices using standard serial or parallel links. The LAC data acquisition used the RABBIT[20] system and is controlled by the MX PDP. The data read out by the four PDPs is coordinated using the VAXONLINE[17] system running on a DEC MicroVax II (μVax) computer. The coordination of the run beginning and ending, checking that all PDPs were indeed reading the same event, online-monitoring for the E706 spectrometer and writing the data to 6250 bpi magnetic tape were accomplished by various processes running under VAXONLINE. Under normal running conditions, a run is defined by writing one full 6250 tape. The readout time for the entire apparatus is around 17 ms, which is dominated by the LAC readout time.

REFERENCES

1) R. Crittenden et al., *Nucl. Instr. and Meth.* **A270**, 99 (1988) .

2) A. Sambamurti, Ph.D thesis, Indiana University, 1988.

3) A. Sambamurti, "16-channel CAMAC Multiplicity Logic Unit", E672 Internal Note No. 112, 1986.

4) "CAMAC Instrumentation and Interface Standards, IEEE, 1982, ISBN 0-471-89737-X.

5) "2738 PCOS III Manual", LeCroy Research Systems Corporation, 1982.

6) R. Benson, Characteristics of Forward Energy ..., Ph.D. thesis, University of Minnesota, (1990).

7) R. Crittenden et al. Proceedings of the Workshop on High Sensitivity Beauty Physics at Fermilab, 1987 page 427.

8) R. Crittenden et al, "High-mass dimuon trigger processor", Draft of NIM publication, E672 Internal Note No. 111, 1986.

9) P. Draper, Ph.D. thesis, Indiana University, 1987.

10) T. Sulanke, "Point PROMs for the Dimuon Trigger Processor", E672 Internal Note No. 128, 1986

11) T. Sulanke, "Track PROMs for the Dimuon Trigger Processor", E672 Internal Note No. 129, 1986

12) T. Sulanke, "Momentum PROMs for the Dimuon Trigger Processor", E672 Internal Note No. 128, 1986

13) T. Sulanke, "Mass PROMs for the Dimuon Trigger Processor", E672 Internal Note No. 129, 1986

14) A. Dzierba et al, "E672 Trigger electronics: A users guide.", E672 Internal Note No. 182, 1987.

15) "Bison Interrupt and Gate Control", Fermilab Computing Department, Publication HN-3.2.

16) L. Dauwe, "E672 CAMAC definition file", E672 Internal Note No. 138, 1987.

17) "VAXONLINE SYSTEM", FNAL Computing Department, PN 252.0.

18) V. Sirotenko, "Guide to E672 VAXONLINE", E672 Internal Note No. 174, 1987.

19) J. Martin,"Dynamic Histogramming Package", E672 Internal Note No. 141, 1987.

20) C. Yosef, "Production of high transverse momentum π^0 ...", Ph.D. thesis, Northeastern University, 1990.

Dimuon Trigger Processor: Schematic diagram

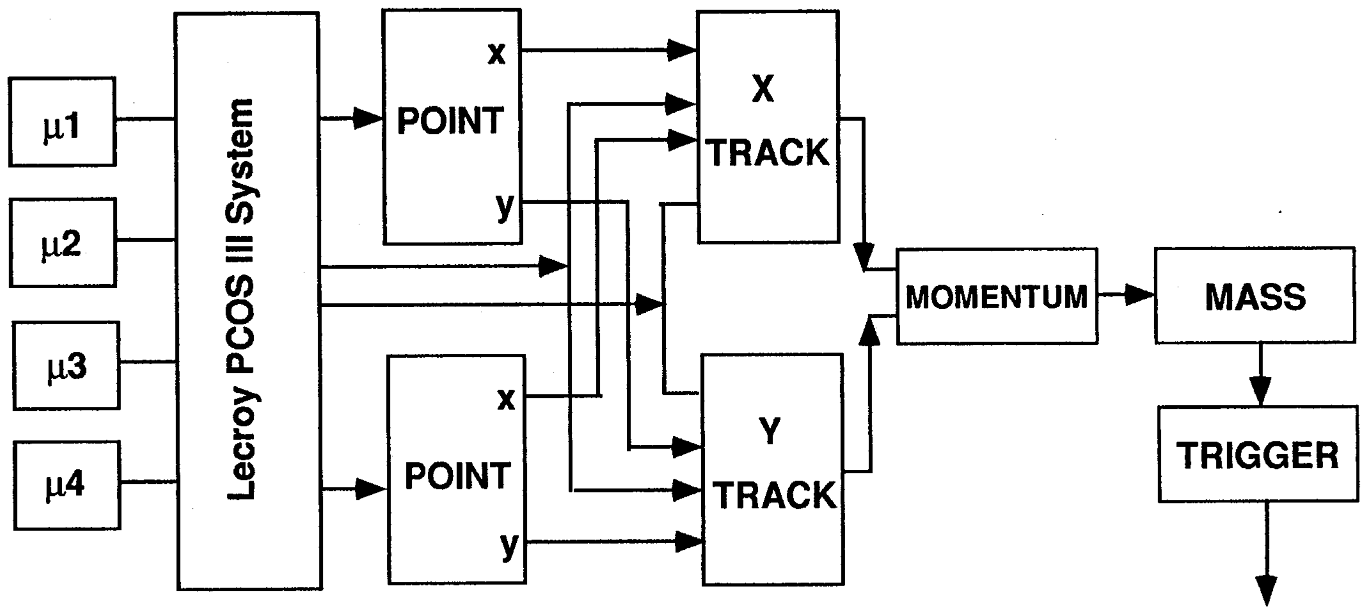

FIGURE 4.1

Trigger processor decision time

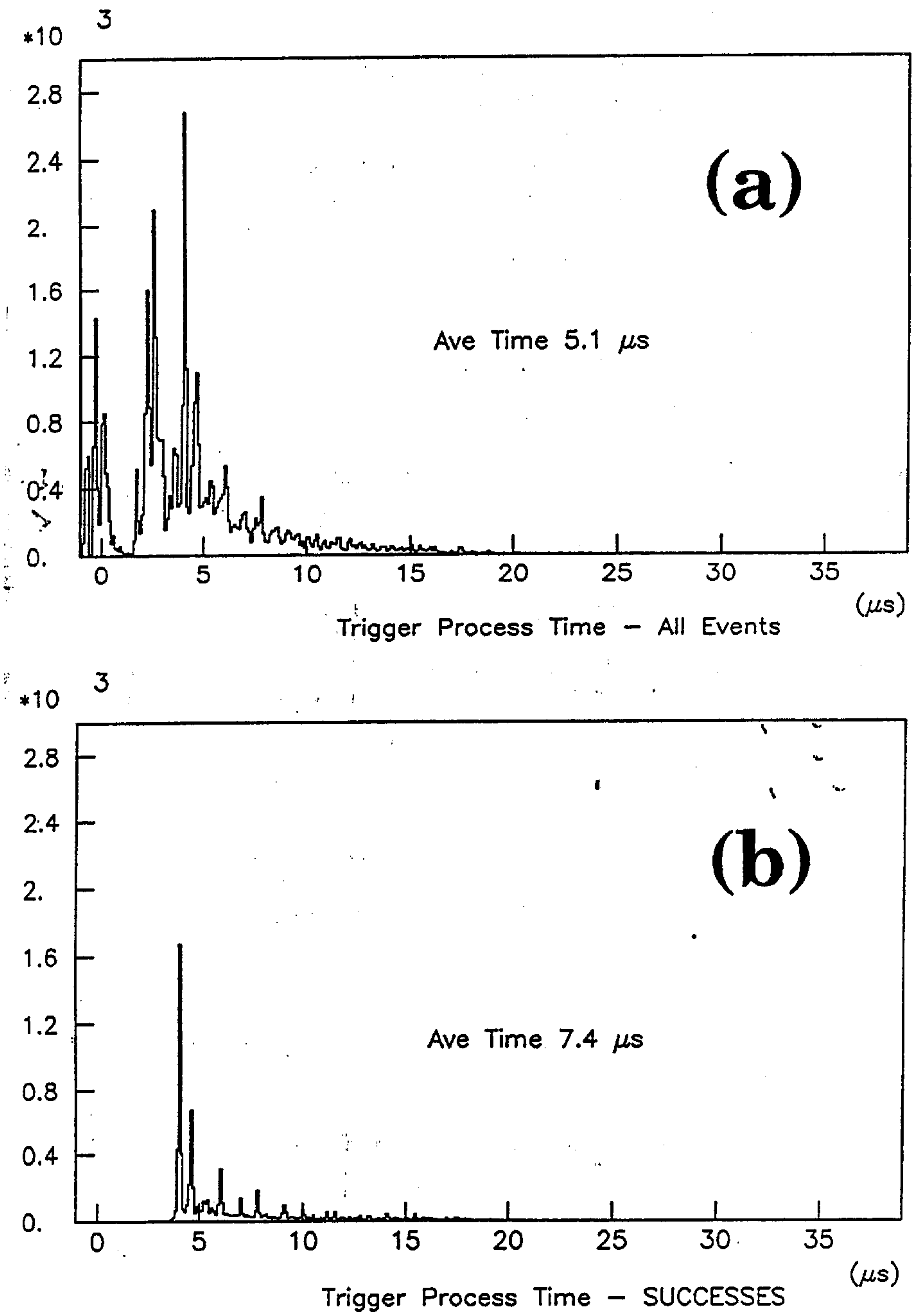

FIGURE 4.2 (a) and (b)

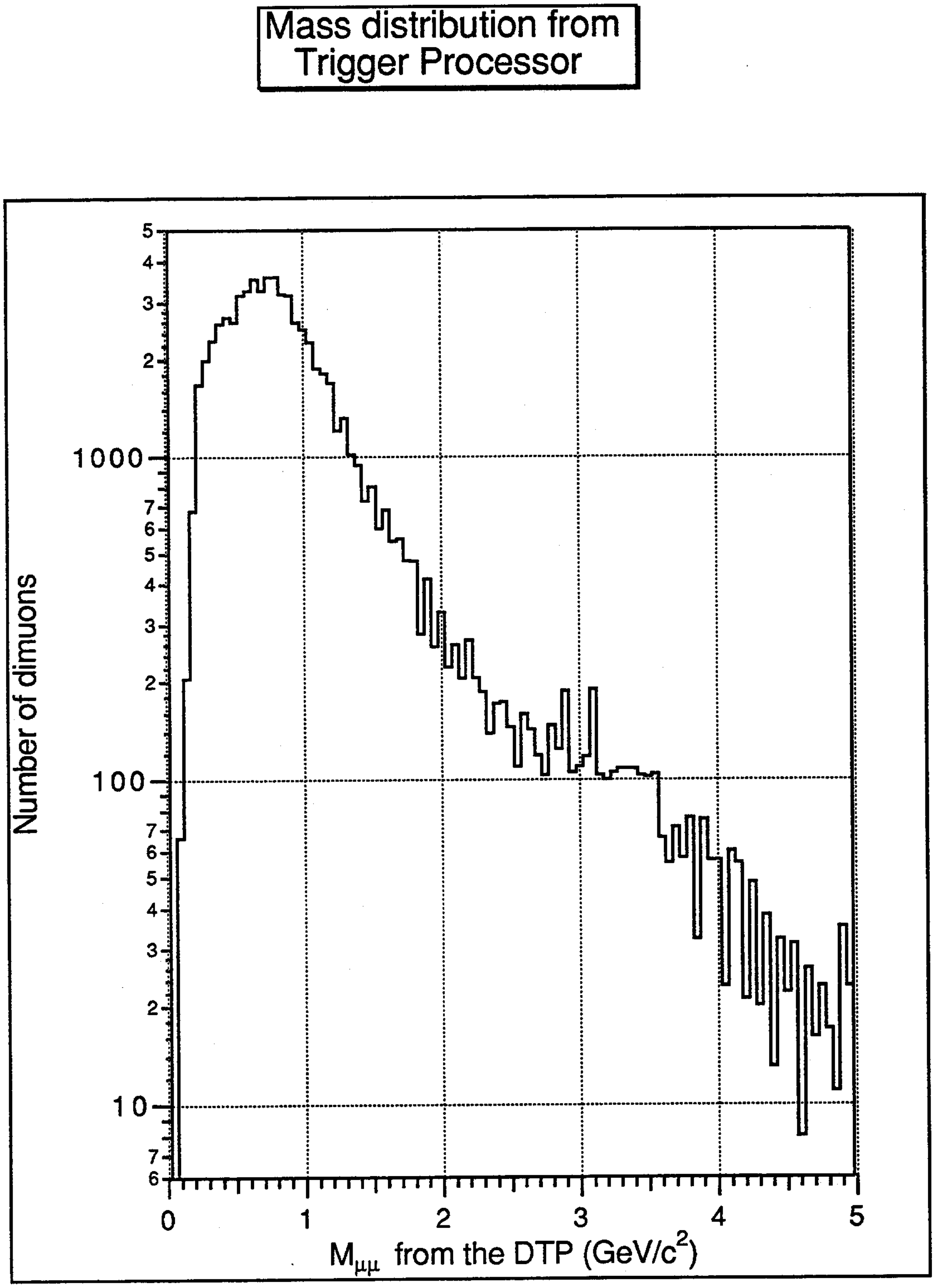
Mass distribution from Trigger Processor
Number of dimuons
1000
100
10
0
1
2
3
4
5
$M_{\mu\mu}$ from the DTP (GeV/c^2)

FIGURE 4.3

E672 Interaction Fast Logic

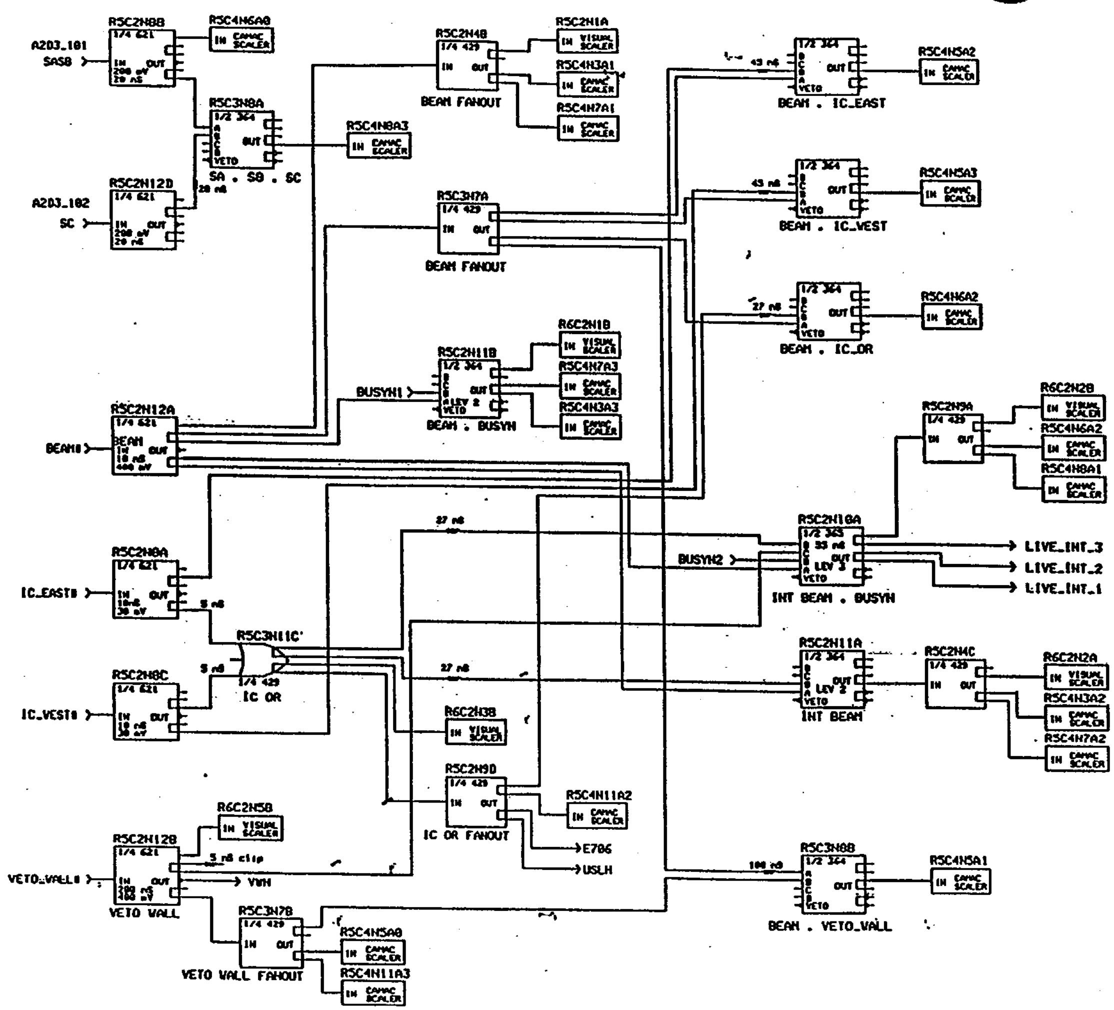

FIGURE 4.5

E672 Pretrigger Fast Logic

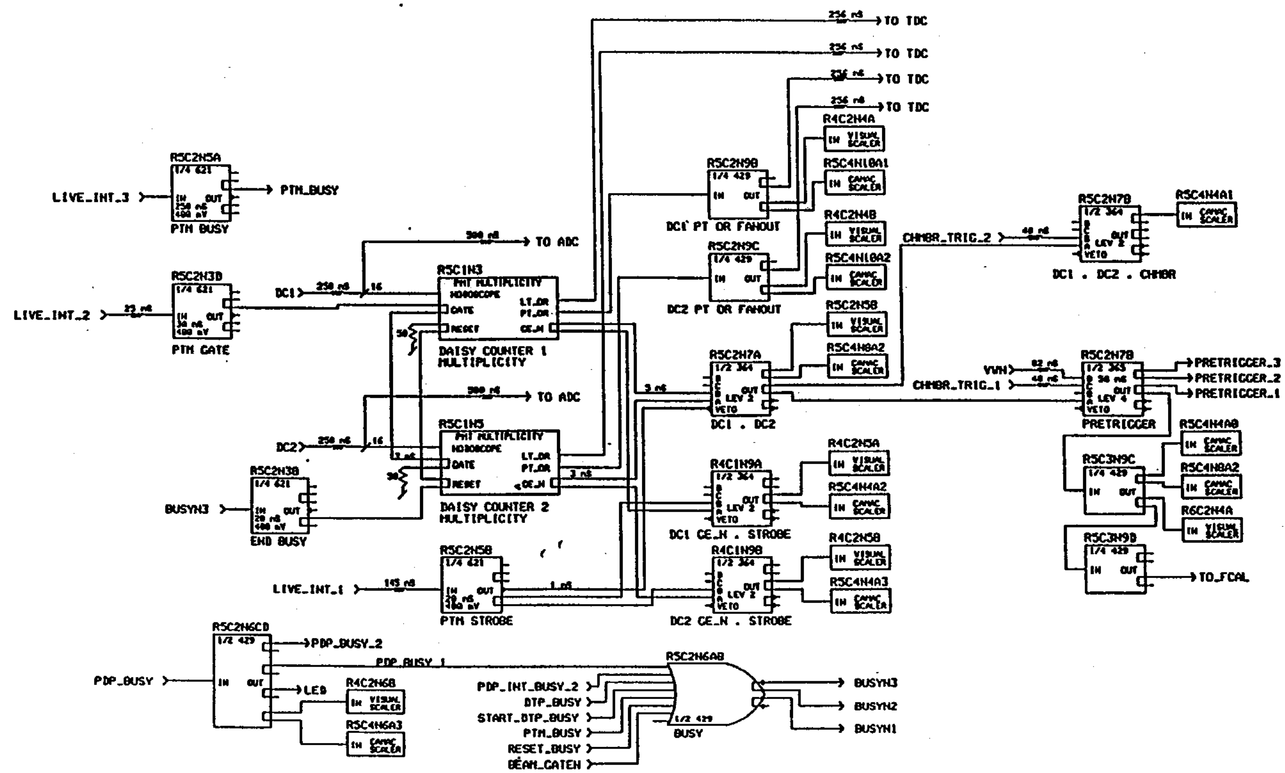

FIGURE 4.6

E672 Trigger Logic

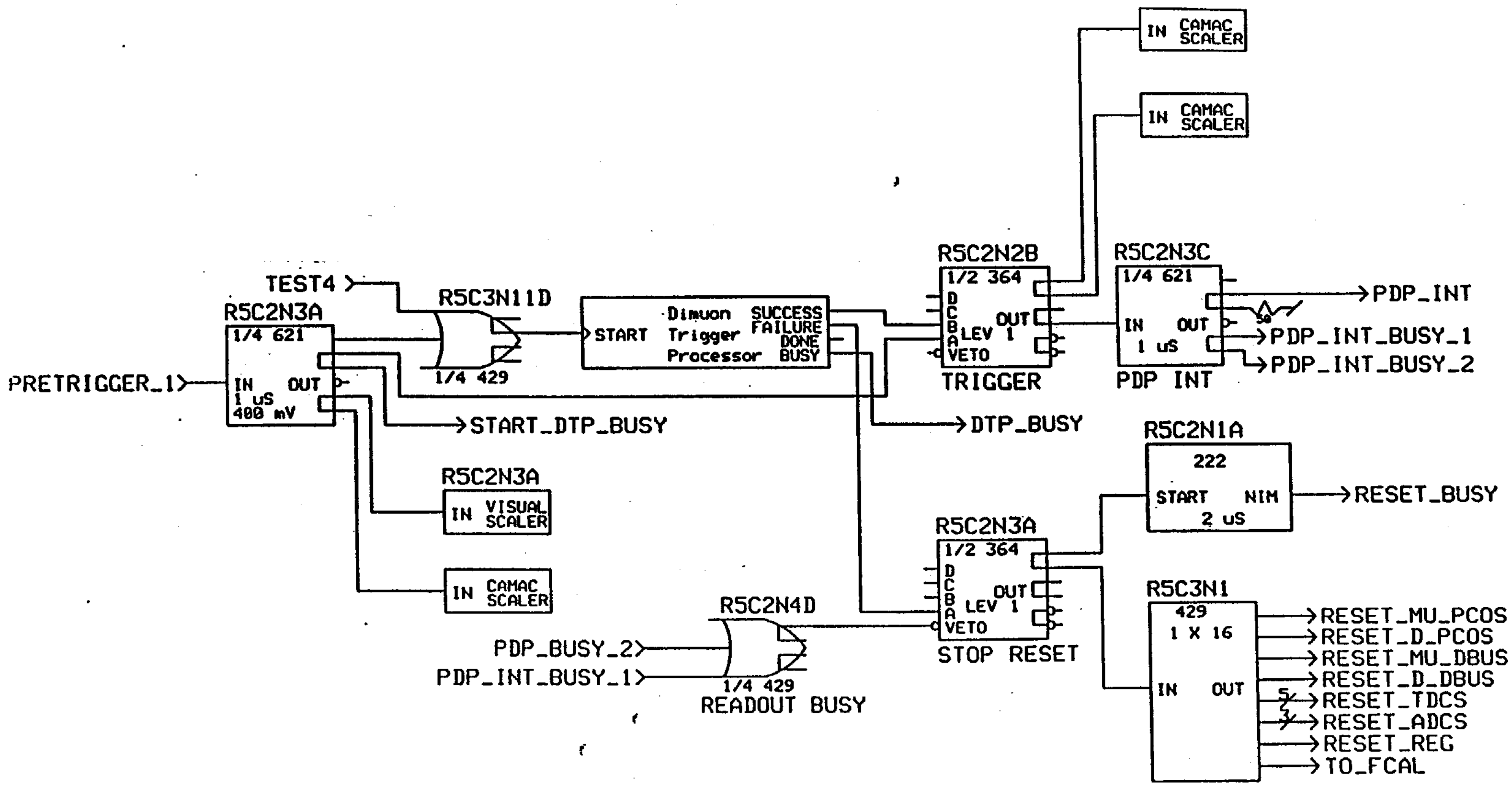

FIGURE 4.7

E672 BUSY timing diagram

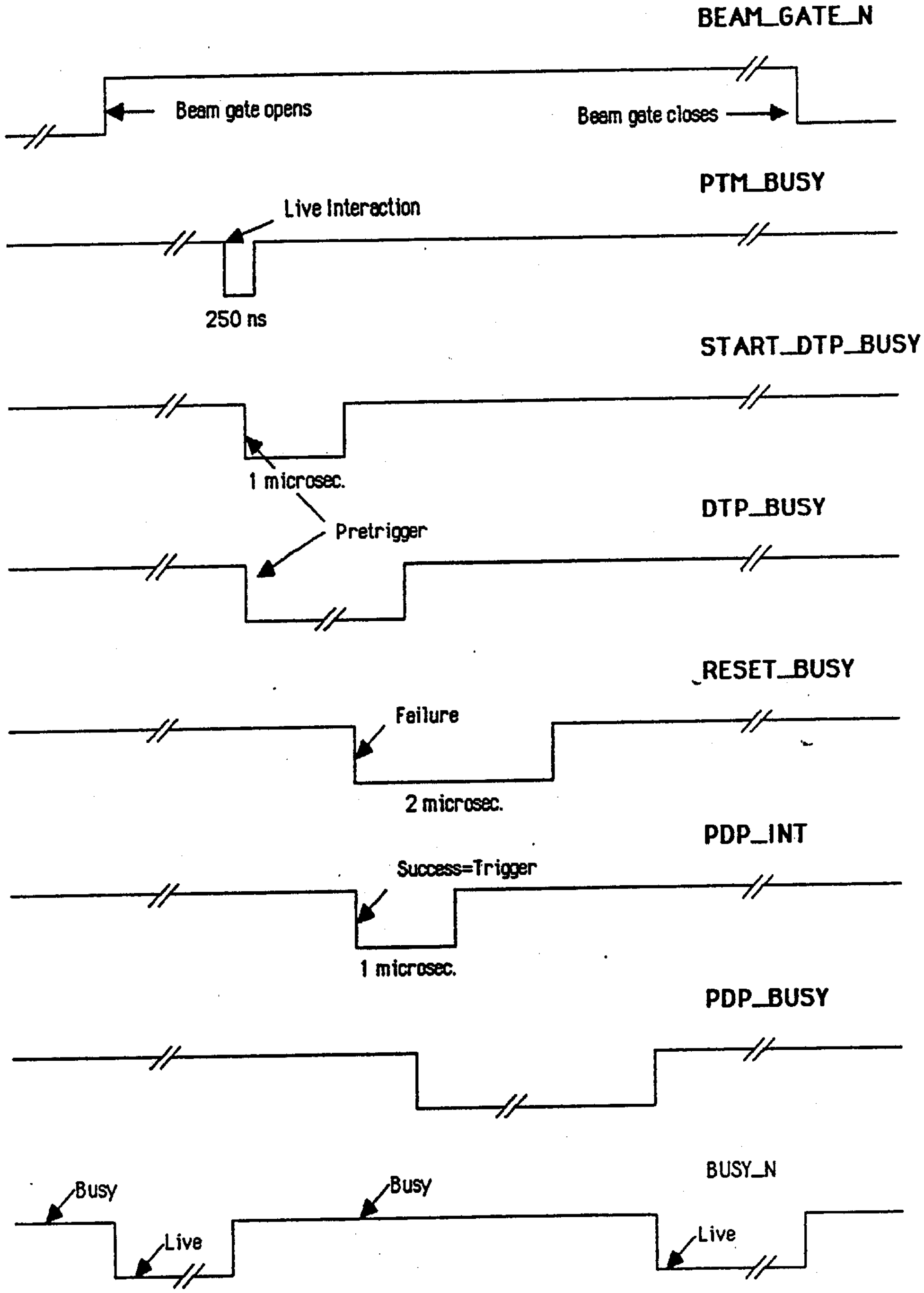

FIGURE 4.8

Data Acquisition for E672: Schematic diagram

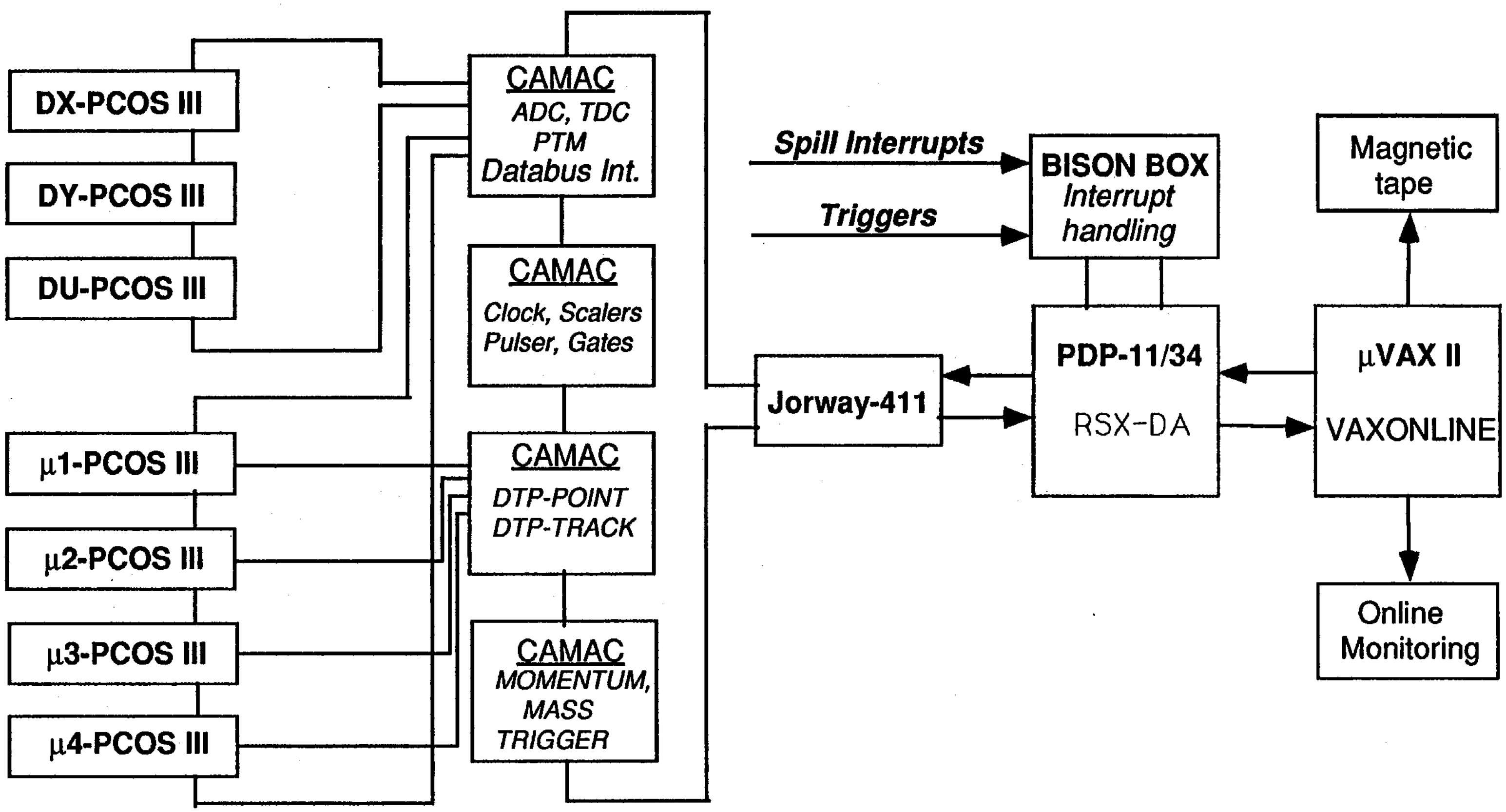

FIGURE 4.9

Schematic of data acquisition computers
for the E672/E706 '88 run

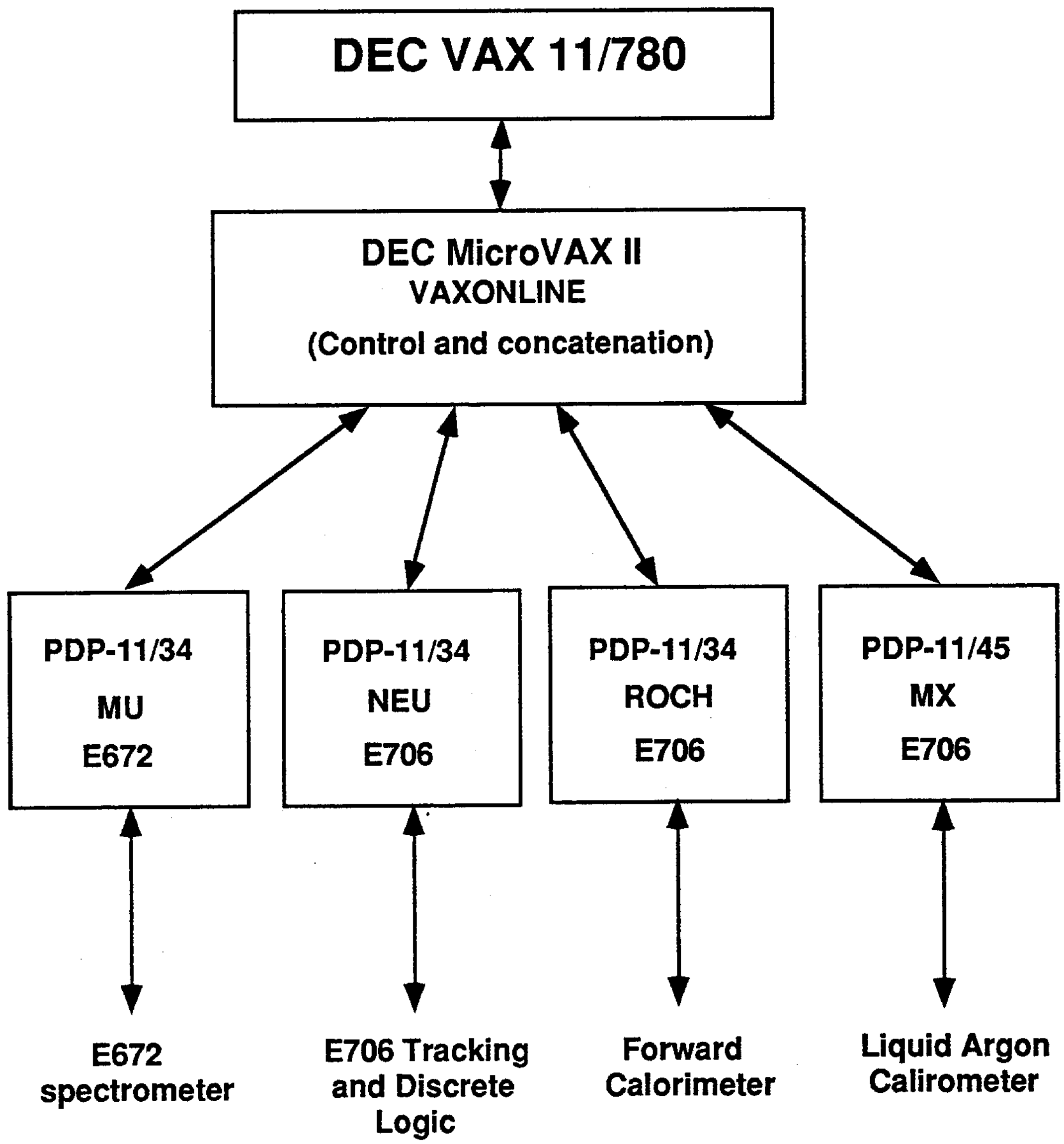

FIGURE 4.10

CHAPTER 5
DATA REDUCTION FOR A-DEPENDENCE ANALYSIS

The E672 spectrometer was used to collect data for π^-–nucleus interactions with thick nuclear targets in September 1987. A distinct J/ψ signal is observed in the $\mu^+\mu^-$ mass spectrum around 3.1 GeV/c^2 with a width of 550 MeV/c^2.

During this period of running, no tracking information was available upstream of the D-station PWC's, as the E706 spectrometer was not yet fully operational. This chapter describes the processing of data leading to the extraction of the J/ψ signal. The first section gives a description of the data collected. The next section discusses the event selection and data reduction. The last section deals with the estimation and subtraction of the background to the dimuon mass spectrum to obtain the "raw" J/ψ signal for each target.

Section 5.1

5.1.1 Description of the data

Data were collected with a 530 GeV/c π^- beam incident on thick targets of Carbon, Aluminum, Copper and Lead. The trigger required at least two hits in each of the two pretrigger hodoscopes, strobed by a valid interaction. About 700,000 events were written on tape, with targets and toroid polarity being changed regularly. Table 5.1 summarizes the break up of the number of triggers as a function of target and target thickness.

Table 5.1

Target	Thickness (cm)	Thousands of triggers
Carbon	4.0 10.2 20.3	196
Aluminum	3.8 12.7 16.5	181
Copper	5.1 10.2	165
Lead	1.0 5.1 7.6	169

As only the E672 part of the apparatus was operational in this running period, no information is available from the target region, and the muons were assumed to come from the vertex. The dimuon invariant mass resolution is dominated by multiple scattering of the muons. Monte Carlo simulations indicate that the expected resolution is 550 MeV/c^2.

5.1.2 AVW and TVW data samples

The data were separated into two classes. In the earlier part of the run, the signals from the Veto Wall were used as an online veto to eliminate spurious triggers arising from beam muon halo (the Anti-Veto Wall or AVW sample). When it was realized that backscatter debris from the target was responsible for eliminating otherwise good triggers, the trigger requirement was modified such that signals from the Veto wall were recorded as data but not used in the trigger requirement (the Tagged Veto Wall or TVW signal)

The recovery of the J/ψ signal from these two samples is done differently, and the TVW sample is used to estimate the losses in the J/ψ signal in the AVW sample. This is described in the next chapter.

Section 5.2

5.2.1 Event selection and data reduction.

The raw data are processed through a track and momentum reconstruction program, which used information from the muon chambers to determine if the event has at least two tracks in the muon system.

The algorithm is described in detail elsewhere [1] and in Chapter 7 of this thesis. Briefly, a road search is done for space track candidates in the E672 muon chamber system. For each such track candidate found, the momentum and sign of the charge of the track are reconstructed under the assumption that the tracks originated in the target, and acquired a p_t kick in the toroid.

The trajectory of the track upstream and downstream of the toroid were constrained to be coplanar. If at least two such tracks were found, point, track, momentum and dimuon mass information are written in the form of a data summary file which is used for subsequent analysis. The data summary files also contain point information for the D-station PWC's and veto wall information.

5.2.2 Cuts used in data reduction

Some additional cuts were applied to the data to reduce the background. These cuts included

1. The tracks were required to have spatially correlated hits in the two hodoscopes. This reduces the possibility of errors in the track reconstruction by imposing an additional constraint on the trajectory.
2. Each track is constrained to be coplanar with the vertex (assumed to be the target) and the mid-point of the toroid. This criterion is implemented when the χ^2 fit[2] for the entire track trajectory is performed.
3. Tracks were required to have a minimum distance of 23 cm at the center of the toroid to reject those which went through the lead absorber in the toroid.

The effect of these cuts is shown in Table 5.2.1

TABLE 5.2.1

Number of events surviving the data cuts

Data cut	Number of events
Triggers	656,910
Two or more tracks in the muon system	279,656
Tracks spatially correlated with hits in the H1 and H2 hodoscopes	276,301
Number of events with at least one $\mu^+\mu^-$ pair	145,394
Coplanarity cut	28,976
Minimum distance of tracks from the beam axis	23,471

the J/ψ signal. Operationally, the J/ψ is defined to be a dimuon with invariant mass between 2.15 GeV/c^2 and 4.05 GeV/c^2 in the background subtracted spectrum.

Figure 5.3.1 shows the invariant mass spectrum integrated over all targets. Also shown on Figure 5.3.1 is the normalized background, summed over all targets and running conditions. The *like*-sign mass spectrum from the data and the generated background have the same shape, indicating that the background is indeed dominated by muons from π and K decays. The invariant mass spectrum in the x_F region from 0.2 to 0.8, integrated over all targets, is shown in Figure 5.3.2, and exhibits an enhanced signal to background ratio compared to Figure 5.3.1.

Figure 5.3.3 shows the background subtracted mass spectrum integrated for all targets. The number of events and the number of J/ψ's, integrated over all targets, after the x_F restriction is shown in Table 5.3.1.

Table 5.3.1

Number of events and J/ψs after cuts

Data cut	Number of events
$0.1 \leq x_F \leq 0.8$	8,901
Number of J/ψs in $0.1 \leq x_F \leq 0.8$	1,300
$0.2 \leq x_F \leq 0.8$	3,910
Number of J/ψs in $0.2 \leq x_F \leq 0.8$	900

In addition to these cuts, the Feynman-x for the dimuon, x_F, is constrained to be between 0.1 and 0.8. This cut is imposed because the experiment acceptance in x_F is very small outside this region, and most of the background corresponds to the low x_F region. The unlike-sign dimuon invariant mass spectrum for Carbon (Figure 5.2.1), Aluminum (Figure 5.2.2), Copper (Figure 5.2.3) and Lead (Figure 5.2.4) shows a clear J/ψ signal at an invariant mass of 3.1 GeV/c^2.

Section 5.3

5.3.1 Estimation of the background.

The background in the resonant part of the dimuon invariant mass spectrum arises mainly from in-flight decays of π and K decays. This background is estimated by mixing muons from *different* events, computing the invariant mass and subjecting the spectrum to the same cuts as in the data.

The data were collected under slightly different running conditions which are described below. Apart from the two samples, AVW and TVW, described in section 5.1, Some of the runs had the Liquid Argon Calorimeter (LAC) centered on the beam line and others had it off center. The background is generated separately for each trigger configuration (AVW/TVW) and for each geometrical configuration (LAC centered and LAC off center), as is the invariant mass spectrum from the data.

5.3.2 Background subtraction

The background is normalized to have the same number of events in the mass region 1.3 GeV/c^2 $\leq M_{\mu\mu} \leq$ 2.0 GeV/c^2 for each target and running condition. Subtraction of the normalized background from the data yields

5.3.3 Number of J/ψ from each target

The number of J/ψ's after background subtraction for the AVW sample is shown in Table 5.3.2, and in Table 5.3.3 for the TVW sample.

Table 5.3.2

Uncorrected number of J/ψ's from the AVW sample

Target	N_ψ $0.1 \le x_f \le 0.8$	N_ψ $0.2 \le x_f \le 0.8$
Carbon	184 ± 17	144 ± 14
Aluminum	250 ± 21	194 ± 16
Copper	363 ± 43	230 ± 30
Lead	171 ± 18	113 ± 13

Table 5.3.3

Uncorrected number of J/ψ's from the TVW sample

Target	N_ψ $0.1 \le x_f \le 0.8$	N_ψ $0.2 \le x_f \le 0.8$
Carbon	115 ± 22	68 ± 19
Aluminum	55 ± 13	24 ± 10
Copper	45 ± 14	31 ± 11
Lead	118 ± 24	76 ± 19

The number of J/ψ's has to be corrected for various effects before the cross section can be calculated. The corrections and cross section calculation are described in Chapter 6.

REFERENCES

1) S. Kartik, E672 Technical note E672/91-3, Section 1.2-1.4.

2) S. Kartik, E672 Technical note E672/91-3, Section 1.4.

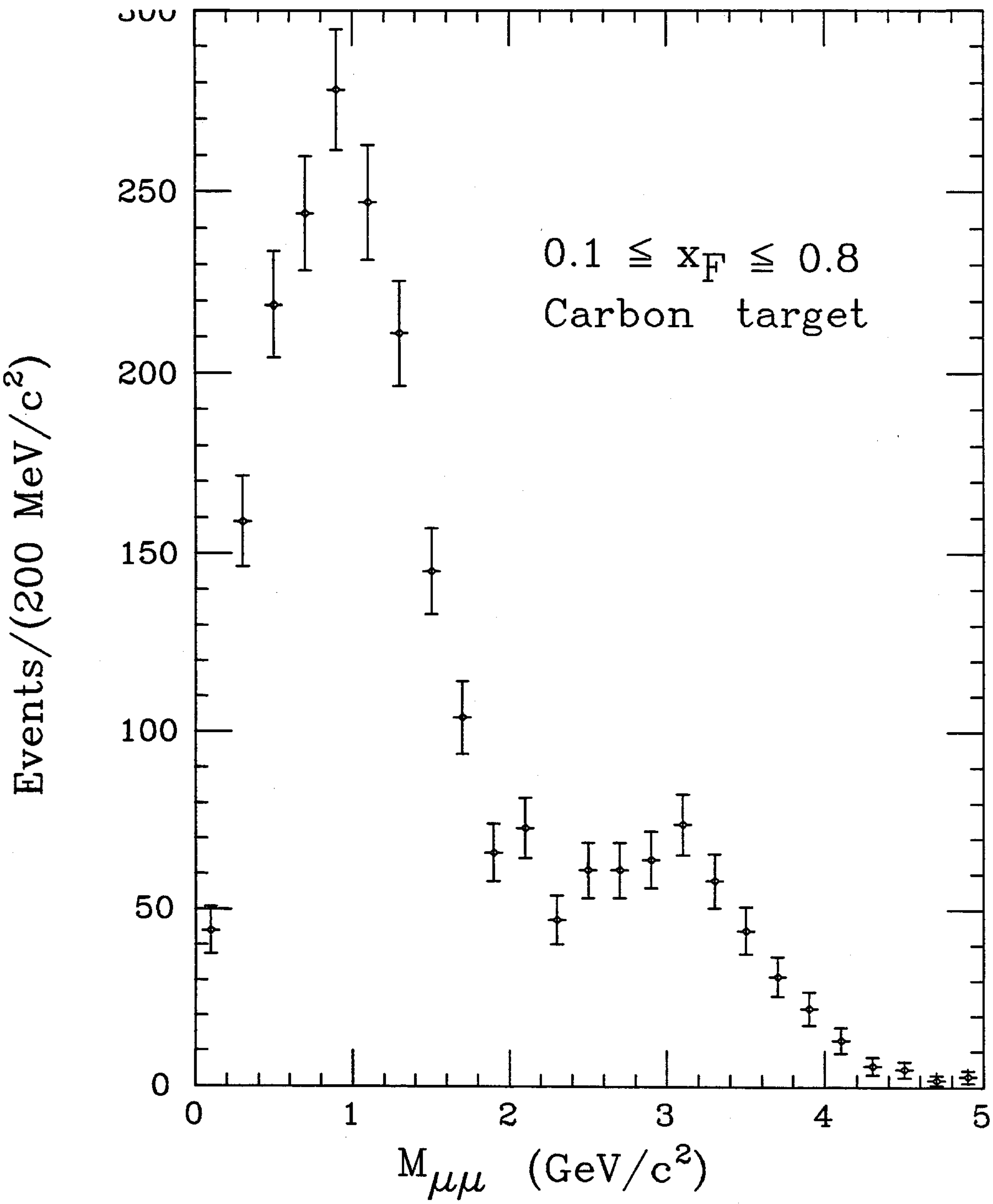

0.1 ≦ x_F ≦ 0.8
Carbon target
Events/(200 MeV/c^2)
$M_{\mu\mu}$ (GeV/c^2)
0
50
100
150
200
250
0
1
2
3
4
5

FIGURE 5.2.1

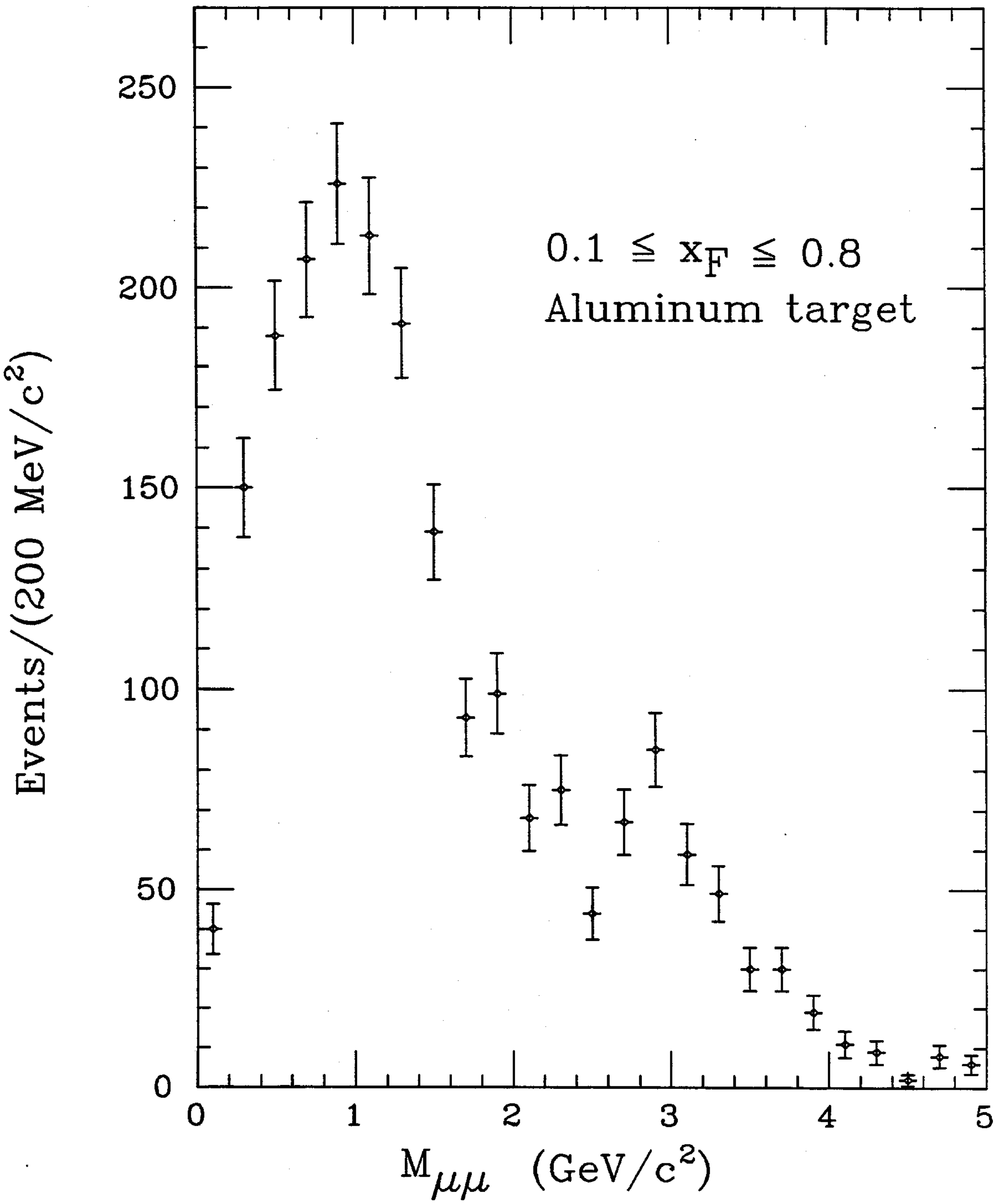

0.1 ≦ x_F ≦ 0.8
Aluminum target
Events/(200 MeV/c^2)
250
200
150
100
50
0
0
1
2
3
4
5
$M_{\mu\mu}$ (GeV/c^2)

FIGURE 5.2.2

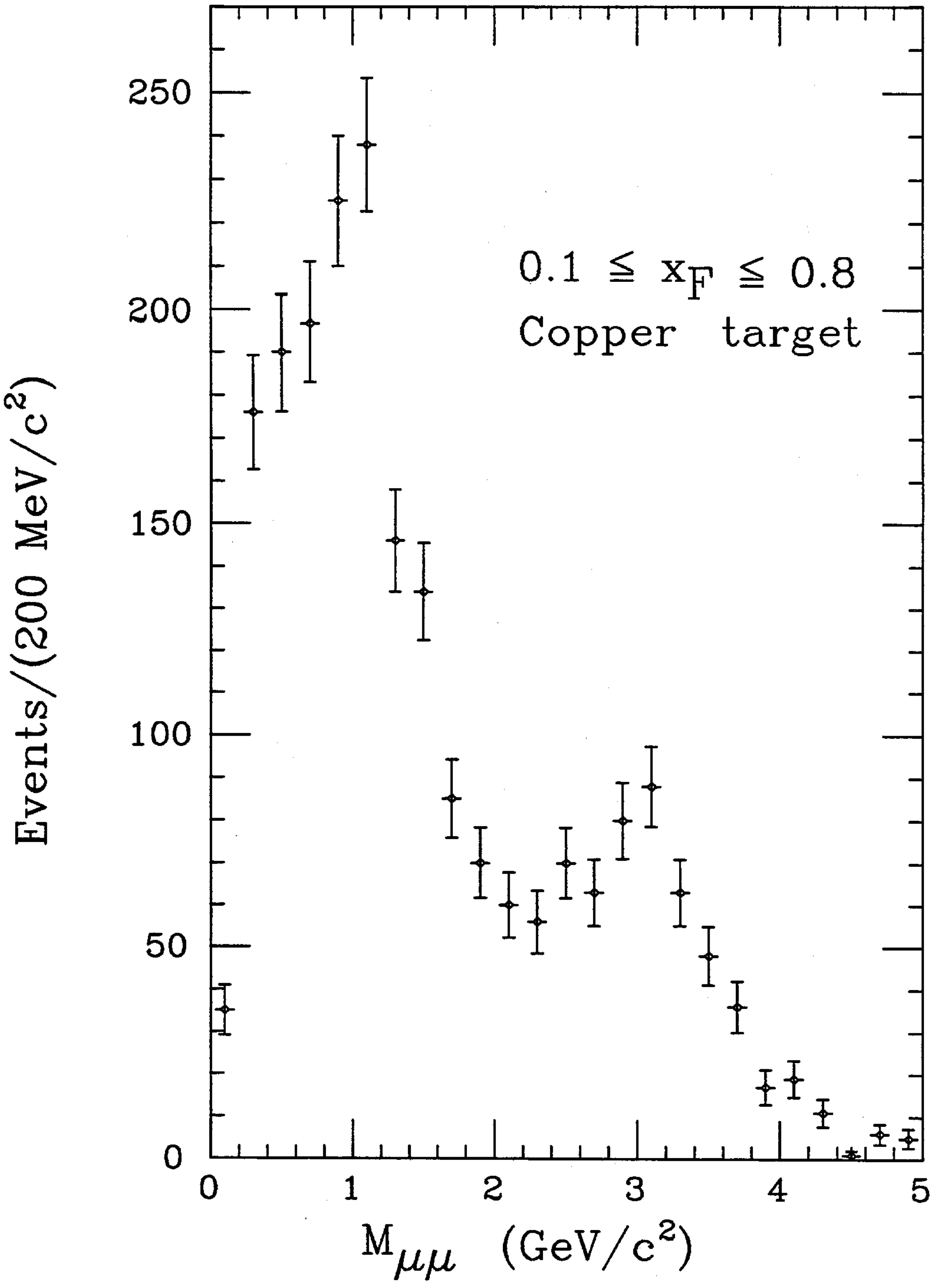
250
200
150
100
50
0
0
1
2
3
4
5
Events/(200 MeV/c²)
M_μμ (GeV/c²)
0.1 ≦ x_F ≦ 0.8
Copper target

FIGURE 5.2.3

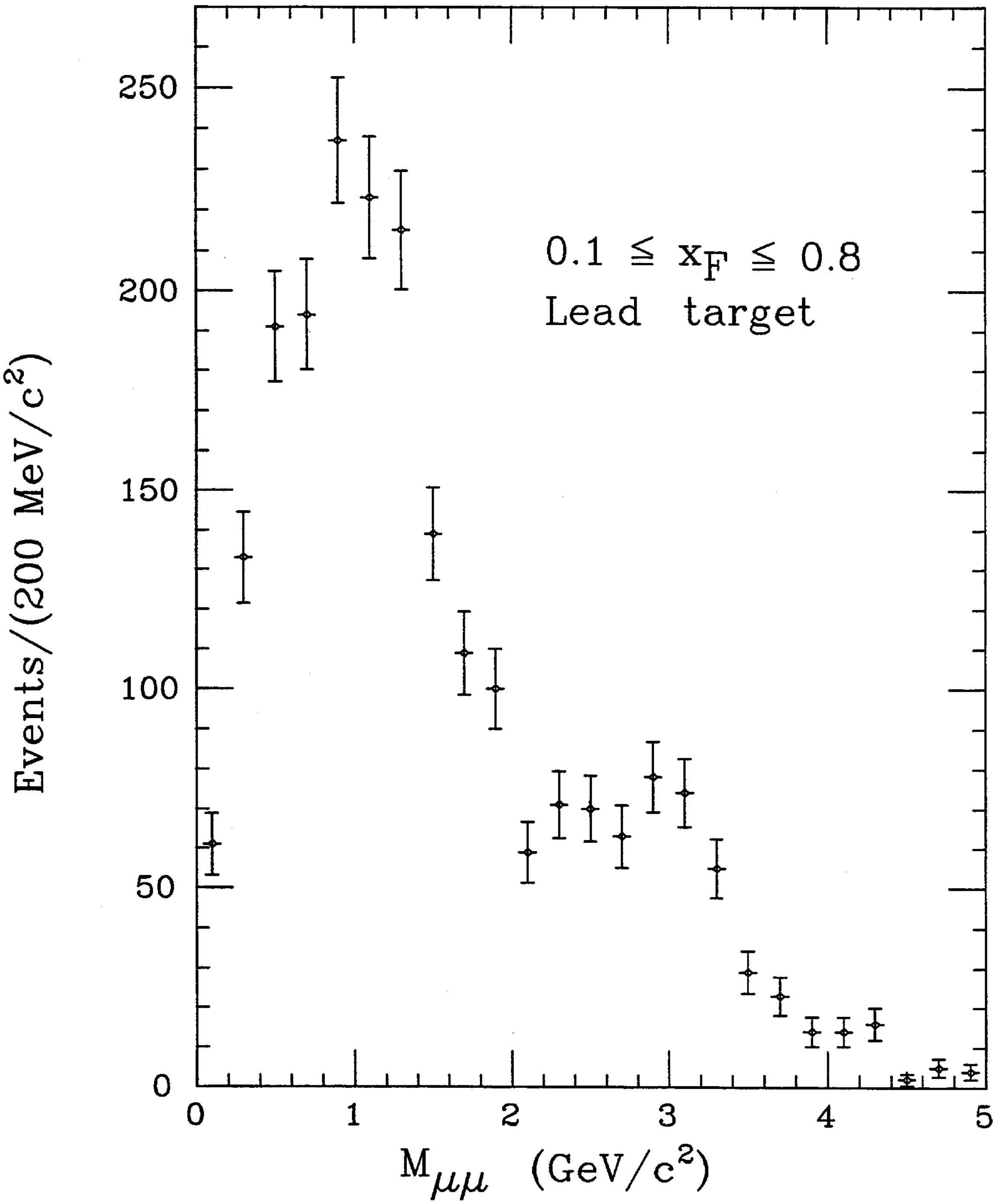
0.1 ≦ x_F ≦ 0.8
Lead target
Events/(200 MeV/c^2)
$M_{\mu\mu}$ (GeV/c^2)
0
50
100
150
200
250
1
2
3
4
5

FIGURE 5.2.4

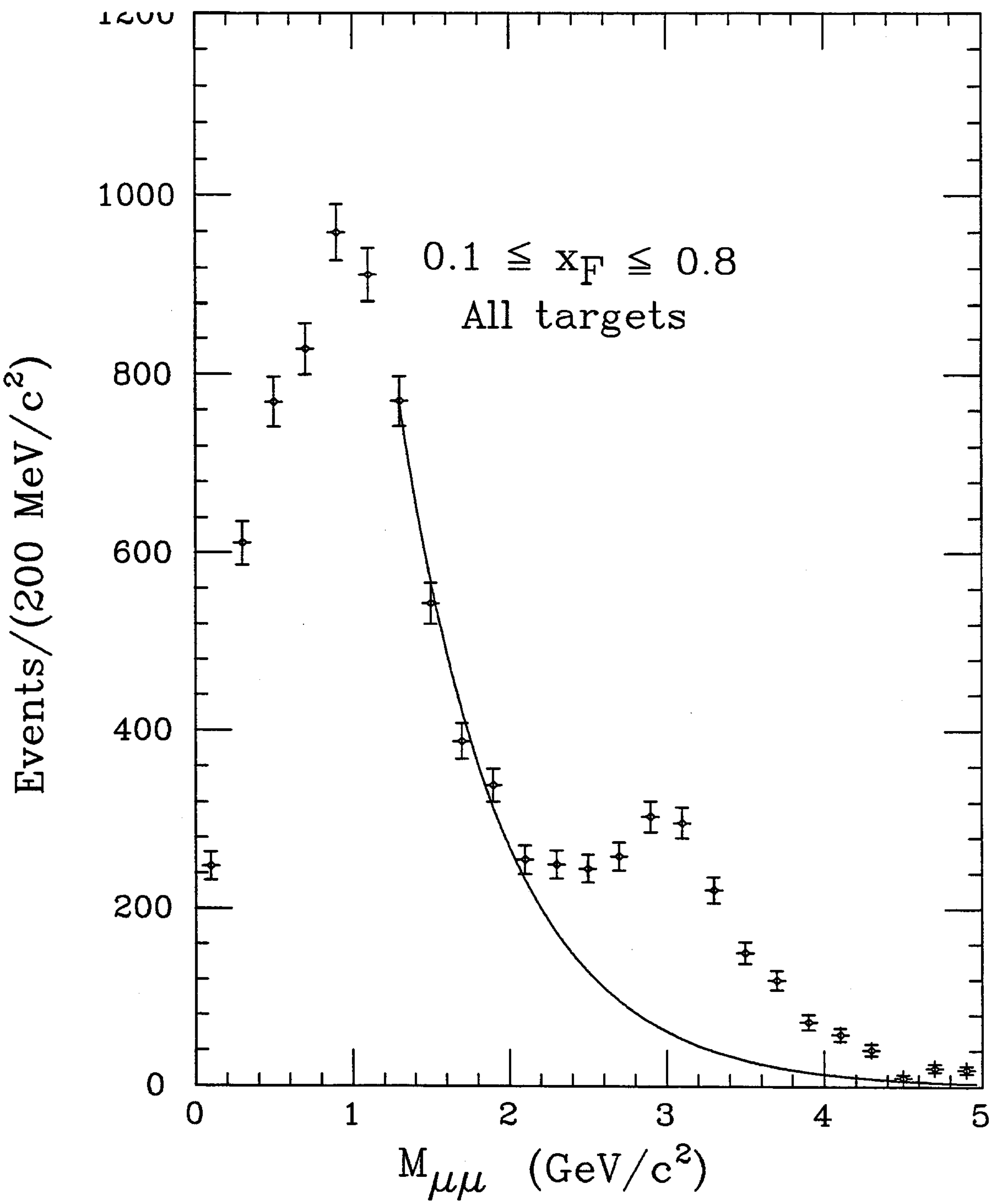
1200
1000
800
600
400
200
0
Events/(200 MeV/c²)
0
1
2
3
4
5
M$_{\mu\mu}$ (GeV/c²)
0.1 ≦ x$_F$ ≦ 0.8
All targets

FIGURE 5.3.1

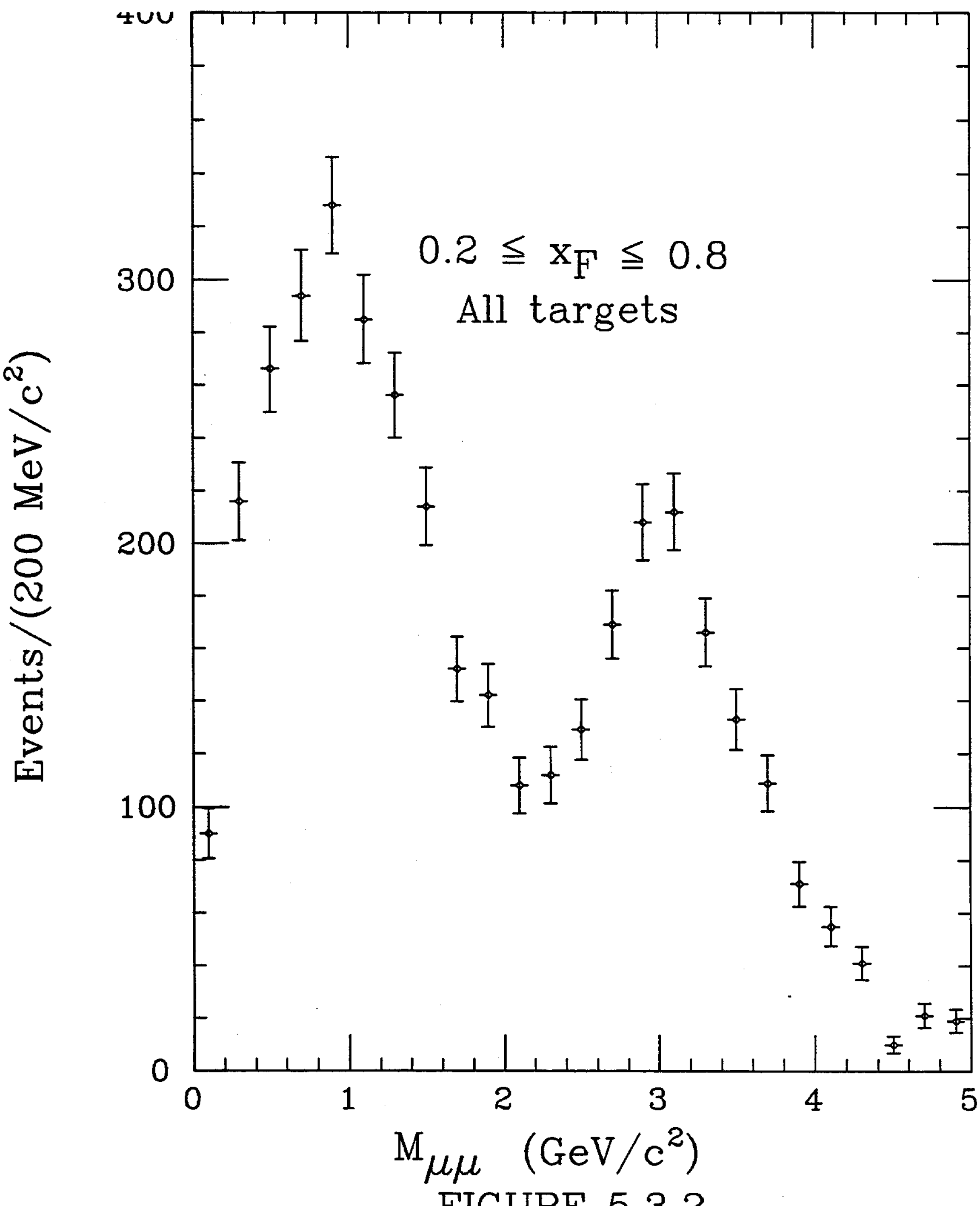

Events/(200 MeV/c²)
400
300
200
100
0
0.2 ≦ x_F ≦ 0.8
All targets
0
1
2
3
4
5
M_μμ (GeV/c²)

FIGURE 5.3.2

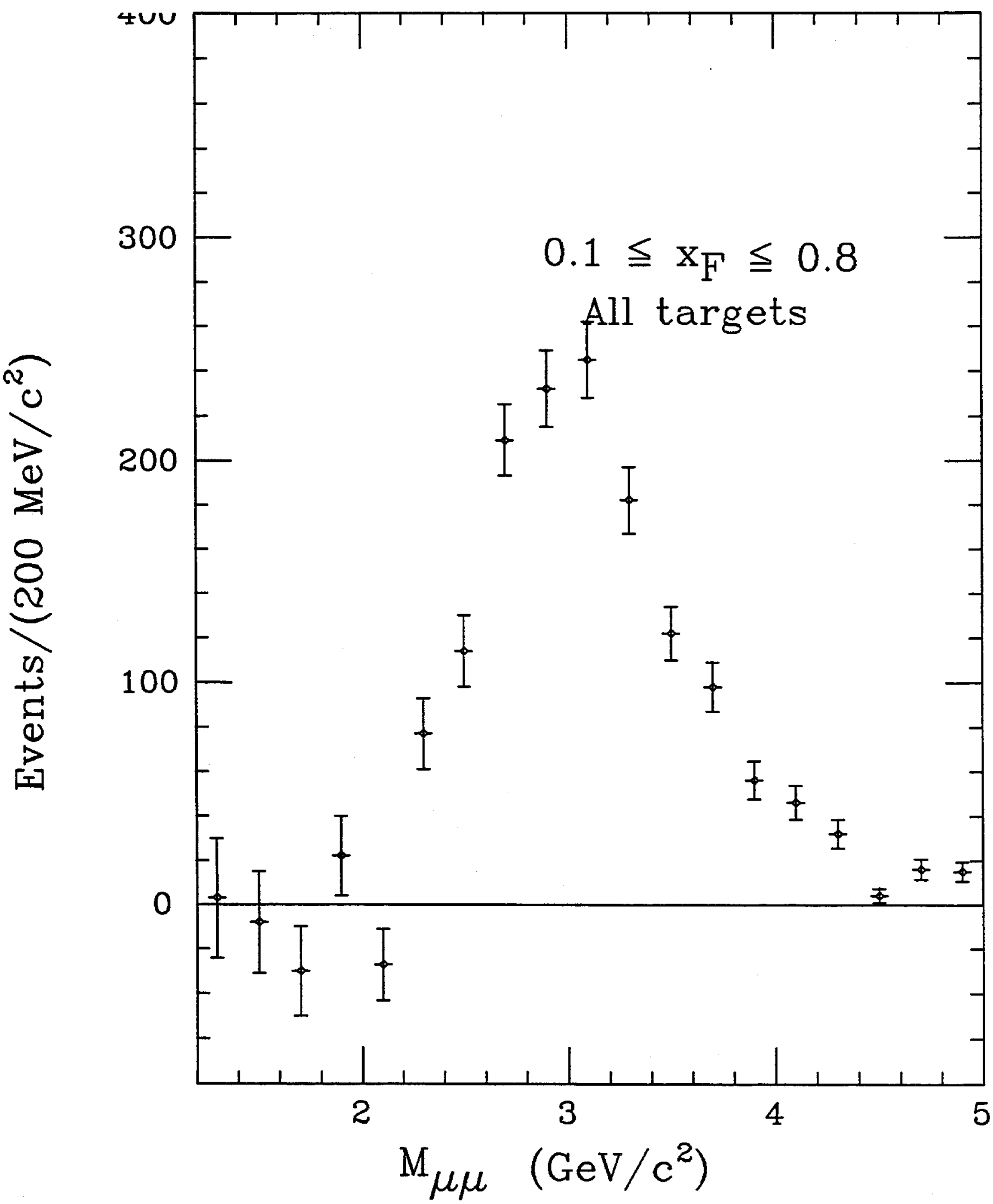

400
300
200
100
0
Events/(200 MeV/c²)
0.1 ≦ x_F ≦ 0.8
All targets
2
3
4
5
M_μμ (GeV/c²)

FIGURE 5.3.3

CHAPTER 6
J/ψ CROSS SECTIONS AND A-DEPENDENCE

The number of uncorrected J/ψ's as obtained in Chapter 5 has to be corrected for various effects before the cross section can be calculated. This chapter describes procedure for the calculation of the cross section for J/ψ production.

The first section details the corrections made to the data before cross section calculation. The next section describes the target independent corrections. The target dependent corrections are described in the following that. The calculation of the cross section for each target and the determination of the A-dependence for J/ψ production is given in section 6.4. The final section presents results on the kinematic distributions for J/ψs and comparison with previous measurements.

Section 6.1

6.1.1 Corrections to the data

The corrections to the 'raw' number of J/ψ's can be separated into two classes, namely those which are target independent and those which are target dependent. The target independent corrections are:

1. Geometrical and kinematical acceptance
2. Apparatus detection efficiency
3. Losses due to the mass region to define the J/ψ
4. Software reconstruction losses

The target dependent corrections are:

1. Backscatter from the target
2. Non–target interactions
3. Target thickness effects

The target independent corrections are described in section 6.2 and the target independent corrections are described in section 6.3. The corrected number of J/ψ's is then used to obtain the per-nucleon cross section for J/ψ production knowing the number of interactions and the interaction cross sections off nuclear targets. These cross sections are used subsequently to extract their A–dependence.

Section 6.2

6.2.1 Geometrical and kinematic acceptance

Due to the amount of material the muons have to traverse before reaching the trigger hodoscopes, muons with a momentum less than 15 GeV/c are not accepted by the apparatus. A Monte Carlo simulation is done to obtain the acceptance functions as a function of the Feynman-x (x_F) and as a function of the transverse momentum (p_t) of the dimuon. The distributions are appropriately "smeared" to account for energy loss and multiple scattering. The input distribution for the x_F of the J/ψ is chosen to be uniform so as to be able to estimate the acceptance better in the high x_F region. The input distribution for J/ψ's p_t is also flat.

The acceptance curve for x_F is shown in Figure 6.2.1. The integrated acceptance is best in the x_F region from 0.2 to 0.8 and is 0.41 ± 0.03 . In the x_F region from 0.1 to 0.8 the integrated acceptance is 0.32 ± 0.01. The acceptance in p_t is shown in Figure 6.2.2 and is seen to be practically flat up to a transverse momentum of 4 GeV/c.

6.2.2 Apparatus detection efficiency

The correction factor for hardware inefficiency losses in the muon chambers is estimated to be 1.01, corresponding to an average point detection efficiency of 99.7 % in each of the muon chambers. The single muon detection efficiency[1] for the trigger hodoscope H1 is 95.9 %, and that for H2 is 94.1 %. The overall correction for detection inefficiencies in the muon chambers and the hodoscopes is 1.24[2] .

6.2.3 Software reconstruction losses

The losses in the number of J/ψ's due to inefficiencies in the point and track reconstruction algorithm are estimated by Monte Carlo techniques to be at about 1%. A sample of Monte Carlo J/ψ events is generated and digitized to simulate the detector configuration using the GEANT program. These are used as input for the reconstruction programs to obtain the fraction of events lost.

6.2.4 J/ψ tail losses

Monte Carlo generated J/ψ events, with the experimental mass resolution folded in, indicate that 7% of the J/ψ signal is lost in the tails of the distribution when the J/ψ is defined to be in the mass region 2.15 GeV/c^2 $\leq M_{\mu\mu} \leq$ 4.05 GeV/c^2. This is corrected for in estimating the true number of J/ψ's produced.

Section 6.3

6.3.1 Correction for target backscatter

Data were collected under two running conditions as described earlier. In the former data sample, the Veto Wall signals are used as an online veto for the interaction in order to reduce spurious triggers arising from beam muon halo. Subsequent analysis and Monte Carlo simulations indicated that a significant fraction of Veto Wall signals arose from backscatter debris from the target, which is located around 10 feet downstream of the Veto Wall. Due to geometrical reasons, these signals populate the RF bucket after the interaction bucket. As the width of the veto gate is 100 ns, otherwise good events with a backscatter hit in the veto wall occur within the veto gate and are lost. This data sample is referred to as the Anti-Veto Wall or AVW sample.

In an effort to understand and correct for these losses, data were collected without the veto wall in the interaction definition. The Veto wall signals are merely recorded as part of the data for this sample, referred to as the Tagged Veto Wall or TVW sample. Information is available about the time structure of the signals with respect to the interaction.

The TDC distribution for the Veto Wall signal from different targets is shown in Figures 6.3.1 (a) to 6.3.1 (d), for Carbon, Aluminum, Copper and Lead respectively. The beam RF structure is clearly evident, with individual buckets being separated by about 20 nanoseconds. The central peak in these distributions corresponds to the interaction RF bucket, and the peak after it is the backscatter peak. As can be seen, the strength of the backscatter peak with respect to the interaction peak is a strong function of the target, and increases with the atomic weight of the target. The peak before the interaction bucket is enhanced due to its proximity to the interaction bucket.

Some of the events in the backscatter peak do arise from true muon halo, and this contribution is estimated by the strength of the peak *preceding* the interaction bucket. Operationally, the backscatter region is considered to be in the interval between 375 ns and 405 ns on the TDC distribution, and the region before the interaction is considered to be from 320 ns to 350 ns.

The number of true backscatter events, N_{BS}, is then the difference between the number in the backscatter region and the number in the region preceding the interaction. The total number of analysed events is known, and by simulating the online veto in the software, one can obtain the number of 'anti-veto wall' events, N_{AVW} can be obtained as well. The correction factor C used to correct the AVW sample for losses is then defined as

$$C = \frac{(N_{AVW} + N_{BS})}{N_{AVW}} \tag{6.1}$$

Thus the total number of J/ψ's after correction for the backscatter is given by

$$N_{J/\psi}^{tot} = N_{J/\psi}^{tvw} + C \cdot N_{J/\psi}^{avw} \tag{6.2}$$

This correction is also dimuon invariant mass region dependent, reflecting the fact that due to the acceptance of the experiment, the dimuon energy increases with the dimuon invariant mass. This correction is calculated for various dimuon mass regions, and the results are presented in Table 6.3.1.

Due to lack of statistics, the correction for the Copper target is obtained by interpolation in the following way. It is assumed that the ratio $\frac{N_{BS}}{N_{AVW}}$

depended on the atomic number as A^γ and thus

$$\left(\frac{N_{BS}}{N_{AVW}}\right)_A = \left(\frac{N_{BS}}{N_{AVW}}\right)_{A=1} \cdot A^\gamma \tag{6.3}$$

The results presented for copper are obtained from a χ^2 fit to this form, and the correction is seen to be reasonably in tune with expectations.

Table 6.3.1

Backscatter correction factors

Target	No mass cut	$M_{\mu\mu} \geq 1.5$ Gev	$M_{\mu\mu} \geq 2.0$ Gev	$M_{\mu\mu} \geq 2.5$ Gev
Carbon	1.176 ± 0.003	1.37 ± 0.03	1.32 ± 0.04	1.31 ± 0.04
Aluminum	1.246 ± 0.004	1.52 ± 0.04	1.40 ± 0.05	1.44 ± 0.07
Copper	1.379 ± 0.011	1.59 ± 0.09	1.55 ± 0.13	1.57 ± 0.16
Lead	1.681 ± 0.008	1.78 ± 0.05	1.84 ± 0.08	1.86 ± 0.10

Note: The results for copper are obtained by interpolation.

6.3.2 Non-target interactions

In the running period when data were collected for this analysis, the part of the spectrometer around the target was not operational. Consequently, no vertex information is available for these events and it is assumed that the muons originate in the target. Since the main goal of this analysis is to obtain the A–dependence of J/ψ production, it is important to correct for the fact that not all interactions occur in the target, and neither do all the J/ψ's. This correction is estimated using the model[3] described below.

For the cross section calculation, the relationship used is the following,

$$\sigma(J/\psi) = \frac{N_{J/\psi}}{N_{IB}} \cdot \sigma(IB) \tag{6.4}$$

where, $\sigma(J/\psi)$ is the J/ψ production cross section, $\sigma(IB)$ is the interacting beam cross section, N_{IB} is the total number of interactions from the scalers and $N_{J/\psi}$ is the total number of J/ψ's produced.

The interaction cross section, $\sigma(IB)$, is well understood and corrected for background interactions. The ratio $N_{J/\psi}/N_{IB}$ needs to be corrected to obtain $N^A_{J/\psi}/N^A_{IB}$, which can then be used to calculate the true cross section for a particular nucleus.

The reason why this correction factor is not unity is due to the fact that the A–dependence for interaction rates is not the same as that for J/ψ production rates. In fact, $N^A_{J/\psi} \sim A^{\alpha}$ where α is between 0.9 and 1.0 and $N^A_{IB} \sim A^{0.75}$ for π^- beams.

The total number of J/ψ's ,$N_{J/\psi}$ is the sum of $N^A_{J/\psi}$ and the J/ψ's from the background $N^B_{J/\psi}$, and similarly for N_{IB}. As a first approximation, the background is taken to be from targets with atomic weight close to that of Carbon ($A = 12$), *i.e.* light nuclear targets. With this assumption, the Carbon data would not need any correction. If we define the quantities[3] ,

$$\beta = \frac{N^A_{IB}}{N_{IB}} \quad , \quad \gamma = \left(\frac{A}{12}\right)^{(\alpha-0.75)} \tag{6.5}$$

$$C_{NT} = \frac{1}{\beta + \frac{(1-\beta)}{\gamma}} \tag{6.6}$$

we can relate the corrected and uncorrected ratios by[3]

$$\frac{N^A_{J/\psi}}{N^A_{IB}} = C_{NT} \cdot \frac{N_{J/\psi}}{N_{IB}} \tag{6.7}$$

The correction is calculated for both $\alpha = 0.9$ and $\alpha = 1.0$ for comparison. The results are presented in Table 6.3.2.

The quantities with the superscript 1 refer to $\alpha = 0.9$ and those with 2 refer to $\alpha = 1.0$. A different correction is calculated for each target thickness, and β is calculated from the known interaction and background rates for different targets and thicknesses.

Table 6.3.2.

Correction for non–target interactions

Target	Thickness (cm)	β	γ^1	γ^2	C^1_{NT}	C^2_{NT}
Aluminum	3.81	0.47	1.130	1.235	1.605	1.108
	12.7	0.869	1.130	1.225	1.015	1.025
	26.9	0.897	1.130	1.225	1.013	1.019
Copper	5.08	0.851	1.285	1.520	1.034	1.054
	10.16	0.909	1.285	1.520	1.020	1.032
Lead	0.95	0.523	1.534	2.040	1.199	1.321
	5.08	0.885	1.534	2.040	1.042	1.062
	7.62	0.880	1.534	2.040	1.044	1.065

6.3.3 Target thickness and rescattering effects

Because of the rather thick targets used for data collecting, some corrections are applied to take into account J/ψ's from secondary interactions. Due to the lack of statistics, a direct measurement of the change in J/ψ yield with target thickness is not possible. A simple model is used to estimate this effect, with the following inputs:

— The average multiplicity of charged secondaries is $< n_{ch} >= 5$.

— For $x_F \geq 0$ the following distributions are assumed for secondaries

$$\frac{d\sigma}{dx_F} \sim e^{-2.4x_F} \quad and \quad \frac{d\sigma}{dp_t^2} \sim e^{-3.6p_t^2} \tag{6.8}$$

— For J/ψ production in secondary interactions

$$\sigma(J/\psi, s) \sim \exp(-\frac{10M_{J/\psi}}{\sqrt{s}}) \tag{6.9}$$

$$\frac{d\sigma(J/\psi)}{dx_F} \sim (1 - x_F) \tag{6.10}$$

$$\frac{d\sigma(J/\psi)}{dp_t^2} \sim \left(1 + \left(\frac{p_t}{2.6}\right)^2\right)^{-3.2} \tag{6.11}$$

With these assumptions, J/ψ's are generated and shifted to the π^-–A center-of-mass frame, where the cut on $x_F \geq 0.1(0.2)$ is applied. The resulting correction factor $\frac{N^{pri}_{J/\psi}}{N^{tot}_{J/\psi}}$ is tabulated in Table 6.3.3.

Table 6.3.3.

Target thickness effect

Target	Thickness(cm)	Correction ($x_F \geq 0.2$)	Correction ($x_F \geq 0.1$)
Carbon	10.2	0.96	0.94
	20.3	0.93	0.89
Aluminum	12.7	0.94	0.91
	16.5	0.93	0.88
Copper	5.08	0.94	0.90
	10.2	0.89	0.83
Lead	5.08	0.94	0.91
	7.62	0.92	0.87

The correction factors are not very sensitive to changes in the input parameters; for example, changes in $< n_{ch} >$ from 4 to 6 or change in the power of the exponential p_t^2 distributions by ± 1 causes a change in the correction by about $\pm 5\%$.

Section 6.4

6.4.1 Interaction cross sections

The cross section for J/ψ production is calculated using the equation

$$\sigma(J/\psi) = \frac{N_{J/\psi}}{N_{IB}} \cdot \sigma(IB) \tag{6.12}$$

where, $\sigma(J/\psi)$ is the J/ψ production cross section, $\sigma(IB)$ is the measured[4] interacting beam cross section for a particular target, N_{IB} is the total number of interactions and $N_{J/\psi}$ is the total corrected number of J/ψ's produced. The number of interactions is available from the CAMAC scaler information for each run used in the analysis.

The interaction cross sections are calculated using the following relationship:

$$\sigma_{IB}(A) = R \cdot \frac{\sigma_0(A)}{1 - \exp\left(-\frac{\sigma_0 T}{MA}\right)} \tag{6.13}$$

where $\sigma_{IB}(A)$ is the observed interaction cross section for a target with atomic weight A, σ_0 is the known cross section[5] , T is the thickness of the target in gm/cm^2, M is the nucleon mass in grams and R is the interaction rate after background subtraction. The background interaction rate information is available from special runs with no target in the beam. The exponential correction to the cross section takes the attenuation of the beam in the target into account. The errors are mainly due to uncertainty in the background subtraction The results are presented in Table 6.4.1. There is an A-dependent inefficiency in the observed cross sections as compared to the cross sections measured in other experiments. This inefficiency is well understood by Monte Carlo studies (GEANT) as being due to geometrical effects concerning the placement of the interaction counters and electromagnetic showering in the targets.

Table 6.4.1

Interacting beam cross sections.

Target	Thickness	Interaction rate	$\sigma(IB)$	σ_0
Carbon	4.0 cm	0.04 ± 0.01	116 ± 15 mb	171 mb
	10.2 cm	0.107 ± 0.005	126 ± 6 mb	
	20.3 cm	0.237 ± 0.005	152 ± 4 mb	
Aluminum	3.8 cm	0.056 ± 0.005	255 ± 23 mb	326 mb
	12.7 cm	0.186 ± 0.005	278 ± 8 mb	
	16.5 cm	0.241 ± 0.005	279 ± 6 mb	
Copper	5.1 cm	0.222 ± 0.005	593 ± 14 mb	625 mb
	10.2 cm	0.388 ± 0.005	588 ± 8 mb	
Lead	5.1 cm	0.216 ± 0.005	1465 ± 37 mb	1460 mb
	7.6 cm	0.285 ± 0.005	1452 ± 25 mb	

6.4.2 J/ψ production cross section

The corrected number of J/ψ's is obtained from the 'raw' number of J/ψ's as given in table 5.3.2 and 5.3.3 and the correction factors described in the preceeding sections. The cross section is calculated for two regions in x_F, namely for $0.1 \leq x_F \leq 0.8$ and $0.2 \leq x_F \leq 0.8$. The per-nucleon cross section for different targets is presented in table 6.4.2. The errors quoted are only statistical. The superscript 1 refers to the x_F region from 0.1 to 0.8 and the superscript 2 refers to the region x_F from 0.2 to 0.8.

Table 6.4.2

J/ψ production cross section per nucleon

Target	Carbon	Aluminum	Copper	Lead
$\sigma(IB)$	152 ± 4 mb	278 ± 5 mb	590 ± 8 mb	1458 ± 22mb
N_{IB}	17.59×10^8	18.28×10^8	29.60×10^8	17.92×10^8
$N^1_{J/\psi}$	1375 ± 168	1540 ± 159	2260 ± 296	1673 ± 217
$N^2_{J/\psi}$	786 ± 116	901 ± 101	1156 ± 172	833 ± 135
$\sigma^1_{J/\psi}$	140.9 ± 17.1 nb	124.7 ± 12.9 nb	98.9 ± 13.0 nb	93.9 ± 12.1 nb
$\sigma^2_{J/\psi}$	80.6 ± 11.9 nb	72.4 ± 8.1 nb	50.7 ± 7.6 nb	46.6 ± 7.6 nb

The cross sections thus obtained are then fitted to the form

$$\sigma_{J/\psi}(A) = \sigma_0 \cdot A^\alpha \qquad (6.14)$$

A χ^2 fit to this for the J/ψ production cross sections gives the following results for α and σ_0.

Table 6.4.3

Fit results for A-dependence of J/ψ production

x_F region	$0.1 \leq x_F \leq 0.8$	$0.2 \leq x_F \leq 0.8$
σ_0	202.9 ± 22.9 nb	140.0 ± 20.0 nb
α	0.85 ± 0.06	0.79 ± 0.07
χ^2 of the fit	0.57	0.94

The cross sections in Tables 6.4.2 and 6.4.3 have the branching ratio for $J/\psi \longrightarrow \mu^+\mu^-$ (6.9 %, from the Particle Data Group) incorporated in them.

Figure 6.4.1 shows the J/ψ cross section as a function of atomic weight A in the x_F region from 0.1 to 0.8. The solid curve is a fit to form $\sigma_0 \cdot A^{\alpha}$. Figure 6.4.2 shows the cross section in the x_F region from 0.2 to 0.8, with the solid curve again being the fit curve.

Section 6.5

6.5.1 Feynman-x (x_F) distributions for the J/ψ

The distribution for the J/ψ as a function of x_F is obtained as described below. The x_F distribution for all dimuons with invariant mass $M_{\mu\mu}$ between 2.15 GeV/c^2 and 4.05 GeV/c^2 is shown in Figure 6.5.1(a) The corresponding distribution for the background is shown in Figure 6.5.1(b). The number of events in the background x_F distribution is normalized so as to have the same number of events as in the background invariant mass spectrum. The background distribution is subtracted from the data on a bin-by-bin basis to obtain the raw J/ψ x_F distribution.

This distribution is corrected for the acceptance in x_F shown in Figure 6.2.1. The acceptance correction is also done on a bin-by-bin basis. The acceptance-corrected, background subtracted J/ψ x_F distribution is shown in Figure 6.5.2. The dashed curve is the result of a fit to the form

$$\frac{dN_{J/\psi}}{dx_F} \sim (1 - |x_F - x_0|)^c \qquad (6.15)$$

with x_0 fixed at 0.2. The fitted value of c is 2.6 ± 0.2 which is consistent with previous measurements at lower energies [6–7]. Due to lack of statistics in the low x_F region, a reliable value is unobtainable for x_0, necessitating the fixing of x_0 in the fit.

6.5.2 Transverse momentum (p_t) distribution for J/ψ

The p_t distributions for the J/ψ are obtained in a similar way. The raw p_t distribution for dimuons in the J/ψ mass range is shown in Figure 6.5.3 (a). The analogous distribution for the background, normalized as for the x_F distributions is shown in Figure 6.5.3(b). After background subtraction the spectrum is corrected for the acceptance. The result is shown in Figure 6.5.4, with the solid curve being the acceptance. The average value of the transverse momentum of the J/ψ at the energy of this experiment is calculated to be 1.16 ± 0.03 GeV/c which is consistent with previous measurements.[7]

6.5.3 x_F dependence for α

The ratio of the x_F distributions for J/ψs from the Pb target and the C target is shown in Figure 6.5.5. Individual distributions are normalized to have the same number of events. That ratio is consistent with unity, indicating that no significant x_F dependence is seen for the A-dependence of J/ψ production.

6.5.4 p_t dependence for α

The ratio of the p_t distributions for J/ψs from the Pb target and the C target is shown in Figure 6.5.6. Individual distributions are normalized to have the same number of events. That ratio is consistent with unity, indicating that no significant x_F dependence is seen for the A-dependence of J/ψ production.

6.5.5 Ratio of mass spectra for C and Pb

The ratio of mass plots for Pb and C targets , normalized to have the same number of events is shown in Figure 6.5.7. In the low mass region, this ratio is seen to be consistent with unity, and is greater than unity in the high mass region. This supports the conclusion that the A-dependence of the J/ψ is different from the dimuons in the low mass region.

6.5.6 Comparison of J/ψ cross sections with others

Figure 6.5.8 compares the A-dependence obtained in this experiments with data from earlier experiments. The cross sections shown have been corrected to apply to the region $x_F \geq 0$, and include the branching ratio for the decay $J/\psi \longrightarrow \mu^+\mu^-$. All values have been scaled to the center-of-mass energy of this experiment, $\sqrt{s} = 31.5$ GeV, using the relation[8] $\sigma \sim e^{-10\sqrt{\tau}} nb$, where $\sqrt{\tau} = M_{J/\psi}/\sqrt{s}$. The J/ψ cross sections presented in this chapter agree well with previously measured values [9–11], and show a similar dependence on the atomic weight of the target nuclei. The measurement of the A-dependence of J/ψ production by the E672 collaboration has been published[12].

REFERENCES

1) Daisy Counter efficiencies ..., E672 Internal note No. 246. May, 1988.

2) Recent results of Thick Target Data Analysis in IHEP, E672-IHEP note, August, 1988.

3) S. Kartik, Corrections for non-target interactions, E672 Internal Note No. 259, February 1989.

4) S. Kartik et al, Measured Interacting beam Cross sections, E672 Internal Note No. 185, September, 1987.

5) A.S. Carroll et al., *Phys. Lett.* **80B**, 319 (1979) .

6) J.G. McEwen et al., *Phys. Lett.* **121B**, 198 (1983) .

7) M.A. Abolins et al., Submitted to the XIX High Energy Physics Conference, Tokyo, 1978 (unpublished).

8) L. Lyons., *Prog. in Part. and Nucl. Phys* **7**, 169 (1981) .

9) Yu. Antipov et al., *Phys. Lett.* **72B**, 278 (1977) , *Phys. Lett.* **76B**, 225 (1978) .

10) M. Corden et al., *Phys. Lett.* **110B**, 415 (1982) .

11) J. Badier et al., *Z.Phys.* **C20**, 101 (1983) .

12) S. Kartik et al., *Phys. Rev.* **D41**, 1 (1990) .

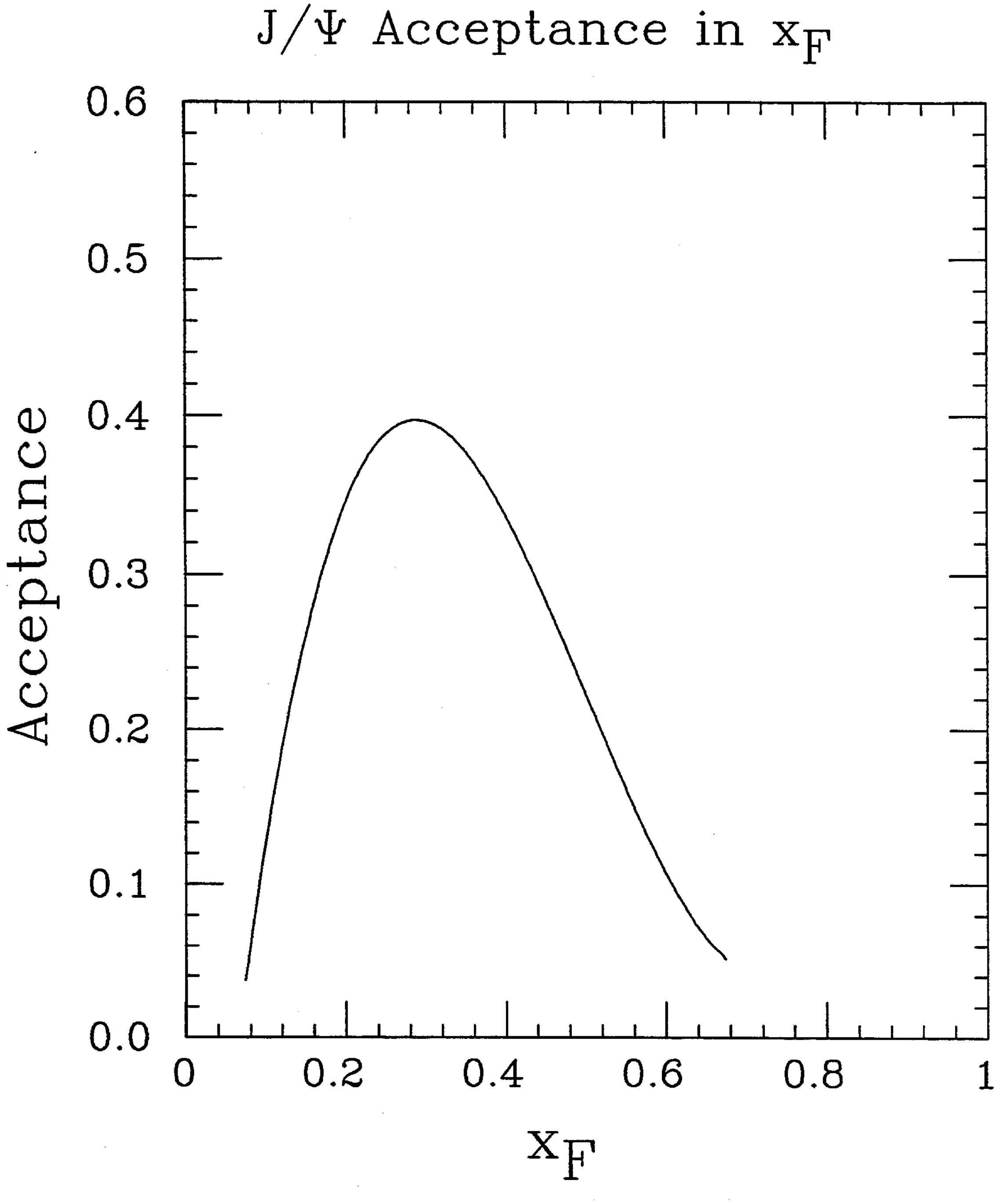

J/Ψ Acceptance in x_F
Acceptance
0.0
0.1
0.2
0.3
0.4
0.5
0.6
0
0.2
0.4
0.6
0.8
1
x_F

FIGURE 6.2.1

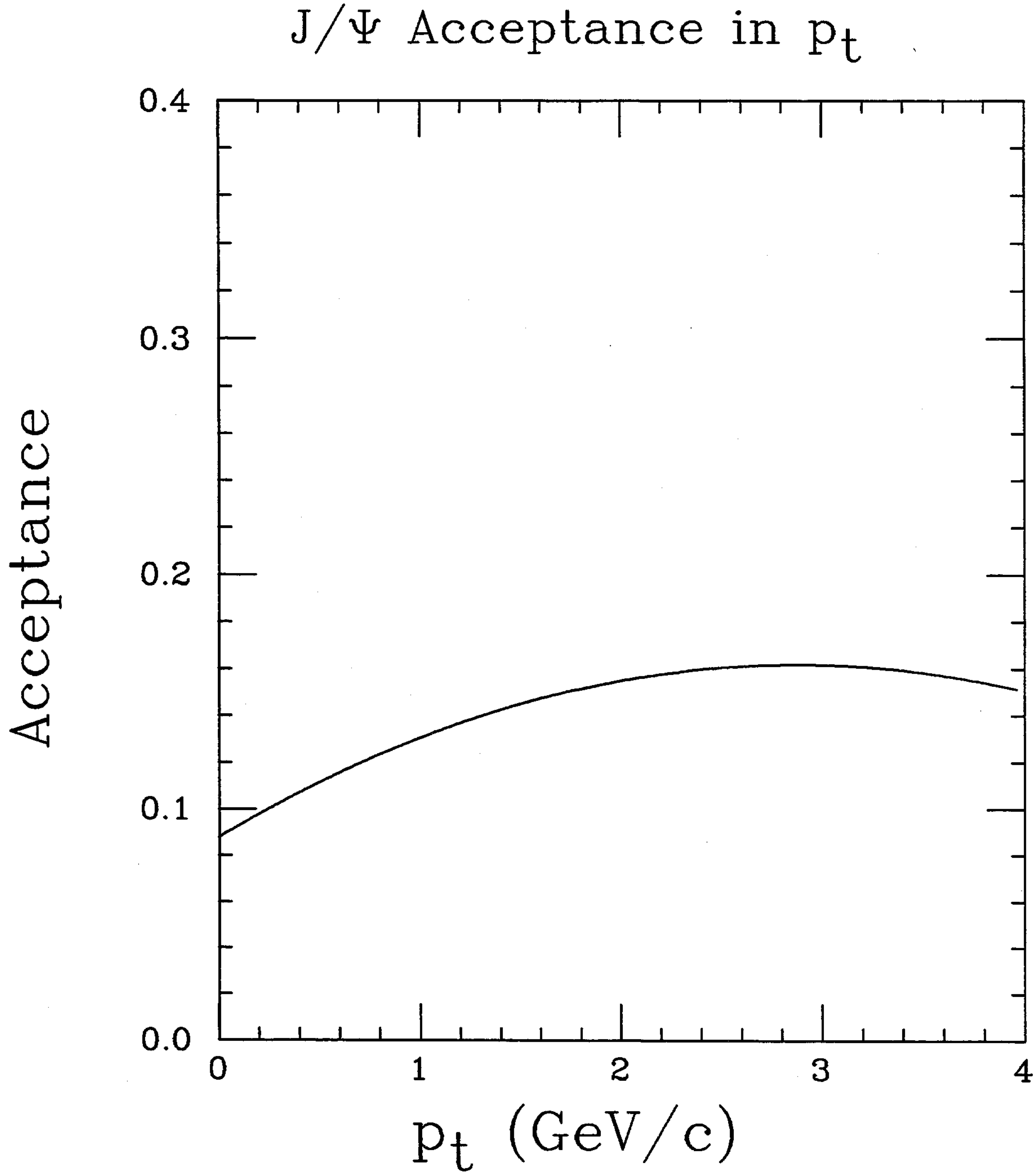

FIGURE 6.2.2

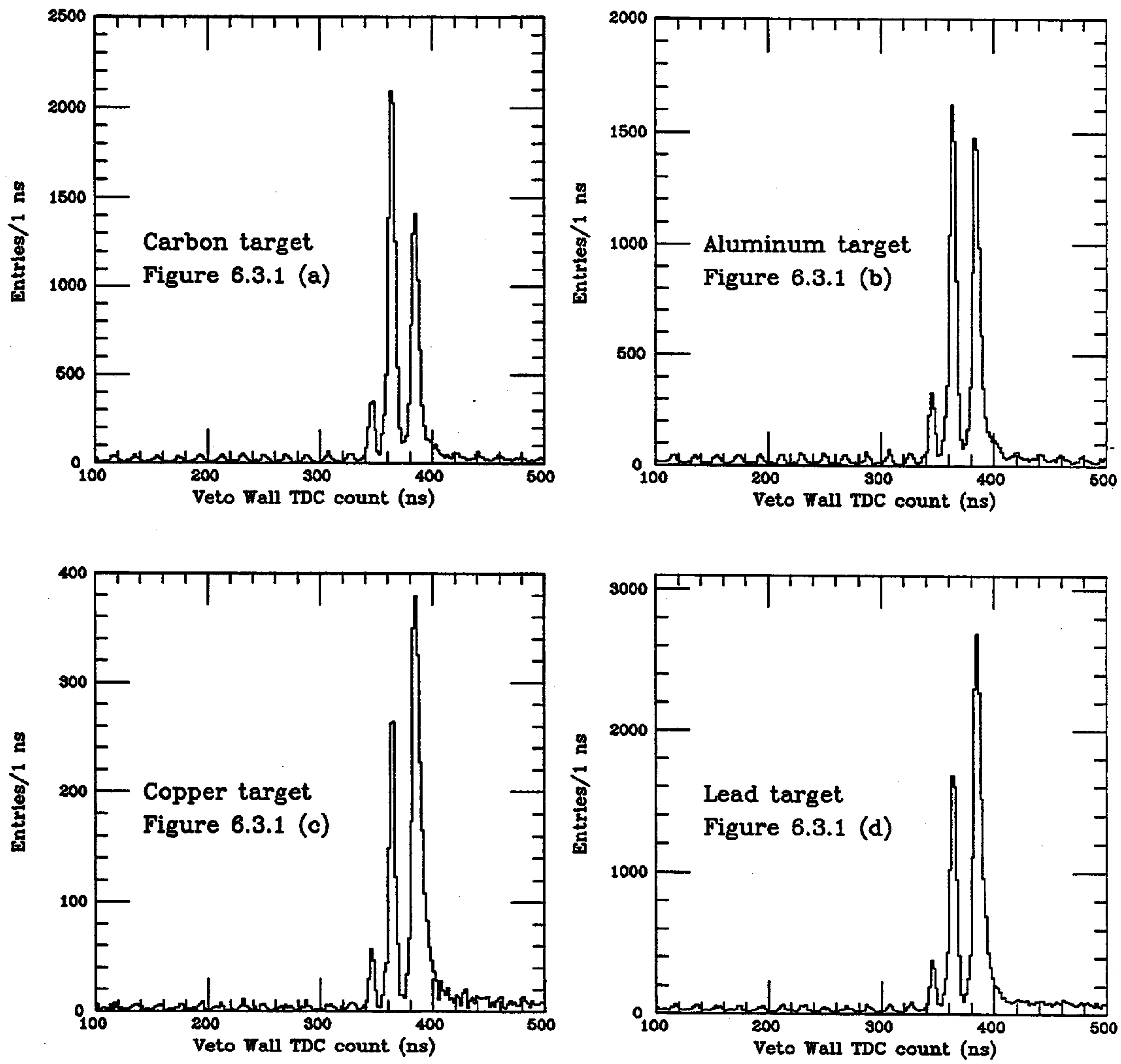
Carbon target
Figure 6.3.1 (a)
Aluminum target
Figure 6.3.1 (b)
Copper target
Figure 6.3.1 (c)
Lead target
Figure 6.3.1 (d)
Entries/1 ns
Veto Wall TDC count (ns)
0
500
1000
1500
2000
2500
100
200
300
400
500
3000

FIGURE 6.3.1

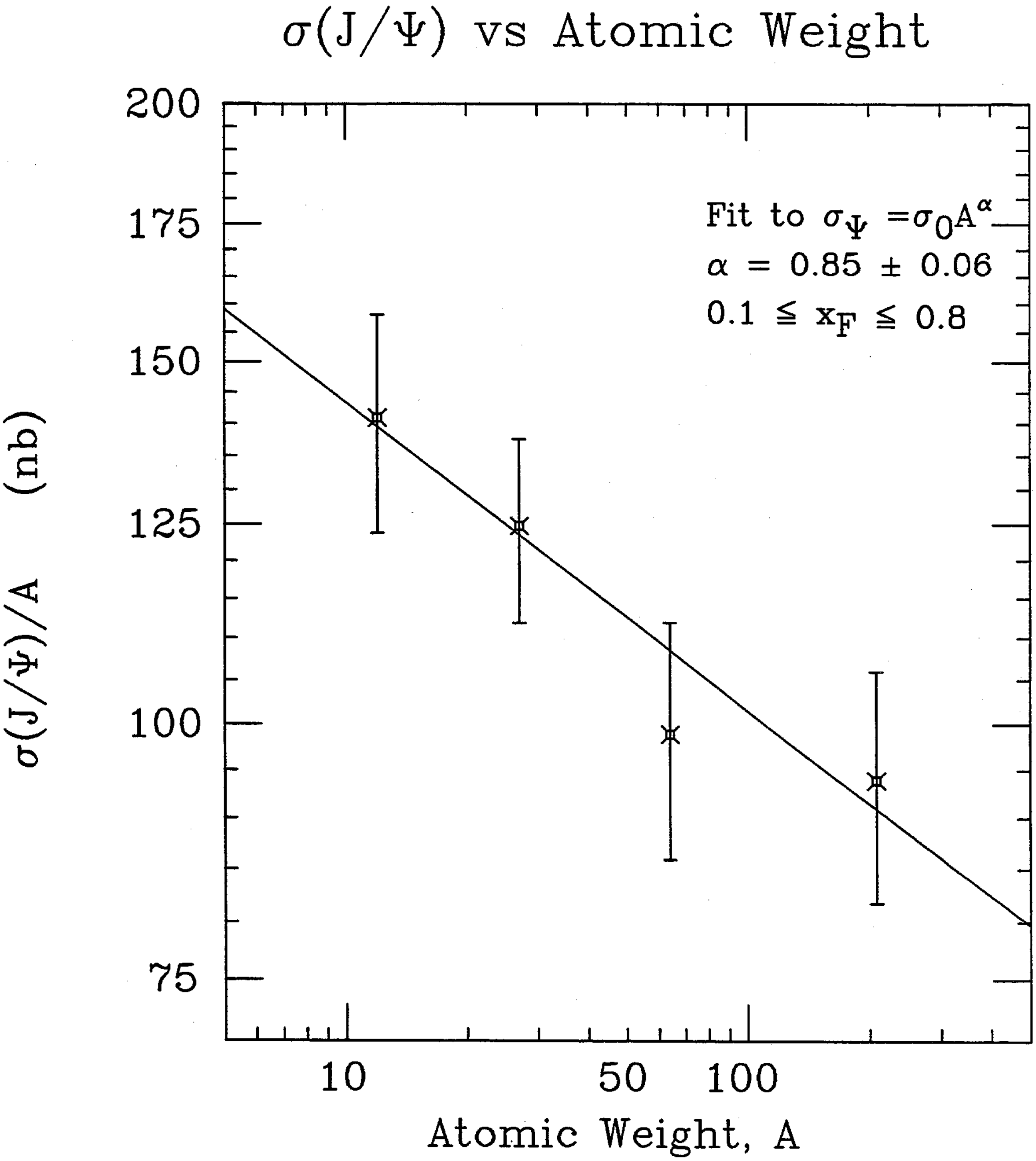

σ(J/Ψ) vs Atomic Weight
200
175
150
125
100
75
Fit to σ_Ψ = σ_0 A^α
α = 0.85 ± 0.06
0.1 ≦ x_F ≦ 0.8
σ(J/Ψ)/A (nb)
10
50
100
Atomic Weight, A

FIGURE 6.4.1

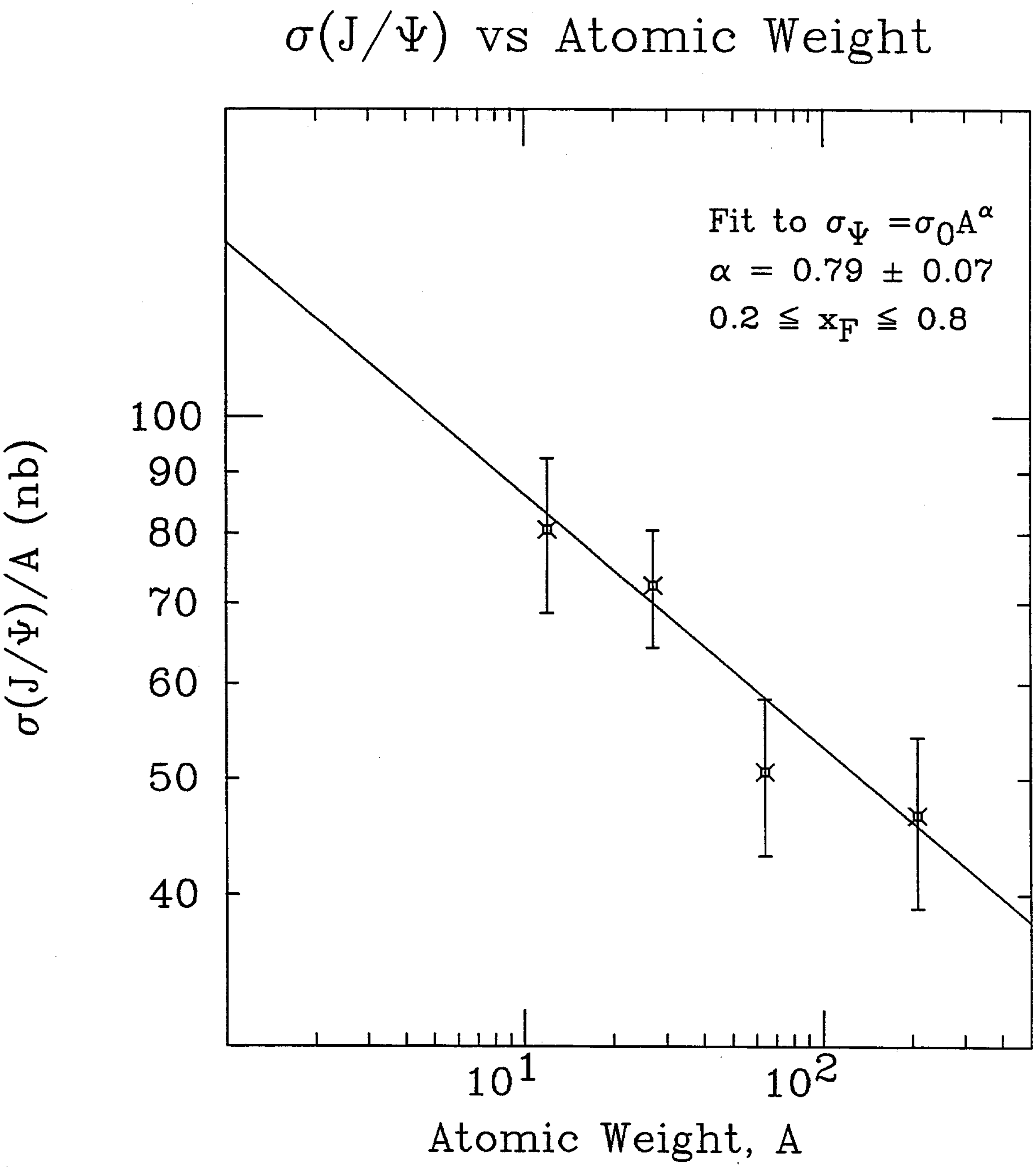

σ(J/Ψ) vs Atomic Weight
Fit to $\sigma_\Psi = \sigma_0 A^\alpha$
$\alpha = 0.79 \pm 0.07$
$0.2 \leqq x_F \leqq 0.8$
100
90
80
70
60
50
40
σ(J/Ψ)/A (nb)
10^1
10^2
Atomic Weight, A

FIGURE 6.4.2

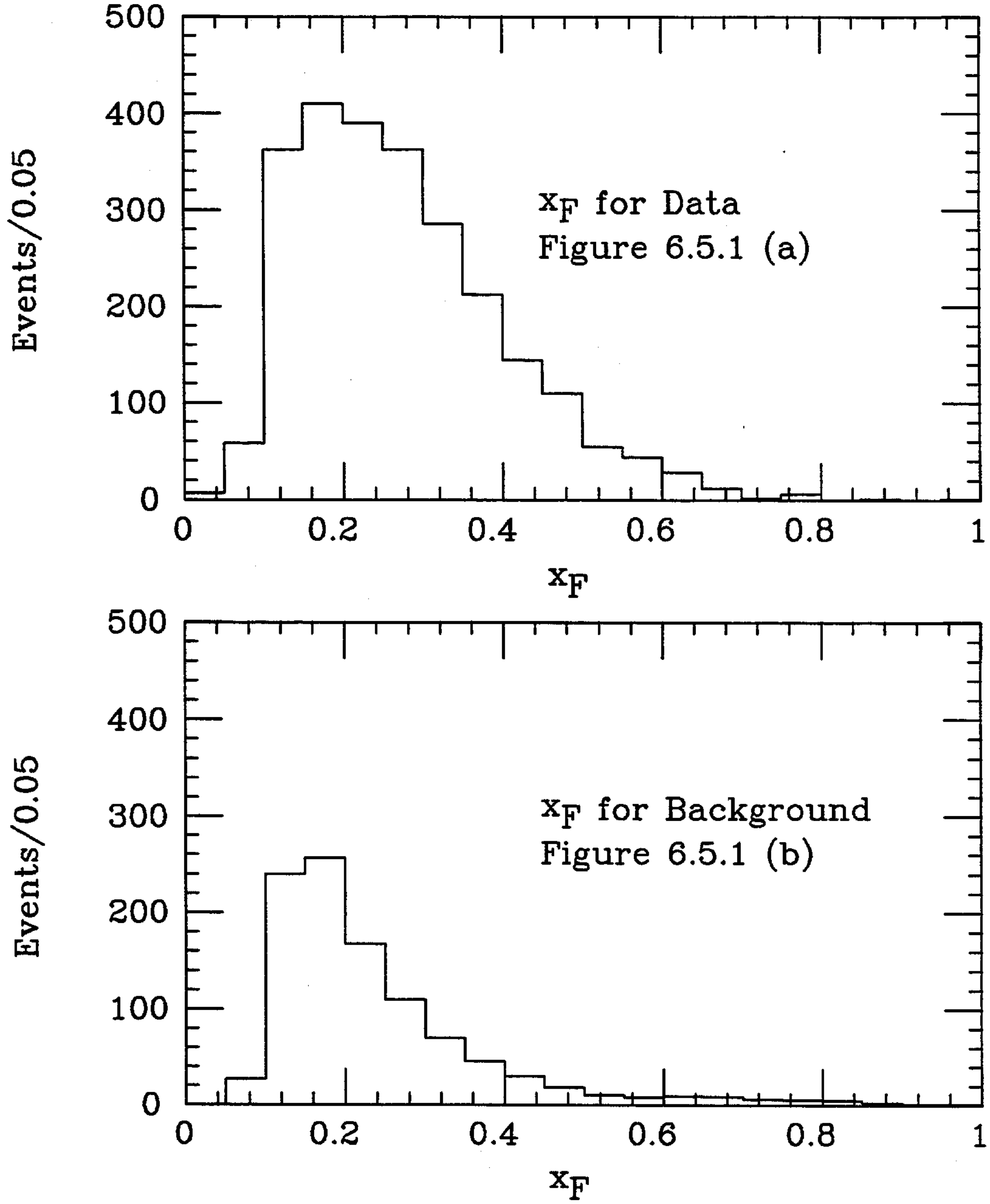

500
400
300
200
100
0
Events/0.05
x_F for Data
Figure 6.5.1 (a)
0
0.2
0.4
0.6
0.8
1
x_F
500
400
300
200
100
0
Events/0.05
x_F for Background
Figure 6.5.1 (b)
0
0.2
0.4
0.6
0.8
1
x_F

FIGURE 6.5.1

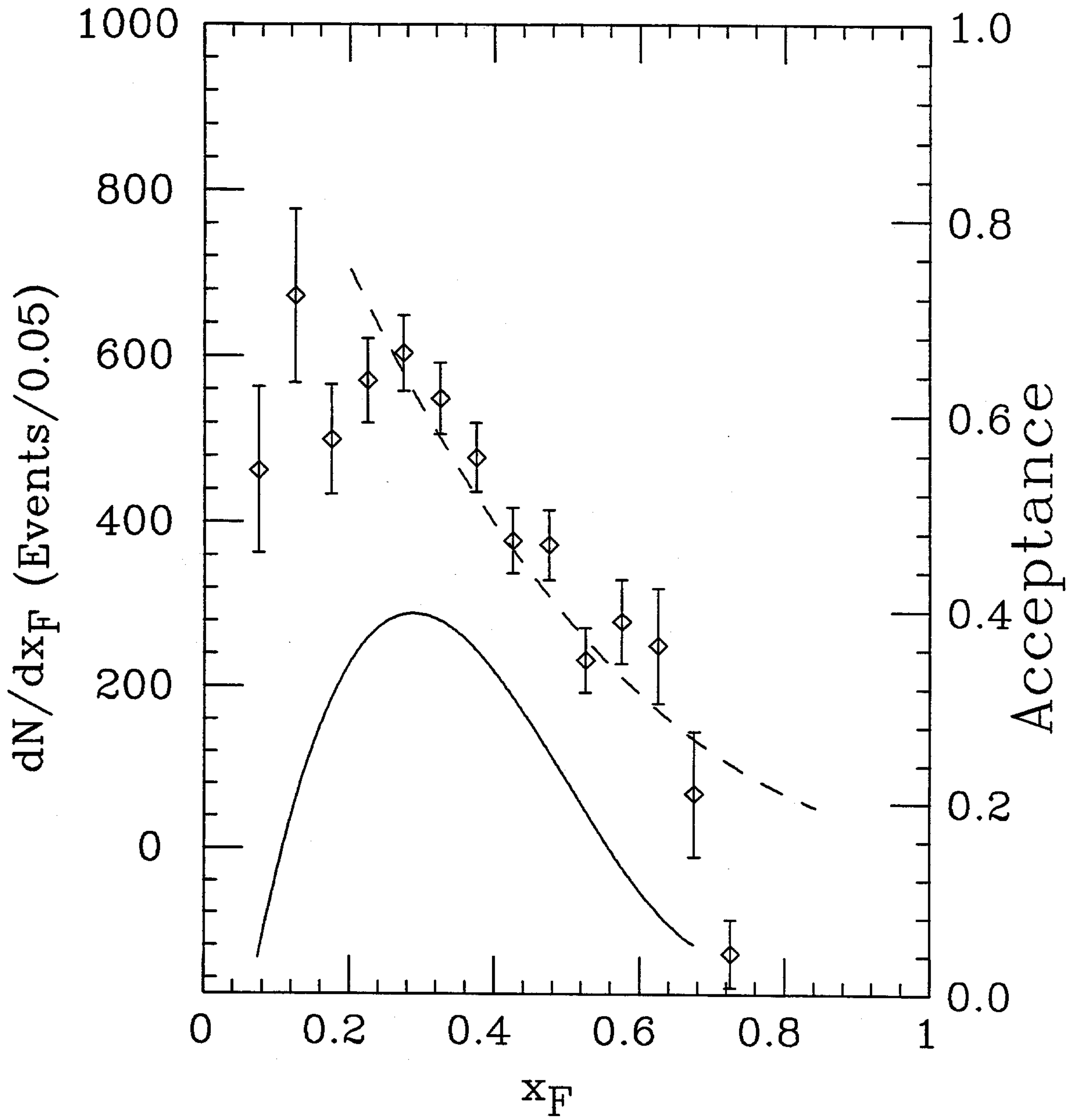
1000
800
600
400
200
0
1.0
0.8
0.6
0.4
0.2
0.0
0
0.2
0.4
0.6
0.8
1
dN/dx_F (Events/0.05)
Acceptance
x_F

FIGURE 6.5.2

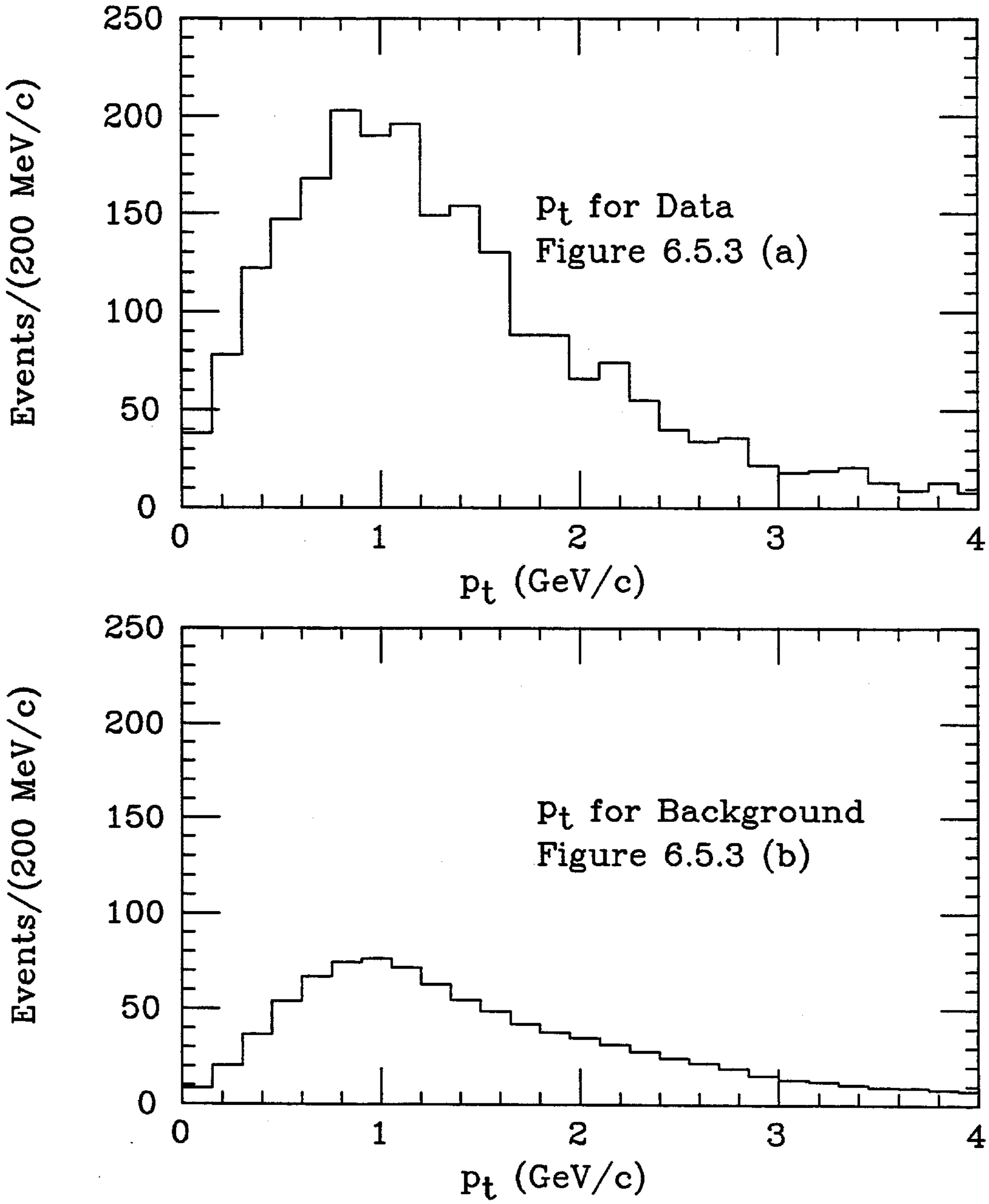
Events/(200 MeV/c)
0
50
100
150
200
250
0
1
2
3
4
p_t (GeV/c)
p_t for Data
Figure 6.5.3 (a)
p_t for Background
Figure 6.5.3 (b)

FIGURE 6.5.3

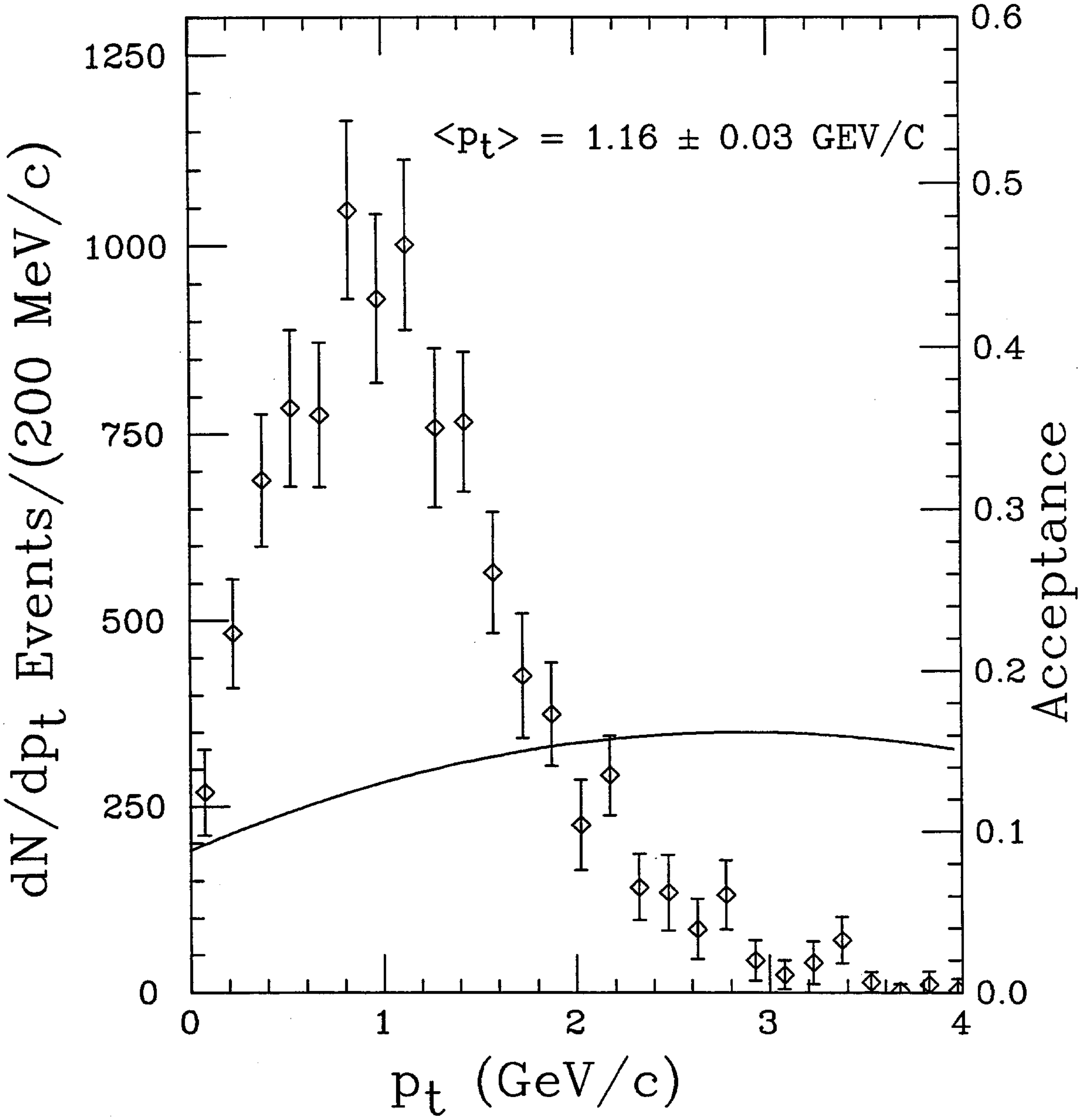

<pt> = 1.16 ± 0.03 GEV/C
dN/dpt Events/(200 MeV/c)
Acceptance
pt (GeV/c)
1250
1000
750
500
250
0
0.6
0.5
0.4
0.3
0.2
0.1
0.0
0
1
2
3
4

Figure 6.5.4

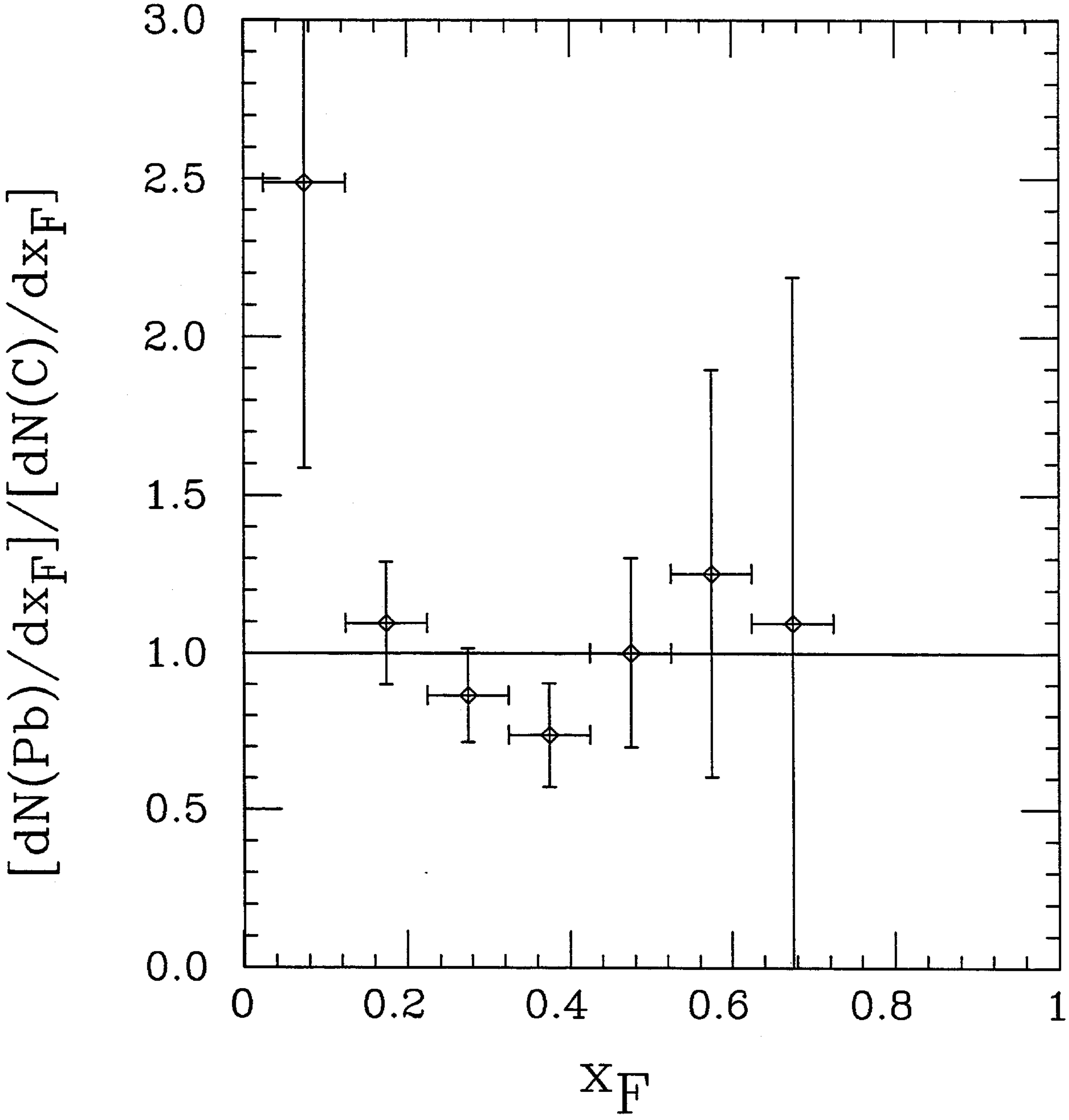

FIGURE 6.5.5

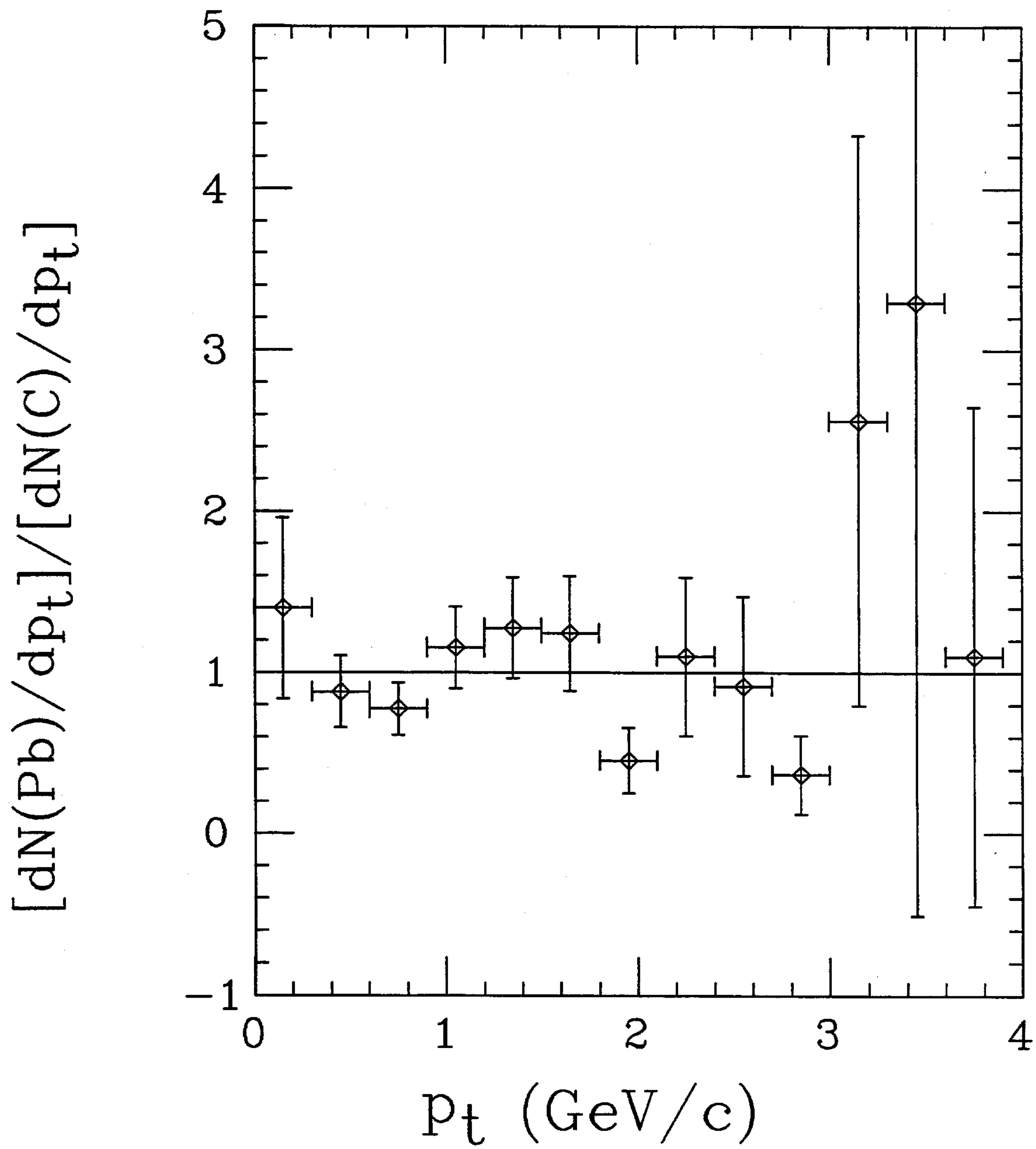

FIGURE 6.5.6

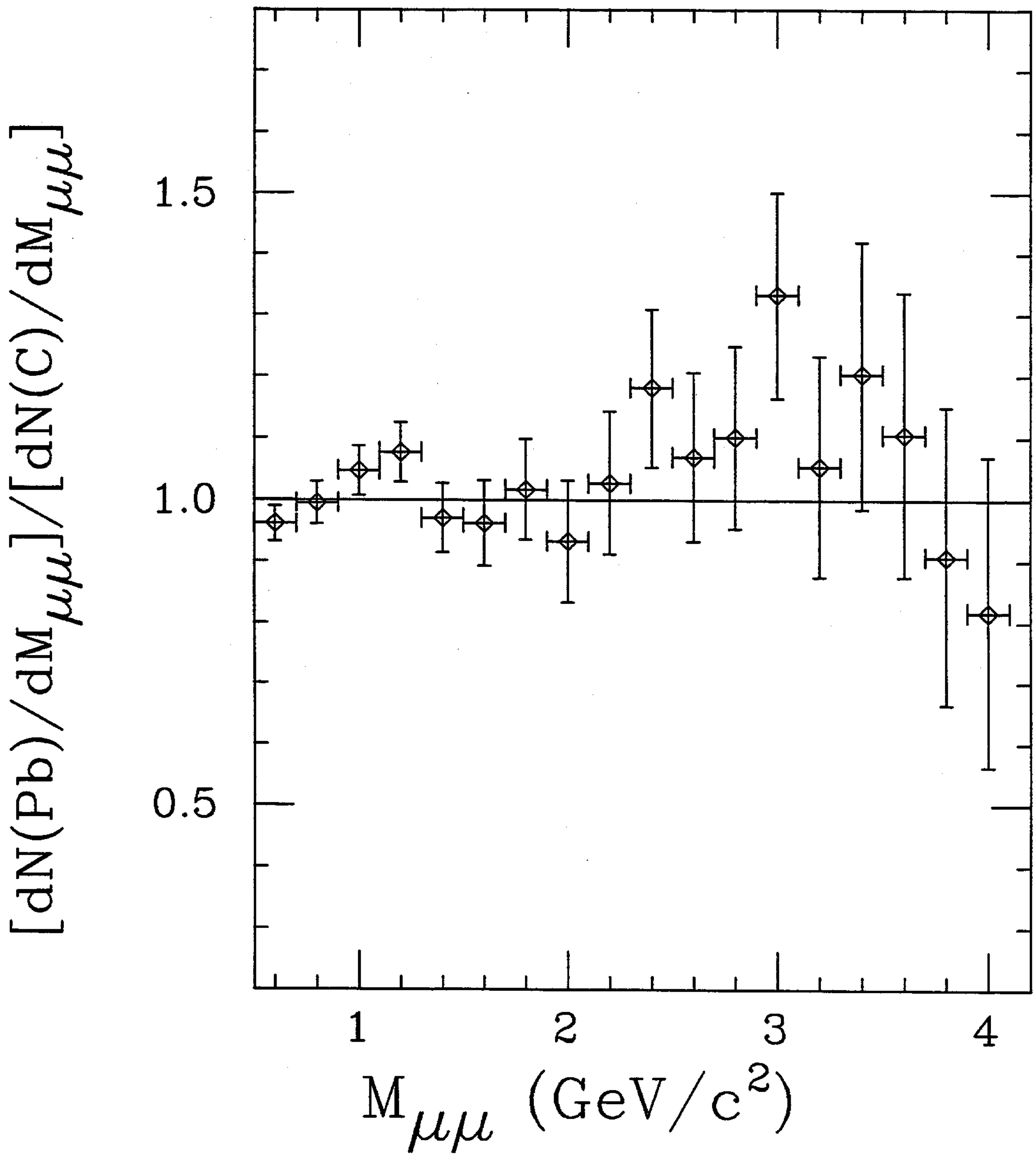

FIGURE 6.5.7

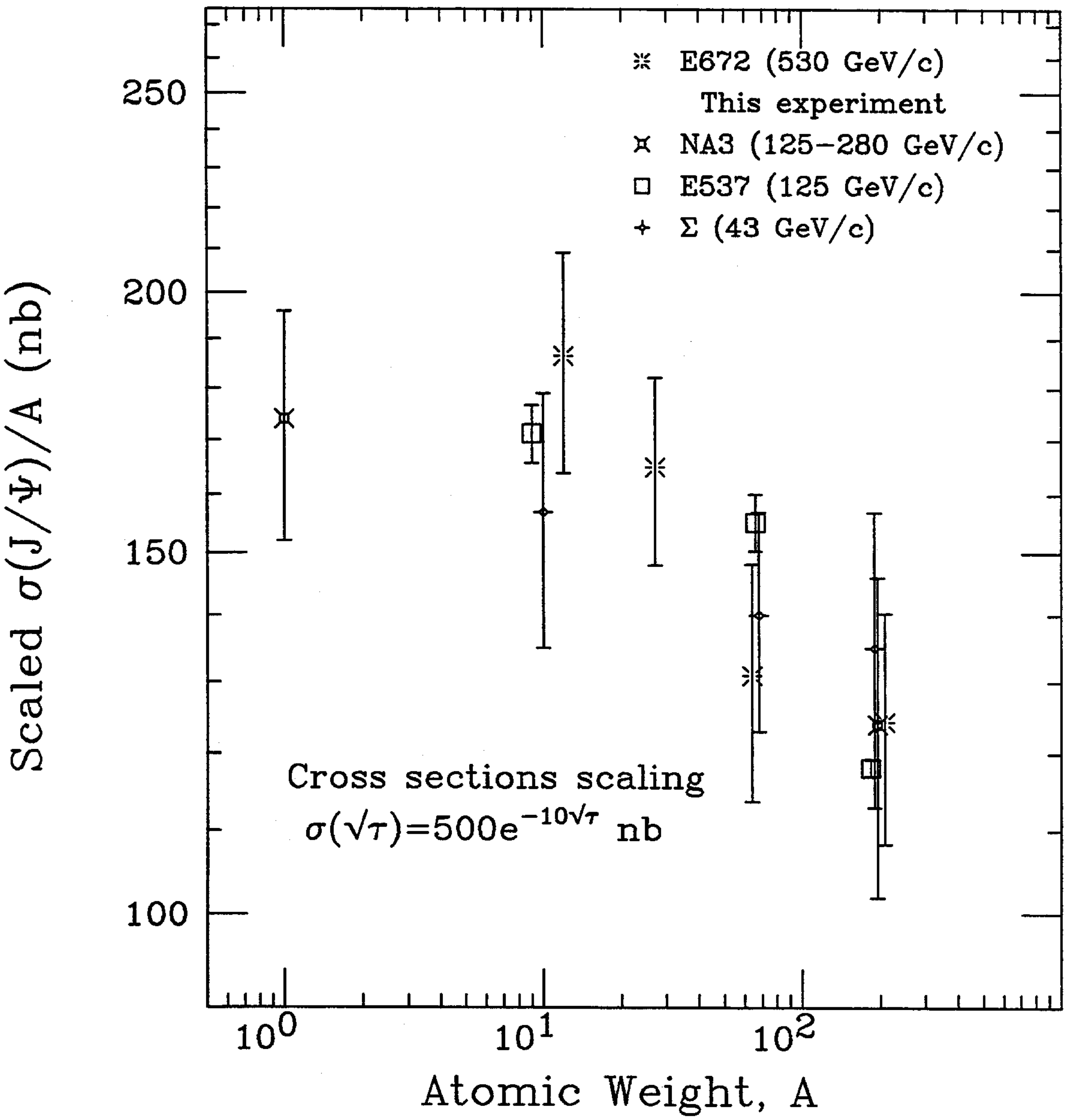
E672 (530 GeV/c)
This experiment
NA3 (125-280 GeV/c)
E537 (125 GeV/c)
Σ (43 GeV/c)
Cross sections scaling
$\sigma(\sqrt{\tau})=500e^{-10\sqrt{\tau}}$ nb
Scaled $\sigma(J/\Psi)/A$ (nb)
250
200
150
100
10^0
10^1
10^2
Atomic Weight, A

FIGURE 6.5.8

CHAPTER 7
DATA REDUCTION FOR VECTOR MESON ANALYSIS

The reconstruction of data collected in the 1987-88 run of E672, when information from the E706 spectrometer was available, is described in this chapter.

The first section of this chapter describes the data collected and its reduction by a factor of 5 by track reconstruction using the muon spectrometer. The next section describes the algorithm and results from linking the muon system tracks with tracks in the upstream PWC's and Silicon Strip Detector. The third section presents some of the general features of the data after complete track reconstruction.

Section 7.1

7.1.1 Description of the data

Data were collected using targets of beryllium, carbon and copper with beams of 530 GeV/c protons and π^-'s. The trigger for this period of running was the SUCCESS signal from the Dimuon Trigger Processor (see Chapter 4). Approximately 2×10^6 triggers were written to magnetic tape. The description of running conditions like targets, beam types etc. are described in detail elsewhere.[1]

The dimuon trigger processor mass threshold was adjusted such that E672 was contributing to about 30 % of the total number of triggers.

7.1.2 Data reduction and preselection

The E672 triggers were processed through a track reconstruction program for the muon PWCs, written by J. Martin.[2] The algorithm first looks for clusters (defined as a group of contiguous hits) in each of the 12 planes (u,v and w) for the 4 muon chambers. The center of the cluster is then associated with an width which is half the cluster width. For each view, a search is done for sets of clusters in the four view planes consistent with being on a narrow (the width of the road is an adjustable parameter in the reconstruction process; this width was optimized to 1/5 the wire spacing) road in the fiducial volume of the muon chambers.[3] The road is found by a binary search of all possible roads. Such sets of clusters are tagged as view track candidates. Figures 7.1 and 7.2 show the construction of the roads in the first step of the binary search.

The search is continued for other groups of clusters that are consistent with being on a view road, with at least one of the clusters in the combination being different from the combinations flagged earlier. Some of the clusters are eliminated at this stage due to lack of a sufficient number of hits on possible roads due to various reasons.[3]

Next, a binary search of space roads is performed to find space tracks. Space roads are constructed and checked to see if a set of view tracks are consistent with belonging to a space road, where a view track is considered as a straight line segment formed from the hits. The subdivision and search is continued, and if view tracks in all three views are consistent with belonging to a given space road with a road width much smaller than the wire spacing, the clusters belonging to these view tracks are flagged as being part of a space track. The pattern recognition algorithm at this stage reduces the data sample by a factor of 2 due to elimination of events without enough clusters.

7.1.3 Determination of the muon trajectory

The equations describing the muon track in the x and y views[2] , constraining its origin to be in the target and having a radial bend angle in the toroid, are:

$$x = a + bz; \quad z \geq z_t \tag{7.1}$$

$$y = c + dz; \quad z \geq z_t \tag{7.2}$$

and

$$x = a + bz + \phi_t \frac{x_t}{r_t}(z_t - z); \quad z_d \leq z \leq z_t \tag{7.3}$$

$$y = c + dz + \phi_t \frac{y_t}{r_t}(z_t - z); \quad z_d \leq z \leq z_t \tag{7.4}$$

and

$$x = a + bz + \phi_t \frac{x_t}{r_t}(z_t - z) + \phi_d(z_d - z); \quad z \leq z_d \tag{7.5}$$

$$y = c + dz + \phi_t \frac{y_t}{r_t}(z_t - z); \quad z \leq z_d \tag{7.6}$$

where the first set represents the trajectory in the muon system, the second the trajectory between the dipole and the toroid and the third upstream

The linking procedure is illustrated in Figure 7.3. Figure 7.4 and 7.5 show the distributions of θ_x^{ms} and θ_y^{ms} respectively for tracks linked through the SSD, E706 PWCs and the MUON systems (SSD-PWC-MUON tracks). The χ^2 distribution for SSD-PWC-MUON linked tracks is plotted in Figure 7.6. The distributions for the signed inverse momentum $(1/p)$ from fits using the MUON, PWC-MUON and SSD-PWC-MUON fits is compared in Figure 7.7. The peak at zero for the MUON fit distribution contains halo muon tracks, which are assigned very high momenta. Including the PWC and the SSDs in the fit removes the halo contribution to the distributions.

Halo muons are identified and rejected[4] at this stage as they have an unacceptable χ^2 .

7.2.3 Determination of the vertex

The vertex search is done using the tracks which have an SSD-PWC link, for which the slope and intercept parameters are known. The algorithm[5] minimizes the distance of closest approach of the tracks to the vertex. A χ^2 is formed as the sum of these distances, in terms of the residuals from the vertex coordinates, and minimized to give the vertex. The track from the beam SSD's is included in the minimization on the same footing as the other tracks.

The information from the tracks that result from the reconstruction is condensed into data summary files which are the basis for the physics analysis.

Section 7.3

7.3.1 General features of the reconstructed data

Out of the approximately 2×10^6 triggers recorded, about 10^5 events were reconstructed with a dimuon, where the muons at least had a link between the muon PWCs and the E706 PWCs. The performance of several hardware devices is described elsewhere[6]. Table 7.3.1 gives a summary of the number of events and results of dimuon selection for positive and negative beams.

TABLE 7.3.1

Event summary of reconstructed data

Selection criterion	Positive beam	Negative beam
2 tracks in the MUON system	43500	61579
2 PWC-MUON linked tracks	31266	47291
1 PWC-MUON linked $\mu^+\mu^-$ pair	20746	30457
1 SSD-PWC-MUON linked $\mu^+\mu^-$ pair	15143	22417

7.3.2 Vertex reconstruction

The targets used for data analysis are the Beryllium , Carbon and Copper[1]. Figure 7.8 shows the distribution of the z-coordinate of the vertex to illustrate the segmentation of the targets. The copper and beryllium slices can be clearly distinguished from each other The SSD planes can also be seen clearly. The inset plot shows the vertex radius (distance from the origin) plot.

of the dipole. Here z_d is the z-coordinate of the center of the dipole magnet, and ϕ_d is the bend angle in the dipole; z_t is the z-coordinate of the center of the toroid and ϕ_t is the bend angle in the toroid, and $r_t = (x_t^2 + y_t^2)^{1/2}$ is the radius of the track at the toroid midplane.

The trajectory is determined completely by the five parameters a,b,c,d and ϕ_t. The other variables can be expressed in terms of these parameters and constants of the spectrometer. The dipole bend angle ϕ_d can be expressed in terms of ϕ_t as

$$\phi_d = \frac{p_{kd}}{p} \quad \text{and} \quad \phi_t = \frac{p_{kt}}{p - \zeta} \tag{7.7}$$

which gives

$$\phi_d = \delta_\pm \cdot \phi_t \frac{p_{kd}}{p_{kt}} \cdot \left[\frac{1}{1 + \frac{\zeta |\phi_t|}{p_{kt}}} \right] = h_d \phi_t \tag{7.8}$$

Here p is the momentum of the particle, p_{kd} and p_{kt} are the momentum impulses imparted by the dipole and the toroid respectively, and ζ is the energy loss in the calorimeters and the first half of the toroid.

The relative polarity of the dipole and the toroid determines the factor $\delta_\pm$ ($\delta_\pm = 0,\ \pm 1$; which is 0 if the dipole is off and, for example, +1 if the particle is bent outward in the toroid and towards the positive x axis by the dipole.)

The parameters are found by minimizing the χ^2

$$\chi^2 = \sum_{k=1}^{N} w_k(x_k \cos\theta_k + y_k \sin\theta_k - u_k^\star)^2 \tag{7.9}$$

where $u_k^\star$ is the hit in the plane k and θ_k is the angle between the measurement axis and the x axis for the muon and D-station PWCs. The sum over the PWC's also includes the vertex (x_v, y_v, z_v) as a 2-plane station. Here $w_k = 1/\sigma_k^2$. So one can write

$$u_k = x_k \cos\theta_k + y_k \sin\theta_k = (a + bz_k)\cos\theta_k + (c + dz_k)\sin\theta_k + g_k\phi_t \tag{7.10}$$

with

$$g_k = \begin{cases} 0 & \text{if } z_k \geq z_t; \\ (x_t \cos\theta_k + y_t \cos\theta_k)\dfrac{(z_t - z_k)}{r_t} & \text{for } z_d \leq z_k \leq z_t; \\ (x_t \cos\theta_k + y_t \sin\theta_k)\dfrac{(z_t - z_k)}{r_t} + h_d(z_d - z_k) & \text{for } z_k \leq z_d. \end{cases} \tag{7.11}$$

g_k is a slowly varying function of the parameters. The χ^2 is minimized by treating it as a linear function of the parameters and iterating; i.e. recalculating g_k using parameter values found in the previous step. Tracks with large χ^2's, (greater than 1.5/degree of freedom) are rejected.

Events which had at least two muons surviving the vertex fit separated out for further reconstruction and analysis. The overall reduction factor from the uncut data to this level is a factor of 5. The accepted tracks are referred to as MUON tracks, and the fit as the MUON fit.

Section 7.2

7.2.1 Linking MUON and PWC tracks

The tracks seen in the PWC's and the SSD's are now linked with the muons in the E672 system. View tracks are found in the E706 PWC's (in the region between the dipole and the LAC) as for the muon system. A space road search is done and suitable candidates are retained as space track candidates, and their x-y view slopes and intercepts determined by a straight line fit.

These tracks are then projected to the toroid to select candidates which have a possibility of linking to the track in the muon system. A wide road of about 20 cm width is considered for this purpose to allow for multiple scattering in the material between the muon system and the E706 PWC's.

Four slope and intercept parameters and their error matrix describe the track segment in each of the systems, giving a total of 8 parameters to describe the linked track. In addition, we have the parameters $1/p$ (the inverse momentum of the track) , and $\theta_x^{ms}, \theta_y^{ms}$, the multiple scattering angles in the x and y views respectively. Out of the total of 11 parameters, only 7 are independent, as we can express the remaining 4 (the parameters in the muon system) in terms of these 7.

A χ^2 fit is done demanding consistency between the momentum assigned, the multiple scattering angles (the angles themselves are constrained to have a central value of zero and an error which depends on the momentum of the track, so the errors are related to the momentum by constraint equations) and the energy loss, demanding that the tracks have a bend which is radial in the toroid. Tracks which give an unacceptable χ^2 per degree of freedom (greater than 2) are rejected. The accepted tracks are referred to as PWC-

MUON tracks, and the fit as the PWC-MUON fit.

7.2.2 SSD-PWC-MUON linking for muon tracks

Next, the SSDs are included in the determination of the track parameters and the momentum. View track candidates are found in the SSD planes and space tracks determined by road searches described in the preceeding sections. link candidates are found by checking to see if there are any linked tracks with the same y-slope upstream and downstream of the dipole.

For such a set of track segments in the SSD, PWC's and the MUON system, we have 12 slope-intercept parameters, two equations for the multiple scattering angle errors and one equation connecting the inverse momentum at the toroid and at the dipole,, giving a total of 15 measured quantities. Out of these, the independent parameters allowed to vary are the slope-intercept parameters in the SSD's(4), the two multiple scattering angle errors, and the inverse momenta at the toroid and dipole, giving a total of 8 parameters. The remaining 7 can be expressed in terms of these. The χ^2 for this track is formed as

$$\chi^2 = (\vec{\mathbf{X}} - \mathbf{A}\vec{\mathbf{P}})^{\mathbf{T}} \cdot \mathbf{E}^{-1} \cdot (\vec{\mathbf{X}} - \mathbf{A}\vec{\mathbf{P}}) \tag{7.12}$$

where $\vec{\mathbf{X}}$ is a 15- element vector with the measurements, $\vec{\mathbf{P}}$ is the vector with the 8 parameters and $\mathbf{A}$ is the matrix (15×8) which connects the measurements with the independent parameters. $\mathbf{E}$ here is the error matrix for the measurements. Minimizing this χ^2 gives the track parameters and the momentum. This fit is referred to as the SSD-PWC-MUON fit, and the tracks as SSD-PWC-MUON tracks.

7.3.3 Characteristics of SSD-PWC-MUON linked tracks

The information for the non-muon tracks is as reconstructed by the E706 reconstruction program PLREC which is a part of the overall E706 reconstruction package MAGIC.[7]

The momentum distributions for muons is shown in Figure 7.9, and that for non-muons is shown in Figure 7.10.

The momentum error distributions for muons is shown in Figure 7.11. A scatter plot of the fractional error $\delta p/p$ is shown as a function of the muon momentum p. The plot shows two distinct bands with different slopes. The band with the smaller slope (better momentum resolution) corresponds to the tracks with an SSD-PWC-MUON link while the other band is for tracks with only a PWC-MUON link. The momentum resolution, described by the straight line for the lower edge of the bands, is

$$\frac{\delta p}{p} = 0.05\% p(GeV/c) \tag{7.13}$$

and the slope is twice that for the other band .

Figure 7.12 shows the analogous plot for the momentum resolution of non-muon tracks.

REFERENCES

1) S. Kartik, E672 technical note E672/91-3 Section 1.1

2) Fits to Muon Track Data. J. Martin. E672 Note 220. 1987

3) S. Kartik, E672 technical note E672/91-3 Section 1.2

4) S. Kartik, E672 technical note E672/91-3 Section 1.4

5) S. Kartik, E672 technical note E672/91-3 Section 2.3

6) S. Kartik, E672 technical note E672/91-3 Section 3.2

7) Structure of events containing Direct Photon or Neutral Pion in Hadronic Interactions., S. Easo. Ph.D Thesis. Penn. State University. 1989

FIGURE ILLUSTRATING THE ALGORITHM FOR FINDING VIEW TRACKS USING ROADS

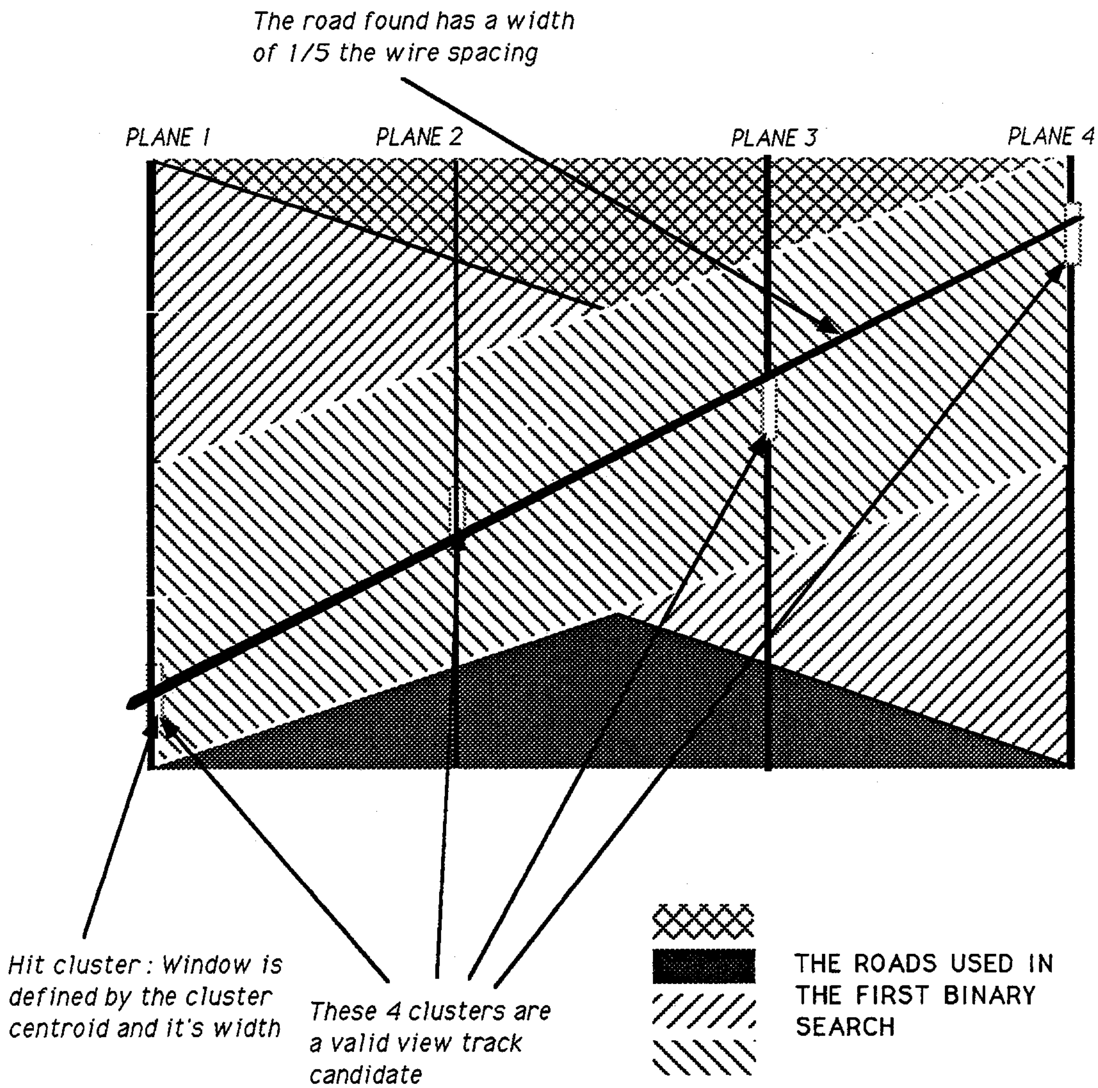

FIGURE 7.1

EXPLODED VIEW OF ROADS IN VIEW TRACK FINDING

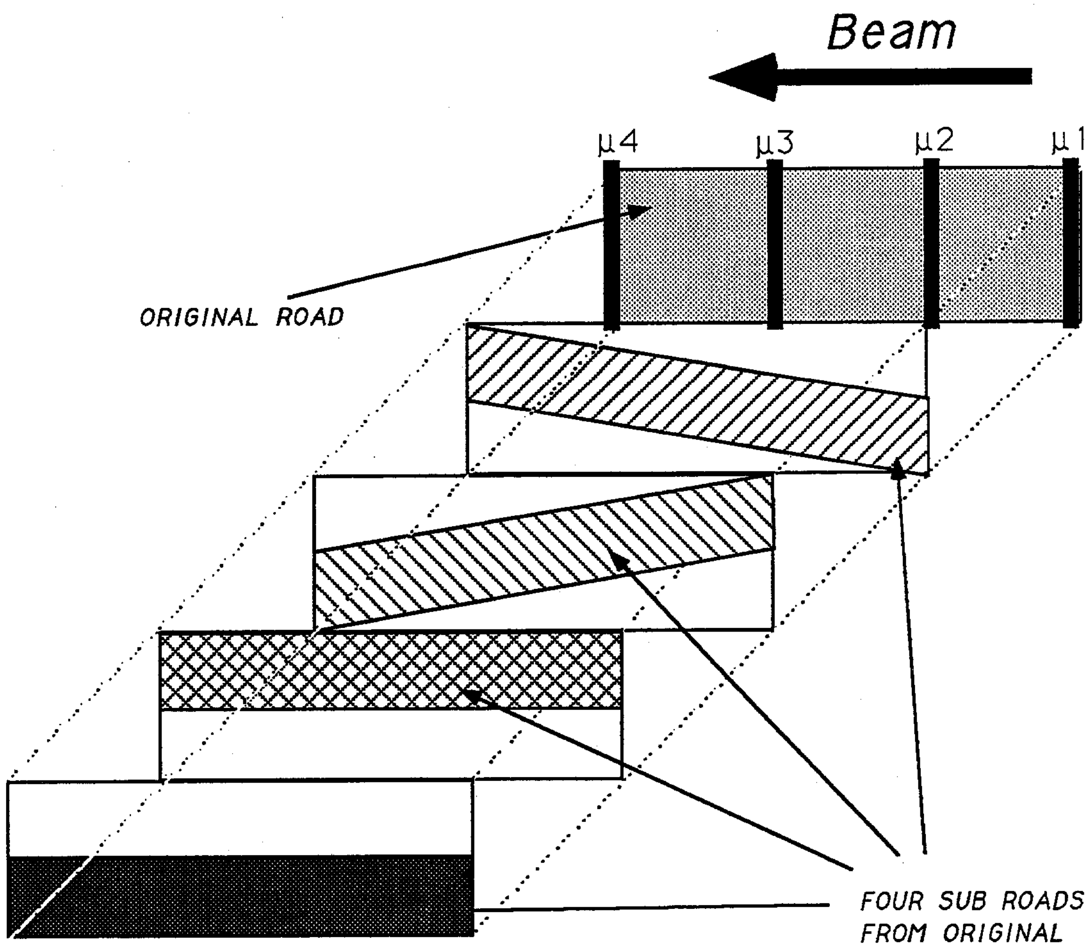

FOUR POSSIBLE ROADS
FROM THE ORIGINAL
ROAD

FIGURE 7.2

LINKING ALGORITHM FOR MUON TRACKS

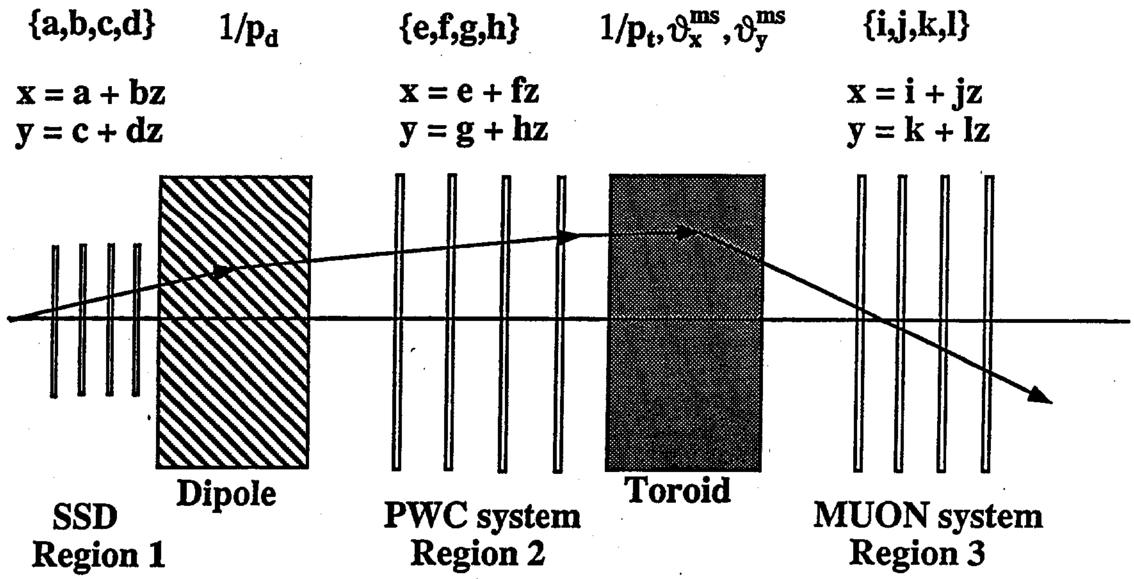

-- 12 slope-intercept measurements: {a,b,c,d,e,f,g,h,i,j,k,l}

-- 2 measurement equations for the multiple scattering errors

-- 1 equation connecting the dipole and toroid momenta

The 8 quantities which are allowed to vary are:

a,b,c,d, the 2 multiple scattering angles and the 2 inverse momenta.

15 quantities expressed in terms of 8 parameters and fitted to yield the track parameters and momentum.

FIGURE 7.3

Multiple scattering angle distribution for the SSD-PWC-MUON linked tracks

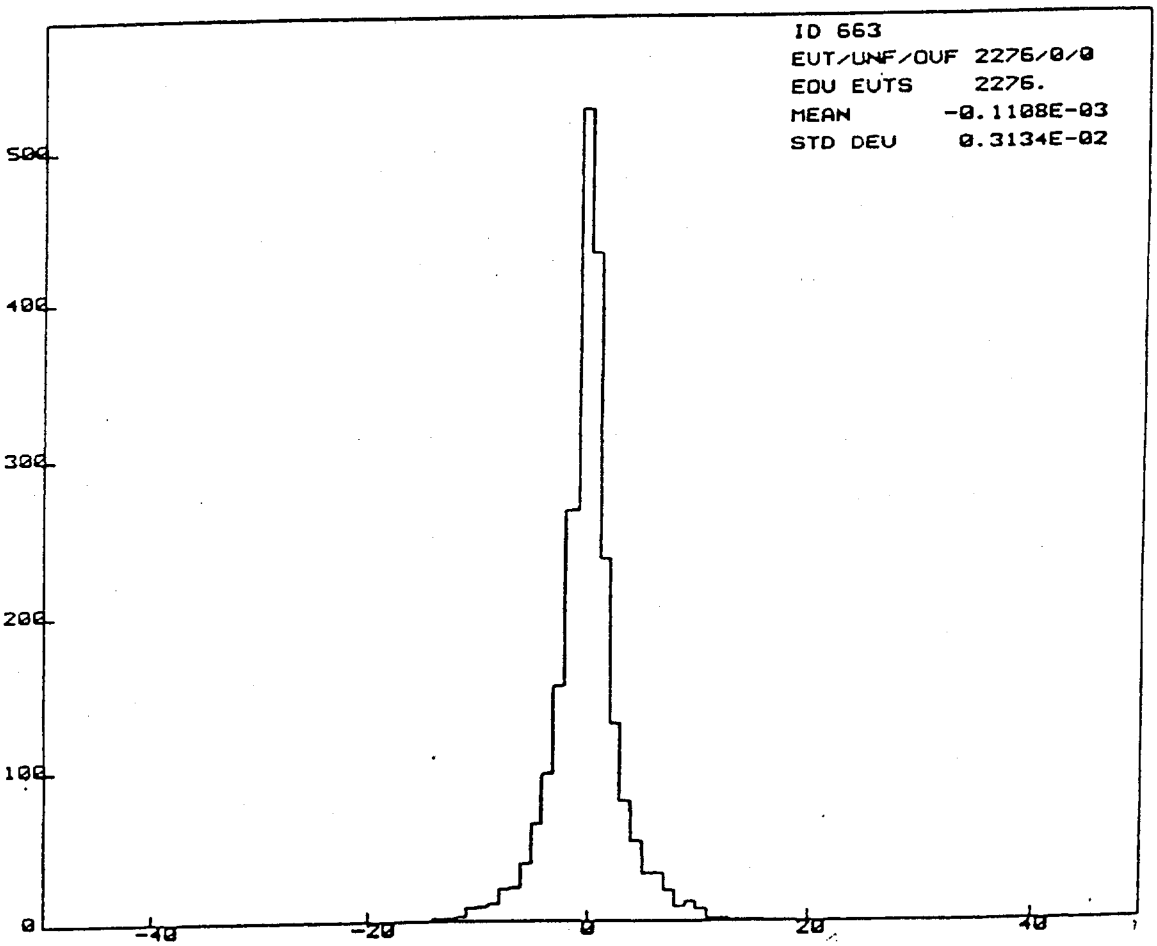

ϑ_x^{ms} in milliradians

FIGURE 7.4

Multiple scattering angle distribution for the SSD-PWC-MUON linked tracks

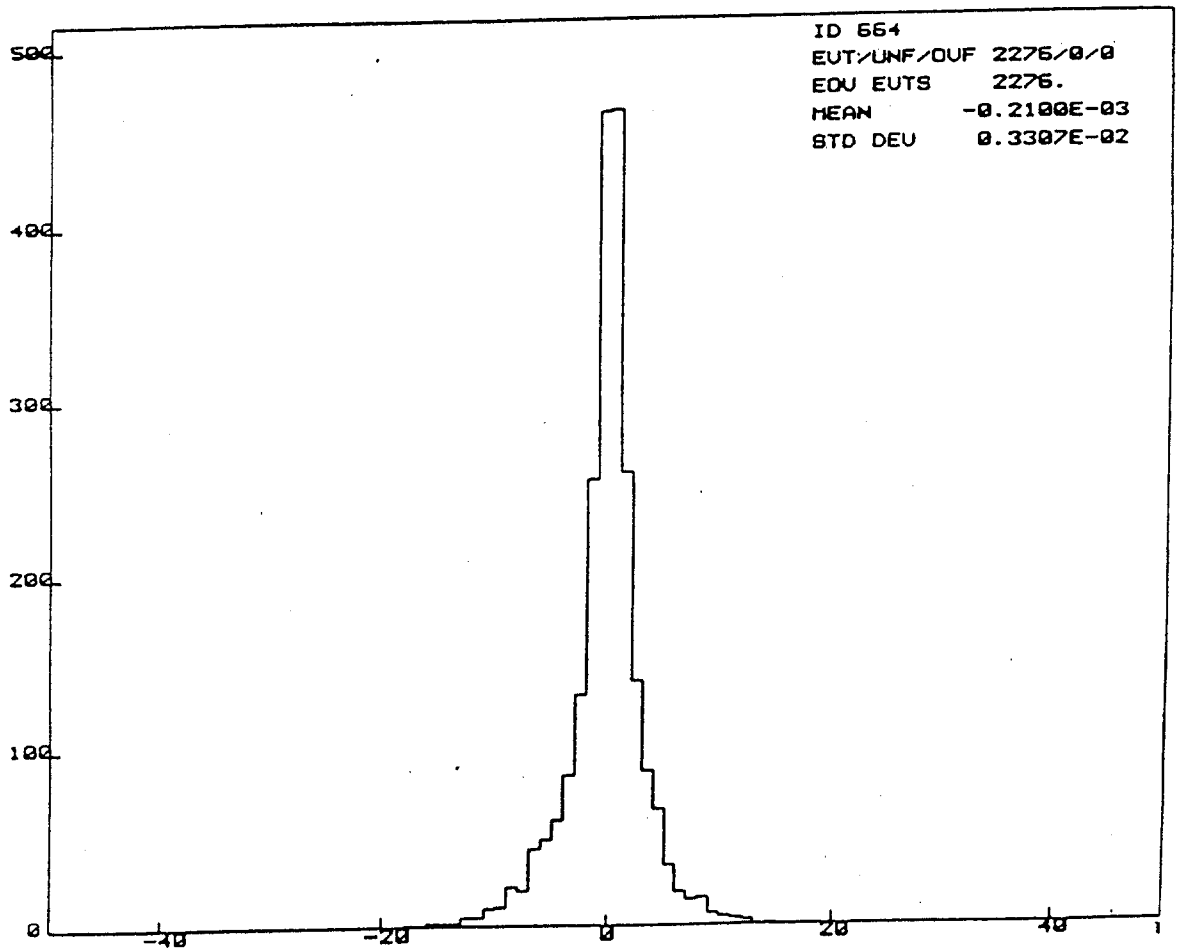

ϑ_y^{ms} in milliradians

FIGURE 7.5

Chisquared distribution for the SSD-PWC-MUON linked tracks

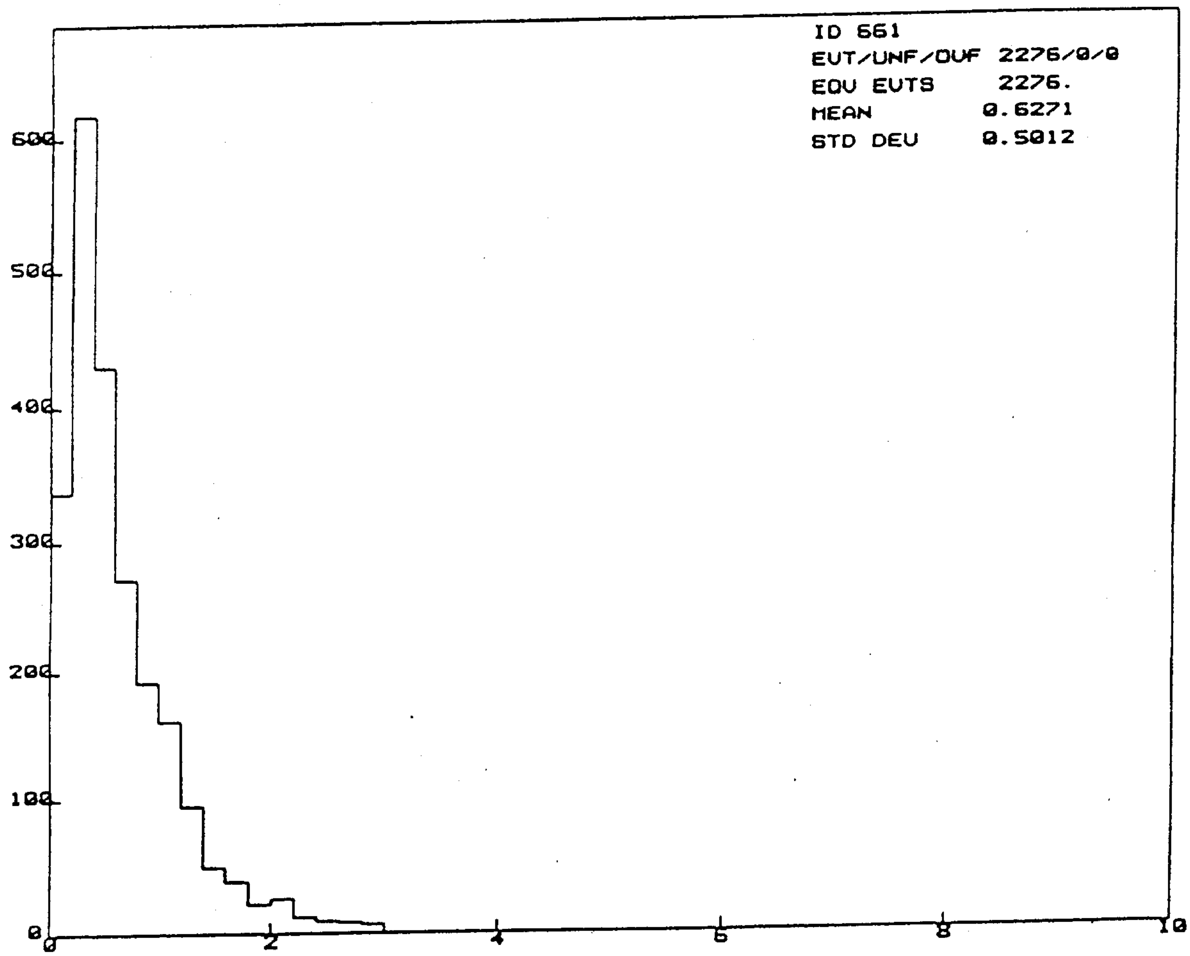

χ^2 for the track

FIGURE 7.6

COMPARISON OF INVERSE MOMENTUM DISTRIBUTIONS FOR VARIOUS FITS

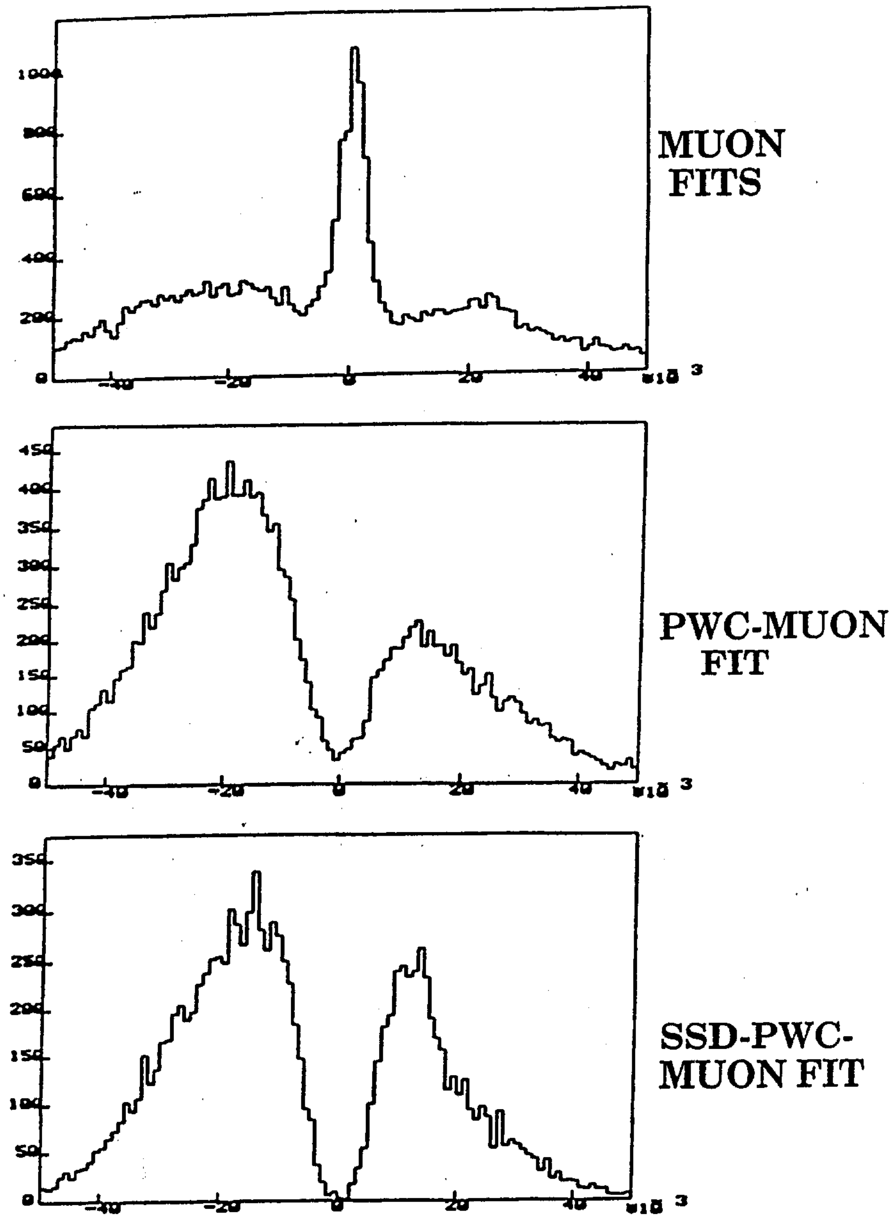

[Horizontal scale: .001/(GeV/c)]

FIGURE 7.7

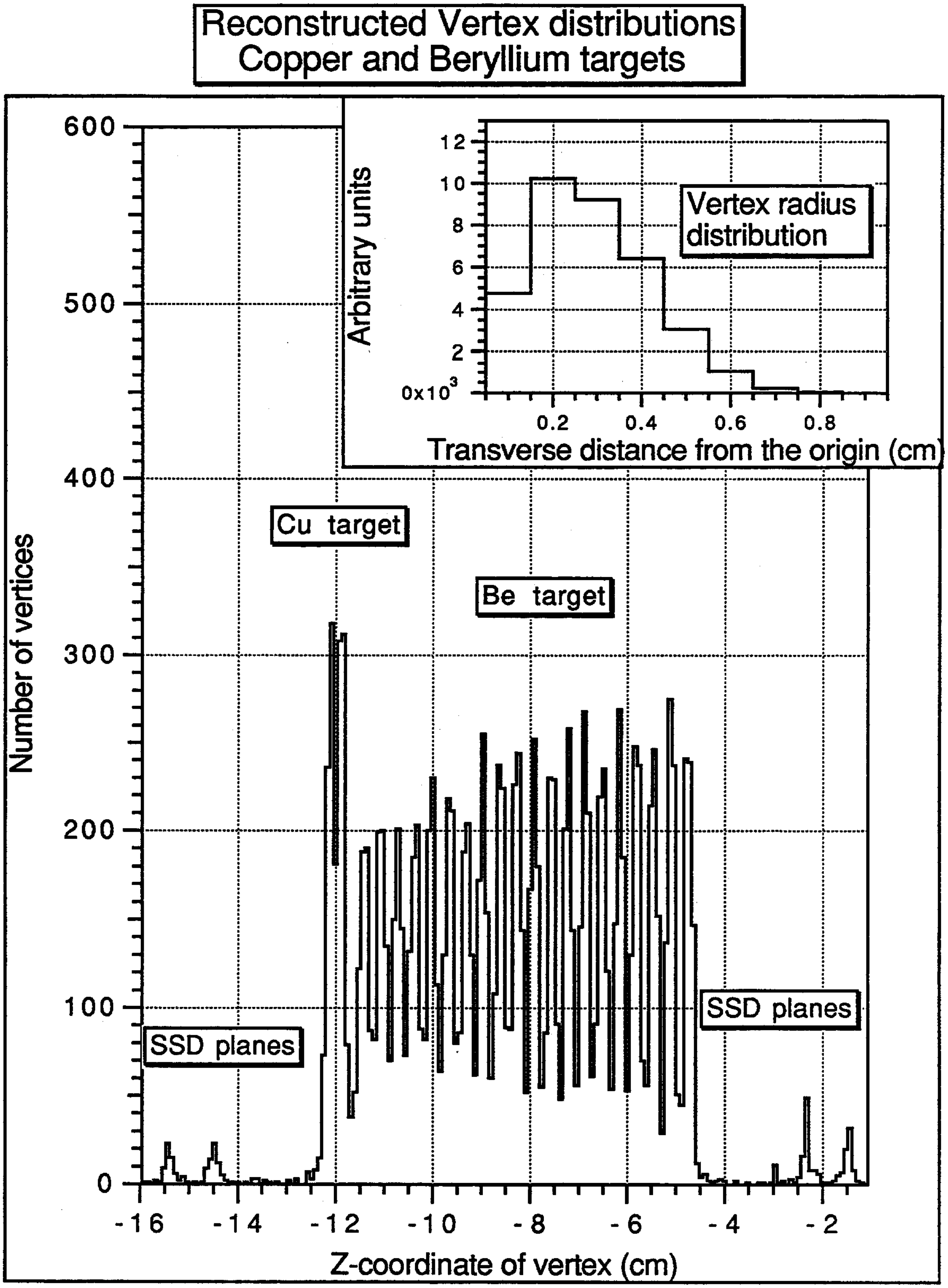
Reconstructed Vertex distributions
Copper and Beryllium targets
Number of vertices
600
500
400
300
200
100
0
-16
-14
-12
-10
-8
-6
-4
-2
Z-coordinate of vertex (cm)
Cu target
Be target
SSD planes
SSD planes
Arbitrary units
12
10
8
6
4
2
0x10³
0.2
0.4
0.6
0.8
Transverse distance from the origin (cm)
Vertex radius distribution

FIGURE 7.8

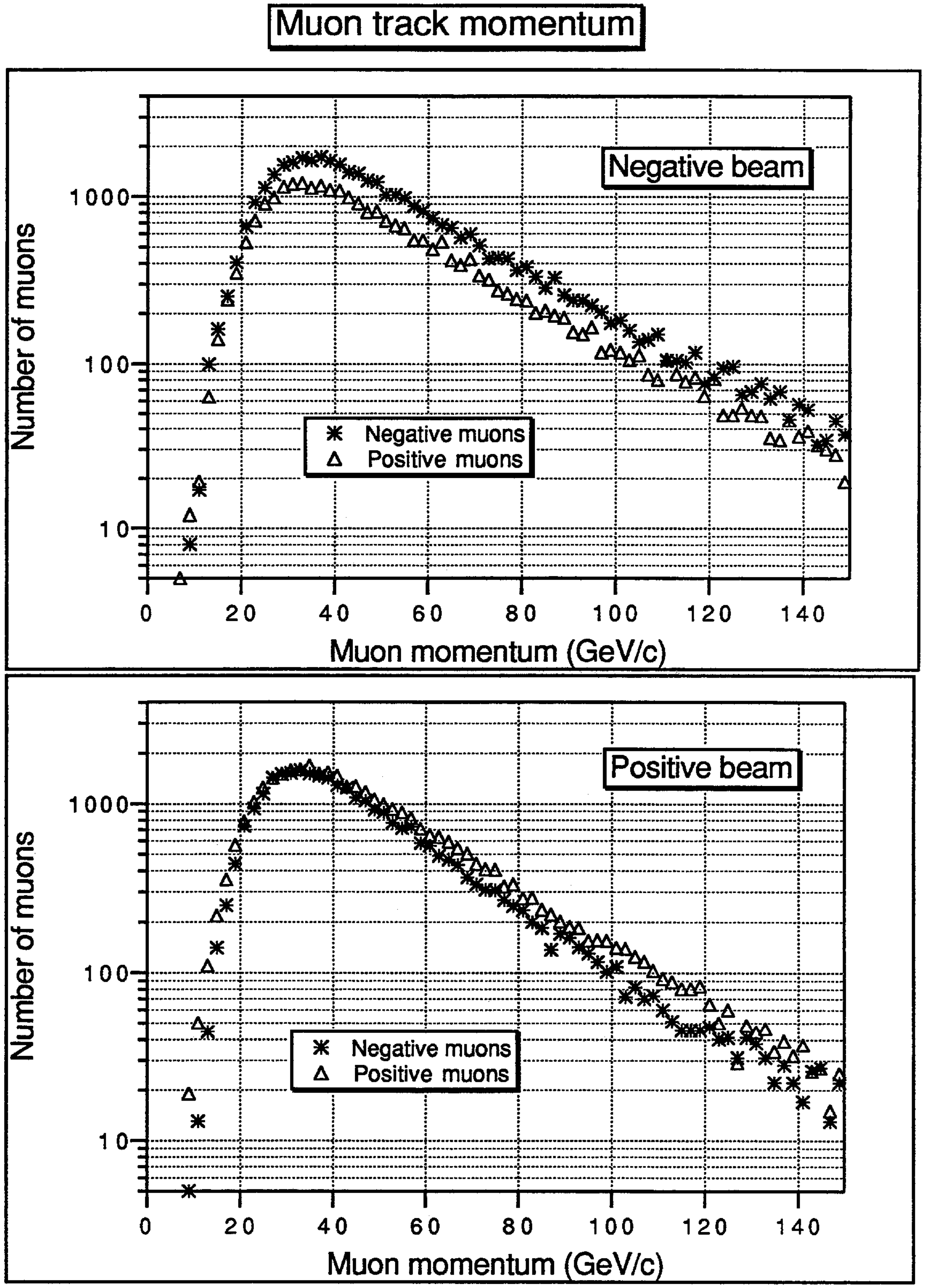
Muon track momentum
Negative beam
Number of muons
1000
100
10
Negative muons
Positive muons
0
20
40
60
80
100
120
140
Muon momentum (GeV/c)
Positive beam
Number of muons
1000
100
10
Negative muons
Positive muons
0
20
40
60
80
100
120
140
Muon momentum (GeV/c)

FIGURE 7.9

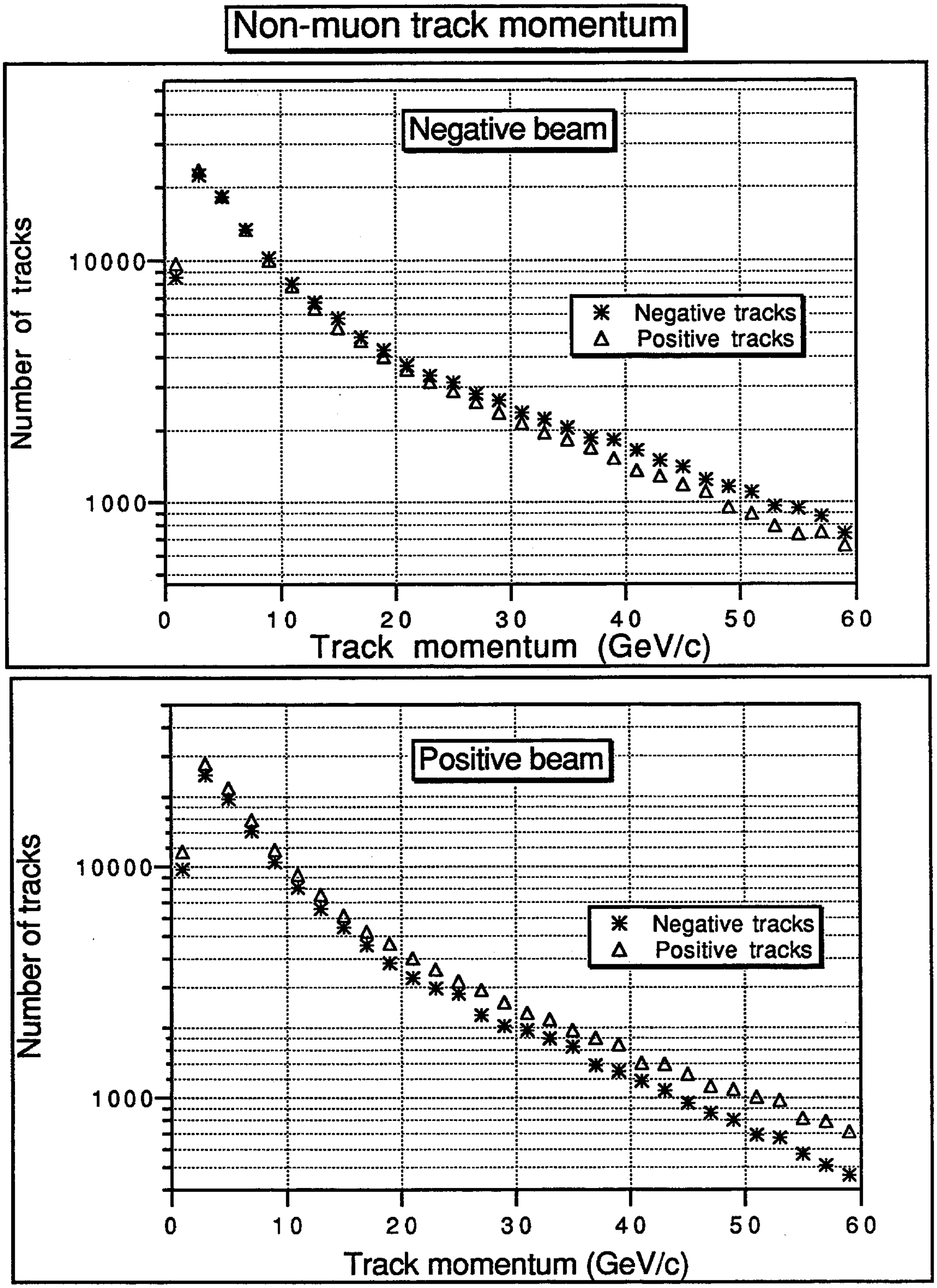

Non-muon track momentum
Negative beam
Number of tracks
10000
1000
Negative tracks
Positive tracks
0
10
20
30
40
50
60
Track momentum (GeV/c)
Positive beam
Number of tracks
10000
1000
Negative tracks
Positive tracks
0
10
20
30
40
50
60
Track momentum (GeV/c)

FIGURE 7.10

Momentum error distributions

E672 muon relative momentum error vs. momentum

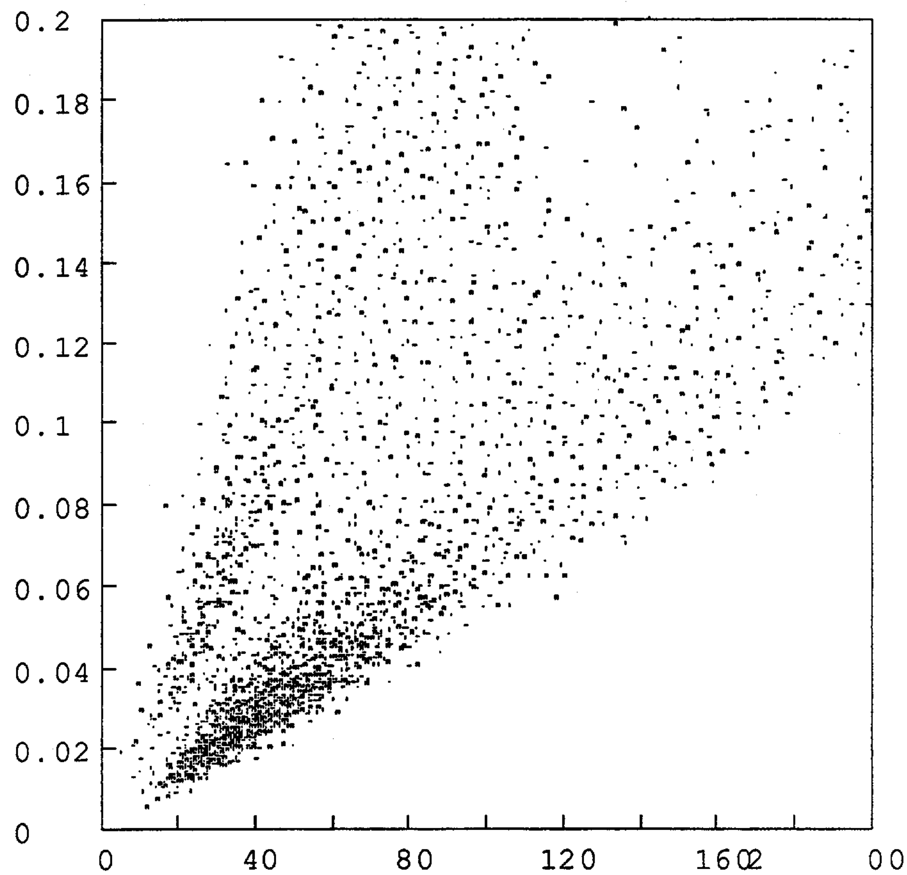

$\frac{\delta p}{p}$ vs p

The band with the smaller slope corresponds to SSD-PWC-MUON linked tracks and the other band to PWC-MUON linked tracks

FIGURE 7.11

Momentum error distributions

E706 non-muon track relative momentum error vs. momentum

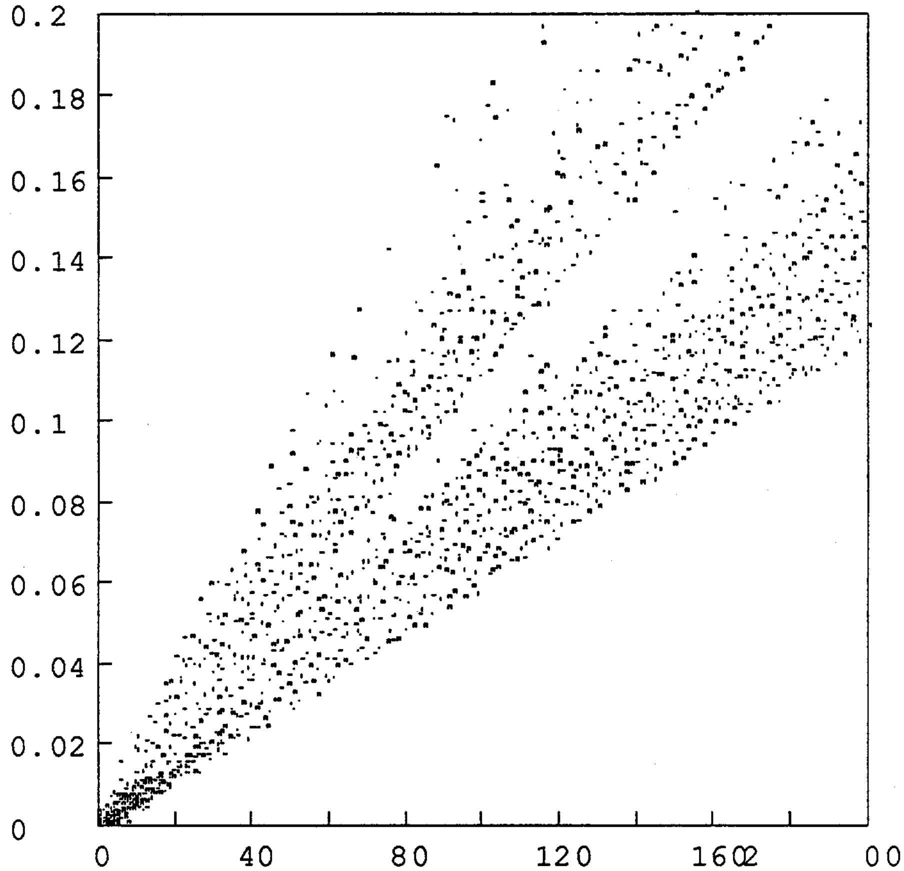

$$\frac{\delta p}{p} \text{ vs } p$$

The band with the smaller slope corresponds to SSD-PWC linked tracks and the other band to PWC tracks.

FIGURE 7.12

CHAPTER 8
VECTOR MESON CROSS SECTION CALCULATION

The vector mesons ρ^0, ω, ϕ and J/ψ are observed decaying into $\mu^+\mu^-$ pairs. The cross sections for the production of $\rho + \omega$ and ϕ is estimated in the forward region ($0.1 \leq x_F \leq 0.6$), and for the J/ψ in the region $0.1 \leq x_F \leq 0.8$.

Section 8.1

8.1.1 Properties of vector mesons and the data sample

The branching ratios for vector meson decays into dileptons are shown in Table 8.1.1 The value for the e^+e^- decay mode is used for ρ and ω cross sections, assuming $e - \mu$ universality.

TABLE 8.1.1

Leptonic Branching Ratios of Vector Mesons

Meson	Γ_{ee}/Γ_{all}	$\Gamma_{\mu\mu}/\Gamma_{all}$
ρ^0	$(4.42 \pm 0.21) \times 10^{-5}$	$(6.7 \pm 1.1) \times 10^{-5}$
ω^0	$(7.05 \pm 0.25) \times 10^{-5}$	$< 2 \times 10^{-4}$
ϕ^0	$(3.11 \pm 0.10) \times 10^{-4}$	$(2.48 \pm 0.34) \times 10^{-4}$
J/ψ	$(6.9 \pm 0.9) \times 10^{-2}$	$(6.9 \pm 0.9) \times 10^{-2}$

The known masses and intrinsic widths are listed in Table 8.1.2. The values for the branching ratios and the masses are taken from the Particle Data Table.[1]

TABLE 8.1.2

Vector Meson Masses and Widths

Meson	Mass (MeV/c^2)	Full Width (MeV/c^2)
ρ^0	768.3 ± 0.5	149.1 ± 2.9
ω^0	781.95 ± 0.14	8.43 ± 0.10
ϕ^0	1019.41 ± 0.01	4.41 ± 0.07
J/ψ	3096.9 ± 0.1	0.068 ± 0.010

The data sample used in the analysis is described in detail elsewhere[2] .

Section 8.2

8.2.1 General features of the dimuon sample

Around 60 % of the dimuons are unlike sign ($\mu^+\mu^-$) dimuons.[3] . Figure 8.1 shows the unlike sign dimuon invariant mass spectrum for the data. The invariant mass plots clearly show resonance structure; the ρ/ω at around 0.8 GeV/c^2, the ϕ at around 1 GeV/c^2 and the J/ψ at around 3.1 GeV/c^2. Only SSD-PWC-MUON linked muons (see Chapter 7) are used in the analysis, as resonance production is less evident[4] in dimuons which do not link all through the spectrometer.

8.2.2 Data cuts for cross section calculation

The following cuts are imposed on the data in this analysis:

1. **Vertex cut:** A vertex is required for all accepted events and cuts on the vertex z-position[5] are imposed to isolate the contribution from the Beryllium/Carbon target.

2. **Muon link cut :** Only muons with SSD-PWC-MUON links are used for cross section calculation.[5]

3. **Same Vertex cut:** Both the muons are constrained to come from the same vertex.

4. **χ^2-cut:**The χ^2 for the dimuon[6] . is constrained to be less than 2.0.

5. **x_F cut:**Due to the low acceptance for events with the dimuon Feynman-x $x_F < 0.1$ and $x_f > 0.6$, such events are rejected.

6. **p_t cut:**The transverse momentum of the dimuon for the ρ and ω resonances (p_t) is constrained so that $p_t \leq 1.6$ GeV/c due to limitations in Monte Carlo statistics

The event summary as a function of the cuts is tabulated in Table 8.2.1 The event sample is smaller than that used in ref.[24] as some of the earlier runs are disregarded in this analysis.

TABLE 8.2.1

Event summary as a function of cuts

Data cut	Positive beam	Negative beam
Events with a dimuon	29262	45630
$\mu^+\mu^-$ pair	17120	26123
SSD-PWC-MUON linked dimuon	12491	19122
Vertex in the target	11755	18402
Dimuon $\chi^2 \leq 2$	7626	11524
$0.1 \leq x_F \leq 0.6$	7241	10972
$p_t \leq 1.6$ GeV/c	6734	10204

8.2.3 Background estimation and subtraction

The background is estimated by mixing muons from different events and forming the invariant mass from these artificially created muon pairs.[7] . These background dimuons are subjected to the cuts used for the data. The background spectra are generated separately for both beam types. The background is scaled so as to have the same number of events in the mass region $1.3\ \mathrm{GeV}/c^2 \leq M_{\mu\mu} \leq 2.0\ \mathrm{GeV}/c^2$.

The background is shown superposed on the data after normalization in Figure 8.2 for negative beam. The resulting signal after background subtraction is also shown in Figure 8.2 . The same set of plots for positive beam are shown in Figure 8.3. For the purposes of cross section estimation, the following mass regions are used to define the resonance regions for the $\rho + \omega$ and ϕ.

$$\rho + \omega : 0.7 \leq M_{\mu\mu} \leq 0.9\ GeV/c^2 \tag{8.1}$$

and

$$\phi : 0.98 \leq M_{\mu\mu} \leq 1.06\ GeV/c^2 \tag{8.2}$$

The number of events in the resonance regions before and after background subtraction are presented in Table 8.3.1 for positive and negative beams.

TABLE 8.3.1

Number of events in the resonance regions

Number of events	Positive beam	Negative beam
$\rho + \omega$ mass region	3018 ± 50	2488 ± 50
Events above background	1804 ± 50	2776 ± 50
ϕ mass region	506 ± 23	474 ± 22
Events above background	309 ± 23	279 ± 17

Section 8.3

8.3.1 Monte Carlo simulations

Approximately 100,000 Monte Carlo events were generated, digitized (i.e. the hardware was emulated) and processed through the same software as the data for each resonance. Events were generated for each resonance decaying into a $\mu^+\mu^-$ pair with input x_F and p_t distributions[8] observed by other experiments. These dimuons were imbedded in a minimum-bias event which is generated in accordance to a Longitudinal Phase Space (LPS) model for associated hadron production.

These events are then processed through the detector simulation package GEANT[9] , which is a standard package from CERN. The response of the E672/E706 detector is then digitized, with the efficiencies, geometrical considerations and kinematic considerations (like energy loss, multiple scattering etc) folded into the response, into the same format as the data. These events are then processed through the chain of reconstruction programs as the real data. The general characteristics of Monte Carlo events are discussed elsewhere.[10]

The Monte Carlo mass plots are combined under the assumption that the ρ and ω are produced with equal cross sections [11–12] and compared with the data. The invariant mass plot after background subtraction is shown for positive and negative beam, with the Monte Carlo expectation[10] superposed on them, in Figure 8.4

8.3.3 Acceptances from Monte Carlo

The integrated acceptances, which fold in the inefficiencies of the hardware and losses due to reconstruction losses, are calculated for the vector mesons from the Monte Carlos. Table 8.3.2 gives the integrated acceptances for the forward x_F region, $x_F \geq 0$, and for the x_F region for this analysis 0.1 to 0.6. The acceptance is also given with all cuts imposed on the Monte Carlo, as for the data .

TABLE 8.3.2

Integrated acceptances for low mass vector mesons

Resonance	Acceptance $x_F \geq 0$	Acceptance $0.1 \leq x_F \leq 0.6$	Acceptance with all cuts
$\rho(770)$	0.0835	0.1356	0.0742
$\omega(783)$	0.0841	0.1377	0.0773
$\phi(1020)$	0.0902	0.1483	0.0873

The acceptance correction is done on a bin-by-bin basis (x_F-p_t^2 bin) for the data. The x_F-p_t^2 acceptance surface[13] is obtained for the data by dividing the accepted and generated surfaces from Monte Carlo. The $x_F - p_t^2$ surface for the data in the mass regions for the resonances is obtained with all cuts imposed. The data is then corrected for acceptance by weighing the data surface by the acceptance surface. The acceptance functions in x_F and p_t^2 for the $\rho + \omega$ and the ϕ are shown Figures 8.5.

8.3.4 Acceptance corrections to the number of events

It is assumed that the ratio of signal to background is the same for the data with and without acceptance correction. Knowing the signal-to-background fraction for each resonance region, the number of acceptance corrected background subtracted events is calculated so as to have the same ratio. The results of this procedure are presented in Table 8.3.4 for both beam types.

TABLE 8.3.4

Corrected events in the resonance regions

Number of acceptance corrected events	Positive beam	Negative beam
$\rho + \omega$ mass region	30947 ± 615	30484 ± 611
$\rho + \omega$ events above background	22101 ± 615	21757 ± 611
ϕ mass region	6094 ± 271	5405 ± 248
ϕ events above background	3721 ± 271	3199 ± 248

Section 8.4

8.4.1 Corrections for tail losses

The losses from the tails of the mass distributions due to the finite mass regions used to define the resonances is estimated from the Monte Carlo events. The ratio of Monte Carlo events is the reconstructed mass spectrum with and without the mass region cut are calculated. Table 8.4.1 presents this ratio for the vector mesons dealt with in this analysis.

TABLE 8.4.1

Resonance tail loss corrections

Resonance	Tail loss correction
ρ	0.72 ± 0.02
ω	0.88 ± 0.02
ϕ	0.68 ± 0.02

8.4.2 Resonance tail contamination losses

It is estimated that 1.5 % of the events in the background subtracted ϕ mass region are from the tails of the ρ mass distribution. The spectrum in the $\rho + \omega$ mass region also has events from the indirect decay mode $\rho \longrightarrow \pi\pi \longrightarrow \mu\mu$. It is estimated that the number of 'indirect' ρs is 13 % of the 'direct' ρs. The overall mass spectrum from Monte Carlo is augmented by the indirect mass spectrum in the fraction indicated, and the mass cut imposed to calculate the fraction of events which came from direct ρ and ω decays. This fraction is found to be 0.97 ± 0.04

The mode $\phi \longrightarrow KK \longrightarrow \mu\mu$ is not considered for this analysis. The number of ϕs showing up in the $\rho + \omega$ mass region from this channel is estimated to be less than 1 %.

8.4.3 Deconvolution of the ρ and ω contributions

The individual contributions from ρ and ω are estimated with the assumption the both the ρ and ω are produced with equal total cross sections, i.e. $\sigma(\rho) = \sigma(\omega)$.[11]

If the total number of events in the mass region is denoted by N_{Tot} and the number of events which come from direct decays of ρ/ωs is $N_{\rho/\omega}$ then

$$\frac{N_{\rho+\omega}}{N_{Tot}} = f_{\pi\pi} = 0.97 \pm 0.04 \tag{8.3}$$

where $f_{\pi\pi}$ is the fraction discussed in Section 8.4.2. Then we can write

$$N_{\rho+\omega} = f_{\rho} \cdot N_{rho} + f_{\omega} \cdot N_{\omega} \tag{8.4}$$

where N_{ρ} and N_{ω} are the true number of ρ's and ω's, and f_{ρ} and f_{ω} are factors that take into account the losses in the tails of the spectrum due to the mass cut, discussed in Section 8.4.1. The values used are $f_{\rho} = 0.72$ and $f_{\omega} = 0.88$.

Assuming that the ρ and ω cross sections are equal, the number of ω's is

$$N_{\omega} = \frac{N_{Tot} \cdot f_{\pi\pi}}{f_{\rho} + \frac{BR(\rho)}{BR(\omega)} \cdot f_{\omega}} \tag{8.5}$$

This gives $N_{\omega} = 0.76 \cdot N_{Tot}$ and $N_{\rho} = 0.48 \cdot N_{Tot}$.[14]

8.4.4 Preselection losses

It is found that about 31 % of the events are lost in the $\rho+\omega$ and ϕ mass region due to preselection of events with two tracks in the muon system.[15] The losses for the J/ψ region are smaller (6 %) than for the $\rho+\omega/\phi$ mass region.

8.4.5 Trigger processor losses

The trigger processor mass threshold was varied between 0.2 and 0.5 GeV/c^2 over the period of the run. The loss for the $\rho + \omega$ region with a threshold of 0.5 GeV/c^2 region is estimated to be 5 % and that for the ϕ region is 2%. This estimation was done by emulating the Dimuon Trigger Processor in the software and processing the Monte Carlo digitized data through the emulator.

In addition, it is found that around 8 % of the Monte Carlo events generated failed the trigger processor emulator software, and this is corrected for.

8.4.6 Total software corrections

The corrections described in Sections 8.4.1 thru 8.4.5 are summarized and an overall correction for the software ϵ_S calculated for each resonance. This is given in Table 8.4.2.

TABLE 8.4.2

Software correction

Correction	ρ	ω	ϕ
Tail losses and contamination	0.48	0.76	0.69
Preselection	0.76	0.76	0.76
Trigger processor software	0.92	0.92	0.92
Trigger processor threshold	0.95	0.95	0.98
ϵ_S	0.32	0.51	0.48

Section 8.5

8.5.1 Luminosity calculations

The cross section calculation requires estimation of the incident beam fluxes and the luminosity $\mathcal{L}$. The luminosity for the data taking for a given target and beam type can be written as:

$$\mathcal{L} = \frac{LIVEBEAM \times PROBINT}{\left[\sigma(A)/A\right]} \tag{8.6}$$

where

$LIVEBEAM$ = is the number of beam particles incident on the target with the experiment ready to accept a trigger.[16]

$PROBINT$ = the probability of interaction in that particular target with that beam type.

$\sigma(A)$ = the absorbtion cross section for the target nucleus with atomic weight A.

The probability of interaction ($PROBINT$) can be calculated knowing the thickness of the target and the interaction length[17] for the target for a particular beam hadron. For a target thickness d and interaction length L the interaction probability is

$$PROBINT = 1 - \exp(-\frac{d}{L}) \tag{8.7}$$

Table 8.5.1 gives $PROBINT$ for various running conditions.

TABLE 8.5.1

Interaction Probabilities

Beam-Target	π-Be	π-Cu	p-Be	p-Cu	p-C
L (gm/cm^2)	108.3	169.1	81.8	137.2	88.6
d (gm/cm^2)	7.392	1.434	7.372	1.434	7.160
$PROBINT$	0.0660	0.0084	0.0864	0.0104	0.0776

The absorbtion cross sections for Beryllium are taken to be 138 mb for negative beam and 183 mb for positive beam[17]. The number $LIVEBEAM$ is obtained from the scalers for each run used in the analysis, and the integrated luminosity per target nucleon calculated[18]. The results are given in Table 8.5.2.

TABLE 5.2

Luminosity for cross section calculation

Beam type	Luminosity $\mathcal{L}$ $(pb/nucleon)^{-1}$
Positive beam	0.685
Negative beam	0.436

8.5.2 Corrections to the Luminosity

The observed interaction rates are corrected for the following losses:

1. The Veto wall signal was used as an online veto for the event to cut down the pretrigger rate for the Liquid Argon Calorimeter. In addition, there was a noisy power supply in the Faraday cage above the Liquid

Argon Calorimeter which faked pretriggers, and a signal was generated to veto them. The losses due to these vetos are taken into account by a correction factor $\mathcal{K}_1$,[19] which is found to be 0.65 on the average.

2. The interaction definition[16] ensured that there are no interactions within ± 3 buckets of the interaction buckets. The losses in the luminosity are corrected for by the factor $\mathcal{K}_2$[19] which is 0.88 on the average.

3. The backscatter debris from the interaction sometimes gives a signal in the veto walls, causing the interaction to be vetoed. This is corrected for by the factor $\mathcal{K}_3$ which is estimated to be 0.95 throughout the run.

These three corrections, and their product $\epsilon_{\mathcal{L}}$ is tabulated in Table 8.5.3 for both beam types.

TABLE 8.5.3

Luminosity Corrections

Beam type	$\mathcal{K}_1$	$\mathcal{K}_2$	$\mathcal{K}_3$	$\epsilon_{\mathcal{L}}$
Positive beam	0.64	0.88	0.95	0.54
Negative beam	0.69	0.92	0.95	0.60

8.5.3 Hardware corrections

Each hodoscope performed at around 93.5 % efficiency for a single hit and this translates to a overall efficiency factor of 0.76.

The trigger processor hardware limitations[20] cause losses which are taken into account by an efficiency factor of 0.92.

Combining these two corrections, a correction ϵ_H=0.70, is used to correct the luminosity.

Section 8.6

8.6.1 Cross section calculation

The cross section for vector meson production (ρ, ω and ϕ) is now calculated using the quantities described in the previous sections. The cross section for the kinematic range $0.1 \leq x_F \leq 0.6$ and $p_t \leq 1.6$ GeV/c per nucleon can be expressed as

$$BR(V^0 \longrightarrow \mu\mu) \cdot \frac{\sigma(V^0)}{A} = \frac{N_{Acc}^{BS}(V^0)}{\mathcal{L} \cdot \epsilon_{\mathcal{L}} \cdot \epsilon_S \cdot \epsilon_H} \tag{8.8}$$

Here $N_{Acc}^{BS}(V^0)$ is the number of acceptance corrected background subtracted events in a resonance region, taken from Table 8.3.2. The luminosity $\mathcal{L}$ is from Table 8.5.2, and the luminosity correction factor $\epsilon_{\mathcal{L}}$ is from Table 8.5.3. The software correction factor ϵ_S is taken from Table 8.4.2 and the hardware correction factor ϵ_H is from Section 8.5.3.

8.6.2 Cross sections

The quantity $BR{\cdot}\sigma(\omega)/A^{21}$ is calculated and tabulated for positive beam in Table 8.6.1. The ρ cross section can be calculated from this under the assumption that $\sigma(\rho) = \sigma(\omega)$. The errors quoted reflect the statistical error in the number of resonance events.

TABLE 8.6.1

$\sigma(\omega)$ for both beams

Beam type	Positive beam	Negative beam
$\mathcal{L}$	0.685 $(pb/nucleon)^{-1}$	0.436 $(pb/nucleon)^{-1}$
$\epsilon_{\mathcal{L}}$	0.54	0.60
ϵ_S	0.51	0.51
ϵ_H	0.70	0.70
$N^{BS}_{Acc}(\omega)$	22101 ± 615	21757 ± 611
$BR \cdot \sigma(\omega)/A$	167.4 ± 4.7 nb/nucleon	233.0 ± 6.5 nb/nucleon

The cross sections for ϕ production[22] are given in Table 8.6.2.

TABLE 8.6.2

$\sigma(\phi)$ for both beams

Beam type	Positive beam	Negative beam
$\mathcal{L}$	0.685 $(pb/nucleon)^{-1}$	0.436 $(pb/nucleon)^{-1}$
$\epsilon_{\mathcal{L}}$	0.54	0.60
ϵ_S	0.48	0.48
ϵ_H	0.70	0.70
$N^{BS}_{Acc}(\phi)$	3721 ± 271	3199 ± 248
$BR \cdot \sigma(\phi)/A$	29.9 ± 2.2 nb/nucleon	36.4 ± 2.8 nb/nucleon

8.6.3 Estimation of systematic errors

The systematic error in the cross section is due to contamination of the beam by minority particles is estimated to be 4 %.[23]

The method used for background estimation introduces and uncertainty in the estimate of the number of resonance events of 5 % The systematic error the method used for acceptance correction error is 6%. The overall systematic error in the number of events used in the cross section[23] is estimated to be 8%.

The corrections for the hardware efficiency ϵ_H have a 3% error associated with them. The factor for tail losses and contamination has an error of 5%, the preselection factor of 1.5% and the Trigger processor software correction 1.6%. Therefore the factor ϵ_S has an overall systematic error of 6%[23] . The variation of the luminosity correction factor ϵ_L gives an estimate of the systematic error in it, and it is 6%.

The total systematic error is found by adding these errors in quadrature, and is 13 %.

8.6.4 J/ψ cross sections

The analysis to obtain J/ψ cross sections and kinematic distributions is done by others[24] in the collaboration. These calculations are re-done and the cross sections calculated for the luminosities used in this chapter. The J/ψ mass region is chosen to be

$$2.9 \leq M_{\mu\mu} \leq 3.4 \ GeV/c^2 \tag{8.9}$$

The background estimation is done by fitting the mass spectrum from 2.0 to 4.0 GeV/c^2 to a second-order polynomial + a gaussian. The invariant mass spectrum is shown in Figure 8.6 for both beam types in the J/ψ mass region. The dashed curve is the fit to the data. The cuts for the analysis differ and these differences are listed below.

— The χ^2 of each muon track is constrained to be less than 2

— There is no cut on the p_t of the dimuon.

— The integrated acceptance is used to correct the number of J/ψ events instead of the acceptance surface.

— The kinematic range for the analysis is $0.1 \leq x_F \leq 0.8$.

— The beam Čerenkov bit is used to obtain the contribution for the majority particle for positive beam. . The luminosity is corrected for this by using the observed fraction of minority to majority events.

The luminosities, luminosity corrections and the hardware corrections are the same as for the low-mass vector meson analysis. The differences are in the software correction ϵ_S, and this is listed in Table 8.6.3.

TABLE 8.6.3

Software correction for J/ψ cross section

Correction	Positive beam	Negative beam
Preselection	0.94	0.94
Geometrical acceptance	0.37	0.44
Reconstruction efficiency	0.57	0.58
Mass cut $2.9 \leq M \leq 3.4$ GeV/c^2	0.89	0.87
ϵ_S	0.18	0.21

In addition, there is a correction ϵ_{sec} of 0.98 for secondary interactions in the target and a correction ϵ_C of 0.92 for the luminosity for positive beam (Č rejection). . The cross sections are given in Table 8.6.4 for positive beam.

TABLE 8.6.4

$\sigma(J/\psi)$ for both beams

Beam type	Positive beam	Negative beam
$\mathcal{L}$	0.685 $(pb/nucleon)^{-1}$	0.436 $(pb/nucleon)^{-1}$
$\epsilon_{\mathcal{L}}$	0.54	0.60
ϵ_S	0.18	0.21
ϵ_H	0.70	0.70
ϵ_{sec}	0.98	0.98
ϵ_C	0.92	1.00
$N_{Acc}^{BS}(\psi)$	194 ± 15	267 ± 18
$BR \cdot \sigma(\psi)/A$	4.6 ± 0.4 nb/nucleon	7.1 ± 0.5 nb/nucleon

8.6.5 Summary of results

The cross sections calculated in the previous sections are summarized to present a cross section for each resonance and beam type. The cross sections for ω and ϕ are in the kinematic region $0.1 \leq x_F \leq 0.6$ and $p_t \leq 1.6$ GeV/c; The J/ψ cross sections are in the region $0.1 \leq x_F \leq 0.8$. The results are given in Table 8.6.5.

TABLE 8.6.5

Summary of cross sections

Resonance cross section nb/nucleon	Positive beam	Negative beam
$BR(\omega)\cdot\sigma(\omega)/A$ nb/nucleon	$167.4 \pm 4.7(stat.)$ $\pm 21.8(syst.)$	$233.0 \pm 6.5(stat.)$ $\pm 30.3(syst.)$
$BR(\phi)\cdot\sigma(\phi)/A$ nb/nucleon	$29.9 \pm 2.2(stat.)$ $\pm 3.9(syst.)$	$36.4 \pm 2.8(stat.)$ $\pm 4.7(syst.)$
$BR(\psi)\cdot\sigma(\psi)/A$ nb/nucleon	$4.6 \pm 0.4(stat.)$ $\pm 0.5(syst.)$	$7.1 \pm 0.5(stat.)$ $\pm 0.7(syst.)$

Section 8.7

8.7.1 A-dependence of massive dimuon production

Data were collected simultaneously with Beryllium and Copper targets for the latter part of the run. This allows the determination of the A-dependence of dimuon production for various resonances and the continuum between them.

The per-nucleon cross section for the production of dimuons with a mass m off a nuclear target with Atomic number A can be expressed in terms of the number of events with mass m observed in the experiment. The expression is

$$\sigma(A)/A = \Lambda \cdot N_m(A) \cdot \frac{\sigma_{abs}(A)}{PROBINT(A) \cdot A} \qquad (8.10)$$

where Λ is a constant independent of A, $N_m(A)$ is the number of events with a dimuon of mass m from the target A, $\sigma_{abs}(A)$ is the absorbtion cross section from that nucleus and $PROBINT(A)$ is the probability of interaction in that target. $PROBINT(A)$ is taken from Table 8.5.1 in Chapter 8and the absorbtion cross sections are taken from Carroll[25] .

Both beam types are combined due to very small statistics from the Copper target. The factor $\frac{\sigma_{abs}(A)}{PROBINT(A)\cdot A}$ is calculated to be 233.9 mb/nucleon for the Beryllium target and 1155.3 mb/nucleon for the Copper target. If the A-dependence is parametrized as A^{α}, the ratio of the cross sections is related to α by

$$\alpha = \frac{ln[\sigma(A_2)/\sigma(A_1)]}{ln(A_2/A_1)} \tag{8.11}$$

with $A_2 = 64$ and $A_1 = 9$. Table 8.7.1 gives the values of α for different mass regions in the dimuon mass spectrum.

Table 8.7.1

A-dependence of massive dimuons

Mass bin (GeV/c^2)	N(Be)	N(Cu)	$\sigma(Be)/\Lambda\cdot 9$ $\times 10^3$ mb/nucleon	$\sigma(Cu)/\Lambda\cdot 64$ $\times 10^3$ mb/nucleon	α
0.55 ± 0.15	2536 ± 50	269 ± 16	593.2	310.8	0.67 ± 0.03
0.80 ± 0.10	3073 ± 55	381 ± 20	718.8	440.2	0.75 ± 0.03
1.00 ± 0.10	1372 ± 37	189 ± 14	320.91	218.4	0.80 ± 0.04
1.90 ± 0.80	1500 ± 39	188 ± 14	350.9	217.2	0.76 ± 0.04
3.10 ± 0.40	323 ± 18	46 ± 7	75.6	53.1	0.83 ± 0.08

The results are shown in graphical form in Figure 8.7. The A-dependence in the J/ψ mass region is in agreement with the previous measurement of this experiment[26] .

Section 8.8

8.8.1 Extrapolation of cross-sections to $x_F \geq 0$

In order to compare the cross sections measured in this thesis with those from other experiments, they have to be extrapolated to the kinematic region $x_F \geq 0$ from the region $0.1 \leq x_F \leq 0.6$. The measured x_F distributions are used to do the extrapolation by calculating the ratio of the acceptances in the two regions. If c is the exponent of the x_F distribution for a given resonance and beam type (as described in Section 9.1.1), then the ratio of the acceptances can be written as

$$\frac{Acc(0 \leq x_F \leq 1)}{Acc(a \leq x_F \leq b)} = \frac{1}{(1-a)^{c+1} - (1-b)^{c+1}} \tag{8.12}$$

and this factor is used to extrapolate the cross sections to $x_F \geq 0$. In this case $a = 0.1$ and $b = 0.6$, and Table 8.8.1 lists the value of the extrapolation factor.

Table 8.8.1

Extrapolation factor for $x_F \geq 0$

Resonance	Proton beam	π^- beam
ρ/ω	2.75 ± 0.37	2.23 ± 0.28
ϕ	3.15 ± 1.39	2.35 ± 0.83

8.8.2 A-dependence correction to the cross section

As most experiments measure the cross sections for a proton target, the A-dependence for resonance production has to be taken into account before a meaningful comparison can be made. The form of this dependence is assumed to be A^α and the values for α chosen are $\alpha_\phi = 0.8$ and $\alpha_\rho = 0.7$, which are consistent with measurements made by this experiment. For these

αs, the correction factor for a Beryllium target (A=9) is 1.93 for the ρ/ω resonances and 1.55 for the ϕ resonance.

8.8.3 Vector meson forward cross sections

The cross sections given in Table 8.7.1 are corrected for these factors. The branching ratios used to get the total cross sections are those for the $V^0 \longrightarrow e^+e-$ decay mode (assuming $e - \mu$ universality) as they are better measured than those for the $\mu\mu$ mode. Table 8.8.2 gives the forward per-nucleon cross section for the ρ/ω and ϕ resonances for a proton beam. The cross sections for the π^- beam are given in Table 8.8.3 for each resonance.

Table 8.8.2

Vector meson cross sections for $x_F \geq 0$: Proton beam

Resonance	ω	ϕ
$BR \cdot \sigma/A$	167.4 ± 4.7 nb	29.9 ± 2.2 nb
$BR(V^0 \longrightarrow e^+e^-)$	7.05×10^{-5}	3.11×10^{-4}
Extrapolation to $x_F \geq 0$	2.75	3.15
A-dependence correction	1.93	1.55
$\sigma(V^0)$	12.6 ± 0.4 mb/nucleon	469.4 ± 34.5 μb/nucleon

Table 8.8.3

Vector meson cross sections for $x_F \geq 0$: π^- beam

Resonance	ω	ϕ
$BR \cdot \sigma / A$	233.0 ± 6.5 nb	36.4 ± 2.8 nb
$BR(V^0 \longrightarrow e^+e^-)$	7.05×10^{-5}	3.11×10^{-4}
Extrapolation to $x_F \geq 0$	2.23	2.35
A-dependence correction	1.93	1.55
$\sigma(V^0)$	14.2 ± 0.4 mb/nucleon	426.3 ± 32.8 μb/nucleon

8.8.4 Ratio of ϕ to ω cross sections

Due to the fact that both the ϕ and ω resonance data were collected simultaneously, the ratio of their cross sections is relatively free of systematic errors due to systematics in luminosities and reconstruction efficiencies. The ratio of the cross sections can be written as

$$\frac{\sigma(\phi)}{\sigma(\omega)} = \frac{N_{Acc}(\phi)}{N_{Acc}(\omega)} \cdot \frac{BR(\omega \longrightarrow e^+e^-)}{BR(\phi \longrightarrow e^+e^-)} \tag{8.13}$$

where N_{Acc} stands for the acceptance corrected background subtracted number of resonance events for each resonance for the same data sample. The branching ratios are taken from Table 8.1.1.

In the kinematic region $0.1 \leq x_F \leq 0.6$, the ratio of cross sections is given in Table 8.8.4.

Table 8.8.4

Ratio of ϕ to ω cross sections

Beam type	$N_{Acc}(\omega)$	$N_{Acc}(\phi)$	$\sigma(\phi)/\sigma(\omega)$
Protons	25891 ± 624	4137 ± 284	0.036 ± 0.005
π^-	24893 ± 620	3820 ± 290	0.035 ± 0.005

If the branching ratio used for the ϕ is taken to be that for $\phi \longrightarrow \mu^+\mu^-$ mode, then the ratios change to 0.046 ± 0.007 for protons and 0.044 ± 0.007 for π^- beams.

REFERENCES

1) Review of Particle Properties., *Phys. Lett.* **B204**, (1988) .

2) S. Kartik, E672 technical note E672/91-4 Section 1.1.

3) S. Kartik, E672 technical note E672/91-4 Section 2.1.

4) S. Kartik, E672 technical note E672/91-4 Section 2.2.

5) S. Kartik, E672 technical note E672/91-4 Section 2.3.

6) S. Kartik, E672 technical note E672/91-3 Section 2.2.

7) S. Kartik, E672 technical note E672/91-4 Section 2.4.

8) S. Kartik, E672 technical note E672/91-4 Section 3.1

9) GEANT3 Users Guide, R. Brun et al. CERN DD/EE/84-1 (1986)

10) S. Kartik, E672 technical note E672/91-4 Section 3.2

11) WA11, M. Abolins et al. XIX HEP Conf. in Tokyo, 1978.

12) M. Aguilar-Benitez et al. CERN/EP 89-58 (1989)

13) S. Kartik, E672 technical note E672/91-4 Section 3.3

14) S. Kartik, E672 technical note E672/91-4 Section 4.3

15) S. Kartik, E672 technical note E672/91-4 Section 4.4

16) Production of high transverse momentum π^0... C. Yosef, Ph.D thesis, Northeastern U. (1990)

17) A.S. Carroll et al., *Phys. Lett.* **80B**, 319 (1979) .

18) S. Kartik, E672 technical note, E672/91-4 Section 5.1

19) S. Kartik, E672 technical note, E672/91-4 Section 5.2

20) S. Kartik, E672 technical note, E672/91-4 Section 5.3

21) S. Kartik, E672 technical note, E672/91-4 Section 6.2

22) S. Kartik, E672 technical note, E672/91-4 Section 6.3

23) S. Kartik, E672 technical note, E672/91-4 Section 6.4

24) V. Abramov et al., Properties of J/ψ production in π^--Be and p-Be collisions at 530 GeV/c, Fermilab Preprint FERMILAB-Pub-91/62-E, 1991.

25) A. S. Carroll et al., *Phys. Lett.* **80B**, 319 (1979) .

26) S. Kartik et al., *Phys. Rev.* **D41**, 1 (1990) .

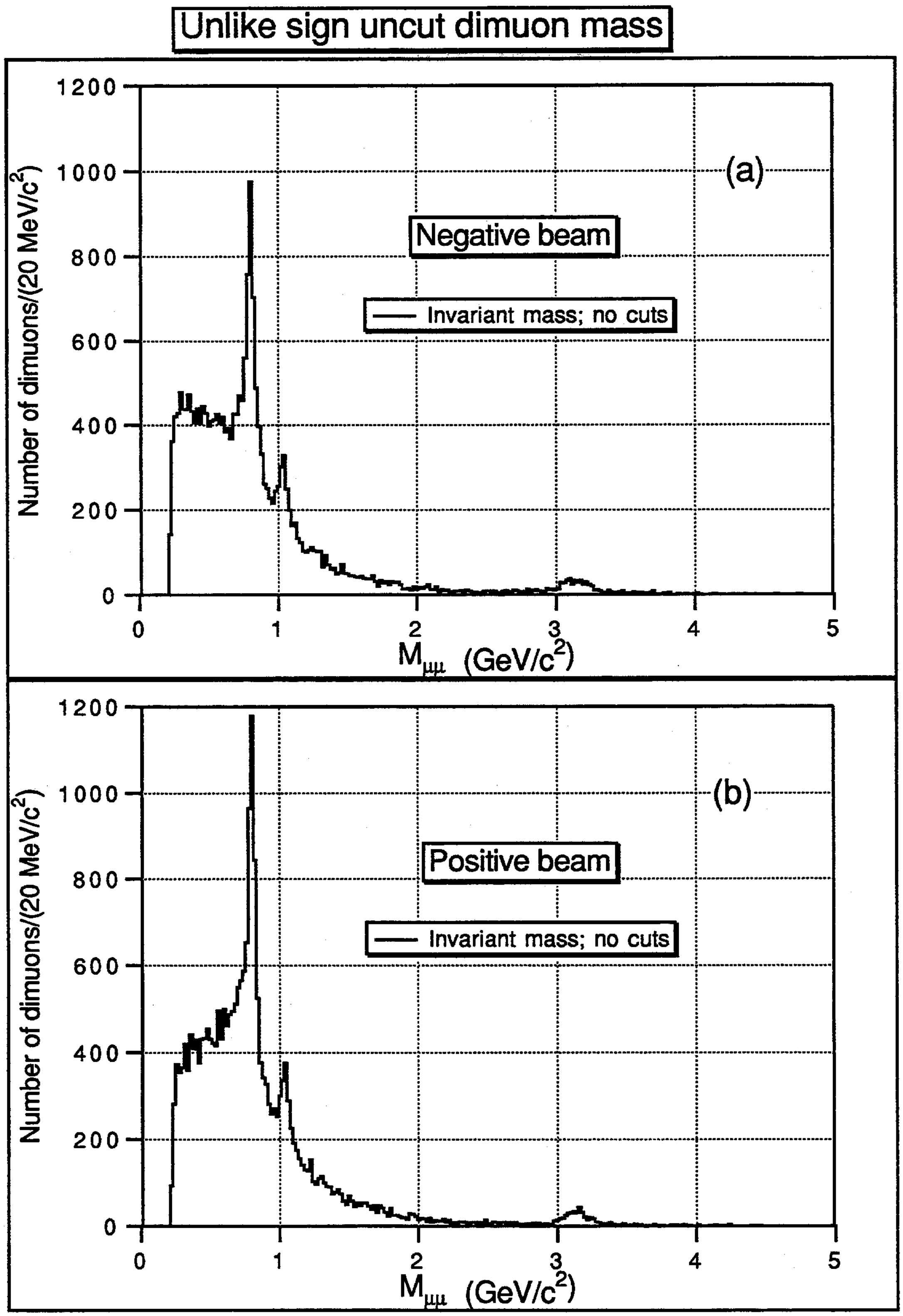
Unlike sign uncut dimuon mass
(a)
Negative beam
Invariant mass; no cuts
Number of dimuons/(20 MeV/c²)
1200
1000
800
600
400
200
0
0 1 2 3 4 5
M_μμ (GeV/c²)
(b)
Positive beam
Invariant mass; no cuts
Number of dimuons/(20 MeV/c²)
1200
1000
800
600
400
200
0
0 1 2 3 4 5
M_μμ (GeV/c²)

FIGURE 8.1

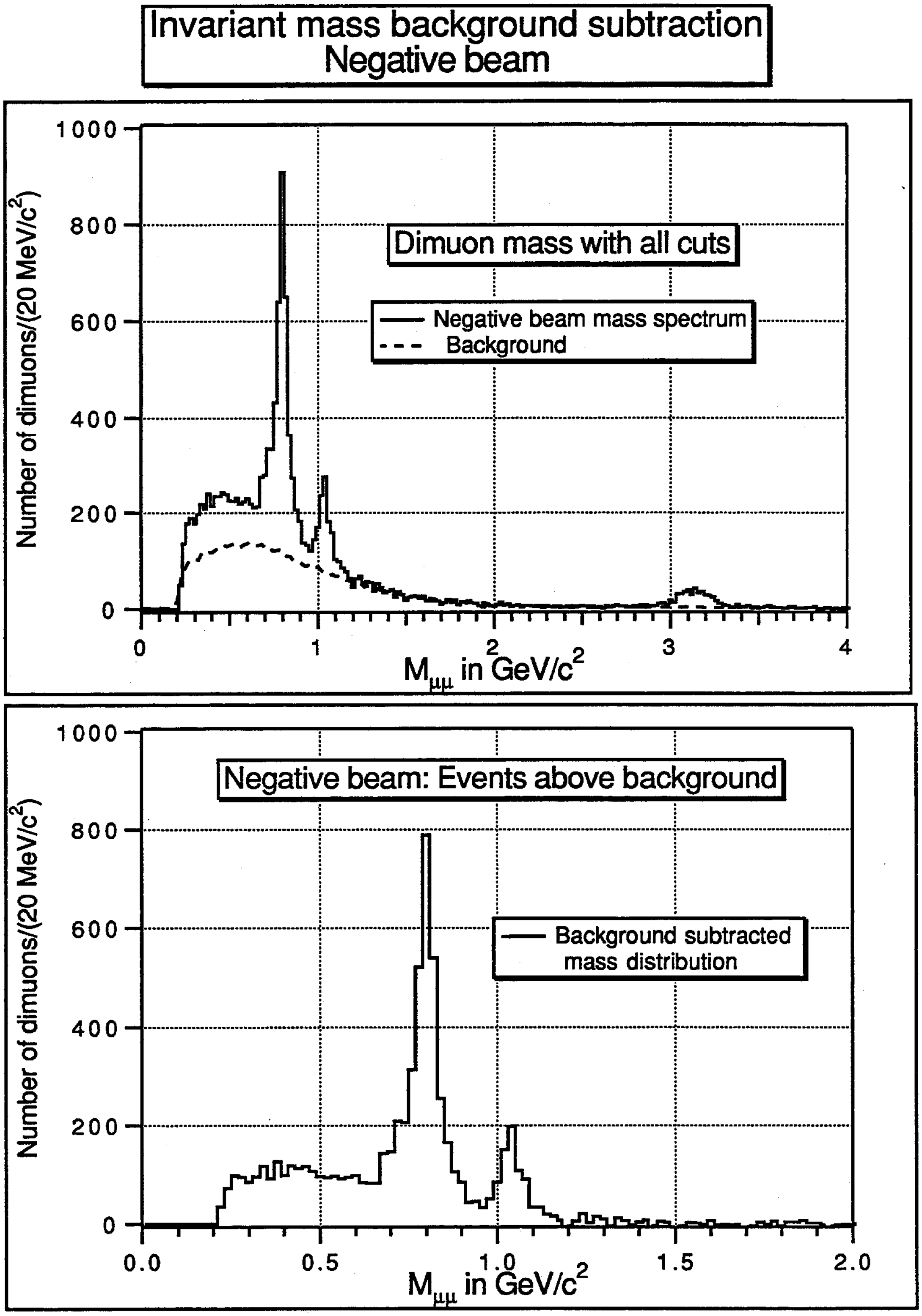
Invariant mass background subtraction
Negative beam
Dimuon mass with all cuts
Negative beam mass spectrum
Background
Number of dimuons/(20 MeV/c²)
1000
800
600
400
200
0
0
1
2
3
4
M_μμ in GeV/c²
Negative beam: Events above background
Background subtracted
mass distribution
Number of dimuons/(20 MeV/c²)
1000
800
600
400
200
0
0.0
0.5
1.0
1.5
2.0
M_μμ in GeV/c²

FIGURE 8.2

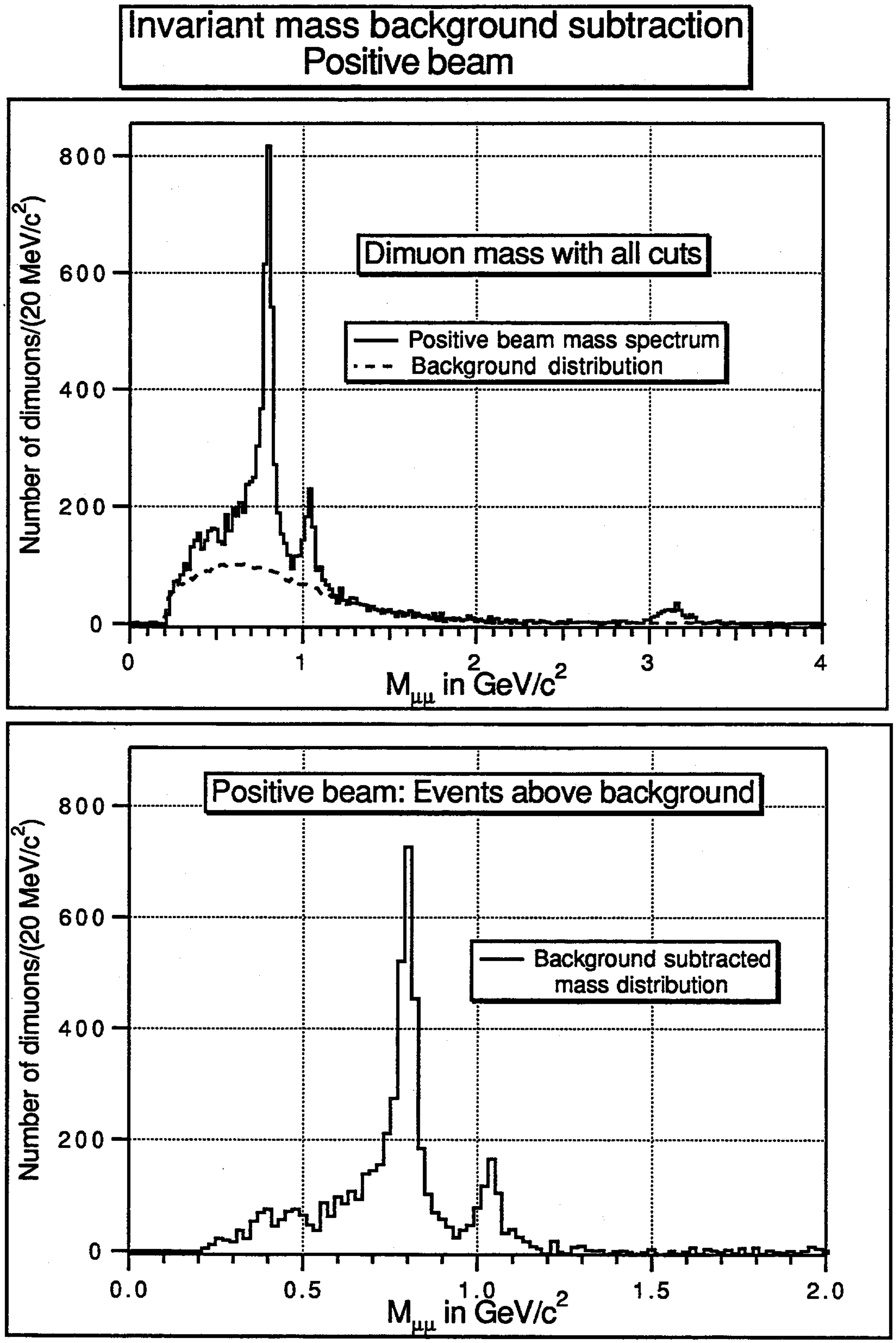

Invariant mass background subtraction
Positive beam
Dimuon mass with all cuts
Positive beam mass spectrum
Background distribution
Number of dimuons/(20 MeV/c^2)
$M_{\mu\mu}$ in GeV/c^2
Positive beam: Events above background
Background subtracted mass distribution

FIGURE 8.3

Comparison of data and Monte Carlo dimuon invariant mass spectra

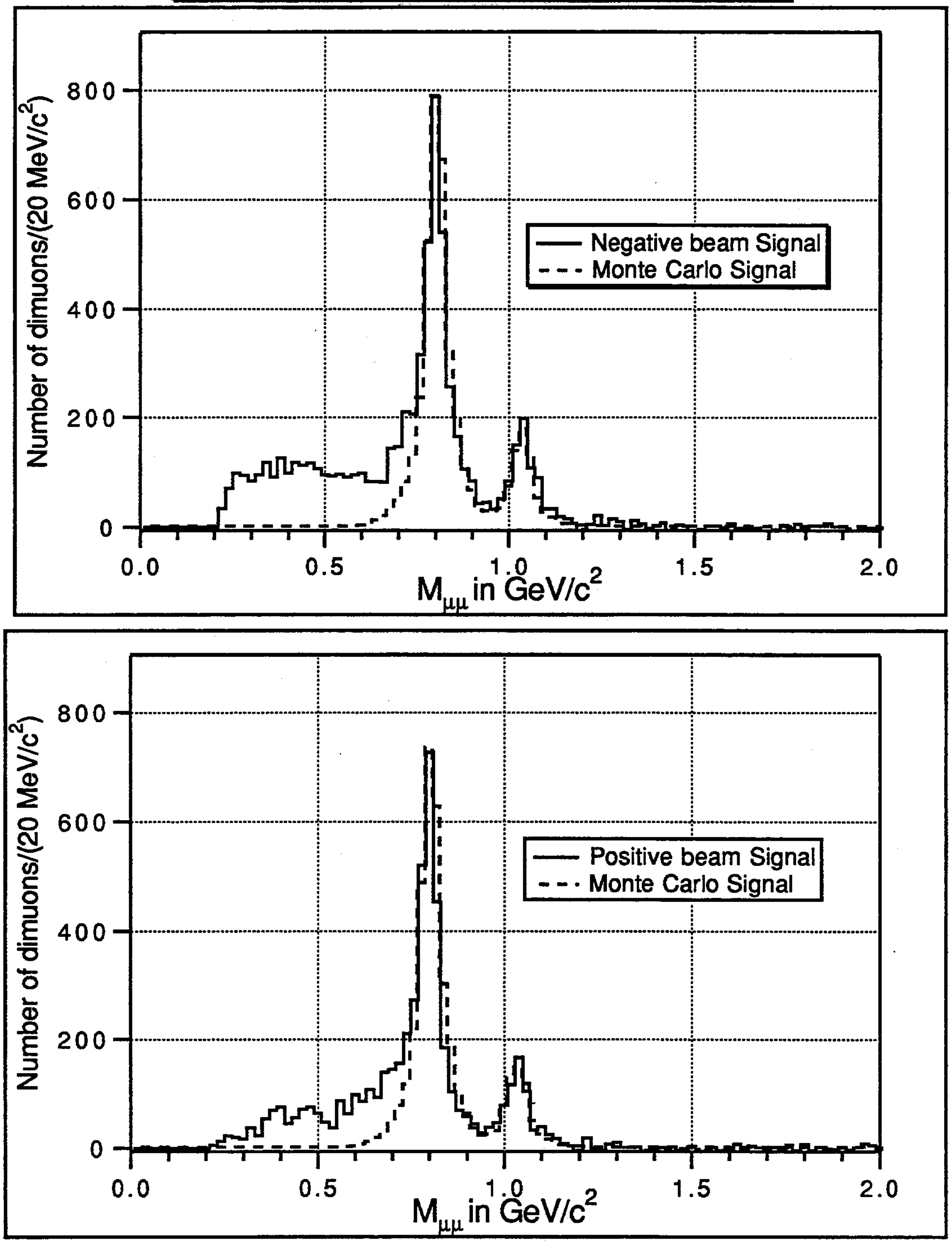

FIGURE 8.4

Vector meson acceptances in kinematic variables

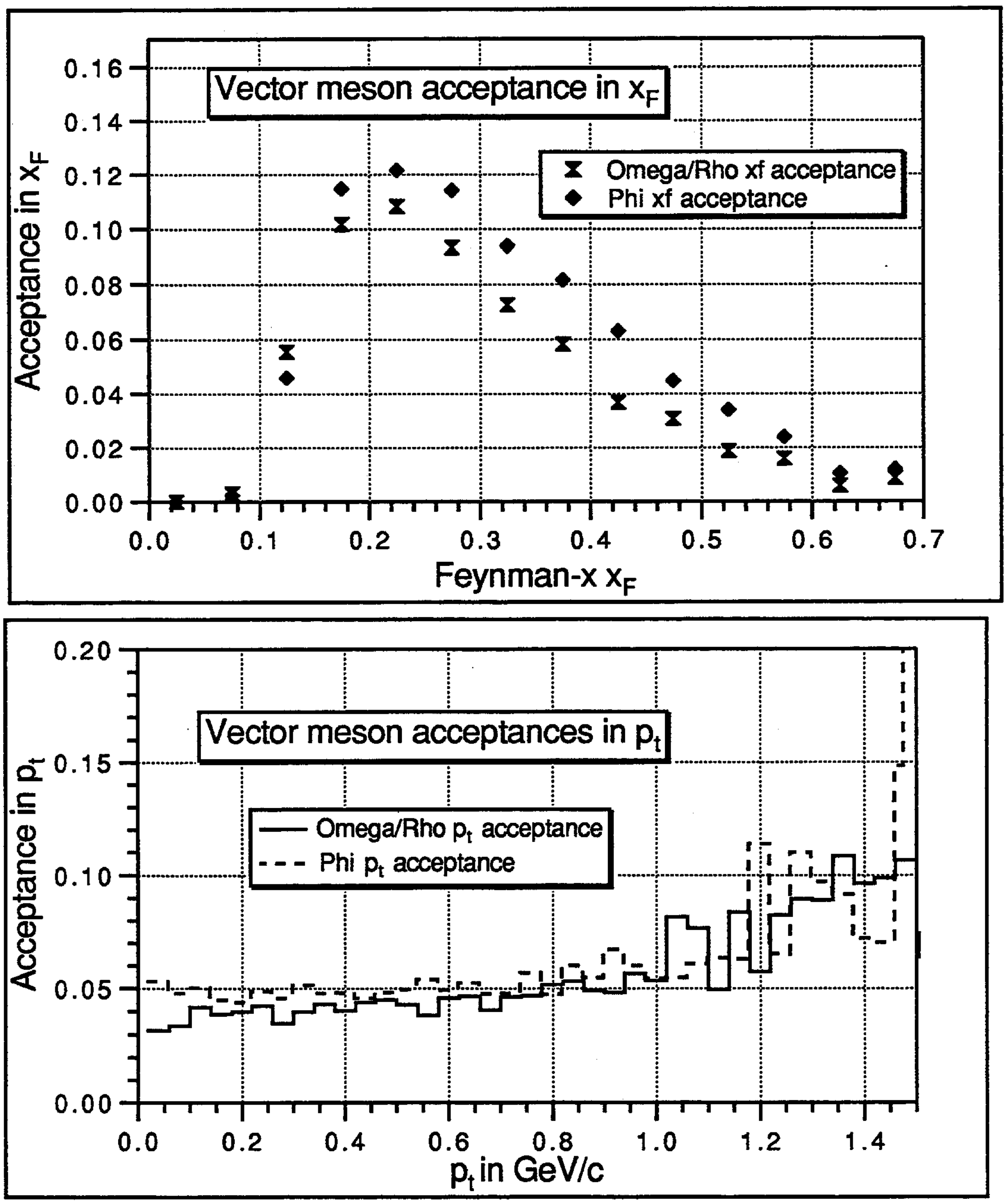

FIGURE 8.5

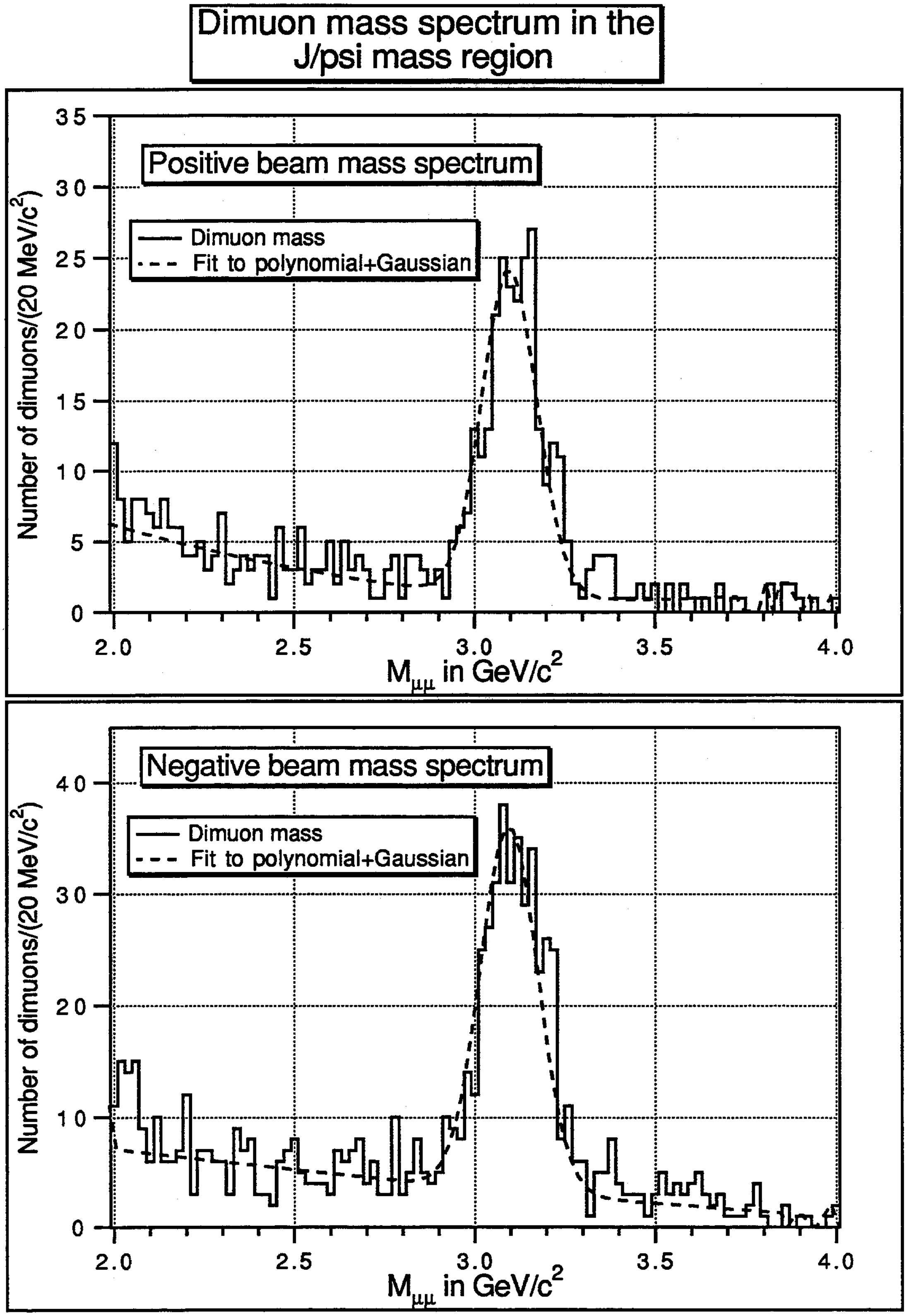
Dimuon mass spectrum in the J/psi mass region
Positive beam mass spectrum
Dimuon mass
Fit to polynomial+Gaussian
Number of dimuons/(20 MeV/c^2)
0
5
10
15
20
25
30
35
2.0
2.5
3.0
3.5
4.0
$M_{\mu\mu}$ in GeV/c^2
Negative beam mass spectrum
Dimuon mass
Fit to polynomial+Gaussian
Number of dimuons/(20 MeV/c^2)
0
10
20
30
40
2.0
2.5
3.0
3.5
4.0
$M_{\mu\mu}$ in GeV/c^2

FIGURE 8.6

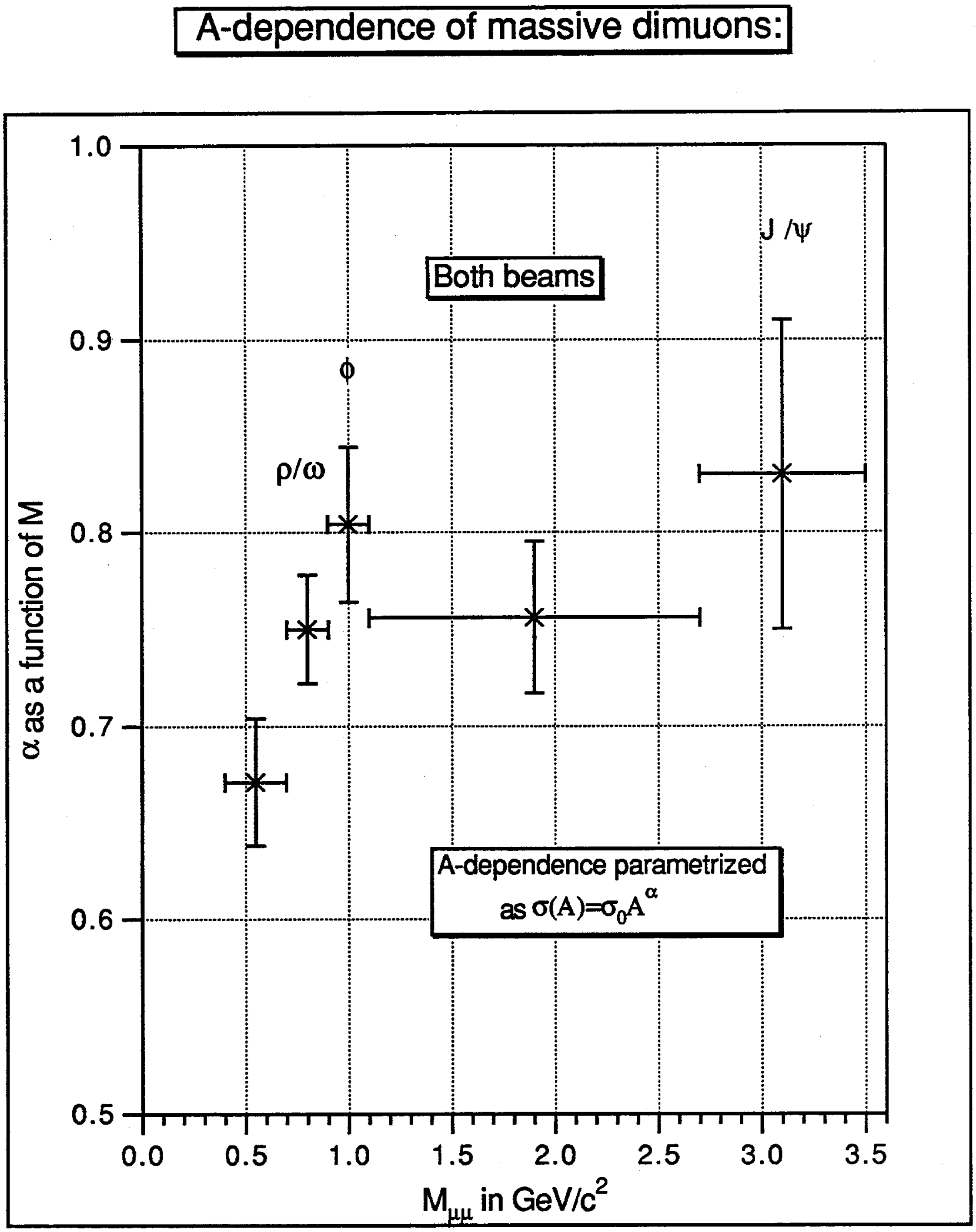
A-dependence of massive dimuons:
Both beams
J /ψ
φ
ρ/ω
A-dependence parametrized
as σ(A)=σ0A^α
α as a function of M
1.0
0.9
0.8
0.7
0.6
0.5
0.0
0.5
1.0
1.5
2.0
2.5
3.0
3.5
Mμμ in GeV/c2

FIGURE 8.7

CHAPTER 9
PROPERTIES OF VECTOR MESON PRODUCTION

In this chapter, the kinematic distributions (x_F and p_t) for the low mass vector mesons (ρ, ω and ϕ) are obtained. The ratio of the ϕ to ω cross section is studied as a function of the scalar charged transverse momentum sum of the events. The associated charged multiplicity of the event is presented as a function of the dimuon mass in that event.

Section 9.1

9.1.1 Vector meson x_F distributions

Due to the fact that the acceptance of the spectrometer is correlated in x_F and p_t^2, the acceptance surface in $x_F - p_t^2$ is used to correct the surface for the data.

The $x_F - p_t^2$ surface for wrong frame background is subtracted from the data , ensuring that the number of events in the background are the same as the number of events in the background under the mass peak which is normalized as described in Chapter 8. The acceptance corrected surface is then integrated over the p_t^2 dimension and the x_F distribution with the appropriate errors is obtained.

The resulting distribution is the fit to the form

$$dN/dx_F = A(1 - x_F)^c \tag{9.1}$$

The value of c differs for different resonances and beam types, and the measurements are presented in Table 10.4. The stability of the exponent c is checked by obtaining the distribution without background subtraction and studying the variation in c. The exponent is found to be stable within statistical errors, and so only the distributions for the background subtracted spectrum are shown. The exponent changes by about 8 % if the unsubtracted spectra are used.

9.1.2 $\rho + \omega$ x_F distributions

The Feynman-x (x_F) distribution for the $\rho + \omega$ mass region is shown in Figure 9.1 for a proton beam (with the requirement that the beam Čerenkov tags the beam hadron as a proton). Also shown for comparison are the curves for lower values of the exponent c. Figure 9.2 shows the x_F distributions for $\rho + \omega$ region for a π^- beam.

The distribution for the π^- beam is flatter then that for the proton beam, as is expected from the fact that the pion has two valence quarks as opposed to three for the proton.

9.1.3 ϕ x_F distributions.

The x_F distribution for the ϕ mass region ($0.98 \leq M_{\mu\mu} \leq 1.06 GeV/c^2$) is shown in Figure 9.3 for a proton beam. Figure 9.4 shown the distribution for a pion beam. Here too, the distribution for π^- beam is flatter than that for protons, as is expected.

9.1.4 Ratios of x_F distributions

The Feynman-x distributions for the $\rho + \omega$ and ϕ for different beams are compared to obtain information on the difference in the beam parton momentum fraction distribution. The ratio of the x_F distributions for p and

π^- beams for the $\rho + \omega$ region is shown in Figure 9.5. The distributions without acceptance correction or background subtraction are used for this purpose in order to minimize any systematic effects. The ratio distribution indicates that the distribution for π^- beams is flatter than that for p beams, so the incident parton momentum distribution is harder in pion beams.

The ratio of protons to π^- x_F distributions for the ϕ resonance mass region is shown in Figure 9.6. The pion distribution for ϕ production is also seen to be flatter than the corresponding distribution for protons.

The ratio distribution for the J/ψ is shown in Figure 9.7 and shows the same trend as for the $\rho + \omega$ and ϕ. This distribution has been investigated in more detail elsewhere[1] to extract information on the mechanism for J/ψ production.

Section 9.2

9.2.1 Vector meson p_t^2 distributions

The p_t^2 distribution for the resonances is obtained in the same way as described in Section 9.1 in this chapter. The acceptance-corrected, background subtracted $x_F - p_t^2$ surface for each resonance mass region is integrated over x_F to get p_t^2 distributions .

The p_t^2 distributions are then fitted to the form[2]

$$dN/dp_t^2 = A[1 + (\frac{p_t}{b})^2]^{-6} \tag{9.2}$$

The average p_t^2 is related to b by $< p_t^2 >= b^2/4$, obtained by averaging over all p_t^2. The fit parameter b is stable with respect to background subtraction, so only the subtracted spectra are shown.

9.2.2 $\rho + \omega$ p_t^2 distributions.

The p_t^2 distribution for the $\rho + \omega$ mass region for a proton beam is shown in Figure 9.8, and that for the π^- beam is shown Figure 9.9. There is no significant difference in the slopes of the distribution for the two beams. An exponential in p_t^2 alone is seen to be insufficient to describe the data, as the data has tails which are not accounted for. The excess at the high p_t^2 end of the spectrum indicates a different mechanism of production from that at lower p_t^2.

9.2.3 ϕ p_t^2 distributions

The p_t^2 distributions for the ϕ mass region after acceptance correction and background subtraction is shown in Figure 9.10 for incident proton beams. The corresponding plot for π^- beams is shown in Figure 9.11. There is no significant difference in the slopes of the distributions for different beams. The average p_t^2 for the ϕ meson is seen to be higher than that for the $\rho + \omega$ resonances.

The spectrum is not well described by an exponential alone, and the excess at the high p_t^2 end is in accordance to trends observed by other experiments at lower energies[3] .

9.2.4 Summary of p_t^2 results

The fit parameter b^2 is given for each resonance and beam type in Table 9.2. 1. The average p_t^2 can be calculated as $b^2/4$. The average p_t for such a distribution is calculated to be

$$< p_t >= \frac{35}{256} \cdot \pi \cdot b \qquad (9.3)$$

Table 9.2.1

Fit parameter b^2 for the p_t^2 distributions

Resonance	Proton beam $(GeV/c)^2$	π^- beam $(GeV/c)^2$
$\rho + \omega$	1.85 ± 0.06	1.63 ± 0.06
ϕ	2.28 ± 0.24	2.35 ± 0.29

The average p_t for the vector mesons using equation 9.3 is given in Table 9. 2.2.

Table 9.2.2

$< p_t >$ from the p_t^2 distributions

Resonance	Proton beam (MeV/c)	π^- beam (MeV/c)
$\rho + \omega$	584 ± 10	548 ± 10
ϕ	649 ± 34	658 ± 41

Section 9.3

9.3.1 Average charged multiplicity vs. dimuon mass

The mean charged multiplicity of the associated event is shown as a function of dimuon mass for positive beam in Figure 9.12, and for negative beam in Figure 9. 13. The charged multiplicity shows a significant dip in the mass region of the ρ and ω. It has been verified that a similar study of like-sign dimuons does not have a dip in the multiplicity.

The dip can be understood in terms of the dominant decay of the ρ, which is $\rho \longrightarrow \pi^+\pi^-$. Events where the ρ decays into a $\mu^+\mu^-$ pair effectively decrease the number of charged pions in the event, which is what the ρ would decay into most of the time.

The suppression (of one unit of charge) in the $\rho+\omega$ region can be understood if, on the average, half of the charged pions in an interaction are due to vector meson decays. In the $\rho+\omega$ mass region, the signal-to-background ratio for resonance production is about 1:1. A dimuon decay of the vector meson reduces the number of pions by 2 for more than half the events, and so the average number of charged particles would be reduced by one.

Section 9.4

9.4.1 Enhancement of $\sigma(\phi)/\sigma(\omega)$ with event inelasticity

The enhancement of ϕ production over ρ production has been suggested [4–6] as a possible signature for the formation of quark-gluon plasma (QGP) by various authors. Recent results from NA38[7] report observing enhancement of $\phi/(\omega+\rho)$ in heavy ion collisions with respect to the transverse energy E_T of the event. It has also been reported that the dependence on E_T is more pronounced for higher dimuon p_t.

9.4.2 Results from this experiment.

As no information concerning the neutral energy of the event is used in this analysis, the charged tracks are used to define a variable characterizing the inelasticity of the event. The scalar p_t sum of the charged tracks associated with the event $\Sigma|p_t|$ is used as a measure of the transverse energy of the event. Figure 9.13 shows the spectrum for the $\Sigma|p_t|$ of the event.

Figure 9.14 shows the ratio of $\sigma(\phi)/\sigma(\rho)$ (arbitrary normalization) as a function of $\Sigma|p_t|$ for dimuon p_t less that 0.8 GeV/c and greater that 0.8

GeV/c. A significant enhancement of the ratio is observed as a function of $\Sigma|p_t|$. The trend is more pronounced for higher dimuon p_t. This enhancement persists with or without background subtraction, and is also seen if the dimuon p_t is included in $\Sigma|p_t|$.

9.4.3 Interpretation of the results

In order to understand whether the ϕ signal is being enhanced or the ρ is being suppressed, the mass spectra for different bins of $\Sigma|p_t|$ are studied. The first plot in Figure 9.15 shows the ratio of the mass spectra for $6 \leq \Sigma|p_t| \leq 12$ GeV/c and $0 \leq \Sigma|p_t| \leq 3$ GeV/c, and the next plot shows the ratio for $6 \leq \Sigma|p_t| \leq 12$ GeV/c and $0 \leq \Sigma|p_t| \leq 6$ GeV/c. The plots are normalized such that the ratio is unity for the J/ψ mass region, as no J/ψ suppression has been observed in this experiment[1] .

The ρ mass region shows a decrease in the first plot as compared to the second plot, while the ϕ mass region does not. This suggests that in fact the ρ signal is being suppressed at high $\Sigma|p_t|$, as opposed to the ϕ being enhanced.

Figure 9.16 shows the average dimuon p_t plotted against the scalar p_t-sum, $\Sigma|p_t|$ of the event. There is a definite correlation between the two, with the average p_t increasing with $\Sigma|p_t|$. Selecting higher inelasticities thus favours resonances with higher transverse momentum, and the ϕ is enhanced with respect to the $\rho + \omega$ for this reason.

REFERENCES

1) V. Abramov et al. Fermilab Preprint FERMILAB-Pub-91/62-E, 1991.

2) D. M. Kaplan et al., *Phys. Rev. Lett* **40**, 435 (1978) .

3) H. Dijkstra et al., *Z. fur Phys.* **C31**, 375 (1986) .

4) A. Shor., *Phys. Rev. Lett.* **54**, 1122 (1985) .

5) P. Koch et al., *Z. fur Phys.* **C47**, 477 (1990) .

6) H. Barz et al., *Phys. Lett.* **B254**, 315 (1991) .

7) A. Baldisseri et al. NA38 Collaboration, Annecy Preprint LAPP-EXP-89-15.

8) J. Gago , NA38 collaboration, Singapore Conference, August 1990.

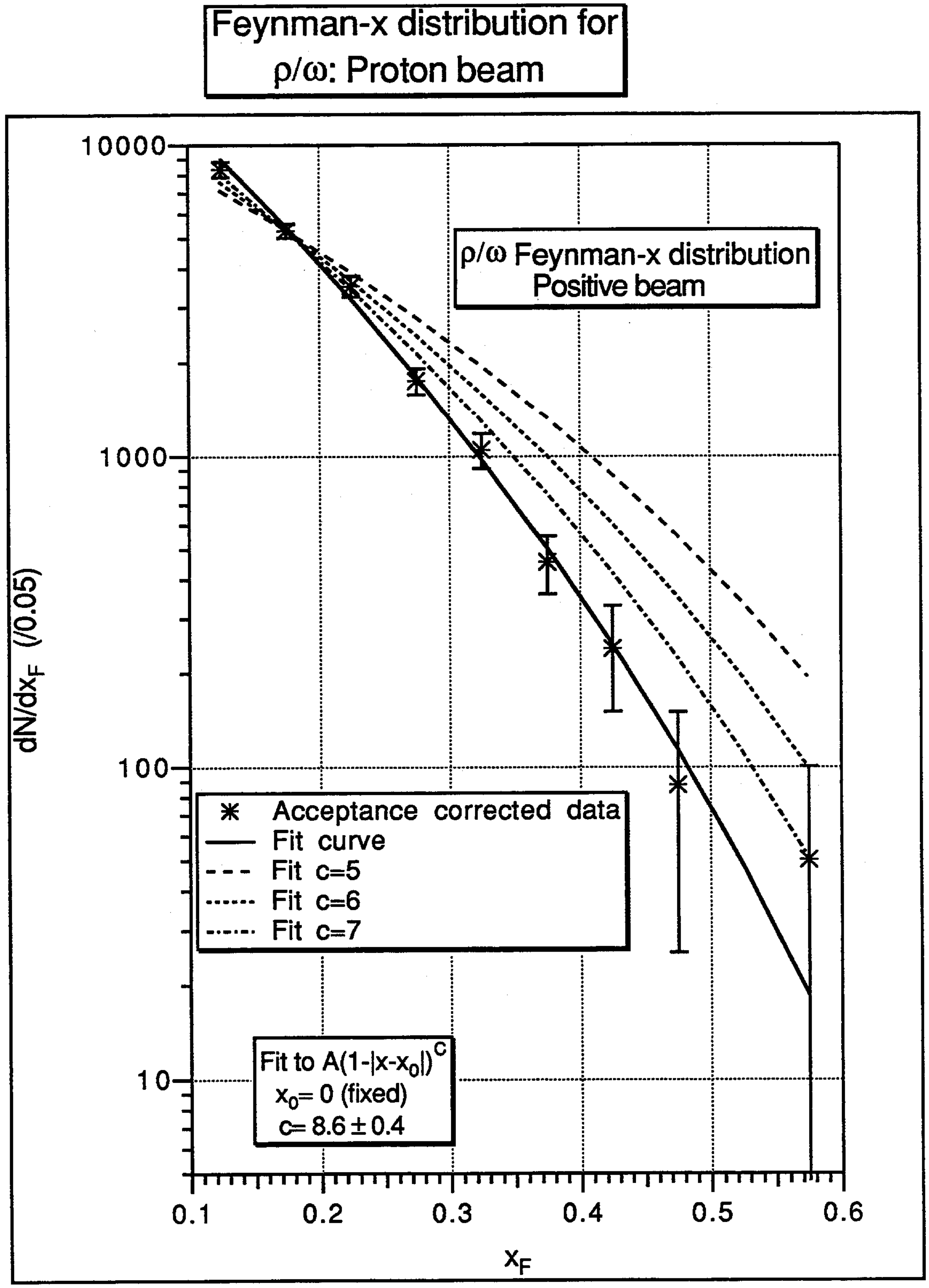
Feynman-x distribution for
ρ/ω: Proton beam
ρ/ω Feynman-x distribution
Positive beam
10000
1000
100
10
dN/dx_F (/0.05)
Acceptance corrected data
Fit curve
Fit c=5
Fit c=6
Fit c=7
Fit to A(1-|x-x0|)^c
x0= 0 (fixed)
c= 8.6 ± 0.4
0.1
0.2
0.3
0.4
0.5
0.6
x_F

FIGURE 9.1

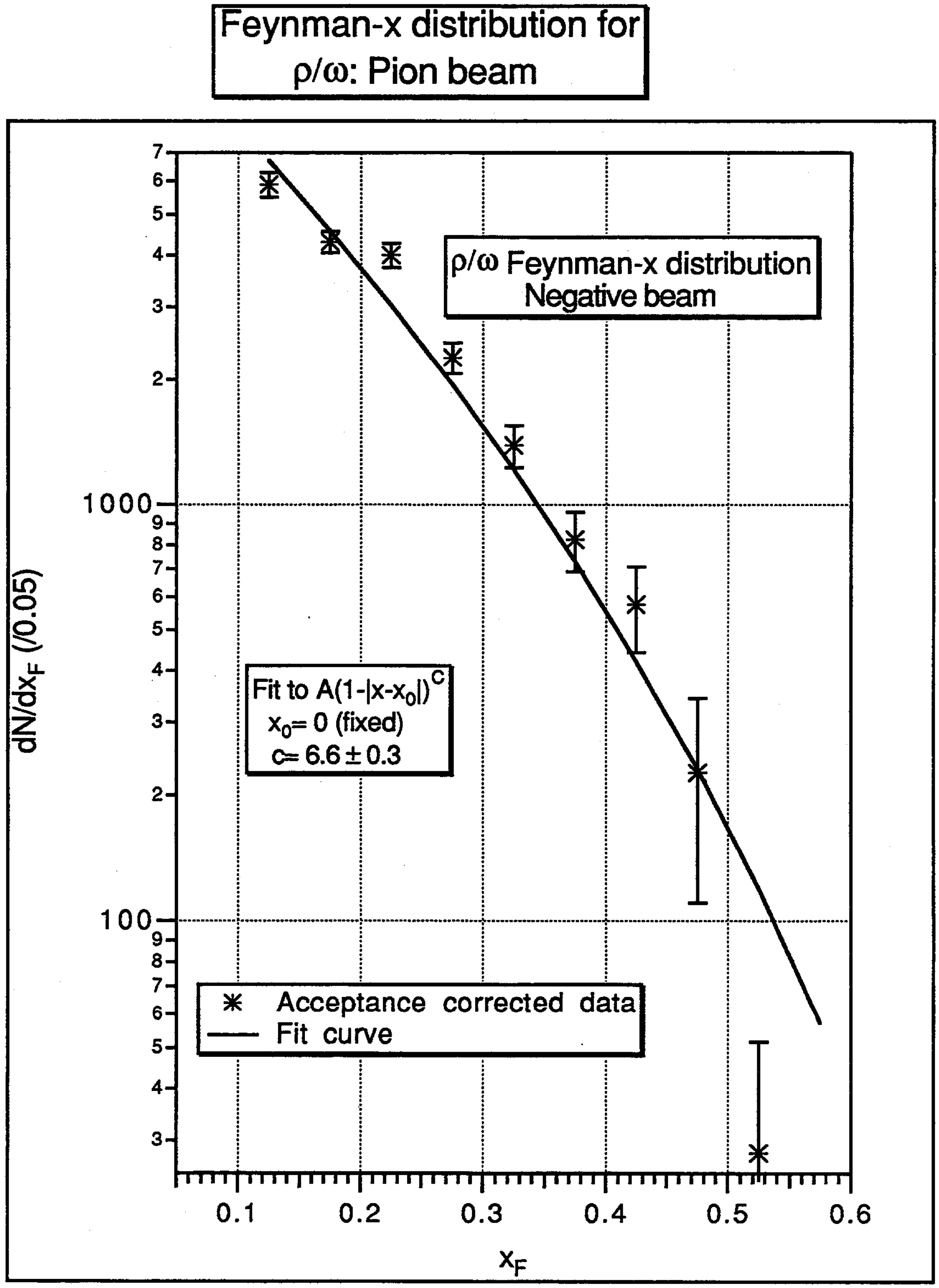
Feynman-x distribution for
ρ/ω: Pion beam
ρ/ω Feynman-x distribution
Negative beam
Fit to A(1-|x-x0|)^c
x0= 0 (fixed)
c= 6.6 ± 0.3
Acceptance corrected data
Fit curve
dN/dxF (/0.05)
xF
1000
100
0.1
0.2
0.3
0.4
0.5
0.6

FIGURE 9.2

Feynman-x distribution for
ϕ : Proton beam

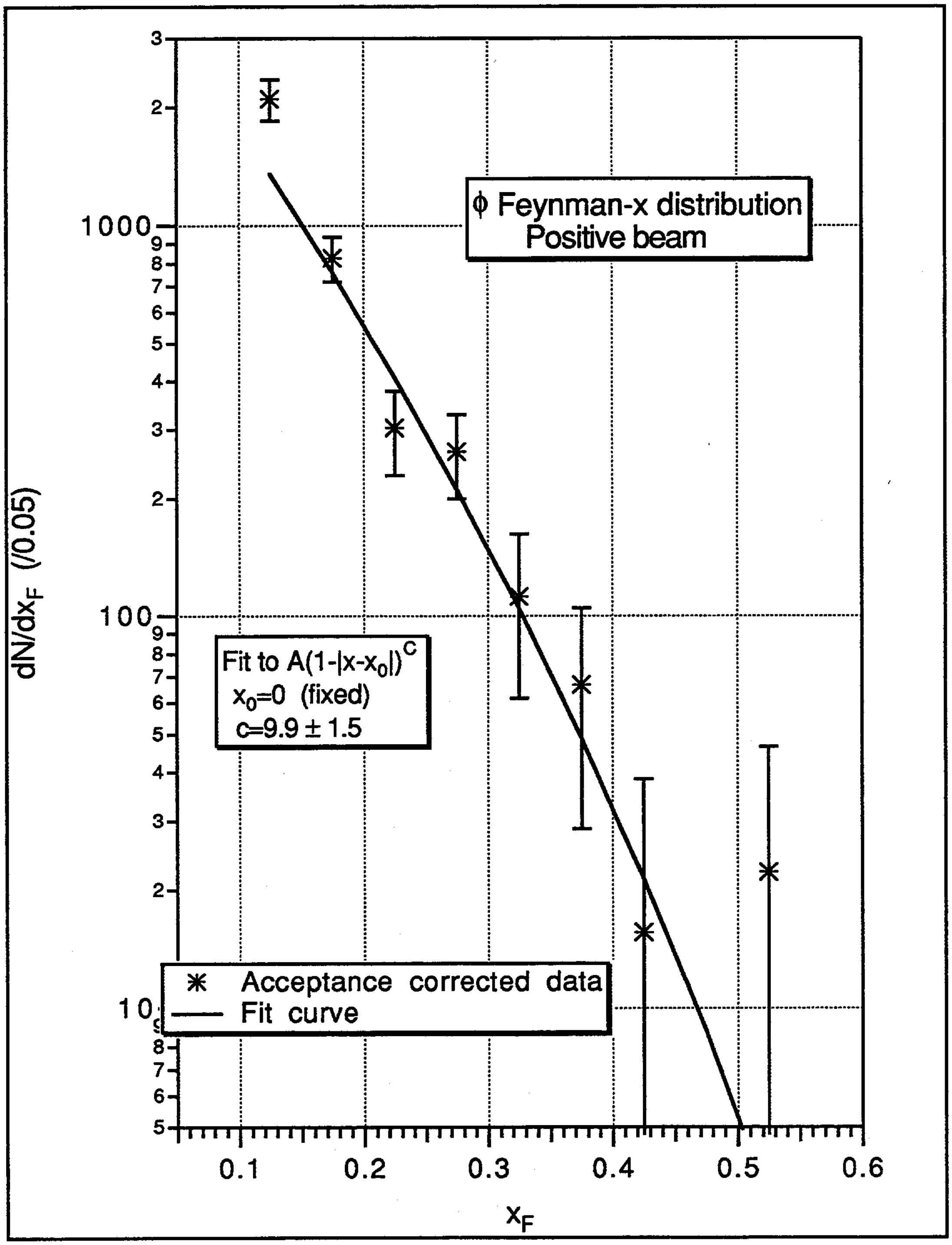

FIGURE 9.3

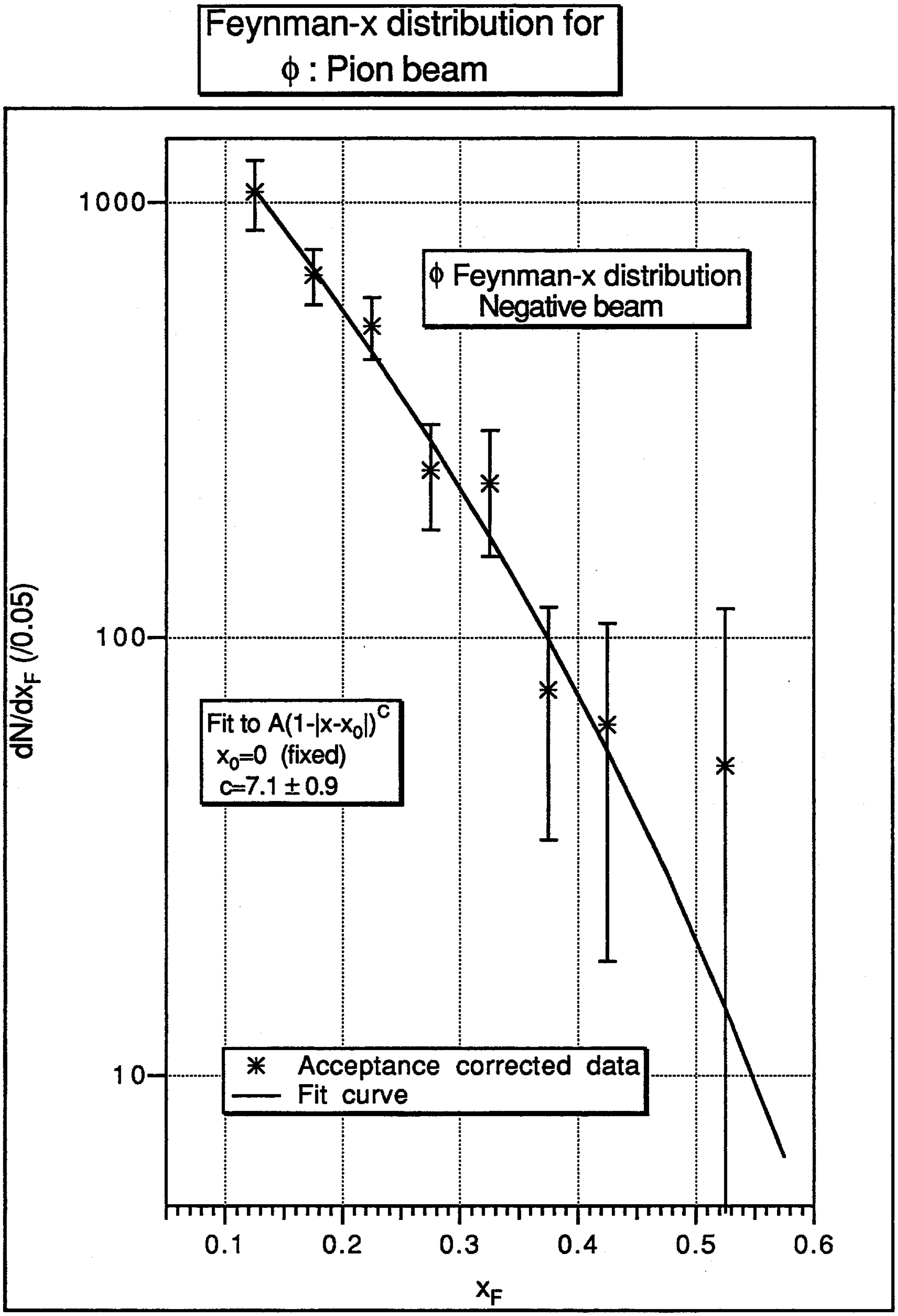
Feynman-x distribution for
ϕ : Pion beam
ϕ Feynman-x distribution
Negative beam
Fit to A(1-|x-x0|)^c
x0=0 (fixed)
c=7.1 ± 0.9
Acceptance corrected data
Fit curve
1000
100
10
dN/dxF (/0.05)
0.1
0.2
0.3
0.4
0.5
0.6
xF

FIGURE 9.4

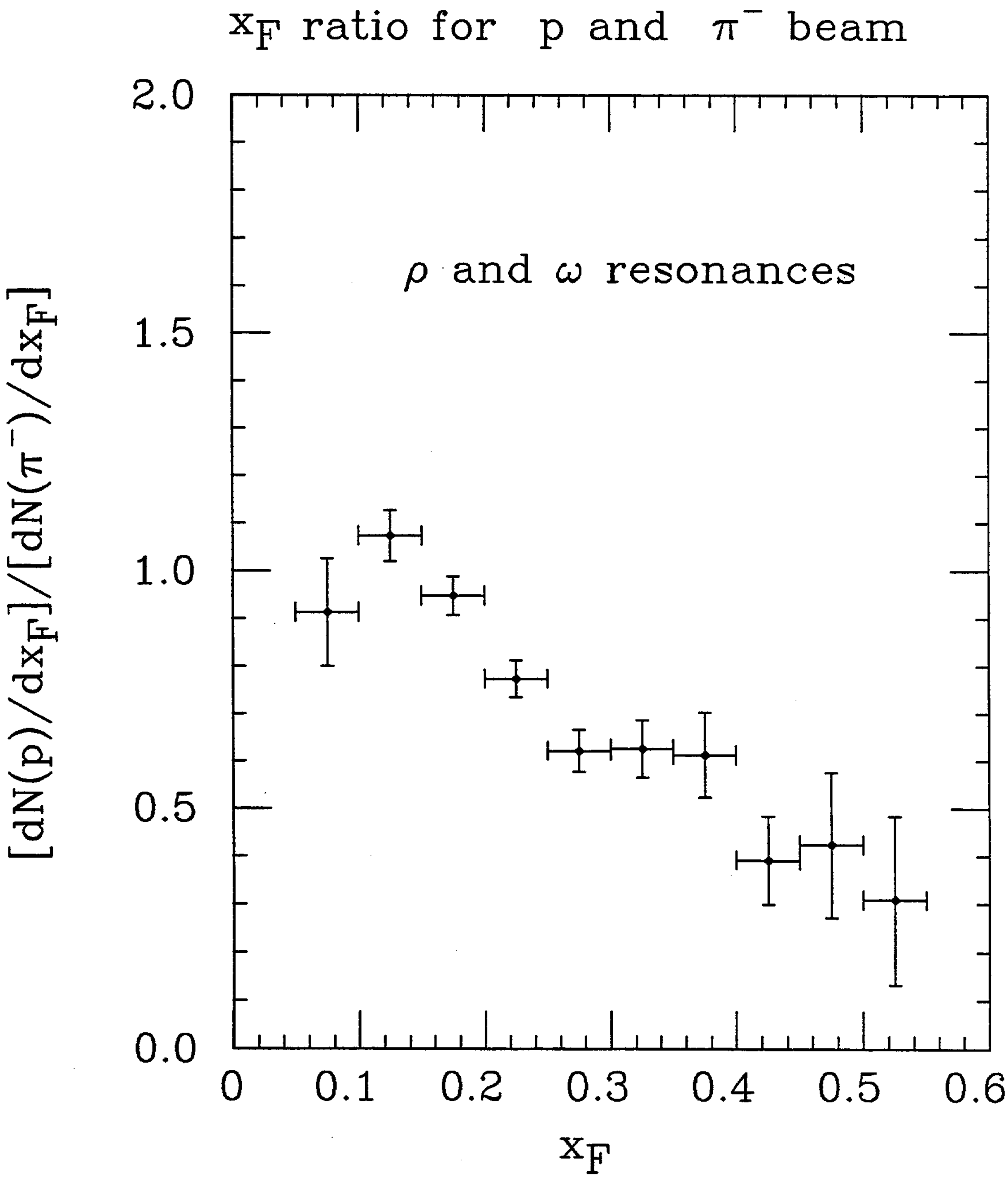

x_F ratio for p and π^- beam
ρ and ω resonances
$[dN(p)/dx_F]/[dN(\pi^-)/dx_F]$
x_F
2.0
1.5
1.0
0.5
0.0
0
0.1
0.2
0.3
0.4
0.5
0.6

FIGURE 9.5

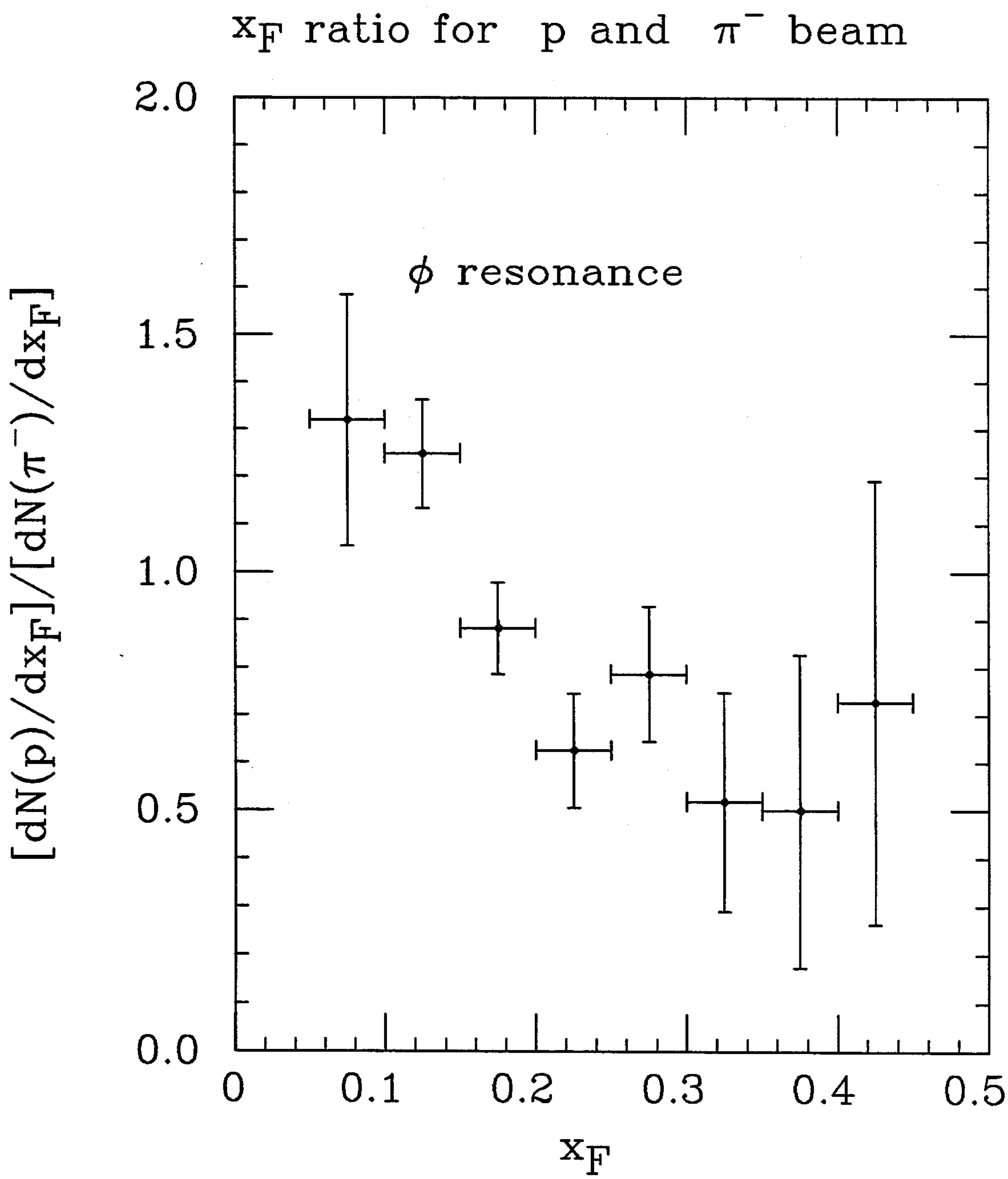

x_F ratio for p and π^- beam
ϕ resonance
$[dN(p)/dx_F]/[dN(\pi^-)/dx_F]$
2.0
1.5
1.0
0.5
0.0
0
0.1
0.2
0.3
0.4
0.5
x_F

FIGURE 9.6

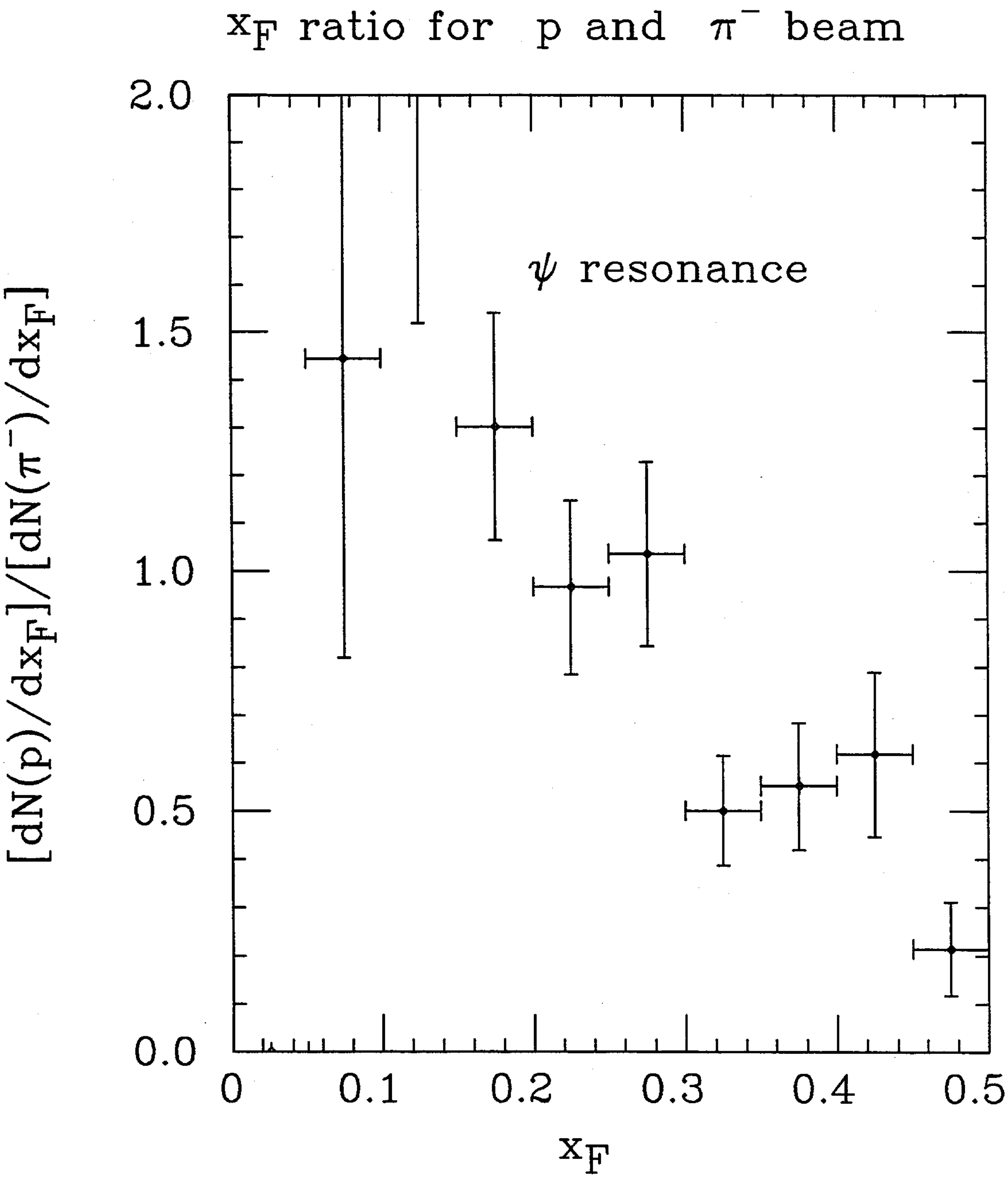

x_F ratio for p and π^- beam
ψ resonance
2.0
1.5
1.0
0.5
0.0
0
0.1
0.2
0.3
0.4
0.5
$[dN(p)/dx_F]/[dN(\pi^-)/dx_F]$
x_F

FIGURE 9.7

Fits to Transverse momentum distribution for $\rho+\omega$ resonance : Positive beam

Kaplan form: $\dfrac{A}{(1+(p_t/b)^2)^6}$

D. M. Kaplan et al. **Phys. Rev. Lett. 40,** 435 (1978)

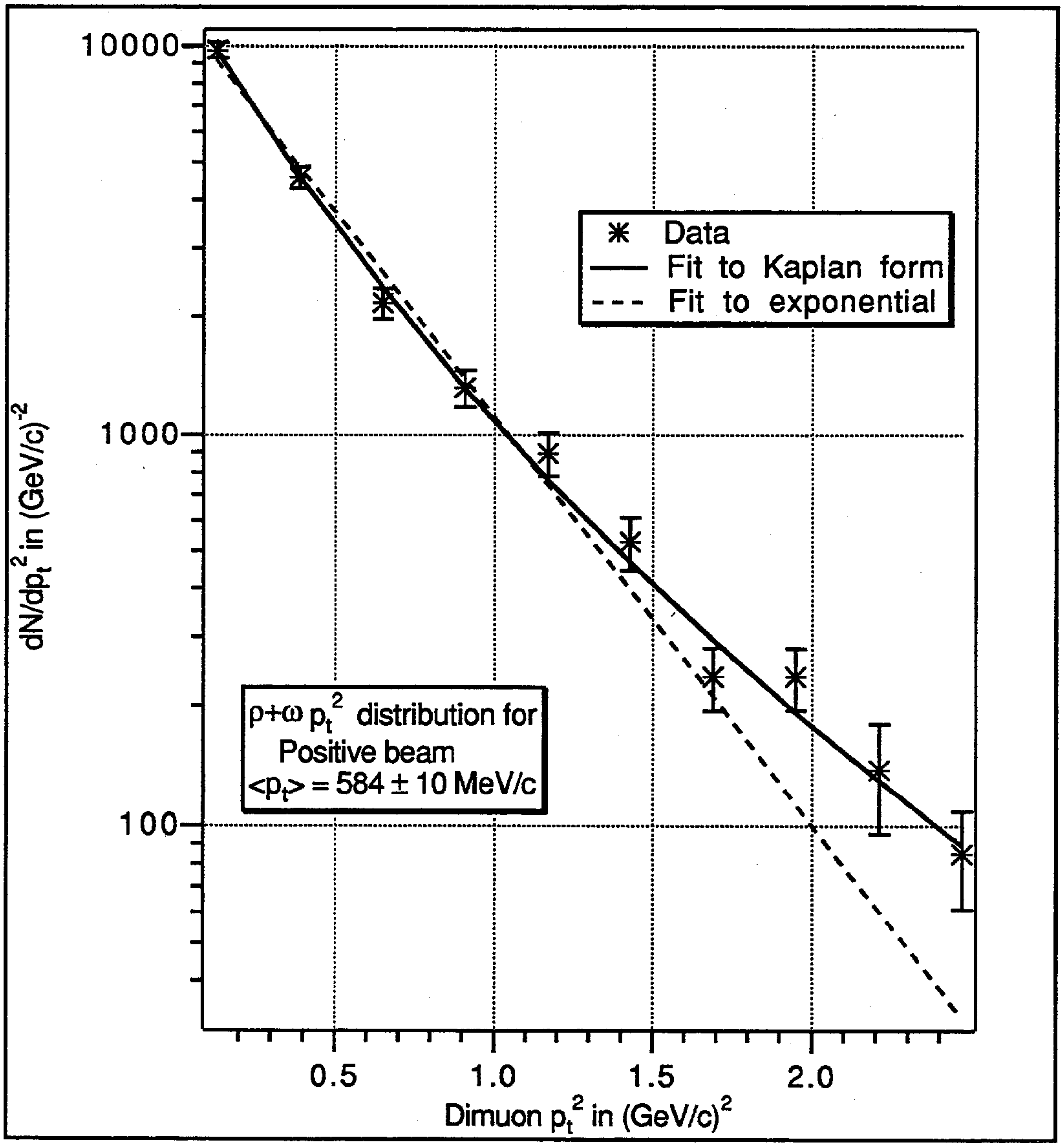

FIGURE 9.8

Fits to Transverse momentum distribution for $\rho+\omega$ resonances: Negative beam

$$\textbf{Kaplan form: } \frac{A}{(1+(p_t/b)^2)^6}$$

D. M. Kaplan et al. Phys. Rev. Lett. 40, 435 (1978)

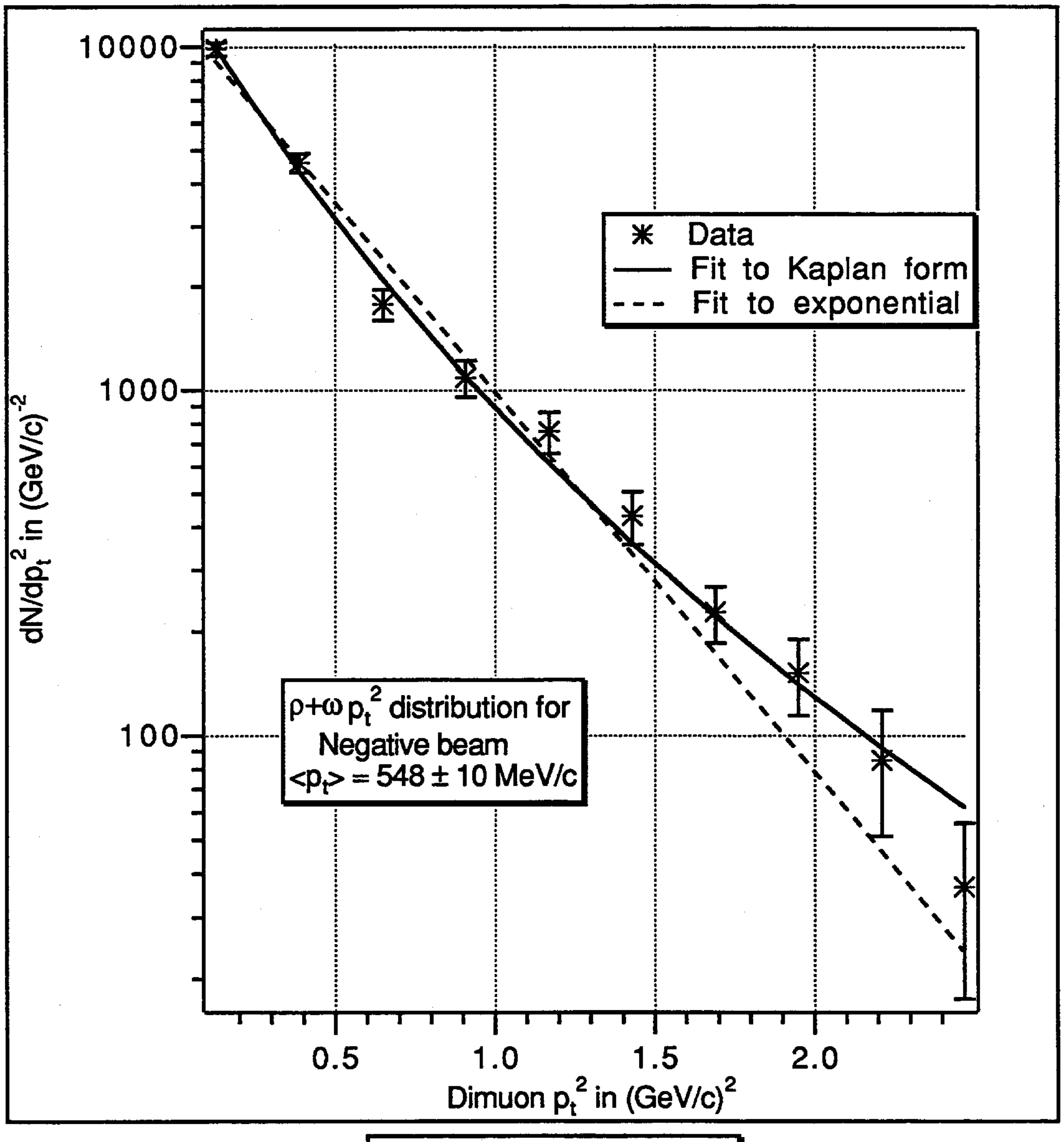

FIGURE 9.9

Fits to Transverse momentum distribution for ϕ resonance: Positive beam

Kaplan form: $\frac{A}{(1+(p_t/b)^2)^6}$

D. M. Kaplan et al. Phys. Rev. Lett. 40, 435 (1978)

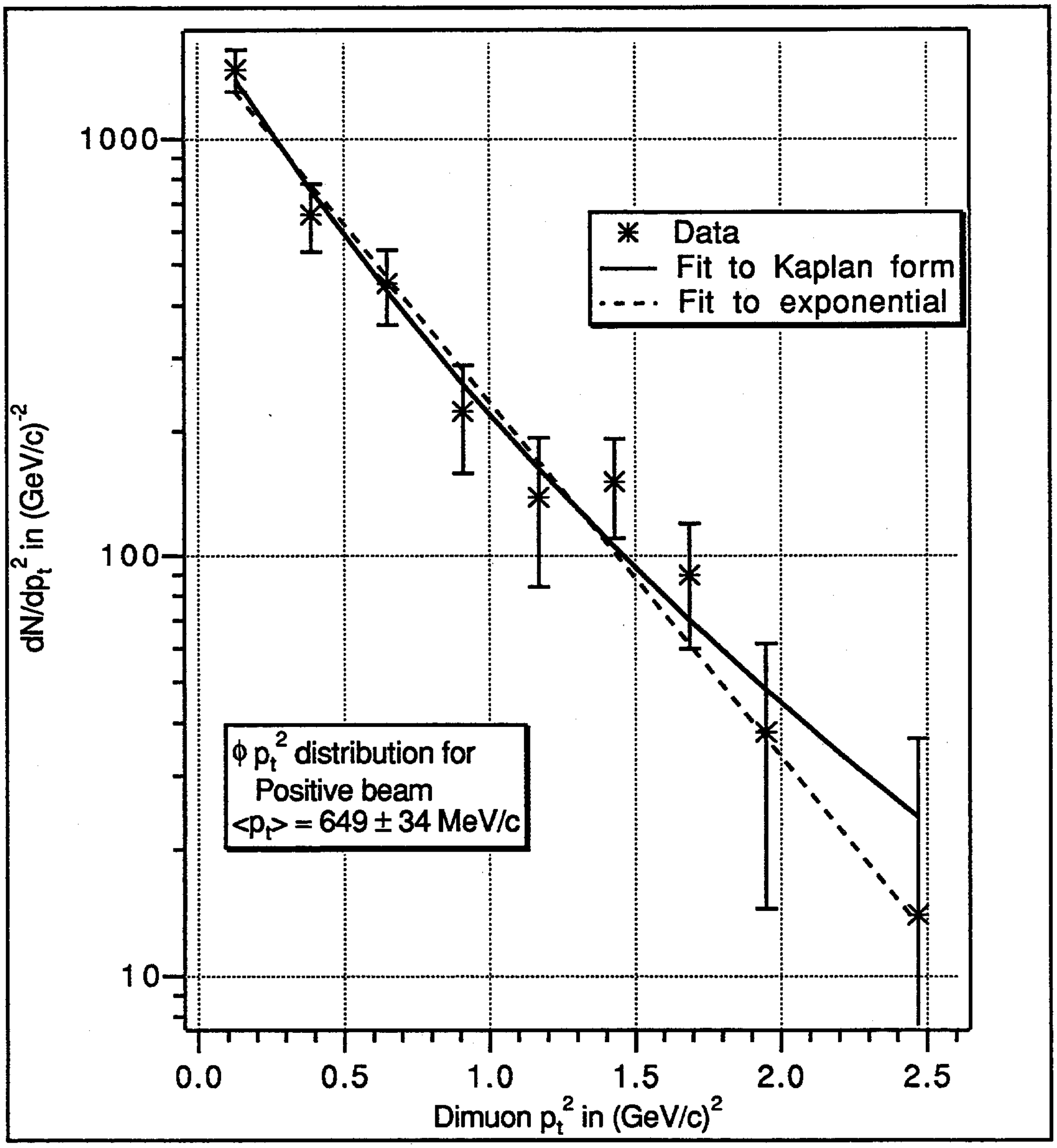

FIGURE 9.10

Fits to Transverse momentum distribution for ϕ resonance: Negative beam

Kaplan form: $\frac{A}{(1+(p_t/b)^2)^6}$

D. M. Kaplan et al. Phys. Rev. Lett. 40, 435 (1978)

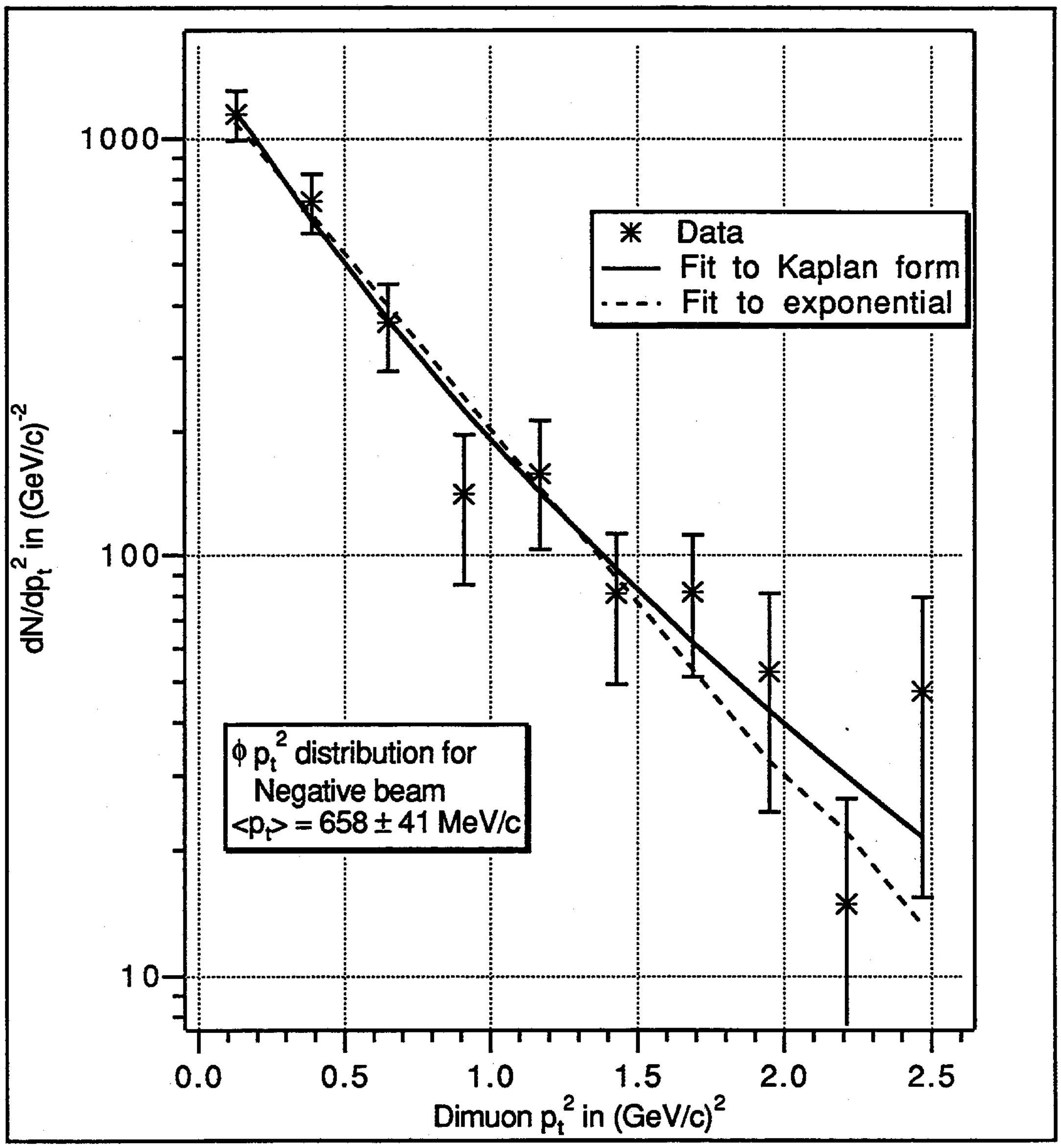

FIGURE 9.11

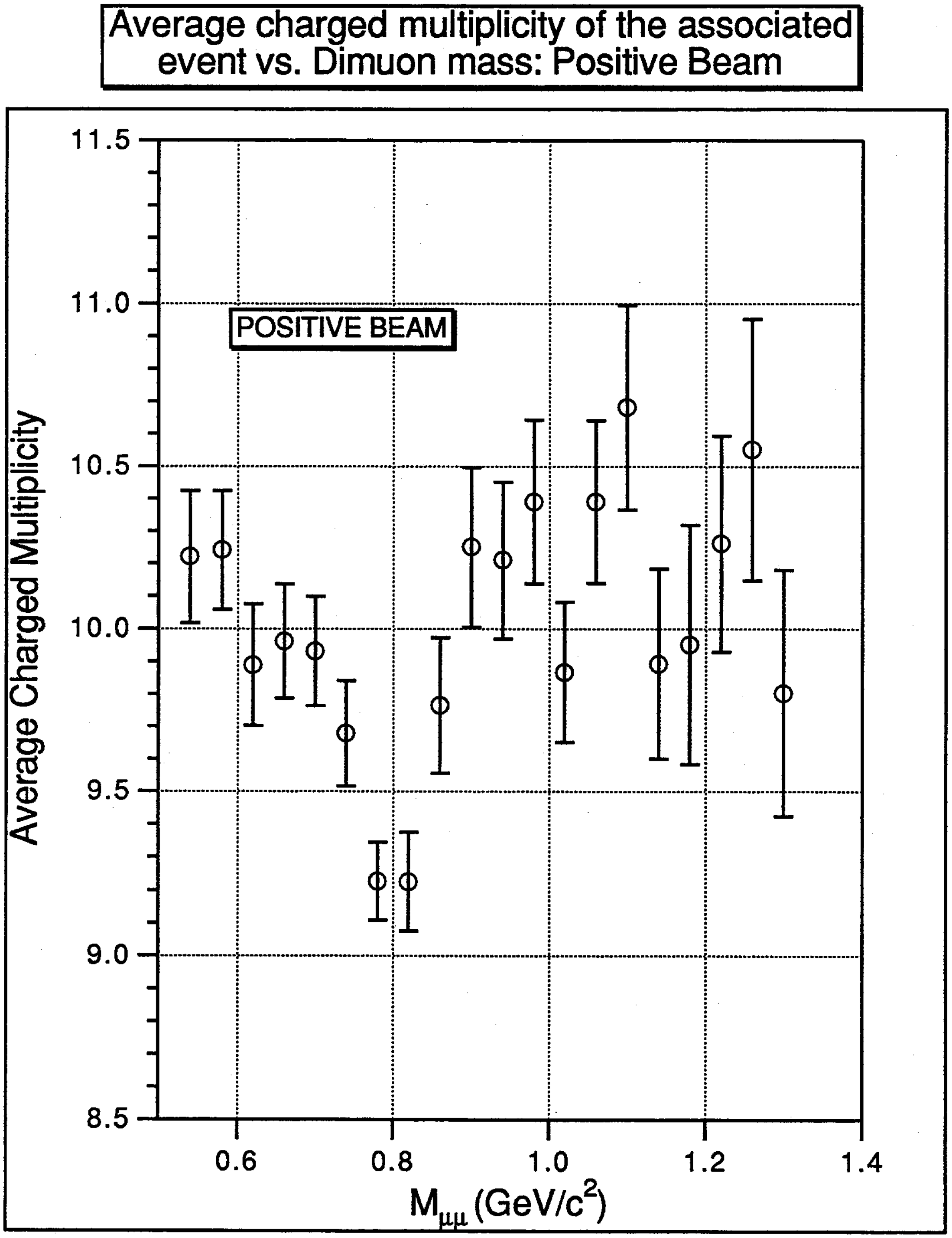

Average charged multiplicity of the associated event vs. Dimuon mass: Positive Beam
POSITIVE BEAM
Average Charged Multiplicity
11.5
11.0
10.5
10.0
9.5
9.0
8.5
0.6
0.8
1.0
1.2
1.4
Mμμ (GeV/c2)

FIGURE 9.12

Average Charged Multiplicity of the associated event vs. Dimuon mass: Negative beam

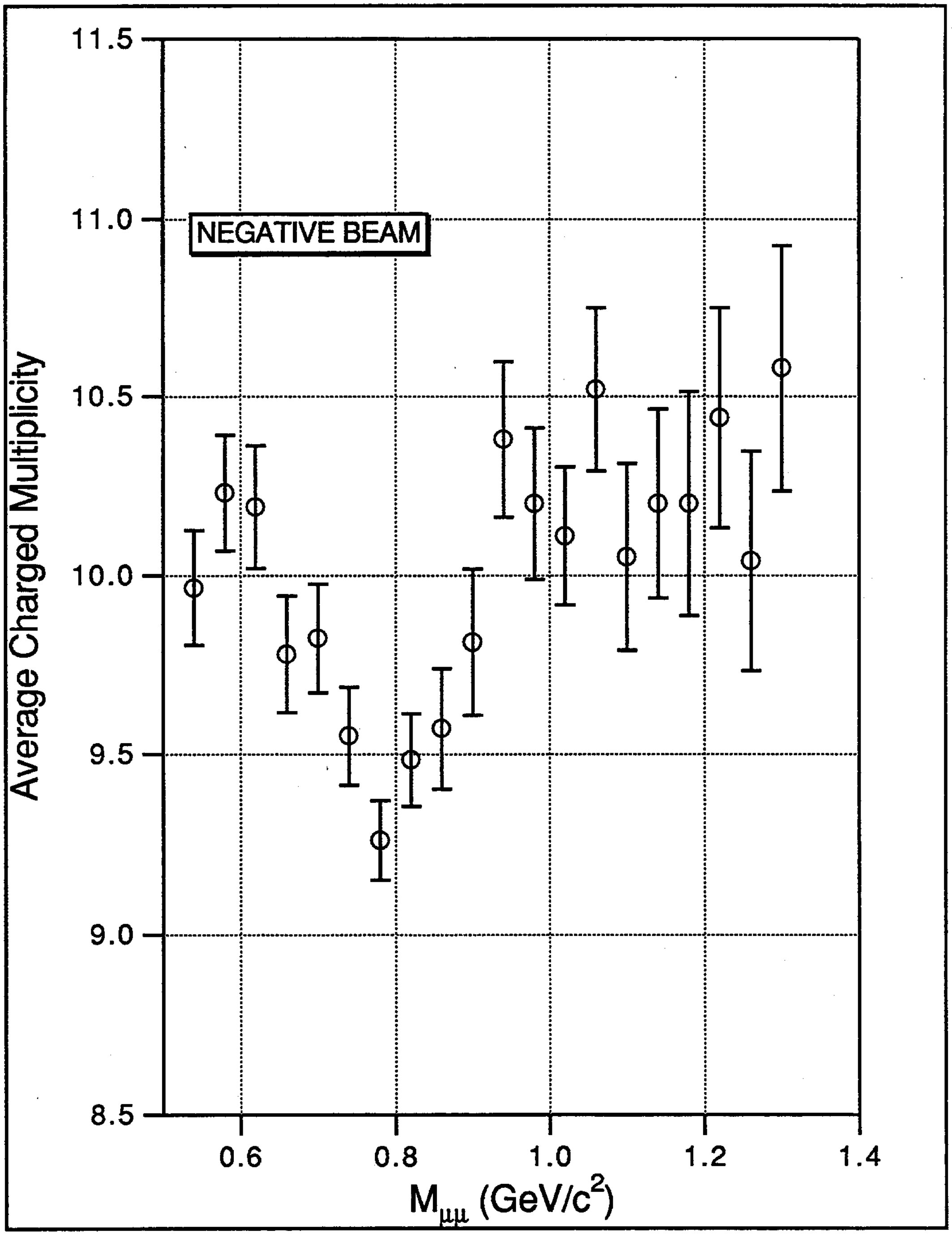

FIGURE 9.13

Scalar p_t sum for the associated event

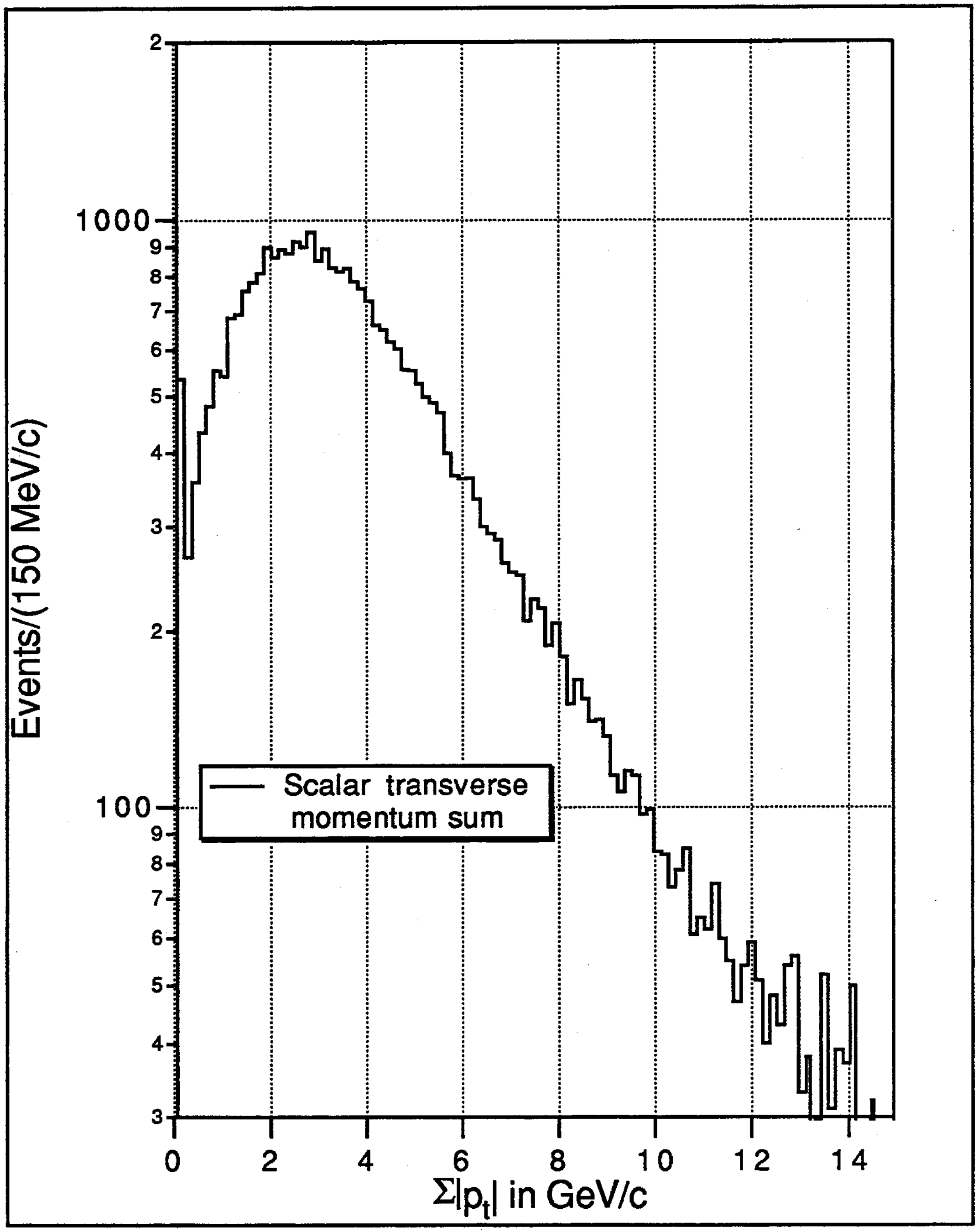

FIGURE 9.14

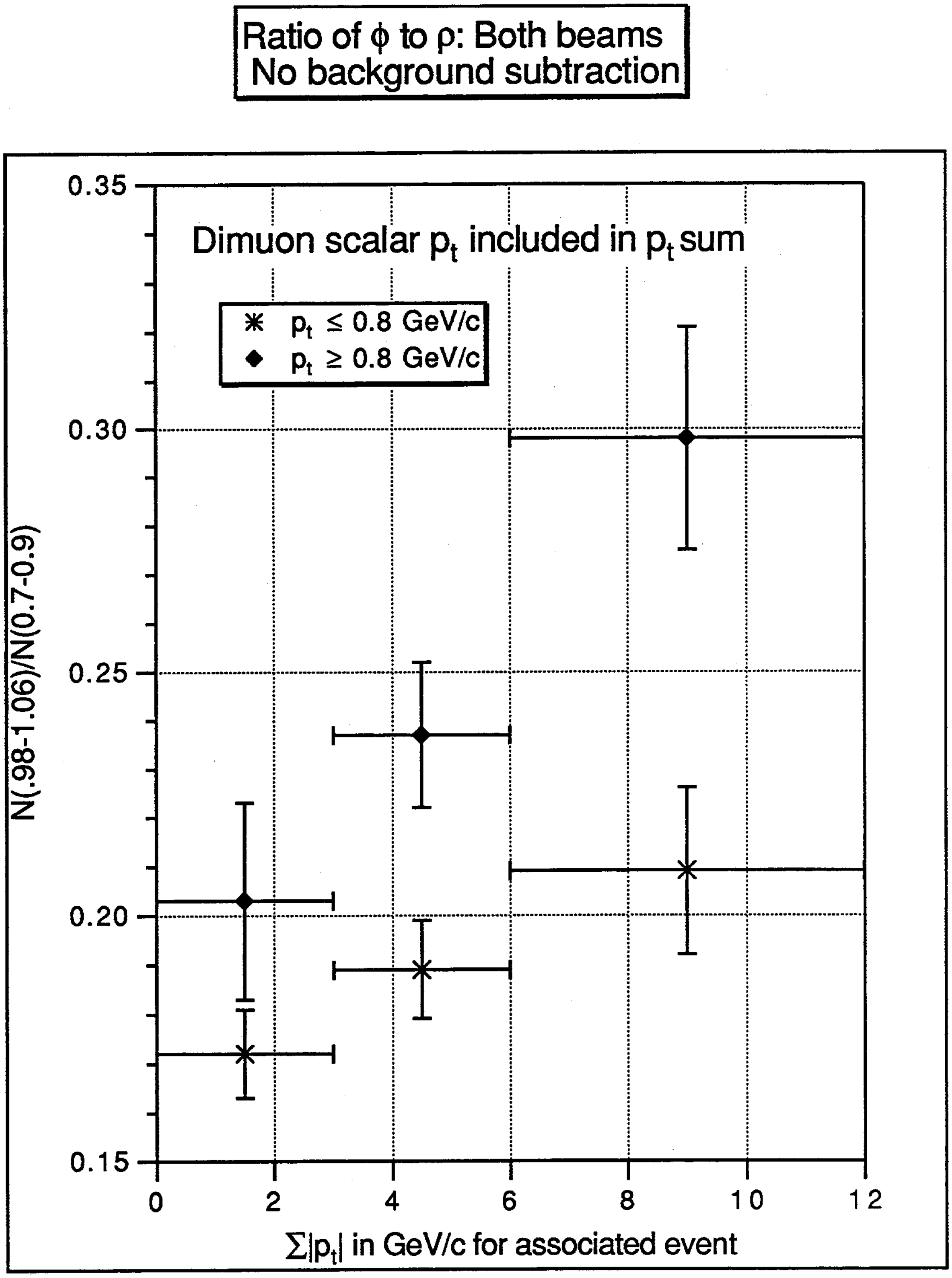
Ratio of ϕ to ρ: Both beams
No background subtraction
Dimuon scalar p_t included in p_t sum
$p_t \leq 0.8$ GeV/c
$p_t \geq 0.8$ GeV/c
N(.98-1.06)/N(0.7-0.9)
0.35
0.30
0.25
0.20
0.15
0
2
4
6
8
10
12
$\Sigma|p_t|$ in GeV/c for associated event

FIGURE 9.15

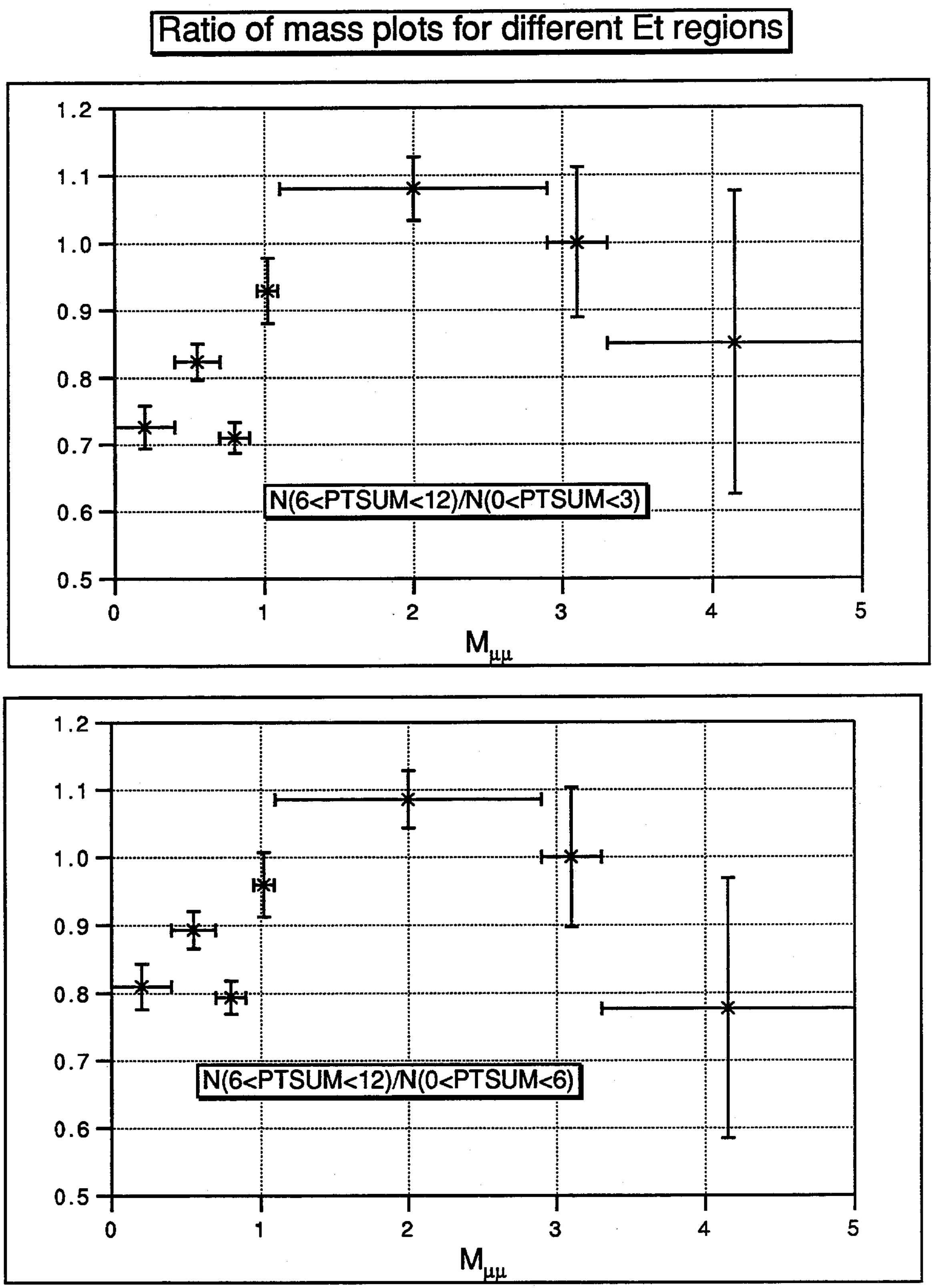
Ratio of mass plots for different Et regions
N(6<PTSUM<12)/N(0<PTSUM<3)
1.2
1.1
1.0
0.9
0.8
0.7
0.6
0.5
0
1
2
3
4
5
$M_{\mu\mu}$
N(6<PTSUM<12)/N(0<PTSUM<6)
$M_{\mu\mu}$

FIGURE 9.16

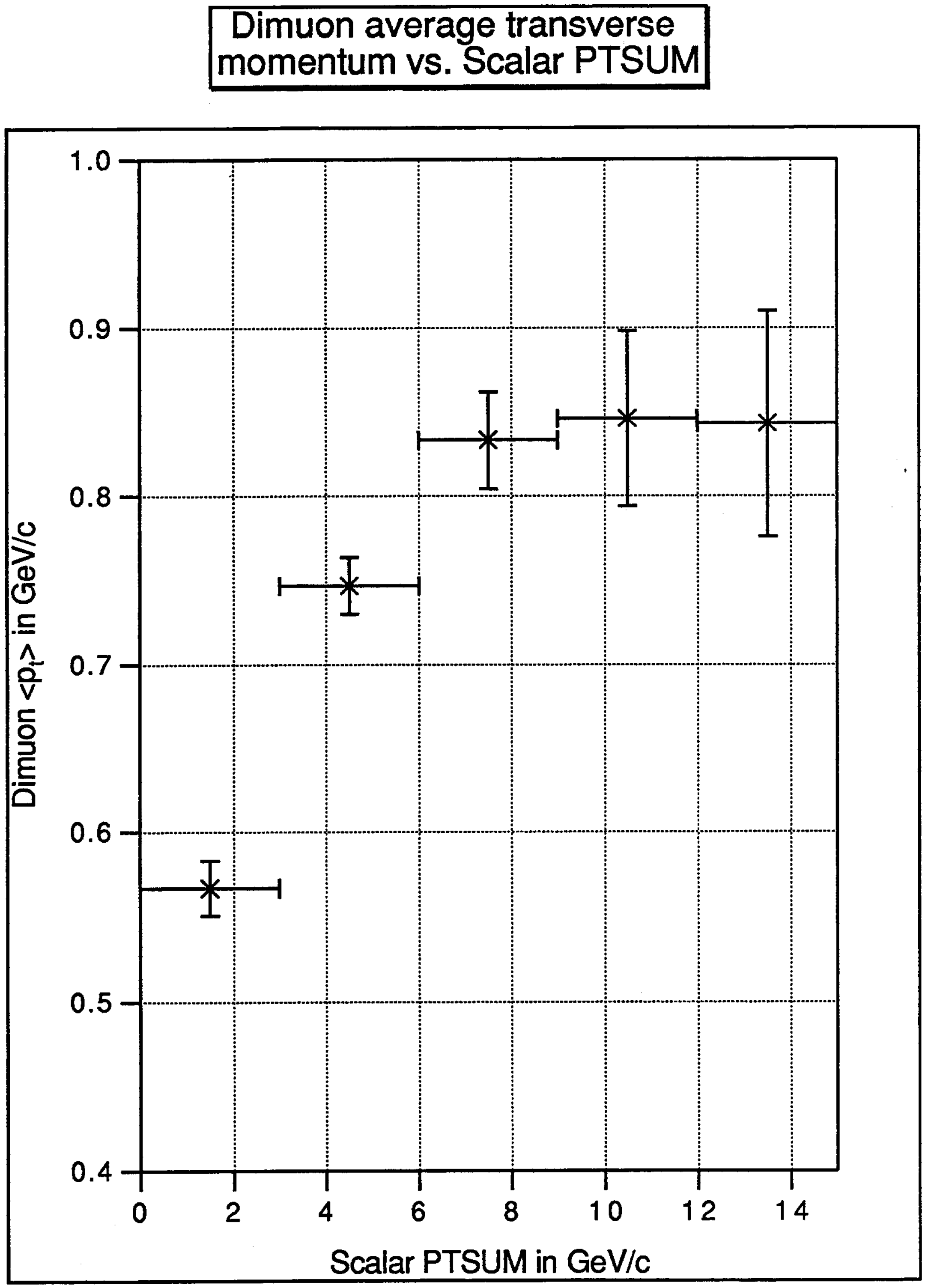

Dimuon average transverse momentum vs. Scalar PTSUM
1.0
0.9
0.8
0.7
0.6
0.5
0.4
Dimuon <p$_t$> in GeV/c
0
2
4
6
8
10
12
14
Scalar PTSUM in GeV/c

FIGURE 9.17

CHAPTER 10
CONCLUSIONS

In this chapter, the results obtained in this thesis are reviewed and compared with expectations from various models for vector meson production.

The A-dependence measurement for J/ψ production is discussed in light of different mechanisms proposed to understand the decreased effectiveness of J/ψ production with nuclear targets. The measurements of low-mass (ρ/ω and ϕ) cross sections are discussed and contrasted for different beams. The centrality of the production of vector mesons at these energies, as is evident from the steep x_F distributions measured, is discussed. The dependence of the average transverse momentum on center-of-mass energy is described and commented on. The expectations for ϕ/ρ enhancement in the Quark Gluon Plasma (QGP) scenario, and the conclusions from the observed enhancement are discussed.

Section 10.1

10.1.1 A-dependence of J/ψ production

The A-dependence for the production of J/ψs by 530 GeV/c negative pions incident on targets of carbon, aluminum, copper and lead was measured, as described in Chapters 5 and 6. In the forward region ($0.1 \leq x_F \leq 0.8$), using the parameterization $\sigma = \sigma_0 \cdot A^{\alpha}$, we obtain $\alpha = 0.85 \pm 0.06$, consistent with previous results at lower energies. No statistically significant dependence of α on either x_F or p_t has been observed. The x_F distribution for the

J/ψ was also measured and was found to be of the form

$$\frac{d\sigma}{dx_F} = A(1 - |x - 0.2|)^{2.6\pm0.2} \tag{10.1}$$

The previous measurements of the A-dependence are summarized in Table 10.1.

10.1.2 Comparison of results with theoretical calculations

Recently, several authors have proposed a comprehensive QCD-based model[1] for the x_F and nuclear dependence of charmonium production. The A-dependent effects in this model are attributed to the following:

— Final state absorption of the $c\bar{c}$ system in the nucleus

— Interactions with comoving partons

— Shadowing of parton distributions

— Intrinsic heavy quark content of the target and projectile

The motivation to introduce the intrinsic charm content as as important effect comes from the fact that the absorptive effects observed in heavy relative to light targets at high x_F are in disagreement with J/ψ production models based only on parton fusion. At moderate values of x_F the perturbative QCD model of parton fusion is dominant, with the intrinsic charm content becoming important at large x_F. Due to the large mass of the charm quark, it contributes significantly to the large x_F portion of the cross section.

Calculations have been done for the E672 results for the A-dependence and the x_F dependence of α and compared to the measurements. The results are shown in Figure 10.1, and are in good agreement with model.

The first plot in Figure 10.1 shows the A-dependence of the cross section as measured by this experiment, with the results of the model shown as the solid line. The next plot shows the ratio of the x_F distributions of Lead to Carbon, with the solid curve being the model predictions.

10.1.3 A model to understand the A-dependence

The A-dependence has been approached in terms of a recent model[2] which attempts to explain the x_F and p_t dependence by including the following processes:

— Incident hadron attenuation: The incident hadron loses energy at a rate of about 8 GeV/fm in the nuclear matter before the interaction producing the J/ψ

— J/ψ scattering/absorbtion: The J/ψ interacts with the nuclear matter before it can leave the nucleus. The absorbtion cross sections are expected to be of the order of 9 nb.

— Nuclear shadowing: The soft component of the gluons in the target nucleus are absorbed by the surrounding nucleons leaving the harder component intact. The preliminary results are in agreement with the data for proton beams, and the calculations for pion beams are in progress.

Section 10.2

10.2.1 Vector meson inclusive cross-sections

The vector meson cross sections were measured in the kinematic region $0.1 \leq x_F \leq 0.6$ for pion and proton beams. These cross sections were extrapolated to the forward region ($x_F \geq 0$) in Chapter 9. The cross section for the ρ is assumed to be equal to that for the ω. The ρ/ω cross sections for proton beams are shown in Figure 10.2 as a function of $\sqrt{s}$, compared to previous measurements [3–6]. Figure 10.3 shows the ρ/ω cross sections for π^- beams as compared to other measurements [6 7–12]. The total cross section was calculated by multiplying the forward cross section by 2, assuming that the production is symmetric about $x_F = 0$.

The ϕ forward ($x_F \geq 0$) cross section for proton beams is shown in Figure 10.4 compared to measurements at different energies[3 7 4 13 14]. Figure 10.5 shows the ϕ cross-sections for π^- beams compared to other experiments[8 7 14 15]

There is a general trend for the inclusive cross section to increase as a function of increasing energy. At high energies it is observed that the rate of increase seems to slow down. The region of the momentum fraction x of the target parton probed at the energies of this experiment for the ϕ is $1.7 \times 10^{-3} \leq x_2 \leq 9.4 \times 10^{-3}$. The structure functions for the partons are very poorly known in this region, and hence no attempt is made to interpret the increase in cross-sections.

The ϕ and ρ cross sections for the 530 GeV/c π^- beam are the highest energy measurements to date.

10.2.2 Vector meson kinematic distributions

The x_F distributions for the low-mass vector mesons were measured and the results shown in Chapter 9. Table 10.4 gives the exponents c as measured by E672 for the ρ/ω and ϕ for proton and pion beams.

Table 10.4

Exponents for x_F distributions

Resonance	Proton beam	π^- beam
ρ/ω	8.6 ± 0.4	6.6 ± 0.3
ϕ	9.9 ± 1.5	7.1 ± 0.9

The x_F distribution for ϕs had been measured by other experiments [16–18]. Figure 10.6 shows the exponent compared to those measured by other experiments at different energies for the ϕ with incident proton beams. The comparison for a π^- beam is shown in Figure 10.7. The production of ϕ's is seen to become very central at high energies, with the exponent rising rapidly as a function of $\sqrt{s}$.

When compared to other experiments at lower energies, there seems to be a tendency for the production of ϕ and ρ/ω to become very central at higher energies. This trend reflects the shape of the parton structure functions in the target.

The p_t^2 distributions for the low-mass vector mesons were also measured. Shown for comparison in Figures 10.8 and 10.9 are the $< p_t >$ values of this experiment as a function of center-of-mass energy, compared to other experiments. Figure 10.8 shows the $< p_t >$ for the ϕ resonance for proton beams and Figure 10.9 shows it for pion beams. There is a tendency for the average transverse momentum to increase as a function of center-of-mass energy, which is consistent with the results of this experiment. In addition, the average p_t for the ϕ is higher than that for the ρ, and this trend for the $< p_t >$ to increase with mass has also been seen to be true. The J/ψ, for example, has $< p_t >= 1.1$ GeV/c.

10.2.3 A-dependence of low mass vector mesons

The A-dependence of the ρ/ω mass region and the ϕ mass region has also been estimated in Chapter 9. The measured A-dependences from other experiments is shown for comparison in Table 10.2 for the ρ/ω and Table 10.3 for the ϕ. The A-dependence for the ρ/ω region is seen to be steeper than that for the ϕ or the J/ψ.

Section 10.3

10.3.1 The ratio of $\sigma(\phi)/\sigma(\rho)$

The ratio of ϕ to ρ cross sections was measured in Chapter 9. This ratio is shown for other experiments for comparison in Figure 10.10. The results are consistent with ϕ production being lower by a factor of 25 or so when compared to ρ/ω production. This ratio is expected to be close to unity in the Quark-gluon plasma (QGP) phase.

10.3.2 $\phi/\rho+\omega$ as a function of inelasticity

The results of the analysis of the ratio of $\phi/\rho + \omega$ as a function of the scalar charged transverse momentum sum of the associated event indicate that the ratio increases as a function of this variable. This would seem to confirm the results of NA38 where a similar enhancement has been reported. On further investigation though, it seems that the $\rho\omega$ production is being suppressed, as opposed to the ϕ being enhanced, as described in Chapter 9.

As the average transverse momentum of the dimuon is correlated with the inelasticity of the event, (as shown in Chapter 9), the enhancement is most naturally understood in terms of the ϕ being favoured at high inelasticity due to its higher $< p_t >$.

Further analysis is needed with higher statistics to investigate this issue.

Section 10.4

10.4.1 Conclusion

The A-dependence of J/ψ production for 530 GeV/c π^- beams has been measured in the region $0.1 \leq x_F \leq 0.8$. No significant dependence on x_F or p_t was seen. The A-dependence and the x_F behaviour of α are seen to consistent with recently proposed[1] QCD-based models.

The inclusive forward cross sections for the vector mesons ρ, ω, ϕ and the J/ψ have been obtained. They are seen to be consistent with trends observed at lower energies. The kinematic distributions for these resonances have also been studied. The enhancement of ϕ to ρ production as a function of event inelasticity have been investigated. Preliminary results indicate $\rho+\omega$ suppression rather than ϕ enhancement.

REFERENCES

1) R. Vogt, S. Brodsky and P. Hoyer, "Systematics of J/ψ Production in Nuclear Collisions", SLAC-PUB-5421 (T/E) 1991.

2) A. Zieminski and B. Kopelovich, Arizona Conference, May 1991

3) M. Albrow et al., *Nucl. Phys.* **B155**, 39 (1979) .

4) V. Blobel et al., *Phys. Lett.* **48B**, 73 (1974) .

5) V. Ammosov et al., *Sov. J. Nucl. Phys.* **24**, 30 (1976) .

6) F. Winkelmann et al., *Phys. Lett.* **56B**, 101 (1975) .

7) K. Anderson et al., *Phys. Rev. Lett.* **37**, 799 (1976) .

8) M. Aguilar-Benitez et al., CERN/EP 89-58 (1989).

9) T. Kitagaki et al. 4'th Int. Conf. on Meson Spec. Boston (Mass.) 1974, pg. 450.

10) J. Brau et al., *Nucl. Phys.* **B99**, 232 (1975) .

11) J. Bartke et al., *Nucl. Phys.* **B107**, 93 (1976) .

12) D. Fong et al., *Phys. Lett.* **60B**, 124 (1975) .

13) Y. Antipov et al., *Phys. Lett.* **110B**, 326 (1982) .

14) C. Daum et al., *Nucl. Phys.* **B186**, 205 (1981) .

15) B. Ghidini et al., *Phys. Lett.* **68B**, 186 (1977) .

16) H. Dijkstra et al., *Z. Fur Phys.* **C31**, 375 (1986) .

17) Y. Antipov et al., *Phys. Lett.* **110B**, 326 (1982) .

18) B. Ghidini et al., *Phys. Lett.* **68B**, 186 (1977) .

Table 10.1 : Experiments Studying the A-dependence of J/Ψ production

Exp.	Year	Beams	Energy (GeV)	Targets	$\sigma_A = \sigma_0 \cdot A^\alpha$ $\alpha =$	Range in x_F	Comments
CERN Ω	'82	$\pi^\pm$	39.5	H_2, W	0.98 ± 0.02	$x_F \geq 0.3$	$\alpha \Uparrow$ as $p_t \Uparrow$ $\alpha \Downarrow$ as $x_F \Uparrow$
IHEP Σ	'78	π^-	43	Be, Cu, W	0.92 ± 0.06	$x_F \geq 0$	$\alpha \Uparrow$ as $p_t \Uparrow$ α constant with x_F
FNAL E537	'88	$\pi^-, \bar{p}$	125	Be, Cu, W	$\pi : 0.87 \pm 0.02$ $\bar{p} : 0.90 \pm 0.03$	$0 \leq x_F \leq 0.8$	$\alpha \Uparrow$ as $p_t \Uparrow$ $\alpha \Downarrow$ as $x_F \Uparrow$
CERN NA3	'83	$\pi^\pm, K^\pm, p^\pm$	150-280	H_2, Pt	0.94 ± 0.03 0.96 ± 0.01	$x_F \geq 0$	$(29 \pm 6)\%$ of J/ψ Diffractive
FNAL CP	'77 '79	$\pi^\pm, K^\pm, p^\pm$	225	C, Cu, W	0.87 ± 0.02 0.97 ± 0.04	$x_F \geq 0$	$\alpha \Uparrow$ as $p_t \Uparrow$ α constant with x_F
FNAL	'76	n	~ 300	Be, Al, Cu, Pb	0.93 ± 0.04	$p_{lab} > 75$ GeV	
FNAL E672	'88 '90	π^-	530	C, Al, Cu, Pb Be, Cu	0.85 ± 0.06 0.87 ± 0.04	$0.1 \leq x_F \leq 0.8$	α constant with x_F α constant with p_t
FNAL E772	'90	p	800	D, C, Ca, Fe, W	0.92 ± 0.02	$x_F \geq 0.1$	$\alpha \Uparrow$ as $p_t \Uparrow$ $\alpha \Downarrow$ as $x_F \Uparrow$
CERN NA38	'91	p, O, S	200	Cu, U	0.91 ± 0.04	$2.8 < y_{lab} < 4$	Fit to $(A_p A_t)^\alpha$

Table 10.2 : Experiments Studying the A-dependence of ρ/ω production

Exp.	Year	Beams	Energy (GeV)	Targets	$\sigma_A = \sigma_0 \cdot A^\alpha$ $\alpha =$	Range in x_F, p_t	Comments
FNAL CP	'76	$\pi^\pm, p$	225	C, Ti	$\pi^+ : 0.72 \pm 0.03$ $p : 0.69 \pm 0.02$	$x_F \geq 0.15$	from the plot
FNAL	'76	n	~ 300	Be, Al, Cu, Pb	0.62 ± 0.03	$p_{lab} \geq 75\ GeV/c$	$\alpha \Uparrow$ as $p_t \Uparrow$ $\alpha \Downarrow$ as $x_F \Uparrow$
FNAL E672	'91	π^-	530	Be, Cu	0.77 ± 0.02	$0.1 \leq x_F \leq 0.6$	no x_F or p_t dependence
CERN NA3	'82	π p	150-200 200	H_2, Pt	$\sim 1.00 \pm 0.05_{sys}$ $\sim 1.00 \pm 0.05_{sys}$	$x_F > 0$ $p_t > 2$ GeV/c	$\alpha \Uparrow$ and $p_t \Uparrow$ $\alpha \Downarrow$ as $x_F \Uparrow$ $0.35 \leq M_{\mu\mu} \leq 1.5$ GeV/c^2

Table 10.3 : Experiments Studying the A-dependence of Φ production

Exp.	Year	Beams	Energy (GeV)	Targets	$\sigma_A = \sigma_0 \cdot A^\alpha$ $\alpha =$	Range in x_F, p_t	Comments
IHEP BIS–2	'90	n	30-70	C, Al, Cu	0.81 ± 0.06	$x_F \geq 0$ $p_t \leq 1\ GeV/c$	Λ, K enhancement
CERN ACCMOR	'83	p	100	H, Be	0.96 ± 0.04	$0.11 \leq x_F \leq 0.24$	Λ, K enhancement
CERN NA11	'84	π^+, p	120	Be, Ta	$\pi : 0.90 \pm 0.02$ $p : 0.86 \pm 0.02$	$0 \leq x_F \leq 0.3$ $p_t \leq 1\ GeV/c$	No x_F dependence $\sigma_{\phi N} = (8.8 \pm 2.2)$ mb
FNAL CP	'77	$\pi^\pm, p$	225	C, Ti	$\pi^+ : 0.77 \pm 0.04$ $p : 0.76 \pm 0.03$	$x_F \geq 0.15$	from the plot
FNAL	'76	n	~ 300	Be, Al,Cu, Pb	0.68 ± 0.03	$p_{lab} \geq 75\ GeV/c$	from the plot
FNAL E672	'91	π^-	530	Be, Cu	0.81 ± 0.04	$0.1 \leq x_F \leq 0.6$	no x_F or p_t dependence
CERN NA38	'91	p	450	C, Al, Cu, W	$\Delta\alpha_{\phi/\omega} =$ 0.09 ± 0.03	$-0.03 \leq x_F \leq 0.04$ $p_t \geq 1.3$ GeV/c	

Comparison of A-dependence results with model calculations

R. Vogt et al, SLAC-PUB-5421 (T/E) 1991.

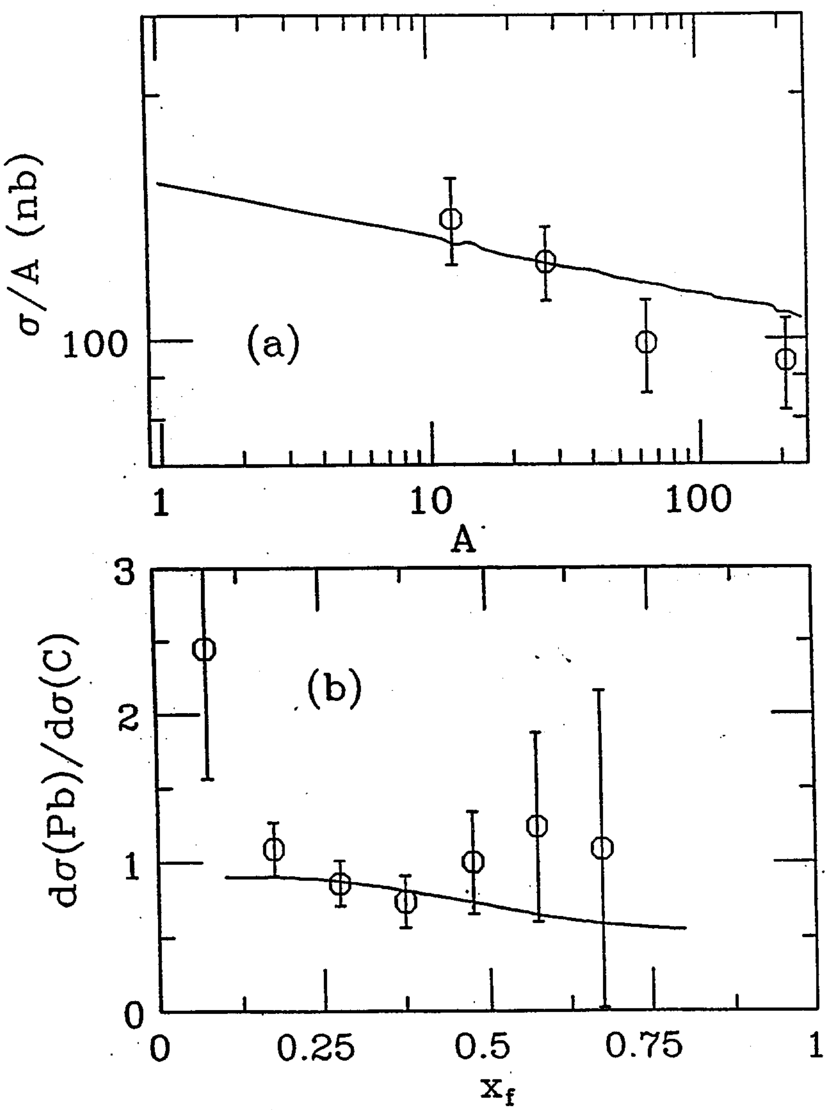

FIGURE 10.1

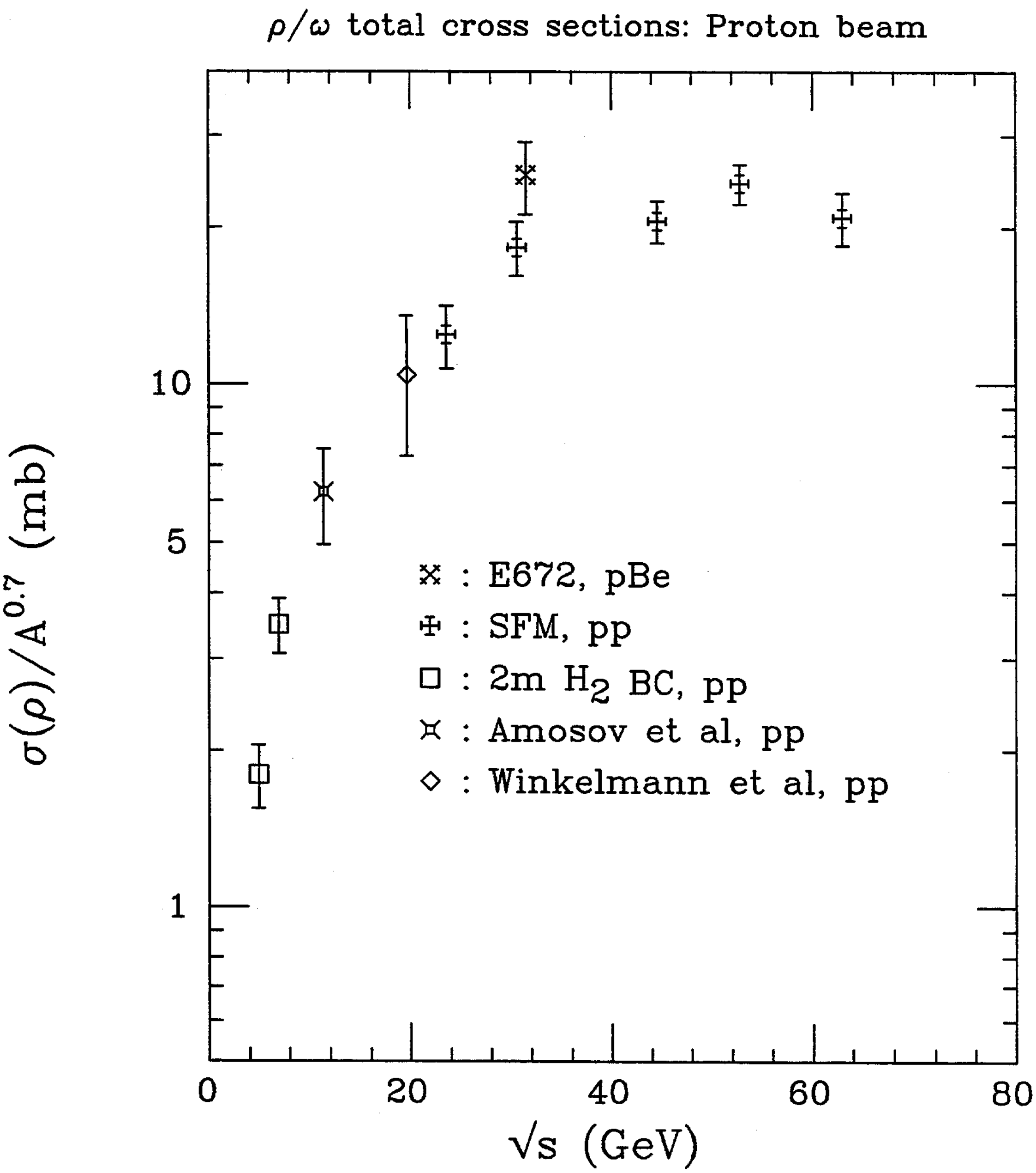

ρ/ω total cross sections: Proton beam
σ(ρ)/A^0.7 (mb)
10
5
1
0
20
40
60
80
√s (GeV)
E672, pBe
SFM, pp
2m H2 BC, pp
Amosov et al, pp
Winkelmann et al, pp

FIGURE 10.2

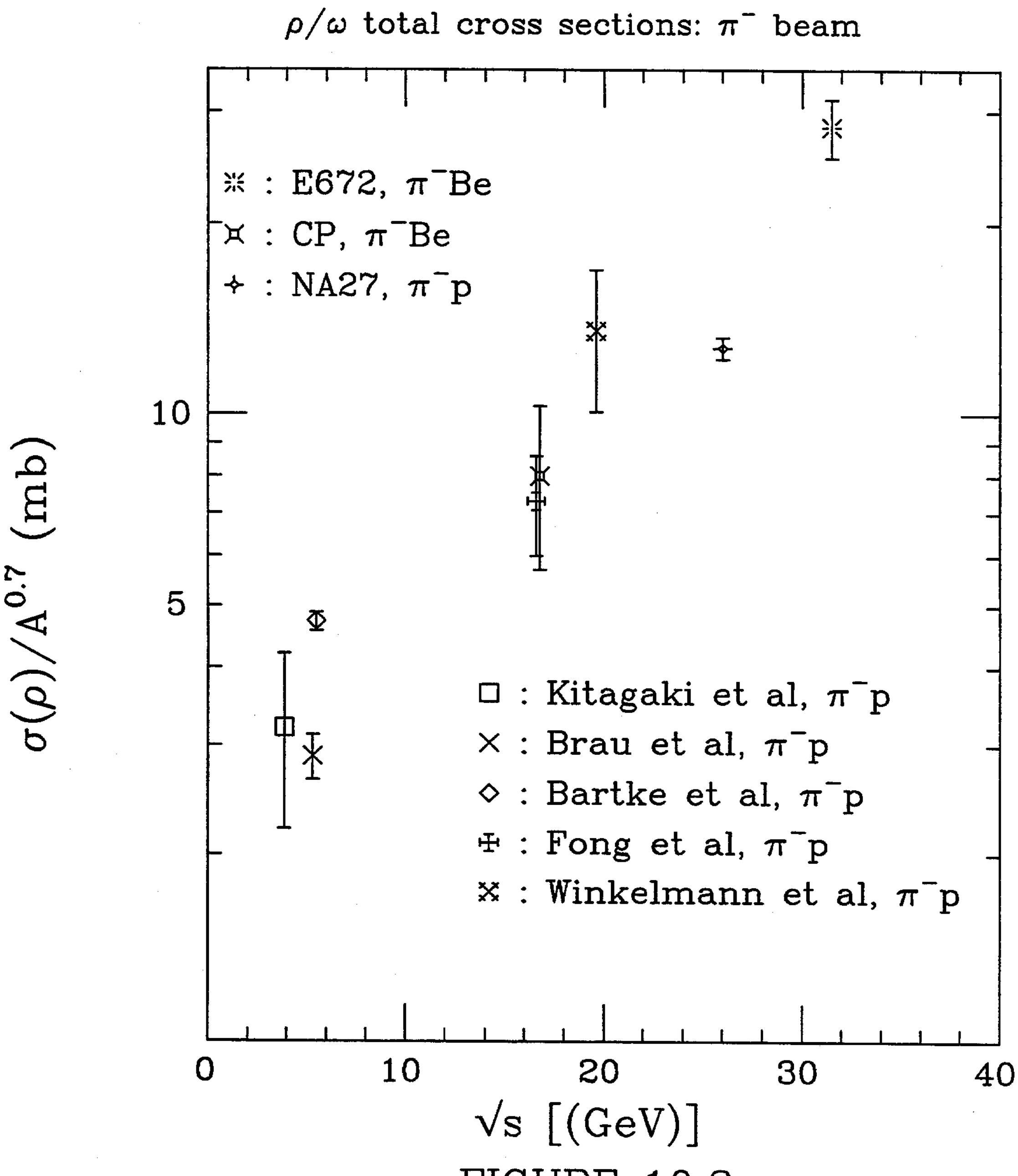
ρ/ω total cross sections: π⁻ beam
E672, π⁻Be
CP, π⁻Be
NA27, π⁻p
Kitagaki et al, π⁻p
Brau et al, π⁻p
Bartke et al, π⁻p
Fong et al, π⁻p
Winkelmann et al, π⁻p
σ(ρ)/A^0.7 (mb)
10
5
0
10
20
30
40
√s [(GeV)]

FIGURE 10.3

Summary of ϕ forward cross sections

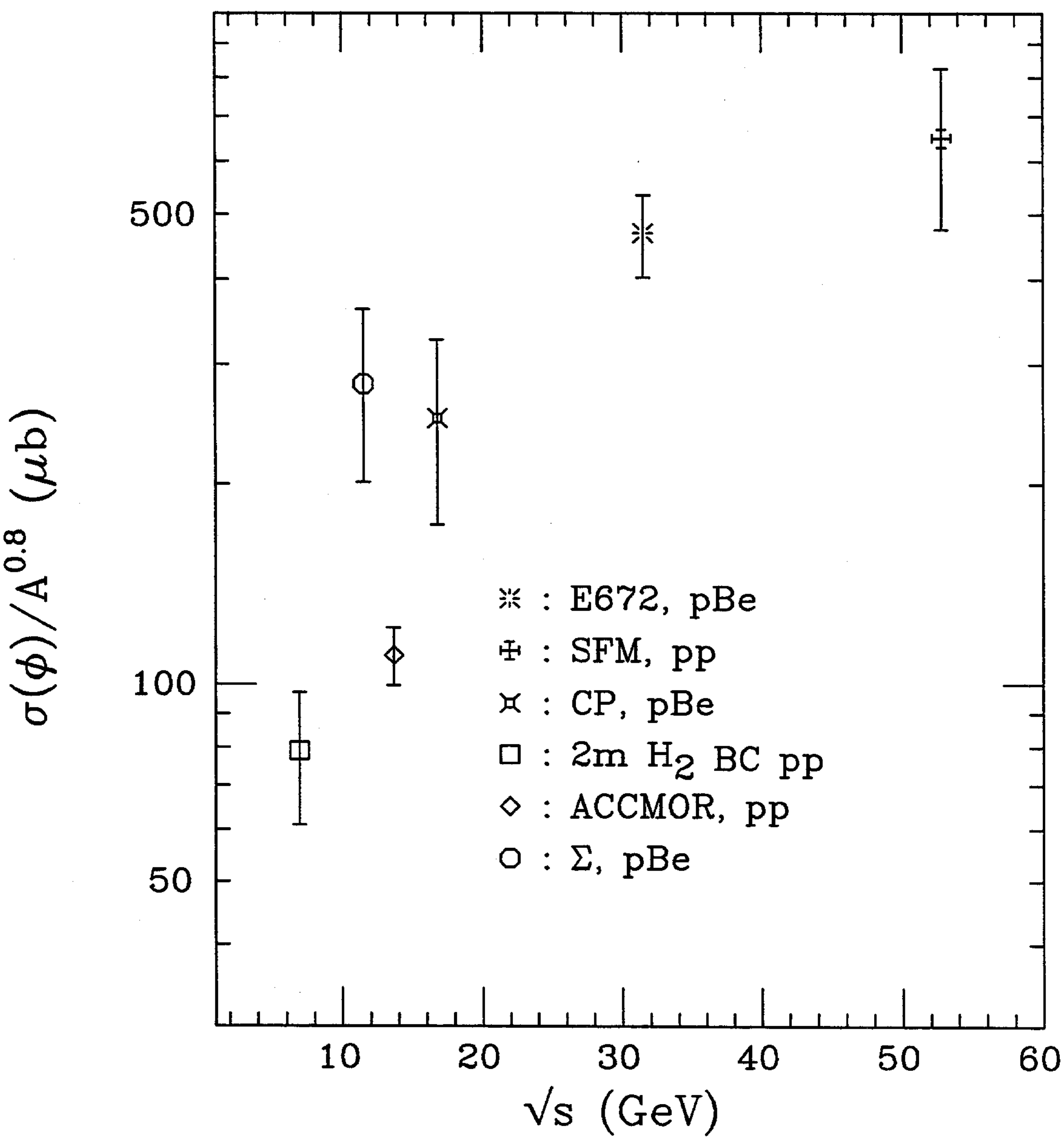

FIGURE 10.4

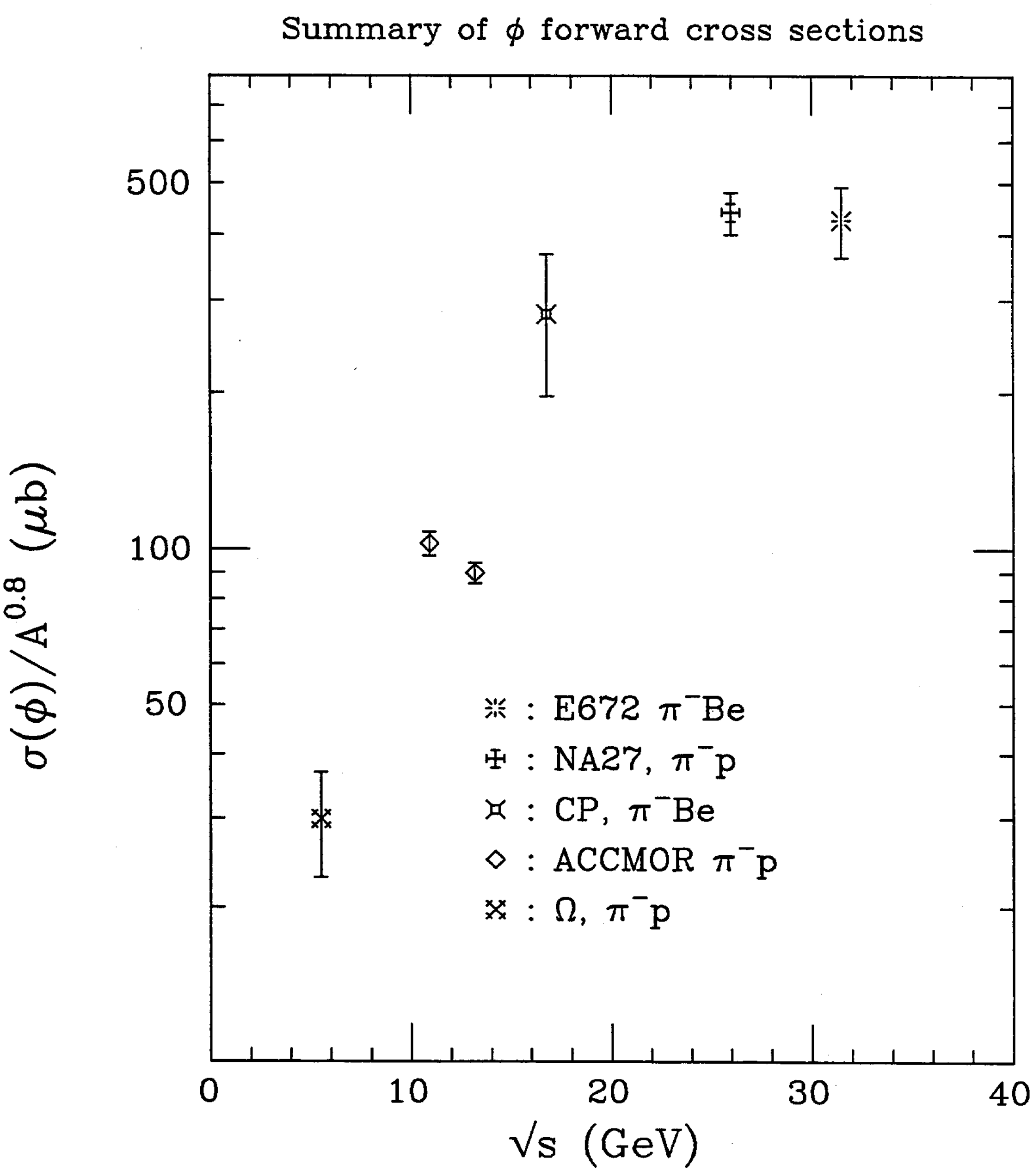
Summary of ϕ forward cross sections
500
100
50
0
10
20
30
40
$\sigma(\phi)/A^{0.8}$ (μb)
$\sqrt{s}$ (GeV)
: E672 π^-Be
: NA27, π^-p
: CP, π^-Be
: ACCMOR π^-p
: Ω, π^-p

FIGURE 10.5

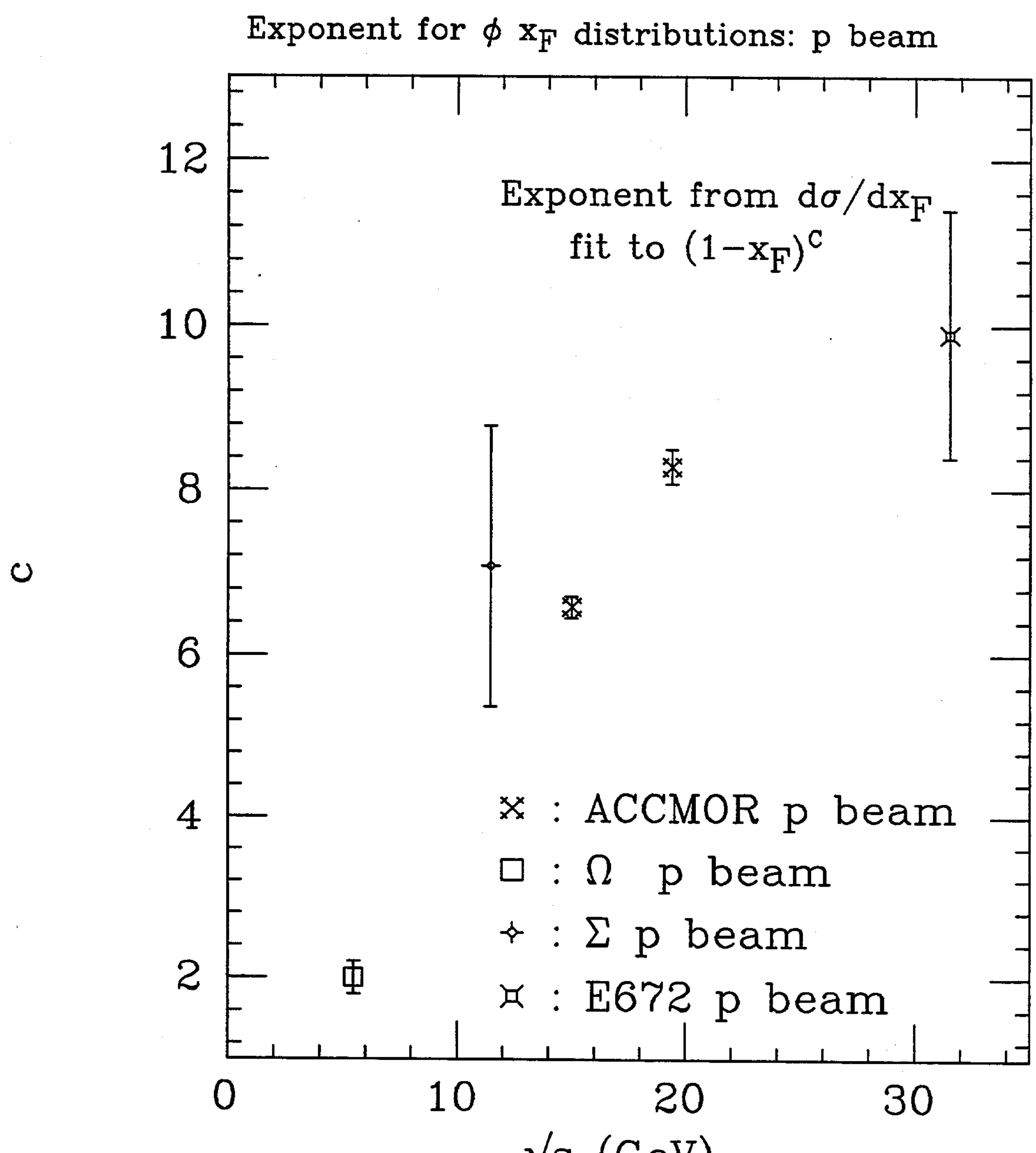

Exponent for ϕ x_F distributions: p beam
Exponent from $d\sigma/dx_F$ fit to $(1-x_F)^c$
12
10
8
6
4
2
0
10
20
30
c
: ACCMOR p beam
: Ω p beam
: Σ p beam
: E672 p beam
√s (GeV)

FIGURE 10.6

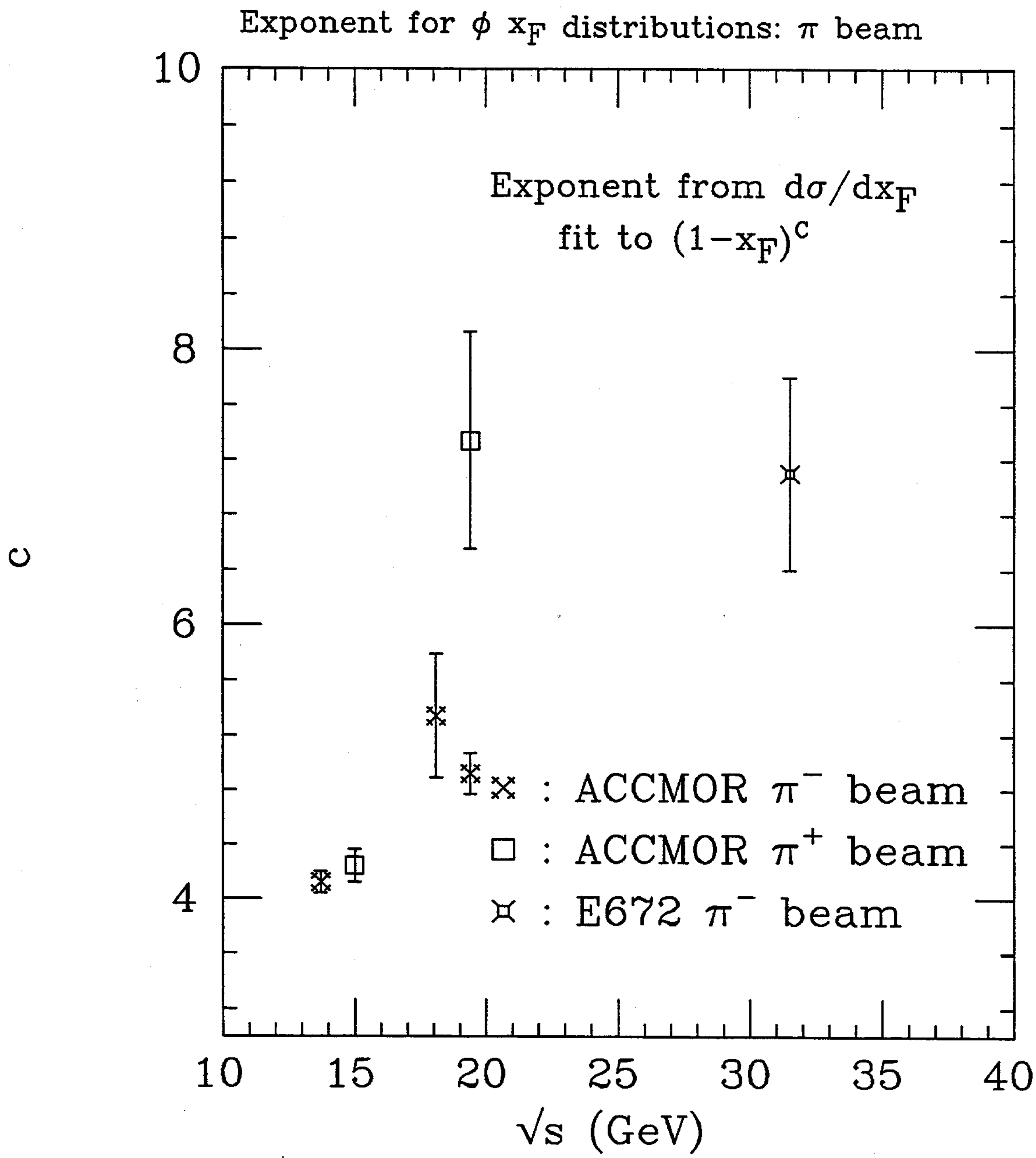
Exponent for ϕ x_F distributions: π beam
Exponent from $d\sigma/dx_F$
fit to $(1-x_F)^c$
: ACCMOR π^- beam
: ACCMOR π^+ beam
: E672 π^- beam
c
$\sqrt{s}$ (GeV)

FIGURE 10.7

$<p_t>$ FOR ϕ RESONANCE

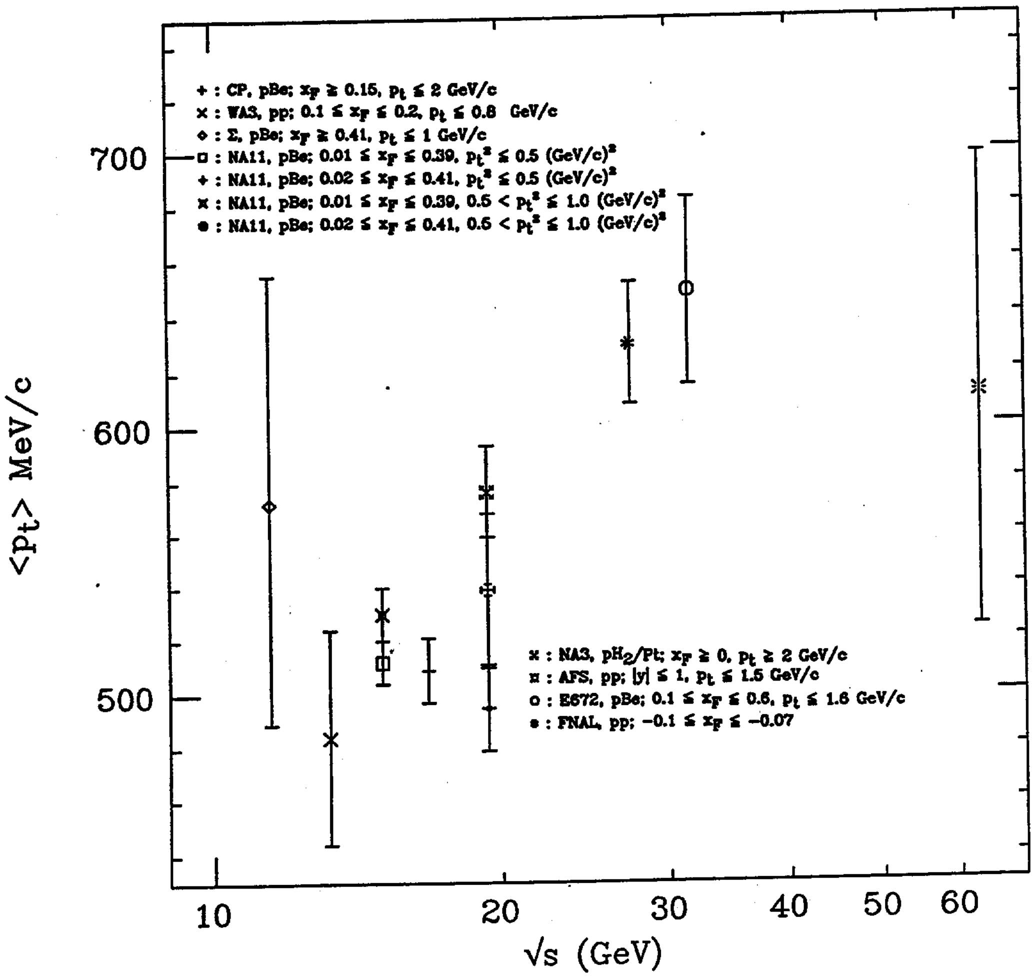

FIGURE 10.8

$\langle p_t \rangle$ FOR ϕ RESONANCE

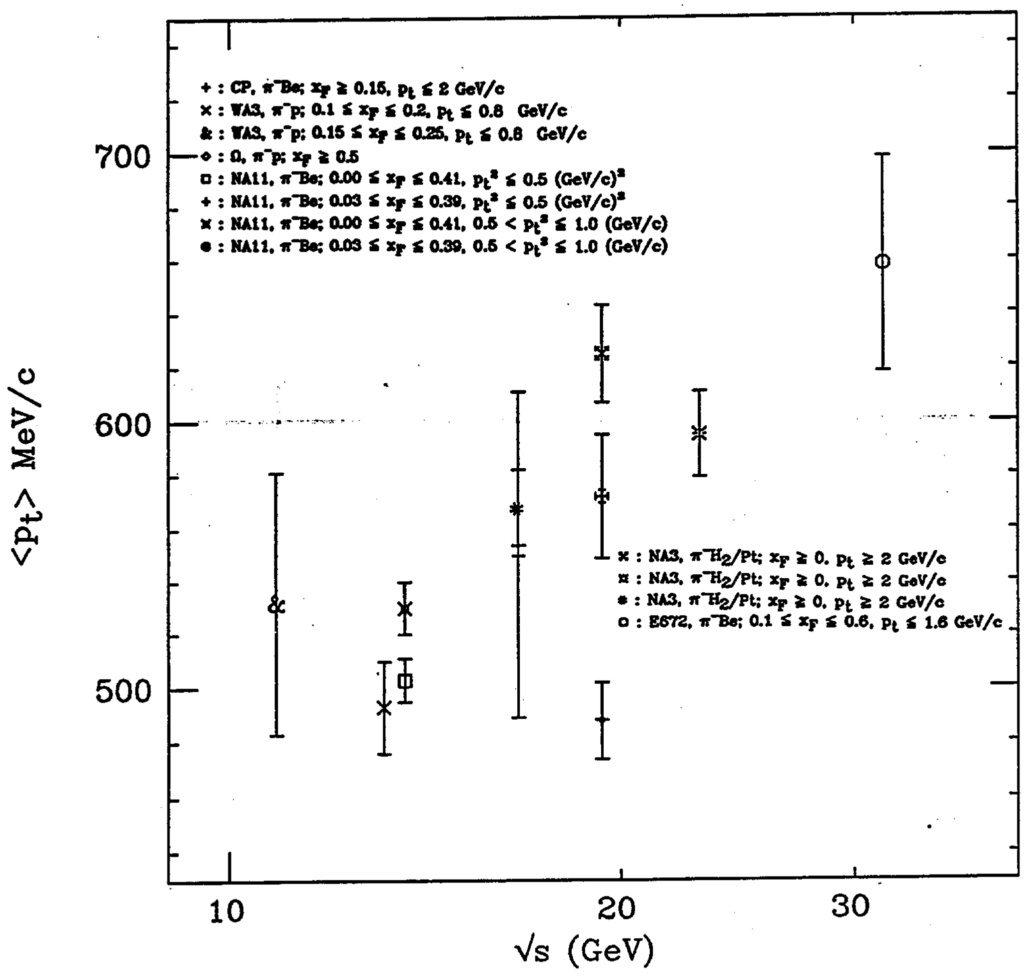

FIGURE 10.9

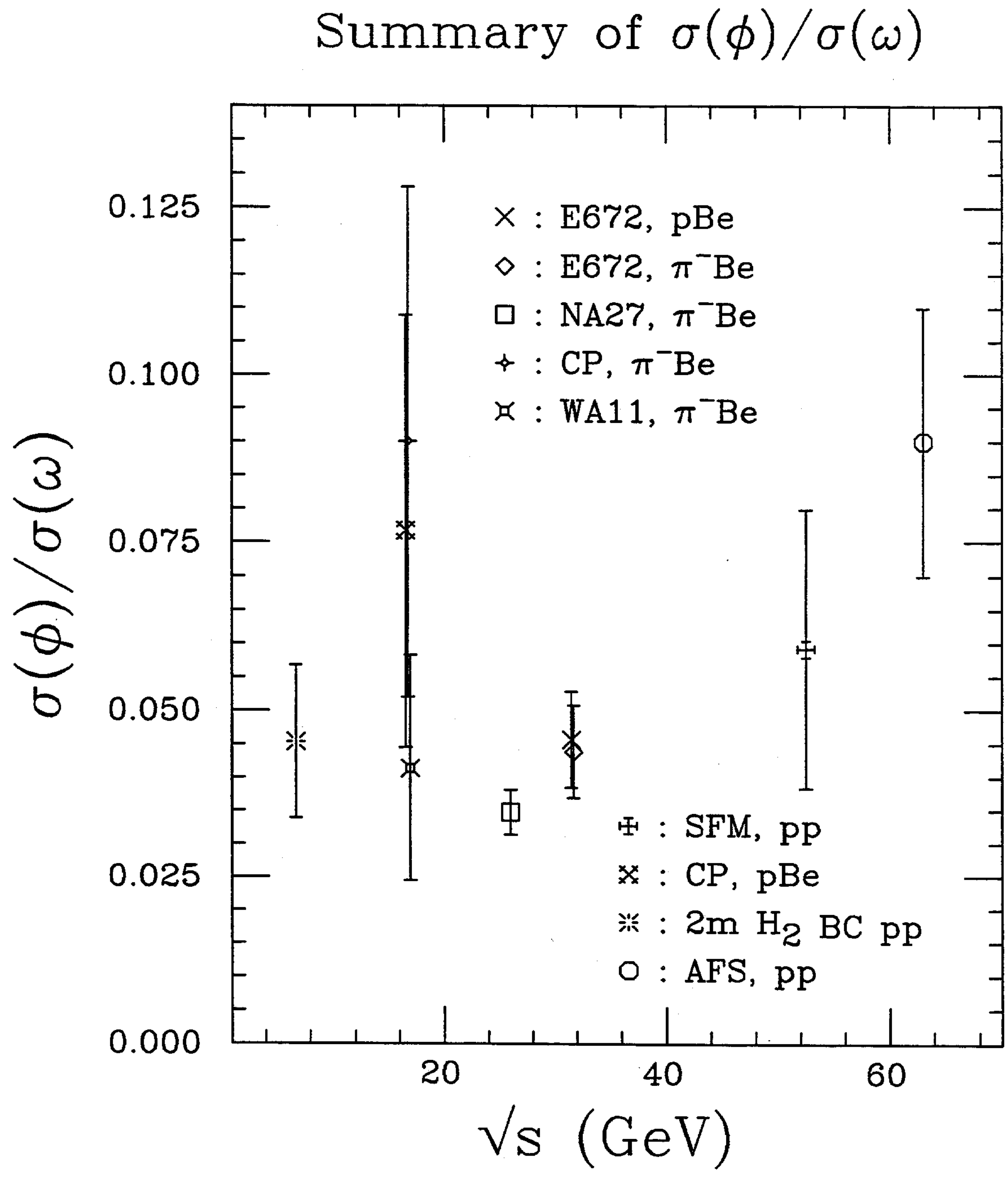

Summary of σ(φ)/σ(ω)
× : E672, pBe
◇ : E672, π⁻Be
□ : NA27, π⁻Be
✧ : CP, π⁻Be
⌘ : WA11, π⁻Be
⊞ : SFM, pp
✖ : CP, pBe
⋇ : 2m H2 BC pp
○ : AFS, pp
0.125
0.100
0.075
0.050
0.025
0.000
20
40
60
σ(φ)/σ(ω)
√s (GeV)

FIGURE 10.10

APPENDIX A

THE E672 COLLABORATION

R. Gomez

California Institute of Technology, Pasadena, CA 91125

J. Krider

Fermilab, Batavia, IL 60510

H. Goldberg, S. Margulies,J. Solomon

University of Illinois at Chicago, Chicago, IL 60680

R. Crittenden, K. De, A. Dzierba, S. Kartik, R. Li, S. Markham

T. Marshall, J. Martin, P. Smith, T. Sulanke, K. Welch, A. Zieminski

Indiana University, Bloomington, IN 47405

C. Davis

University of Louisville, Louisville, KY 40292

L. Dauwe

University of Michigan at Flint, Flint, MI 48503

V. Abramov, Yu. Antipov, B. Baldin, S. Denisov, V. Glebov,

Yu. Gorin, V. Koreshev, V. Kryshkin, S. Petrukhin, S. Polovnikov,

V. Sirotenko, R. Sulyaev

Institute for High Energy Physics, Serpukhov, USSR

5.) V. Abramov *et al.*, Properties of J/ψ production in π^--Be and p-Be collisions at 530 GeV/c, Fermilab preprint FERMILAB-Pub-91/62-E, 1991.